UNIVERSITÉ DE GENÈVE

Département de physique nucléaire et corpusculaire

CERN

FACULTÉ DES SCIENCES

Professeur Giuseppe Iacobucci

Dr. Andreas Salzburger

Jet Substructure Techniques for the Search of Diboson Resonances at the LHC and Performance Evaluation of the ATLAS Phase-II Inner Tracker Layouts

THÈSE

présentée à la Faculté des sciences de l'Université de Genève
pour obtenir le grade de Docteur ès sciences, mention physique

par

Noemi Calace

d'Italie

Thèse n° 5233

GENÈVE
Atelier d'impression ReproMail
2018

DOCTORAT ÈS SCIENCES, MENTION PHYSIQUE

Thèse de Madame Noemi CALACE

intitulée :

«Jet Substructure Techniques for the Search of Diboson Resonances at the LHC and Performance Evaluation of the ATLAS Phase-II Inner Tracker Layouts»

La Faculté des sciences, sur le préavis de Monsieur G. IACOBUCCI, professeur ordinaire et directeur de thèse (Département de physique nucléaire et corpusculaire), Monsieur A. SALZBURGER, docteur et codirecteur de thèse (Organisation européenne pour la recherche nucléaire (CERN), Suisse), Madame A. SFYRLA, professeure assistante (Département de physique nucléaire et corpusculaire), Monsieur X. WU, professeur associé (Département de physique nucléaire et corpusculaire) et Monsieur C. REMBSER, professeur (Département de physique, CERN - Organisation européenne pour la Recherche nucléaire, Genève, Suisse), autorise l'impression de la présente thèse, sans exprimer d'opinion sur les propositions qui y sont énoncées.

Genève, le 20 juin 2018

Thèse - 5233 -

Le Décanat

N.B. - La thèse doit porter la déclaration précédente et remplir les conditions énumérées dans les "Informations relatives aux thèses de doctorat à l'Université de Genève".

a Francesco
a te che fai danzare la mia anima

Wait for me to come home

Abstract

Jet and track reconstruction are two of the most difficult parts of the event reconstruction of hadron-hadron collisions, and yet they are crucial for the majority of the Large Hadron Collider (LHC) physics analyses. This thesis describes major contributions to jet reconstruction performance and its application in the search for diboson resonances in fully hadronic final states and, in a second part, it presents the design and preparation of the ATLAS tracking system for the future High Luminosity LHC (HL-LHC) physics program.

For the reconstruction of boosted hadronic jets, a new object, the Track-CaloCluster, has been developed to unify track and topo-cluster information and maximally benefit, at high transverse momentum, from the energy resolution of the calorimeter and the spatial resolution of the tracker. The combination of the strengths of both the calorimeter and the tracking systems into Track-CaloCluster jets has shown to significantly improve jet substructure performance over a wide range of the kinematic spectrum. This can be directly translated into an increase in sensitivity for the ATLAS physics program, especially in analyses where the jet substructure plays a critical role.

Profiting from the improved jet-substructure performance, a novel boosted boson tagging algorithm has been developed and optimised. The optimal working point for the boson tagger is evaluated in order to maximise the sensitivity to the hadronic decay of highly boosted W and Z bosons. The boson identification algorithm has led to improved sensitivity in the search for hadronic decays of boosted vector boson pairs. Compared to topo-cluster jets, Track-CaloCluster jets can provide approximatively 45% higher significance for 4 TeV W' resonances from the heavy vector triplet model.

In the HL-LHC conditions, that will be reached after the LHC upgrade between 2024 and 2026, the usage of the tracking system information will become even more fundamental. To cope with the high luminosity levels, ATLAS foresees important changes and upgrades of the detector which consists of the Phase-II upgrade program. It is crucial that the detector design maintains sensitivity to beyond Standard Model signatures, characterised by high-p_T leptons, photons, jets, and missing E_T, while improving and extending existing techniques to further expand the experimental physics reach. One of the main components of the ATLAS Phase-II upgrade program is the complete replacement of the Inner Detector with an entirely new tracking system. The new system is required to maintain and even surpass the performance of the current ATLAS Inner Detector, even at the harsh environment after the LHC upgrade. It is imperative to grant high reconstruction efficiency for the different physics objects, provide good vertex definition and pile-up mitigation extending the track-to-vertex matching to the currently-uncovered very-forward region in pseudo-rapidity, improve tracking in dense environment and b-tagging performance.

The design of the ATLAS Phase-II Inner Tracker and the evaluation of the performance of the candidate layouts are described in detail in the second part of this thesis. The process of defining benchmark performance requirements for the layout candidates to be able to optimise the design of the future detector is discussed in details taking into account many different aspects: tracking performance and their effects on the physics reach, impact on other sub-systems, detector buildability, mechanical properties, etc. The outcome of this process laid the groundwork for the decision of the layout presented in the ATLAS Phase-II Strip and Pixel Technical Design Reports.

Résumé

La reconstruction des traces et celle des jets hadroniques font partie des aspects techniques les plus difficiles dans l'analyse des données d'un collisionneur hadronique. Ces tâches sont malgré tout cruciales pour l'immense majorité des analyses de physique réalisées au Large Hadron Collider (LHC). Cette thèse décrit dans un premier temps un nouvel algorithme utilisé pour améliorer les performances de la reconstruction des jets hadroniques et son application à la recherche de résonance étroite dans un état final contenant une paire de bosons de jauge, chacun se désintégrant en deux quarks. Dans un second temps, la conception et la préparation de la mise à niveau du trajectographe de l'expérience ATLAS pour la prise de donnée à haute luminosité du LHC est présentée.

Pour la reconstruction des jets hadroniques, et notamment pour les jets hadroniques de haute impulsion transverse, un nouvel objet physique appelé Track-CaloCluster a été développé pour combiner de manière optimale les informations provenant du trajectographe, possédant la meilleure résolution spatiale, et celles des calorimètres ayant la meilleure résolution en énergie. La combinaison de ces deux mesures permet en effet d'améliorer grandement les performances de la reconstruction de la sous-structure des jets dans un large spectre en impulsion transverse.

Un nouvel algorithme de classification des bosons W et Z boostés se désintégrant hadroniquement, tirant partie des performances accrues de la sous-structure des jets, a été développé et optimisé. Les performances de cet algorithme d'étiquetage mènent à une amélioration de la sensibilité de la reconstruction aux bosons vecteurs boostés se désintégrant hadroniquement. Comparé aux jets obtenus grâce aux topo-cluster classiques, les jets reconstruits à partir de Track-CaloCluster peuvent fournir une sensibilité supérieure d'approximativement 45% pour des résonances W' de 4 TeV du modèle de triplet de vecteur lourd.

Vu les conditions difficiles prévues pour la prise de donnée à haute luminosité du LHC, après les mises à niveau de Phase-II entre 2024 et 2026, l'utilisation des mesures du trajectographe sera encore plus importante pour mitiger les effets liés au bruit d'empilement des événements. Le programme de mise à niveau de Phase-II d'ATLAS prévoit des changements importants du détecteur, notamment le remplacement complet du trajectographe actuel ainsi que son système de reconstruction, pour faire face aux niveaux de luminosité élevés attendus. Il est crucial que la conception du futur détecteur permette de maintenir ou d'améliorer le niveau de performance actuel pour la reconstruction et l'identification d'objets de haute impulsion transverse (photons, jets, leptons, énergie transverse manquante), et ceci afin d'améliorer la sensibilité aux scénarios de nouvelle physique. Il est donc impératif d'assurer la meilleure efficacité de reconstruction pour tous ces objets ainsi que d'améliorer la reconstruction du vertex d'interaction primaire tout en atténuant le bruit d'empilement et en étendant la trajectographie dans la région située le plus avant du détecteur et qui n'est actuellement pas instrumentée, ainsi que d'améliorer l'étiquetage des jets b.

La conception du trajectographe pour la mise à niveau de Phase-II du détecteur ATLAS et l'évaluation des performances des différentes options disponibles sont décrites en détails dans la seconde partie de cette thèse. Le processus permettant de décider de la meilleure option de detecteur possible prend en compte de nombreux aspects : performance de la trajectographie et effet sur la portée physique des analyses d'ATLAS, impact sur les autres sous-systèmes, propriétés mécaniques, etc.. Le résultat de ce processus de sélection a notamment été utilisé dans les Technical Design Reports des mises à niveau de Phase-II des détecteurs à Strips et à Pixel de l'expérience ATLAS.

Contents

Introduction

The Large Hadron Collider (LHC) is the world's largest and most powerful particle collider. It accelerates protons which are brought to collide inside independent experiments. The first LHC collisions took place in 2009 with a centre-of-mass energy of 900 GeV, which was increased to 7 TeV in 2010 and 2011. In 2012 the energy was raised to 8 TeV and since 2015 protons collide with bunch spacing of 25 ns (previously 50 ns) at a centre-of-mass energy of 13 TeV. The unprecedented collision energy and the considerable integrated luminosity made possible the discovery of the Higgs boson and the extension of the physics reach in the search for physics beyond the Standard Model in a completely new mass range.

This thesis focuses on the improvement of jet reconstruction algorithms and substructure techniques of the ATLAS experiment for the search for diboson resonances in fully hadronic final states. Indeed, one possible signature of new phenomena that may become visible in high energy proton-proton collisions is the production of pairs of boosted vector bosons (WW, WZ, ZZ) resulting from the decay of a heavy resonance, whose hadronic decay products are often reconstructed in two large radius jets. However, the production cross section for such heavy resonances is orders of magnitude smaller than that of jets initiated by quarks or gluons. New reconstruction and tagging techniques are therefore needed in order to distinguish jets containing the decay products of W and Z bosons from QCD-jets, mainly exploiting the internal substructure of these jets. This has been achieved thanks to the combination of the strengths of both the calorimeter and the tracker sub-systems into a new jet reconstruction method and to the implementation of a novel boosted boson identification algorithm.

In the High-Luminosity LHC (HL-HLC) conditions, the sensitivity to beyond the Standard Model signatures will rely even more on the tracking system information. The future ATLAS Inner Tracker that will replace the current inner detector, has to cope with the extremely harsh high-luminosity conditions while providing equal or better performance than that achieved by the current tracking system. The optimisation of the design of the future Inner Tracker and the evaluation of the performance of the candidate layouts are described in details in this thesis.

This thesis is structured in three major parts, where Part I introduces the Standard Model of particle physics, the LHC and the ATLAS experiment.
After a general overview of the jet reconstruction algorithms, Part II focuses on the development of a new object, the Track-CaloCluster, that unifies track and topo-cluster information and on the implementation and optimisation of a boosted boson tagging algorithm to identify boosted hadronically decaying vector bosons exploiting the improved jet substructure performance of Track-CaloCluster jets. Part III aims to describe the optimisation process of the design of the ATLAS Phase-II Inner Tracker and to discuss the performance evaluation of the main candidate layouts. It starts with listing the limitation of the current inner detector and the physics motivation of the HL-LHC, moves through the description of the candidate layouts and the software environment developed to implement and study them, and continues with the presentation of the basic tracking reconstruction performance. The third part is completed by the discussion of the list of recommendations that guided the design of the ATLAS Phase-II tracker and its optimisation, as described in the ATLAS Phase-II Strip and Pixel Technical Design Reports.

Personal Contribution

The ATLAS Collaboration is comprised of about 3000 scientists who are involved in the construction of detector components, the operation of the detector, the analyses of the collected data and many other tasks. The studies presented in this thesis thus rely on the work of many other people in the collaboration and are not performed by only one individual. The major contributions of the author in this thesis are listed below.

Part II – Improving Jet Substructure Techniques for Searching for Resonances with Boson-Tagged Jets

The author is one of the principal developers of the Track-CaloCluster (TCC) object and its reconstruction framework. Track-to-cluster matching studies and TCC reconstruction performance were studied by the author. The TCC jet collection was studied, especially focusing on the resolution of the jet mass and jet energy correlation variable D_2. The author derived the jet energy and mass calibration for the TCC jet collections that was studied in the optimisation of boosted boson tagging identification.

The author is the developer of the boosted boson identification algorithm that will be adopted in the search for narrow diboson resonances decaying to fully hadronic final states in 79.4 fb^{-1} of proton-proton collision data collected by the ATLAS experiment between 2015 and 2017 at $\sqrt{s} = 13$ TeV. This included (but is not limited to) the determination of the optimal working point in three different configurations: maximum-significance, fixed-signal-efficiency and fixed-background-rejection working points. The author was responsible of significance studies using the novel identification algorithm.

Part III – The ATLAS Tracking System Towards High-Luminosity LHC

The author worked on the optimisation of the *Inclined* Layout defining the position of the active sensor and iterating with mechanics groups in order to integrate engineering inputs, e.g. on the detector buildability, mechanical properties and amount of services.

The author has played a decisive role in the implementation of the main algorithms and tools to support the simulation of the ATLAS Phase-II Inner Tracker (ITk). Together with few other developers, the entire framework was put in place in a dedicated release. The author has shared the responsibility of the release coordination and has lead layout studies and the simulation and performance work for the optimisation of the ATLAS ITk layout. The author has done a valuable work in adapting the ATLAS Inner Detector track reconstruction to reflect the characteristics of the ITk layouts. The author also developed new algorithms needed to evaluate the optimistic and pessimistic performance of the different layouts under consideration.

The author has developed the framework to test the coverage of the layout options. It was studied considering multiple transverse and longitudinal vertex-smearing scenarios and different track transverse momenta. The author gave a relevant contribution to evaluate the performance of the ITk layout candidates in the contest of the ATLAS ITk Layout Task Force. Track parameter resolutions, efficiencies and fake rates were studied for different layout configurations and tested in presence of pile-up events, module misalignment and detector ageing effects.

The author is one of the principal analysers that defined the optimisation process of the ITk *Inclined* Layout which converged in the ITk *Inclined Duals* Layout, whose performance are described in the Technical Design Report for the ATLAS Inner Tracker Pixel Detector.

Part I

Theory and the ATLAS Experiment

1

Standard Model of Particle Physics

Contents

1.1 Introduction to the Standard Model

The Standard Model is the theory that describes elementary particles and their interactions [1–3]. It aims to interpret nature at the most fundamental level. Since its initial formulation in the 1970s, more than four decades of experiments have tested it and confirmed its predictions meticulously up to the TeV energy scale, providing a satisfactory explanation of nearly all known microscopic physical phenomena. Moreover, with the recent discovery of the Higgs boson the last missing piece has been added to the theory, making it one a very robust and successful physics model.

However, some open questions still remain: the Standard Model doesn't provide an explanation why there are three fermion generations and why their masses spread over more than twelve orders of magnitude. Moreover, it doesn't include a quantum theory for gravity and doesn't describe the dark-matter content of the universe. These and other unanswered questions suggest that a more fundamental theory is likely to exist. The Standard Model is indeed considered as an effective theory corresponding to the low-energy approximation of a more fundamental theory.

1.1.1 Particle Content and Interactions

The particle content of the Standard Model is shown in Figure 1.1. The force carriers are spin-1 bosons and mediate the fundamental interactions: the massless photon γ mediates the electromagnetic

interaction, the massive bosons $W^{\pm}$ and Z the weak interaction while the eight gluons the strong interactions. Fermions are spin-1/2 particles; the first generation of fermions (u, d, e^- and ν_e) forms ordinary. Fermions can be in turn divided into two families: quarks and leptons. While leptons have electroweak charge but no color charge, each quark with a given electroweak charge appears in three different stong-force charges (dubbed "colors", conventionally labelled as red, green, blue). For each of the particle, an antiparticle exists with identical properties and opposite charges. Quarks can not exist freely, but they form hadrons: baryons are made up of three quarks (qqq) while mesons are made up of one quark and one anti-quark ($q\bar{q}$). Leptons and quarks are arranged into three generations of increasing masses each consisting of a charged lepton (electron e, muon μ, tau τ) and the corresponding neutrino (ν_e, ν_μ, ν_τ), and an up-type (u, c, t) and a down-type (d, s, b) quark. The number of fermion generations is not predicted by the Standard Model. Anyhow, the number of light neutrinos can be inferred from precise measurements of the width of the Z resonance.

The spin-0 Higgs boson was introduced to explain the electroweak symmetry breaking and give mass to fermions and bosons via the Higgs mechanism [4, 5]. Although shown in Figure 1.1, the graviton, mediator of the gravitational force, is not included in the Standard Model as no quantum description of gravity is available.

The Standard Model is a quantum field theory [6]. It is defined by symmetry transformations of the Lagrangian and by the representation of the particles under these symmetries. The symmetry group of the Standard Model is

$$G_{SM} = SU(3)_C \times SU(2)_L \times U(1)_Y \tag{1.1}$$

where $SU(3)_C$ and $SU(2)_L \times U(1)_Y$ describe the strong and electro-weak interactions, respectively. The Lagrangian of the Standard Model is summarised in:

$$\mathcal{L}_{SM} = \mathcal{L}_{QCD} + \mathcal{L}_{EW}. \tag{1.2}$$

1.1.2   Quantum Chromodynamics

The strong interaction is described in the gauge theory called Quantum ChromoDynamics (QCD) [7] by the corresponding symmetry group $SU(3)_C$. The QCD Lagrangian is defined as:

$$\mathcal{L}_{QCD} = i \sum_r \bar{q}_{r\alpha} \gamma^\mu D_{\mu,\beta}^{\alpha} q_r^\beta - \frac{1}{4} \sum_i F_{\mu\nu}^i F_i^{\mu\nu} \tag{1.3}$$

with

$$F_{\mu\nu}^i = \partial_\mu G_\nu^i - \partial_\nu G_\mu^i - g_F f_{ijk} G_\mu^j G_\nu^k \tag{1.4}$$

where G^i, with $i = 1, ..., 8$, are the gluon fields, g_F is the strong coupling constant and f_{ijk} are the QCD structure constants. In the first term of Equation 1.3, q_r indicates the quark field of flavour r, with α and β the colour indices and the covariant derivative is defined as:

$$D_{\mu,\beta}^{\alpha} = \partial_\mu \mathbb{1}_\beta^\alpha + \frac{i}{2} g_F \sum_i G_\mu^i \lambda_\beta^{i,\alpha} \tag{1.5}$$

where λ^i are the three dimensional Gell-Mann matrices, generators of $SU(3)_C$.

The Lagrangian detailed in Equation 1.3 describes the interaction among the quark fields q_r mediated by the gluons, G^i, and the dynamics of the gluon fields (second piece in Equation 1.3), introducing as well the self-interaction of the exchange bosons coming from the non-abelian nature of $SU(3)$. This characteristic of the QCD Lagrangian translates in the behaviour of the coupling constant of the strong
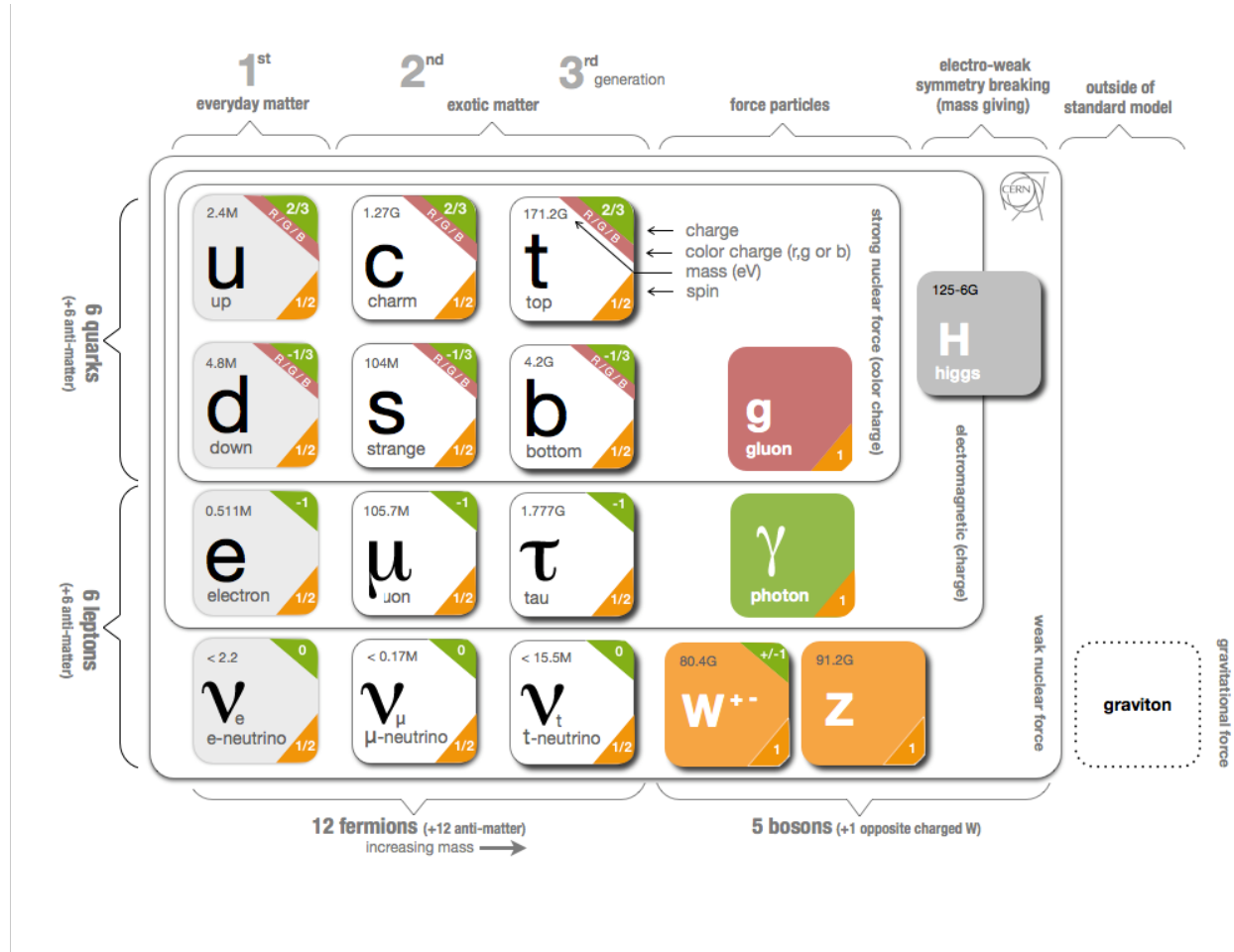
Figure 1.1: Schematic view of the particle content of the Standard Model. The interactions among them are also shown.

interaction $\alpha_s = \sqrt{4\pi g_F}$. In the one-loop approximation, α_s can be expressed as a function of the energy in:

$$\alpha_s(Q^2) = \frac{12\pi}{(11n_c - 2n_f)\log\left(\frac{Q^2}{\Lambda_{QCD}^2}\right)}, \tag{1.6}$$

where n_c is the number of colours, n_f the number of the quark flavours at a certain energy scale Q and Λ_{QCD} a chosen energy scale of about 200 MeV, defined as the scale where $\alpha_s(Q^2)$ formally diverges. Fixing the scale, α_s varies only with Q^2. When $Q^2 > \Lambda_{QCD}^2$, i.e. at large energy scales, the coupling constant is so small that the quarks can be considered free (asymptotic freedom) allowing a perturbative treatment of QCD. On the other hand, for $Q^2 \to 0$ (i.e. at long distances), α_s becomes larger and larger and the region of confinement is reached: quarks cannot be observed as free particles but they form colourless hadrons.

1.1.3 Electroweak Theory

Historically, the basic structure of the electroweak theory was formulated by S. Glashow [1], which was subsequently completed with the introduction of the electroweak symmetry breaking mechanism by S. Weinberg [2] and A. Salam [3]. Suggesting that electromagnetic and weak interactions were different manifestation of the same interaction, Glashow, Weinberg and Salam have formulated the electroweak theory based on a $SU(2)_L \times U(1)_Y$ gauge symmetry.
The $SU(2)_L$ symmetry is called weak isospin, and describe the weak interactions. As a chiral theory, it affects right-handed and left-handed fields in different ways.
The left-handed fields are doublets of $SU(2)_L$:

$$\begin{pmatrix} \nu_l \\ l^- \end{pmatrix}_L = \frac{1}{2}(1-\gamma_5)\begin{pmatrix} \nu_l \\ l^- \end{pmatrix}, \quad \begin{pmatrix} u \\ d' \end{pmatrix}_L = \frac{1}{2}(1-\gamma_5)\begin{pmatrix} u \\ d' \end{pmatrix} \tag{1.7}$$

where l indicates the leptons (e, μ, τ), u the up-type quarks (u, c, t) and d the down-type quarks (d, s, b). The down-type quarks are denoted with the prime to indicate the weak eigenstates which are combination of the mass eigeinstate via the unitary 3×3 Cabibbo-Kobayashi-Maskawa [8,9] matrix:

$$\begin{pmatrix} d' \\ s' \\ b' \end{pmatrix} = \begin{pmatrix} V_{ud} & V_{us} & V_{ub} \\ V_{cd} & V_{cs} & V_{cb} \\ V_{td} & V_{ts} & V_{tb} \end{pmatrix}\begin{pmatrix} d \\ s \\ b \end{pmatrix} \tag{1.8}$$

The generator of $SU(2)_L$ are the three Pauli matrices σ_i, with $i = 1, 2, 3$, and the corresponding quantum numbers for the $SU(2)$ doublets are:

$$t = \frac{1}{2} \quad \text{and} \quad t_3 = \pm\frac{1}{2}. \tag{1.9}$$

where t is the weak isospin and t_3 its third component. The right-handed fields have $t = 0$ and are singlets of $SU(2)_L$, i.e. they are invariant under weak isospin transformations:

$$l_R, u_R, d'_R \tag{1.10}$$

where again l indicates the leptons (e, μ, τ), u the up-type quarks (u, c, t) and d the down-type quarks (d, s, b).
The missing right-handed neutrinos in the Standard Model derive from the fact that they are treated as massless particles. However, neutrino oscillation experiments have proven that they have mass,

although small. An extension of the Standard Model introduces the Pontecorvo-Maki-Nakagawa-Sakata matrix to describe the mixing between neutrino flavour eigenstates ν_α ($\alpha = e, \mu, \tau$) and the mass eigenstates ν_i ($i = 1, 2, 3$).

The symmetry group $U(1)_Y$ is associated to the weak ipercharge Y, which is related to the electric charge Q and the weak isospin through the Gell-Mann-Nishijima relation:

$$Q = t_3 + \frac{Y}{2}. \tag{1.11}$$

The bosons of the $SU(2)_L \times U(1)_Y$ gauge group are W_μ^i, $i = 1, 2, 3$, and B_μ respectively for the $SU(2)_L$ and $U(1)_Y$ groups. From the linear combination of the four boson fields, it is possible to obtain the physical gauge bosons:

$$A_\mu = B_\mu \cos\theta_W + W_\mu^3 \sin\theta_W \tag{1.12}$$

$$Z_\mu = W_\mu^3 \cos\theta_W - B_\mu \sin\theta_W \tag{1.13}$$

$$W_\mu^\pm = \frac{W_\mu^1 \mp iW_\mu^2}{\sqrt{2}} \tag{1.14}$$

where A_μ is the photon field γ and Z_μ and $W_\mu^\pm$ are associated to the neutral and charged weak boson fields, respectively. The Weinberg angle θ_W, introduced in the previous equations, is defined as:

$$\sin\theta_W = \frac{g'}{\sqrt{g^2 + g'^2}} \tag{1.15}$$

$$\cos\theta_W = \frac{g}{\sqrt{g^2 + g'^2}} \tag{1.16}$$

where g and g' are the coupling constants corresponding to $U(1)_Y$ and $SU(2)_L$, respectively. The electric charge can be then written as a function of g and θ_W is the following way:

$$e = g \sin\theta_W = g' \cos\theta_W. \tag{1.17}$$

The analytical expression of the electroweak Lagrangian is:

$$\mathcal{L}_{EW} = -\frac{1}{4} \sum_G F_G^{\mu\nu} F_{G,\,\mu\nu} + i \sum_f \bar{f} D_\mu \gamma^\mu f. \tag{1.18}$$

with the indices G and f summed over the vectorial fields and the fermions, respectively. More in detail, the tensors $F_G^{\mu\nu}$ describe the dynamic of the boson fields, while the second term in Equation 1.18 describes the interaction among fermions mediated by the four bosons, which is contained in the covariant derivative D_μ:

$$D_\mu = \partial_\mu - ig_G(\lambda^\alpha G_\alpha)_\mu \tag{1.19}$$

where g_G is the coupling constant of the field G ($G = A, Z, W^\pm$) and λ^α are the generators of the group the field G refers to.

1.1.3.1 The Higgs Mechanism

In the way it is described, the Standard Model Lagrangian is invariant under local gauge transformations and describes massless particles. This contradicts the experimental evidence of the mass of all the particles, except for gluons and photons. Moreover, it is not possible to introduce a mass term in Equation 1.2 without losing the gauge invariance of the theory. This puzzle was solved with the

introduction of the electroweak symmetry breaking mechanism, known as Brout-Englert-Higgs mechanism [4,5].

Let us introduce a new self-interacting isospin doublet of scalar fields:

$$\Phi = \begin{pmatrix} \phi^+ \\ \phi^0 \end{pmatrix} \tag{1.20}$$

with

$$\phi^+ = \frac{\phi_1(x) + i\phi_2(x)}{\sqrt{2}} \qquad\qquad \phi^0 = \frac{\phi_3(x) + i\phi_4(x)}{\sqrt{2}} \tag{1.21}$$

where $\phi_i(x)(i = 1, 2, 3, 4)$ are scalar real fields.

An additional piece has to be introduced into the Standard Model Lagrangian in order to contain the dynamic of the new field:

$$\mathcal{L}_H = (D^\mu \Phi)(D_\mu \Phi) - V_H \tag{1.22}$$

where the covariant derivative is defined as:

$$D^\mu = \partial^\mu + \frac{i}{2} g \sigma_j W_j^\mu + \frac{i}{2} g' Y B^\mu \tag{1.23}$$

where g and g' are the $SU(2)_L$ and $U(1)_Y$ gauge couplings, respectively, σ_j, with $j = 1, 2, 3$, are the usual Pauli matrices and Y the weak ipercharge. The potential is dependent on two parameters λ and μ as follows:

$$V_H = \mu^2 \Phi^\dagger \Phi + \lambda [\Phi^\dagger \Phi]^2. \tag{1.24}$$

Requiring a stable theory, i.e. that the Hamiltonian has at least one minimum, implies that the coupling constant λ is positive, $\lambda > 0$. The sign of the parameter μ^2 can be either positive or negative. The symmetry of $SU(2)_L \times U(1)_Y$ can be broken if $\mu^2 < 0$ so that degenerate minima are present. As a consequence, the vacuum expectation value is:

$$< 0|\Phi(x)|0 >= \Phi_0 = \begin{pmatrix} \phi_0^+ \\ \phi_0^0 \end{pmatrix} \tag{1.25}$$

with $\Phi^\dagger \Phi = -\frac{\mu^2}{2\lambda}$. In order to preserve the Lagrangian $U(1)_Y$ gauge invariance and leave the photon massless, the ground state is chosen to be:

$$\Phi_0 = \frac{1}{\sqrt{2}} \begin{pmatrix} 0 \\ v \end{pmatrix} \tag{1.26}$$

where

$$v = \frac{|\mu|}{\sqrt{\lambda}} \tag{1.27}$$

is the vacuum expectation value for the Higgs field. As no preferred direction is present, the ground state is not symmetric under $SU(2)_L \times U(1)_Y$ transformation and therefore the electroweak symmetry is spontaneously broken.

The physics behind the Higgs mechanism is obtained considering the perturbative expansion of the Lagrangian around the ground state. Usually, the field Φ is expanded around the ground state as:

$$\Phi = \frac{1}{\sqrt{2}} \begin{pmatrix} 0 \\ v + h(x) \end{pmatrix} \tag{1.28}$$

where $h(x)$ is the real scalar Higgs field which corresponds to the Higgs boson. Inserting Equation 1.28 into Equation 1.22 yields the mass terms of the gauge bosons:

$$L_H = \underbrace{\frac{1}{2}\partial_\mu h \partial^\mu h}_{\text{kinetic term}} + \underbrace{\frac{1}{4}g^2 v^2 W_\mu^+ W^{-\mu} + \frac{1}{8}(g^2 + g'^2)v^2 Z_\mu Z^\mu - \lambda v^2 h^2}_{\text{mass terms}} - \underbrace{\lambda v h^3 - \frac{1}{4}h^4}_{\text{Higgs self-coupling}} . \tag{1.29}$$

where the terms of the order $\mathcal{O}(HW^+W^-, HZZ, HHW^+W^-, HHZZ)$ have been neglected. Three out of the four degrees of freedom of the complex scalar Higgs field are absorbed as longitudinal modes of the Z and $W^\pm$ bosons and generate their masses which can be expressed as:

$$m_Z = \frac{v}{2}\sqrt{g^2 + g'^2} \qquad m_W = \frac{v}{2}g. \tag{1.30}$$

The remaining degree of freedom gives the mass to the Higgs boson

$$m_H = \sqrt{2}\mu = \sqrt{2\lambda}v \tag{1.31}$$

which is not predicted by the theory because of its dependence on the unknown parameter λ.

Now, it is possible as well to give the mass to the fermions via the Yukawa coupling of the Higgs and the fermions field. $\mathcal{L}_{EW}$ gains therefore two additional pieces for both the lepton and the quark sectors. For leptons:

$$\mathcal{L}_{lep} = -G_l \left[(\bar{\nu}, \bar{l})_L \begin{pmatrix} \phi^+ \\ \phi^0 \end{pmatrix} l_R + h.c. \right]. \tag{1.32}$$

Using Equation 1.28, $\mathcal{L}_{lep}$ becomes:

$$\mathcal{L}_{lep} = -m_l \bar{l}l - \frac{m_l}{v}\bar{l}lh \tag{1.33}$$

which contains a mass term and an interaction term between the leptons and the Higgs field. Analogously, for the quark sector it is possible to introduce the mass terms in the Lagrangian as:

$$\mathcal{L}_{quark} = -m_d^i \bar{d}_i d_i \left(1 + \frac{h}{v} \right) - m_u^i \bar{u}_i u_i \left(1 + \frac{h}{v} \right). \tag{1.34}$$

Both Equation 1.33 and Equation 1.34 show that the coupling constant g_f, describing the Higgs boson coupling to the fermion f, is proportional to the mass of the fermion m_f:

$$g_f = \frac{\sqrt{2}\, m_f}{v}. \tag{1.35}$$

Almost 50 years after its prediction, the discovery of the Standard Model Higgs boson was announced on July 2012 by the ATLAS and CMS Collaborations at the Large Hadron Collider [10, 11]. Both collaborations focused on the decay of the Higgs boson into boson pairs in the most sensitive channels: $H \to ZZ^* \to 4l$, $H \to \gamma\gamma$ and $H \to WW^* \to e\nu\mu\nu$. The most recent mesurement of the Higgs mass using the combined ATLAS and CMS datasets is $m_H = 125.09 \pm 0.21(\text{stat.}) \pm 0.11(\text{syst.})$ GeV [12], while the spin $= 2$ hypothesis was excluded by the ATLAS Collaboration with a confidence level above 99.9% [13]. Recently, the coupling of the Higgs boson to bottom quarks was measured by the CMS Collaboration [14], resulting in the first measurement of the Higgs boson coupling to a fermion.

1.1.4 Limitations of the Standard Model

Figure 1.2 shows that the Standard Model of particle physics predicts experimental measurements over a wide range. Although its remarkable success, several experimental observations cannot be explained in the current theoretical framework.

- The experimental observation of neutrinos oscillations requires that neutrinos have mass in order to allow for the mixing between mass and flavour eigenstates. Two main models, describing neutrinos as Dirac or Majorana fermions, can introduce massive neutrinos in the Standard Model: if neutrinos are Dirac fermions their right-handed component has to be added to the Standard Model Lagrangian, while if they are Majorana fermions neutrinos are their own antiparticles[1]. However, the nature of neutrinos has not been determined yet.

- The Standard Model doesn't explain the source of the asymmetry between matter and antimatter. At the Big Bang, matter and antimatter were produced in equal quantities. Nowadays, there is no antimatter in the universe. This asymmetry can be partially explained introducing CP violation in the Standard Model: it has been theoretically described and experimentally measured in the electroweak sector, but still too small to be the only responsible for the matter-antimatter asymmetry.

- The amount of ordinary (baryonic) matter corresponds only to roughly 4.9% of the entire mass-energy content of the observable universe while the remaining $\sim 95\%$ consist of dark matter and dark energy, which are not included in the Standard Model.

- The Standard Model does not provide an explanation why there are three fermion generations and why their masses spread over more than twelve orders of magnitude.

- By construction the Standard Model describes three of the four fundamental interactions, leaving so far gravity outside the mathematical formulation.

- Another peculiar problem of the Standard Model is the so-called hierarchy problem which indicates the difference of the Standard Model theory at the electroweak scale ($\mathcal{O}(10^2 \text{ GeV})$) and at the Plank scale (10^{19} GeV). At the tree-level, the mass of the Higgs boson receives contributions from fermionic loops in the form:

$$\delta m_H^2 = \sum_f -\frac{g_f^2 \Lambda^2}{16\pi^2} \tag{1.36}$$

  where Λ is the cut-off scale[2] and g_f is the Yukawa coupling of the Higgs boson to the fermion f (which is proportional to the fermion mass m_f). Indicating with m_{H_0} the bare Higgs mass, which is the parameter of the Lagrangian, the effective mass can be written as:

$$m_H^2 = m_{H_0}^2 + \delta m_H^2 \tag{1.37}$$

  with δm_H^2 containing all the radiative corrections. If Λ corresponds to the Plank scale, i.e. the Standard Model is the only theory up to that energy scale, the bare mass of the Higgs boson should be fine-tuned until the 17$^\text{th}$ decimal figure in order to result in the observed Higgs mass $m_H \sim 125$ GeV. Although the fine-tuning is not a problem per se, cancellations of loop corrections at a precision of the order of 10^{-17} seem to be rather unnatural.

---

[1] Signals on the neutrinos nature might come from the evidence of the neutrinoless double β decay.

[2] The Standard Model can be considered as an effective field theory valid until the energy scale Λ, known as cut-off scale.

Figure 1.2: Summary of Standard Model production cross-section measurements and their comparison with the corresponding theoretical expectations. The luminosity used for each measurement is indicated close to the data point in the legend. The cross-section measurements spread over 14 orders of magnitude [15].
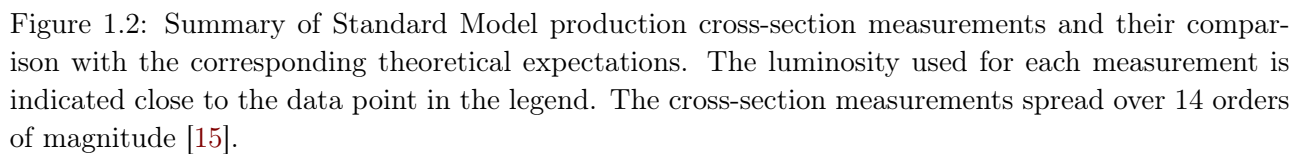
1.2   Looking Beyond the Standard Model

In order to address some of the aforementioned open questions, several models and theories beyond the Standard Model (BSM) have been developed over the last decades.

1.2.1   Diboson Signatures for Beyond Standard Model Theories

The content of this thesis will not focus on a particular BSM theory but rather on a specific signature which can be produced in many of these models. One possible signature of new phenomena that may become visible in high-energy proton-proton collisions is the production of pairs of vector bosons (WW, WZ, ZZ) resulting from the decay of a heavy resonance. Many models predict such a signature: extended gauge symmetry models [16, 17], composite-Higgs model [18] as well as little Higgs [19] and two-Higgs-doublet models [20], Grand Unified Theories [21, 22], theories with new strong dynamics [23], including technicolour [24], theories with warped extra dimensions [25, 26]. The main three models considered as benchmarks in previous diboson resonance searches will be discussed in this section mentioning as well the most recent results obtained by the ATLAS and CMS collaborations.

1.2.1.1   Extended Gauge Symmetry Model

The Extended Gauge Symmetry Model (EGM) [16, 17] is a general theory that predicts the existence of heavy spin-one vector bosons $W'^{\pm}$ and Z' similar to the Standard Model $W^{\pm}$ and Z. For the W', which will be the only case discussed in the next sections, the coupling to both leptons and quarks are assumed to be equivalent to the Standard Model ones. Because of the mixing of the EGM and Standard Model bosons, the triple boson coupling $W'WZ$ is suppressed by a factor $c \cdot (m_W^2/m_{W'}^2)$. The suppression factor implies a linear increase of the width of the EGM boson with its mass, approximately of 3.5% the resonance mass. In absence of the suppression factor, i.e. $c = 1$, the width would increase with the fifth power of the new boson mass. The off-shell production of the W' via $q\bar{q}$ generates a low-mass tail in the W' mass spectrum: the bigger the mass of the EGM W' boson, the more the low-mass tail is pronounced.

1.2.1.2   Heavy Vector Triplet Model

The phenomenological heavy vector triplet (HVT) [27] model introduces a new HVT (W', Z') in the Lagrangian. Thanks to the parameterisation of the coupling between those new bosons and the Standard Model ones, this theory is able to describe a broad class of models based on the introduction of a charged ($W'^{\pm}$) and a neutral (Z') heavy spin-one particle, degenerate in mass, that can mix with the Standard Model vector bosons. Unlike the EGM, the low-mass tail in the mass spectrum of the heavy vector bosons is absent, requiring the new resonances to be produced on-shell.
The coupling with the Standard Model field are parametrised using free parameters, labelled as c_H and c_F for the bosons and fermions' fields respectively, to account for possible deviations from the typical Standard Model couplings. The coupling to Standard Model bosons is given by $c_H g_V$ where g_V is the strength of the interaction of the HVT to Standard Model vector bosons. Analogously, the coupling to fermions is expressed as $c_F (g^2/g_V^2)$ where g is the $SU(2)_L$ coupling constant.
Two different models, referred as model A and B, are generally used as benchmarks. In the HVT model A, with $g_V = 1$, $c_F \simeq 1$ and $c_H \simeq -g^2/g_V^2$, the HVT couples weakly to Standard Model particles and arises from an extension of the Standard Model gauge group. The HVT model B is assuming $g_V = 3$ and $c_F \simeq c_H \simeq 1$. In this model, strong dynamics give rise to the Standard Model Higgs boson and naturally include a new HVT field with electroweak quantum numbers. Because of $c_F \simeq c_H \simeq 1$,

m [TeV]		HVT Model A (B)			bulk RS Model	
		$Z' \to WW$	$W' \to WZ$		$G_{RS} \to WW$	$G_{RS} \to ZZ$
	Γ	$\sigma \times$ BR [fb]	$\sigma \times$ BR [fb]	Γ	$\sigma \times$ BR [fb]	$\sigma \times$ BR [fb]
2.0	72	3.8 (6.0)	8.3 (13)	123	0.54	0.32
3.0	109	0.34 (0.55)	0.75 (1.3)	187	0.026	0.015

Table 1.1: Cross-section times branching ratio, $\sigma \times$ BR, and resonance width, Γ, of the diboson final states described in the heavy vector triplet (HVT) and bulk Randall-Sundrum (bulk RS) models for two resonance's masses. The HVT model A and B are described in the text. [28].

the couplings to fermions are suppressed, implying larger branching ratios for either $W' \to WZ$ or $Z' \to WW$ decays than in model A. The expected cross-sections times branching ratios and resonance widths are listed in Table 1.1 for the HVT model A and model B at two resonance mass points.

1.2.1.3 Bulk Randall-Sundrum Model

The hierarchy problem can be solved in the Randall-Sundrum (RS) [25, 26] model which describes the four-dimensional space-time as encapsulated in a larger dimensional bulk with one warped extra dimension.

In the original model, which has been already ruled out by precision electroweak and flavour measurements, the Standard Model fields are confined in the four-dimensional space-time with only the gravitational interaction able to propagate through the bulk. The extension of the initial model, referred as bulk RS model, allows all Standard Model fields to propagate in the bulk of the extra dimension. The space-time metric has therefore to depend on the coordinate of the extra dimension:

$$\mathrm{d}s^2 = e^{-2kr_c|\phi|}\eta_{\mu\nu}\mathrm{d}x^\mu\mathrm{d}x^\nu + r_c^2\mathrm{d}\phi^2 \tag{1.38}$$

where $\eta_{\mu\nu}$ is the Minkowsky metric in the four-dimensional space-time with coordinates x^μ, k is the theory energy scale, r_c the curvature of the warped extra dimension and ϕ its coordinate ($0 \le \phi \le \pi$). The hierarchy problem between the Plank scales and the TeV brane is then solved introducing the exponential warp factor in Equation 1.38. The first brane at $\phi = 0$ is often called the Planck brane, whereas the second brane at $\phi = \pi$ is called the TeV brane, where the Higgs field is confined. The gravitational interaction is mostly localised at the Plank brane.

The exponential wrap factor applies as well on the vacuum expectation value of the Higgs field, and hence on the mass parameters of the Standard Model. Thus, if the value of the bare Higgs mass is of the order of the Planck scale, the physical Higgs mass could be warped down to the weak scale. In this way, hierarchy can be naturally generated between the weak and the gravity scale.

In addition, the problems related to the hierarchy of the masses of the fermions and the unification of the coupling constants can be addressed in the bulk RS model.

This model predicts the existence of Kaluza-Klein (KK) excitations, with masses of the order of the TeV, resulting from the propagation of the Standard Model fields through the bulk. For the graviton, a corresponding exited KK spin-two graviton G_{RS} is expected close to the TeV scale, whose favoured decays involve heavy fermions ($G_{RS} \to t\bar{t}$), gauge bosons or Higgs bosons ($G_{RS} \to WW$, $G_{RS} \to ZZ$, $G_{RS} \to HH$). The strength of the coupling depends on $k/\overline{M}_{PL}$ where $\overline{M}_{PL}$ is the effective four-dimensional Plank scale ($2 \cdot 10^{18}$ GeV). The expected cross-sections times branching ratios and decay widths at two resonance mass points are listed in Table 1.1 assuming $kr_c \sim 11$ and $k/\overline{M}_{PL} = 1$.

1.2.1.4   Previous Diboson Resonance Searches

Diboson resonance searches have been performed previously by the CDF and D∅ Collaborations at the TeVatron Collider at Fermilab and subsequently by the ATLAS and CMS Collaborations at the LHC. These experiments have investigated many signatures of possible decay of a new heavy resonance into WW, ZZ and WZ whose final states are characterised by the subsequent decay of the vector bosons. Except for the fully leptonic channel, all the other signatures involve the hadronic decay of at least one vector boson. Due to the high Lorentz boost, the products of such a decay are collimated and are typically reconstructed in a single larger jet. Although the benefit deriving from the larger branching ratios of the vector bosons decaying to quarks [(3)], the hadronic final states suffer from the large multi-jet background. In order to identify the reconstructed jets as W or Z bosons and suppress the multi-jet background, both the ATLAS and CMS Collaboration have developed new reconstruction techniques that exploit the two-body nature of $V \rightarrow qq$ decays making use of jet substructures. This section present the most recent results obtained by the ATLAS and the CMS Collaborations for the the three models described in the previous section.

After Run1 data-taking, about 20 fb^{-1} of 8 TeV proton-proton collision data has been used by the ATLAS and CMS Collaborations to set exclusion limits on the production and decay of the EGM W' boson. Using leptonic final states, EGM W' bosons with masses below 1.52 TeV and 1.55 TeV have been excluded, at 95% confidence level (CL), by the ATLAS [29] and CMS [30] Collaborations, respectively. Semileptonic final states allowed to exclude EGM W' bosons with masses below 1.59 TeV [31,32], while using the fully hadronic channel ATLAS [33] and CMS [34] Collaborations have excluded EGM W' with masses below 1.5 TeV and 1.7 TeV, respectively. To improve the sensitivity of the search for diboson resonances, the ATLAS Collaboration has also performed a combination of the four independent searches for diboson resonances with the Run1 dataset [35]. Limits have been evaluated on both the cross-section and the mass for EGM W': the observed lower limit has been extended to 1.81 TeV (see Figure 1.3a).

The HVT models are used as benchmarks in the interpretation of the results obtained by the ATLAS Collaboration using the full dataset of 36.7 fb^{-1} of proton-proton collisions at a centre-of-mass energy of $\sqrt{s} = 13$ TeV recorded in 2015 and 2016. In searches using the semileptonic final states, a HVT Z' with a mass below 2.73 TeV (3.00 TeV) [36] and a HVT W' with a mass below 2.9 TeV (3.2 TeV) [37] in model A (model B) of the HVT parametrization have been excluded. Considering the fully hadronic final state, a spin-1 vector triplet has been also excluded for masses between 1.2 TeV and 3.1 TeV (1.2 TeV and 3.5 TeV) in the context of the HVT model A (model B) [28] (see Figures 1.3b and 1.3c). The same dataset has been used to extended previous lower mass limits for a KK spin-two graviton: a bulk RS graviton has been excluded up to 1.75 TeV studying semileptonic and fully hadronic final states [28,36] (see Figure 1.3d). Limits on the production cross sections times branching ratios for new heavy scalar particles have been also derived at 95% CL [28,36,37].

[(3)]BR($W \rightarrow q\bar{q}'$) ≈ 68% and BR($Z \rightarrow q\bar{q}$) ≈ 69% compared to BR($W \rightarrow l\nu$) ≈ 10.8%, BR($Z \rightarrow ll$) ≈ 3.4% and BR($Z \rightarrow \nu\nu$) ≈ 20%.
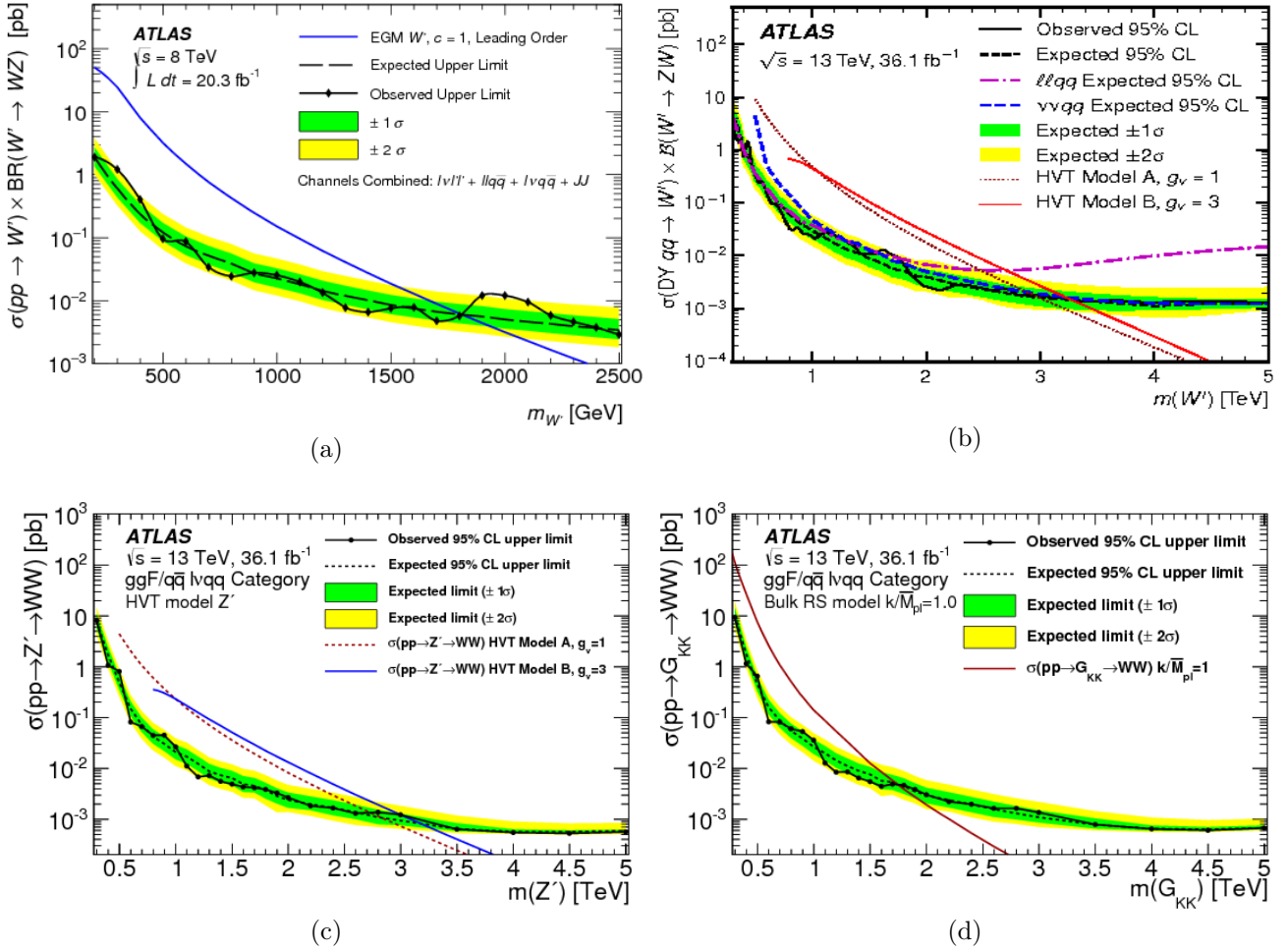
Figure 1.3: Observed and expected cross-section upper limits at the 95% confidence level as a function of the resonance mass for (a) EGM W' using the $l\nu ll$, $llqq$, $l\nu qq$, and $qqqq$ final states [35], (b) W' boson in the HVT model, combining $W' \to WZ \to llqq$ and $W' \to WZ \to \nu\nu qq$ searches [37], (c) Z' boson in the HVT model considering the $Z' \to WW \to l\nu qq$ decay [36] and (d) KK spin-two graviton, in the picture indicated with G_{KK}, in the bulk RS Model [36] for $l\nu qq$ final states. Theoretical predictions for HVT model A and B are overlaid in (b) and (c). The green (yellow) bands representing the 1σ (2σ) intervals of the expected limit including statistical and systematic uncertainties.

2

The ATLAS Experiment at the Large Hadron Collider

Contents

2.1   The Large Hadron Collider and its Experiments

The Large Hadron Collider (LHC) [38] is a circular proton-proton collider presently operating at CERN. It occupies the underground tunnel, located at a medium depth of 100 meters[(1)], which was previously hosting the CERN's previous big accelerator, the Large Electron Positron Collider (LEP). The LHC is the final step of the multi-stage accelerator system as shown in Figure 2.1

As any other circular accelerator, LHC makes use of accelerating sections to increase the protons' energy and magnets to steer and focus the beam. Radio frequency superconducting cavities accelerate

---

[(1)]Due to geological and cost considerations the tunnel ring is tilted, its depth varying from 175 to 50 meters.

the protons with a gradient of 16 MV/m. Because of this technique no continuous beam is possible, but the protons are grouped into bunches[2]. About two thousand superconducting dipoles provide a magnetic field of about 8.4 T to assure the proton are kept on their circular path. About every fourth dipole magnet is a quadrupole magnet, whose task is to focus the beam. To keep their superconducting state, the magnets are cooled with superfluid helium to a temperature of 1.9 K. To further correct the beam trajectory higher order magnets, e.g. sextupoles, octupoles, decapoles, etc. are installed in the cold mass of the dipole and quadrupole magnets. Within the LHC, the bunches of particles run in opposite directions until they are brought to collision in the interaction regions.

To achieve precision measurements of interesting physics events, with typical cross sections of the order of picobarn[3], a particle collider must operate at very high luminosity. The instantaneous luminosity expresses the number of interactions occurring per units of area and time. For a collider this quantity depends on the number of bunches per beam, N_c, the number of particles per bunch, n_1 and n_2, the overlapping area of the colliding bunches A, and on the revolution frequency f:

$$\mathcal{L} = f \frac{N_c n_1 n_2}{A}. \tag{2.1}$$

In the case of head-on collisions between symmetric beams (i.e. $\sigma_{x,1} = \sigma_{x,2}$ and $\sigma_{y,1} = \sigma_{y,2}$) this area is defined by:

$$A = 4\pi \sigma_x \sigma_y \tag{2.2}$$

where σ_x and σ_y are the beam sizes in the transverse x and y planes respectively, assuming Gaussian-shaped beams for the two colliding bunches.

The integrated luminosity, defined as $L = \int \mathcal{L}dt$, is commonly used to express the size of a dataset and is related to the expected number of occurrences N of a physics process via its cross section σ:

$$N = \sigma \cdot \int \mathcal{L}dt. \tag{2.3}$$

Equation 2.3 states that increasing the instantaneous luminosity allows for the increase of the number of events for a given physics process, and hence the dataset's size.

The first LHC collisions took place in 2009 with a centre-of-mass energy of 900 GeV, which was increased to 7 TeV in 2010 and 2011. In 2012 the energy raised to 8 TeV and since 2015 protons collide with bunch spacing of 25 ns (previously 50 ns) at a centre-of-mass energy of 13 TeV. Figure 2.2 shows the cumulative luminosity delivered by the LHC to ATLAS from 2011 to 2017 per year.

In each bunch crossing, i.e. when two bunches circulating in opposite directions are set on a collision, one or more pairs of protons may collide. A Poissonian distribution regulates the probability to observe a certain amount of proton interactions. The number of simultaneous collisions in the same bunch crossing is labelled as in-time[4] pile-up and the mean of the Poissonian is generally denoted by μ. For a fixed number of colliding bunches, the number of protons per bunch and their collimation determine the value of μ which is proportional to the instantaneous luminosity. Since the first collisions, the mean number of interactions per bunch crossing has increased reaching an average value of $\langle \mu \rangle = 38.0$ in 2017 (see Figure 2.3) [39, 40].

The LHC supports four main independent experiments located in experimental halls where the two beam lines cross and protons are brougth to collide (Figure 2.1). ATLAS [41] and CMS [42], multiple-purpose experiments, are located roughly on two opposite points on the LHC ring. ALICE [43] is a

---

[2]At design luminosity the protons are accelerated in 2808 bunches of $1.15 \cdot 10^{11}$ protons each, with 40 MHz bunch spacing (i.e. collisions every 25 ns).

[3]A barn is a unit of area, equal to 10^{-28} m^2, used to express the cross section.

[4]Out-of-time pile-up refers to the residual effects in the detector due to the signal of adjacent bunch crossings on the signal of the current bunch crossing.
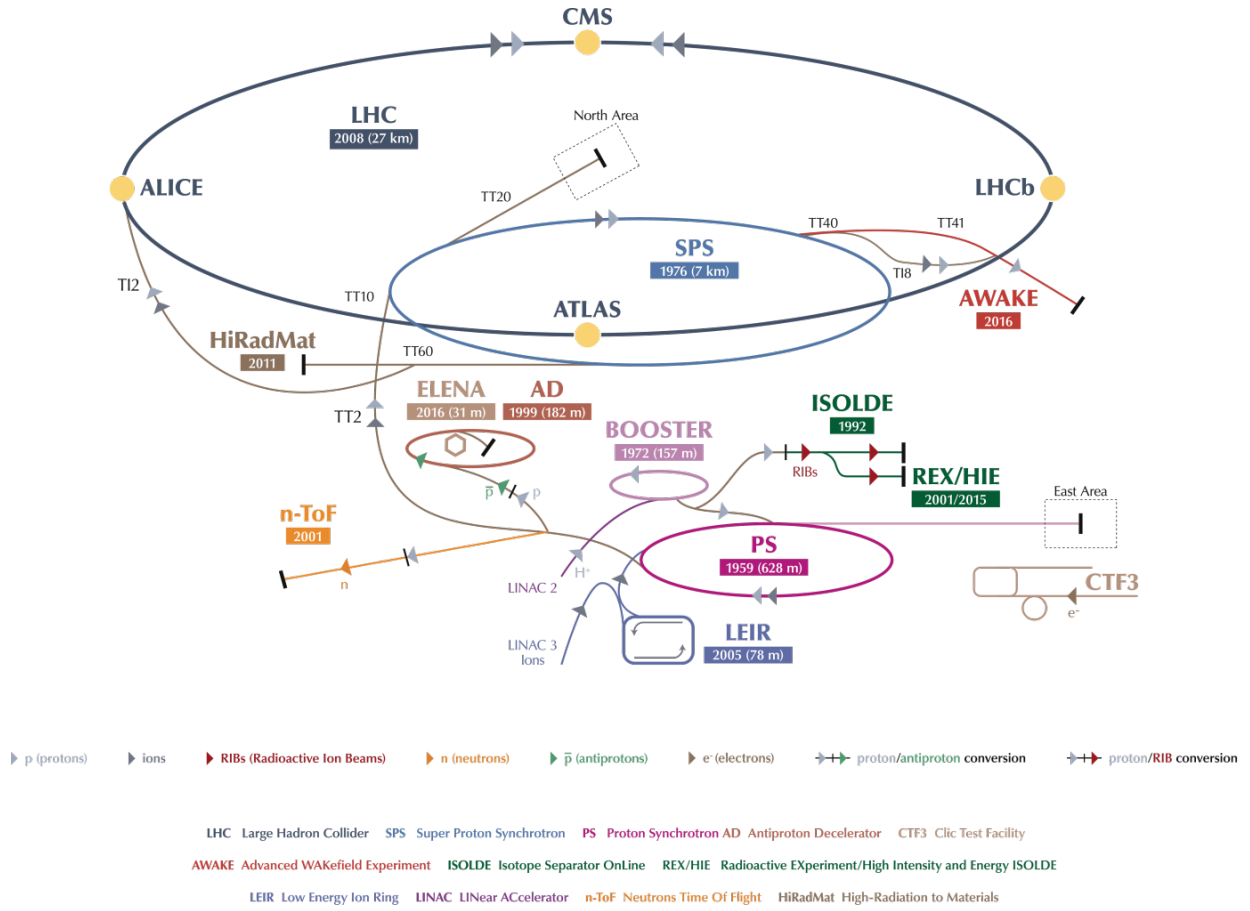
Figure 2.1: The CERN accelerator complex.

dedicated experiment to study the quark-gluon plasma created in heavy ion collisions (proton-lead or lead-lead) while LHC*b* [44] is specialized in precision measurements of CP violation and rare decays of *b*-hadrons and searchs for indirect evidence of new physics in the *b*-physisc sector. Nevertheless, four smaller experiments with very specialized physics programs are installed: TOTEM [45], LHCf [46], ALFA [47] and MoEDAL [48].

2.2 The ATLAS Experiment

ATLAS [41] (*A T*oroidal *LHC Apparatu*S) is a multi-purpose detector. It has a total weight of 7000 tons, a length of 44 m and a diameter of 25 m. A drawing depicting the layout of the detector is shown in Figure 2.4.

ATLAS has a cylindrical geometry with the various sub-detectors arranged in concentric layers and disks in order to cover the full solid angle around the interaction point. The Inner Detector (ID) sits in the innermost region. It is designed to reconstruct the trajectories of charged particles and measure their momenta via a curvature measurement in a 2 T solenoidal magnetic field. A calorimetry system, consisting of an electromagnetic and a hadronic calorimeter, surrounds the ID. They measure energies of electrons/photons and hadrons thanks to the detection of the showers produced in the interaction of particles with the absorber materials. The outermost part of ATLAS consists of the muon spectrometer, which includes a magnet system providing a toroidal field. The muon spectrometer
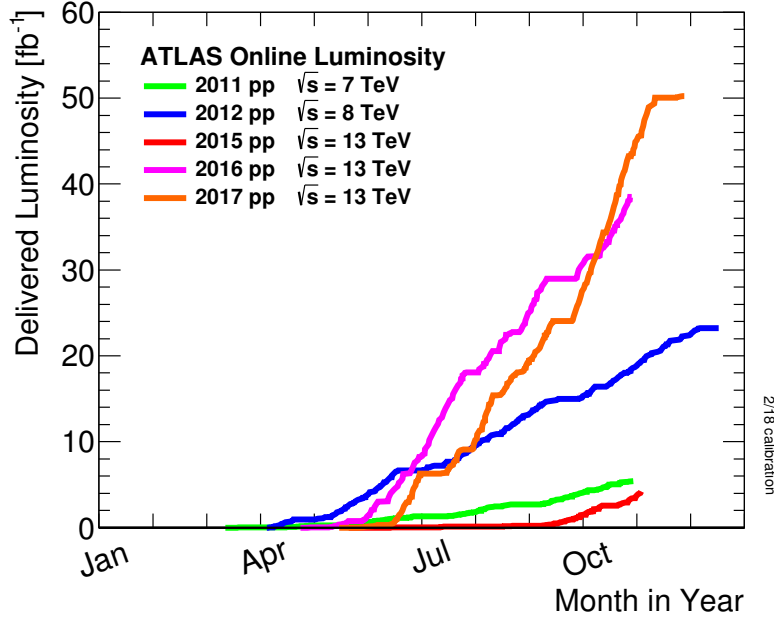
Figure 2.2: Cumulative luminosity versus day delivered to ATLAS during stable beams and for high energy p-p collisions [39, 40].
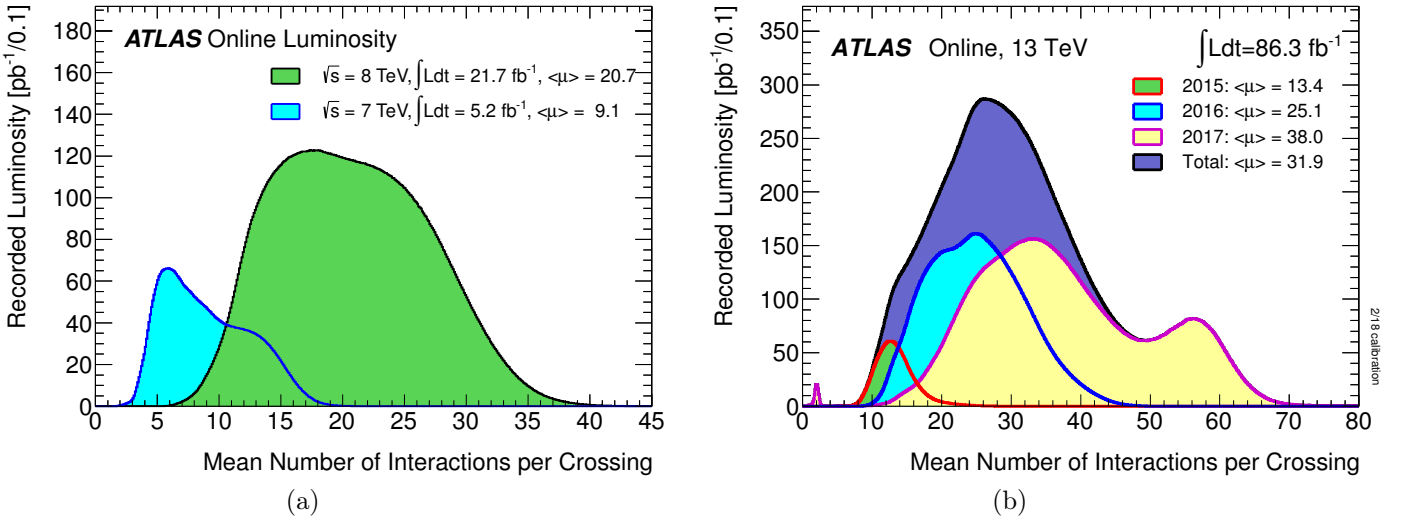
Figure 2.3: Luminosity-weighted distribution of the mean number of interactions per crossing for the (a) 2011 and 2012 proton-proton collision data at 7 and 8 TeV centre-of-mass energy, respectively, and for the (b) 2017 proton-proton collision data at 13 TeV centre-of-mass energy [39, 40].

is a standalone tracking system for the muon detection.

The main detector requirements are the identification and the measurement of the kinematic properties of a large spectrum of particles produced in the proton-proton collisions over a wide energy range (from MeV to TeV). The following specifications have been taken into account for the construction of the detector [41]:

- good track reconstruction efficiency and charged-particle momentum resolution to separate particles coming from different interaction processes and to precisely measure track parameters and production vertices for offline tagging of b-/c-jets and τ-leptons;

- a very good electromagnetic calorimeter to measure with high accuracy electrons and photons complemented by a hermetic hadronic calorimeter with a very large angular coverage for the measurement of jets and missing transverse energy;

- good muon identification and momentum reconstruction and small charge misidentification up to highest luminosities and over a wide range of momenta;

- large acceptance in pseudo-rapidity with full azimuthal angle coverage, to identify events containing neutrinos or new weakly-interacting particles through the measurement of transverse-momentum imbalance in the event;

- a flexible trigger system able to maintain high selection efficiency and sufficient background rejection even for low- and medium-p_T objects.

Additional constraints on the detector design were posed because of specific conditions from the LHC operation. Due to the high interaction rate, the large number of interactions per bunch crossing and consequently the large particle flux, fast, radiation-hard electronics and sensor elements are essential. At the same time, high detector granularity is necessary to reduce the influence of overlapping interactions.

2.2.1 Coordinate System

As shown in Figure 2.4, the origin of the coordinate system is chosen to be the nominal interaction point. The x, y, and z axis are defined as follows: the positive x-axis points from the interaction point to the centre of the LHC ring, and the positive y-axis points upwards. The side-A and side-C of the detector define the positive and the negative z, respectively, the former pointing towards the location of the LHCb experiment and the latter towards the ALICE experiment. The azimuthal angle ϕ is measured around the beam axis, and the polar angle θ from the beam axis. Since the momentum for colliding partons along the z-axis is unknown, it is useful to define the boost-invariant transverse component of the variables of interest, like energy and momentum, defined as projection on the xy plane:

$$p_T = \sqrt{p_x^2 + p_y^2} = |\vec{p}| \sin\theta; \qquad E_T = E \sin\theta. \qquad (2.4)$$

Another very useful quantity used in hadron colliders is the rapidity y:

$$y = \frac{1}{2} \ln\left(\frac{E + p_z}{E - p_z}\right). \qquad (2.5)$$

It is preferred to the polar angle θ, as it brings the advantage that the difference in rapidity Δy between a pair of particles is invariant under the boost of the center of mass along the beam direction[5]. In

---

[5]This property of rapidity is very useful at hadron colliders such as LHC. Because of the composite nature of the colliding protons, the interacting constituents (quarks and gluons) carry only a variable fraction of the proton momentum thus implying that their center of mass is boosted along the beam direction by a variable amount.
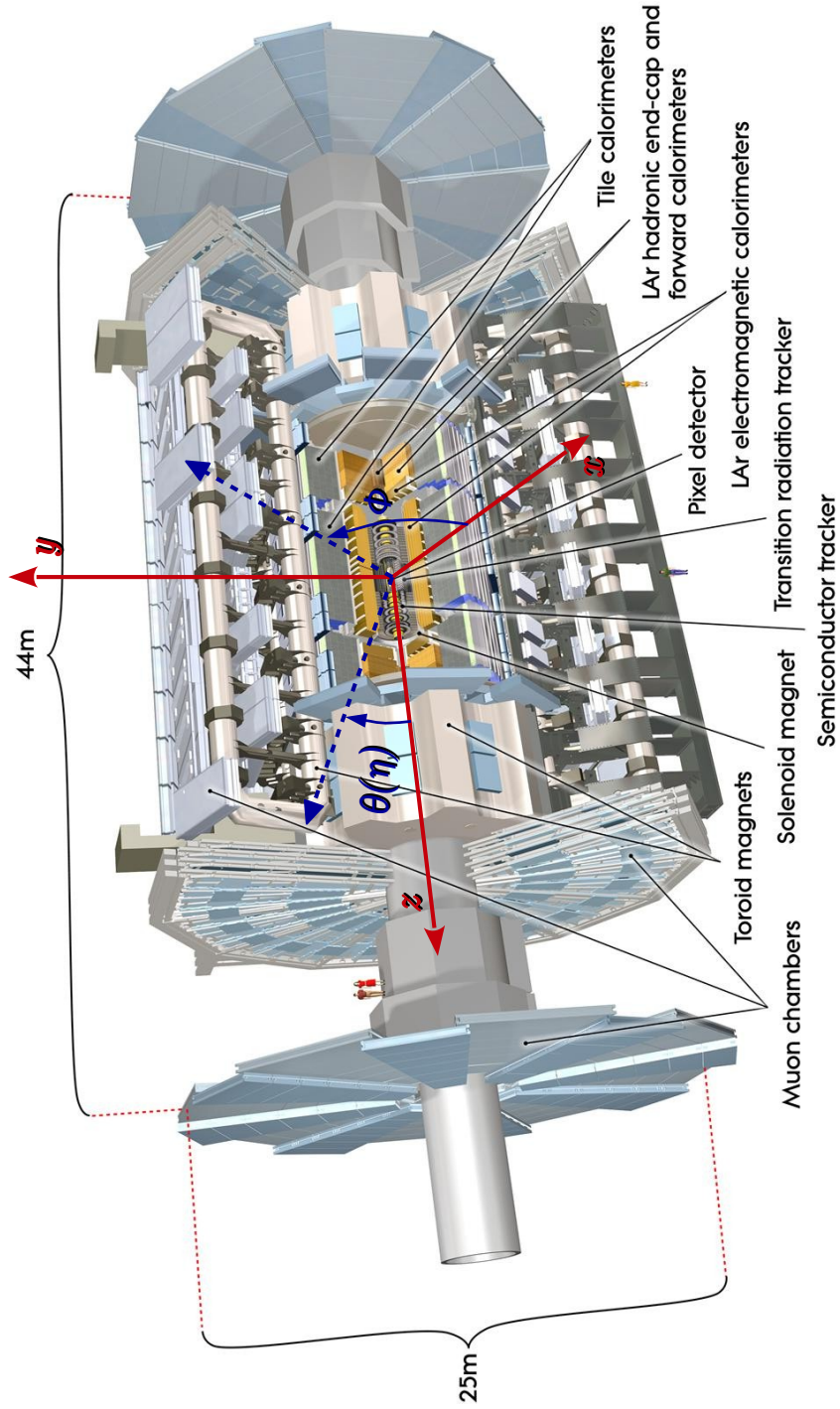
Figure 2.4: Three-dimensional view of the ATLAS detector. The individual sub-detectors and the reference frame are indicated.

the massless particle approximation rapidity turns into the so-called pseudo-rapidity η:

$$\eta = -\ln\left(\tan\frac{\theta}{2}\right). \tag{2.6}$$

The distance ΔR in the $\eta - \phi$ plane is defined as

$$\Delta R = \sqrt{(\Delta\eta)^2 + (\Delta\phi)^2}. \tag{2.7}$$

Cylindrical coordinates are also frequently used: with z pointing along the beam line, $R = \sqrt{x^2 + y^2}$, and $\phi = \tan^{-1}\frac{x}{y}$.

The complete detector is split into Barrel Region (BR) sections and End-cap Regions (ER) sections: in the former the detector layers are positioned on cylinders around the beam axis, in the latter are positioned in wheels of constant z perpendicular to the beam pipe.

2.2.2 Magnet System

The magnet system [49] of the ATLAS detector is composed of four large superconducting magnets, cooled with liquid helium at 4.5 K, designed to provide a field mostly orthogonal to the particle trajectory, while minimising the degradation of resolution due to multiple scattering. It consists of a central solenoid and three air-filled toroids, as shown in Figure 2.5. This hybrid system has the advantage of extending the pseudo-rapidity coverage ($|\eta| < 3$), while maintaining zero field in the calorimeters, where the presence of the magnetic field leads to a performance degradation.

The central solenoid, located between the ID and the electromagnetic calorimeter, provides a 2 T magnetic field parallel to the beam axis used to bend charged particles in the ϕ direction within the acceptance of the tracking system. To achieve the desired calorimeter performance, the coil of the solenoid was optimised to be as thin as possible in order to limit the amount of material in front of the calorimeters, while being still thick enough to ensure safety and reliability during operation. As the distance from the interaction point increases in the z direction, the field strength decreases as result of the finite dimension of the solenoid.

The toroidal system generates the field necessary to bend particles in the muon spectrometer. The system consists of two end-cap toroids at the extremities of the detector and a barrel toroid centrally located around the calorimeters. Each toroid is composed of 8 rectangular coils arranged in the radial direction from the beam axis. In order to generate a radial overlap for a higher magnetic field uniformity and to optimise the bending power in the transition region, the end-cap toroids are rotated with respect to the barrel one. The resulting magnetic field, that varies from 0.15 to 2.5 T in the barrel and from 0.2 to 3.5 T in the end-cap regions, is oriented in the ϕ direction causing charged particles to bend in the η direction in the muon spectrometer.

2.2.3 Inner Tracking System

The ATLAS Inner Detector (ID) [41] is designed to provide hermetic and robust pattern recognition and good momentum resolution for charged particles within the pseudo-rapidity range $|\eta| < 2.5$ from p_T as low as 0.4 GeV up to a few TeV. At the same time, it has the capability of precisely reconstructing primary vertices, to distinguish the hard-scatter vertex from pile-up vertices, and secondary vertices to identify e.g. B-hadrons and converted photons. Moreover, its fine granularity allows a precise measurement of the track curvature in the 2 T solenoidal magnetic field also in presence of a high density of particles. It is also required to have as little material as possible in order to minimally affect the energy measurement in the calorimeter and optimise the momentum and vertex resolution
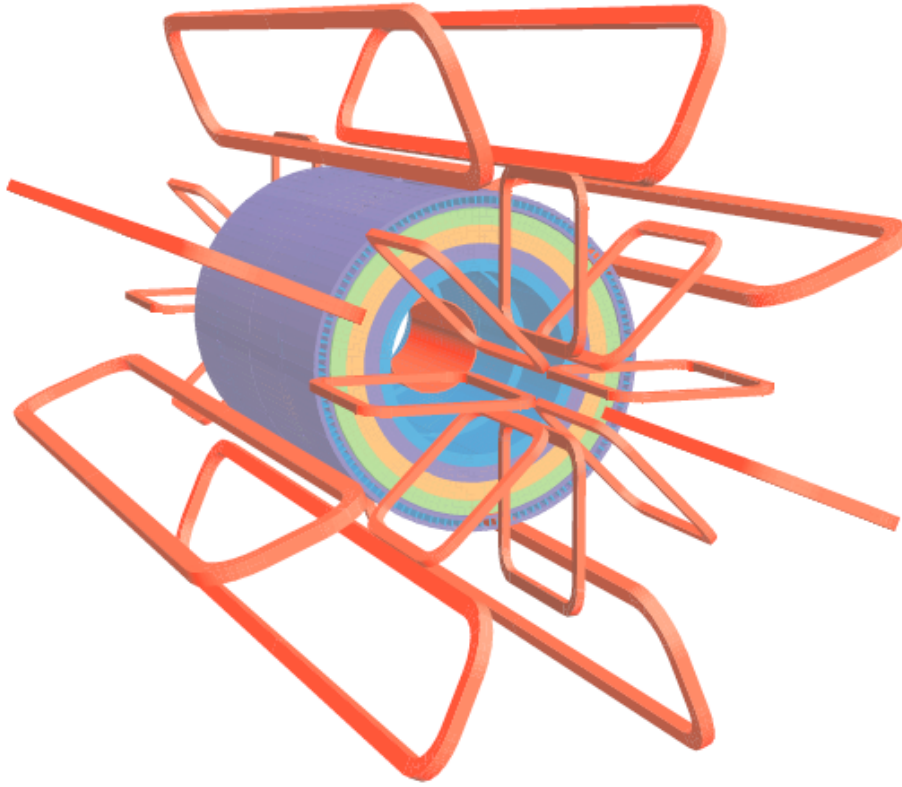
Figure 2.5: Schematic of the ATLAS magnet system. The outer system, composed by the eight barrel and eight end-cap coils, are visible while the solenoid structure is shown inside the calorimeter volume.

for lower momentum particles.

To satisfy all these requirements, the ID consists of three different sub-detectors: the pixel detector, the Semiconductor Tracker (SCT) and the Transition Radiation Tracker (TRT).

The pixel and SCT detectors are solid state detectors using silicon. These devices can provide a high granularity and highly precise position measurements. However, silicon sensors are expensive and require a lot of material both in the form of cooling pipes and support structures which can have a negative effect on the tracking performance in general (see § 2.2.3.7). The outermost sub-detector, the TRT, is using straws filled with a gas mixture. It allows to collect a large number of measurements working in a continuous tracking mode. The relative precision of the three sub-systems is comparable so that no single measurement dominates the momentum resolution. This redundancy also guarantees high efficiency even in case of sensor and module inefficiencies. The layout of the ID is shown in Figure 2.6.

Before describing the components of the ID, an introduction on the general characteristic of silicon detectors and the basic strategy of tracking systems is provided. This will allow a better understanding of the choices that drove the layout definition.

2.2.3.1   Silicon Detection Principle

Silicon detectors are widely used in particle physics experiments and offer a good position resolution and a high granularity. The principle of such a semiconductor detectors is the measurements of the free
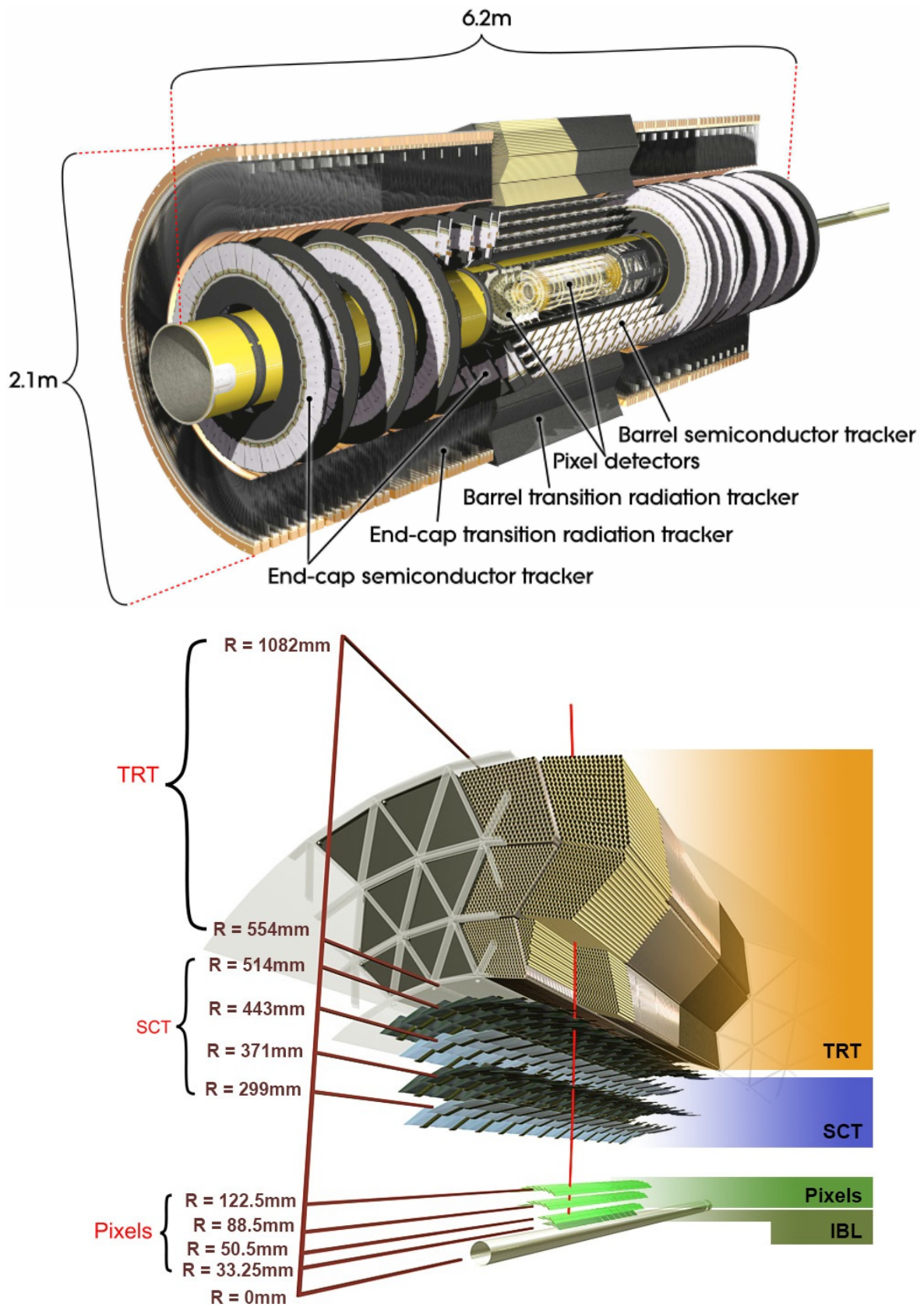
Figure 2.6: Schematic views of the ATLAS Inner Detector and its three sub-detectors.

charge produced via ionisation by charged particles traversing the medium. As the name suggests, they are profiting of the properties of semiconductor materials which have electrical conductive properties in between conductors and insulator. The energy gap present between the conduction and the valence band is lower compared to insulators ($\sim$ eV), which allow electrons to jump to the conduction band even at room temperature. In addition, each electron leaves a hole in the valence band behind which can be filled with other electrons in the valence band. Thus electrons and holes act as charge carriers in the material. Unlike metals, the conductivity increases with increasing temperature as more and more electrons are freed. The electrical properties of semiconductors can be changed in an useful way with a controlled introduction of impurities into the crystal structure. This process in called doping of the semiconductor.

Because of the conductivity features of silicon, the energy needed to produce one electron-hole pair is only 1.14 eV (at 302 K) very low compared to the one needed to produce ionisation in a gas detector. Consequently, these detectors result to have high energy and time resolution. Compared to gaseous detectors, the high density of the semiconductor materials allows for a big number of electron-hole pairs produced in very small sensors. The large majority of silicon detectors used nowadays are realized as so-called planar structures: the production process starts from a surface of a silicon wafer that is treated by etching, implantation, material deposition, etc. to achieves the required structures.

A semiconductor sensor is composed of a bulk material, in which the free charge is produced, and a segmented readout electronics able to measure the induced pulse. The bulk material of the silicon wafer is doped by generally adding boron or gallium (Group III) and arsenic or phosphorus (Group V) atoms to form respectively n-type or p-type wafers with high specific resistivity (> 1 k$\Omega \cdot$cm). One segmented side of the wafer (e.g. into pixels or strips) characterises single-sided detectors with implantation of the opposite type to form a multitude of pn-junctions with the bulk material, i.e. diode structures. Electrons start to diffuse[6] in the contact region between the bulk and the implants. The different charges in the implant and in the bulk produce a small potential difference, which results into a non-zero electrical field that spreads only in a small region near the contact area which is called depletion region. The diffusion of electrons towards the implant continues until the electrical field precludes any additional electrons from reaching the implant. Free charges created in the depletion region, resulting e.g. from an ionising particle penetrating the silicon, can be collected at the junction, while charges created in the non-depleted zone recombine with the carriers and are lost. The size of the depletion region can be further increased by applying an external reverse bias voltage. Due to the different effective doping concentration between the implanted structures and the bulk, the former generally lower than the latter, when the reverse bias voltage is high enough the depletion zone can develop deeper into the bulk reaching the backside of the wafer. The depletion voltage is the voltage needed to fully deplete the bulk material. At this point, the full sensor volume is sensitive to charged particles that create electron-hole pairs while they are traversing bulk. For Minimum Ionizing Particles (MIPs) with the minimum deposited energy the most probable number of electron-hole pairs generated in 1 μm of silicon is $\sim$ 80, while the average is $\sim$ 110. The electric field created by the reverse bias voltage separates the electron-hole pairs before they recombine again, and the electrons and holes drift through the bulk respectively to the positive and negative voltage connection. External electronics measure the current pulse corresponding to the drift of these charges. When a magnetic field is present, the free charges will not drift perpendicular to the surface, but with an angle, called the Lorentz angle, which causes a systematic shift in the position of the collected charges, and hence a systematic shift in the determined position of the original particle. This shift is corrected for during the reconstruction. How a silicon microstrip detector works is shown in Figure 2.7.

---

[6] The electrons diffuse from the bulk to the implants in case of n-type bulk with p-type implant
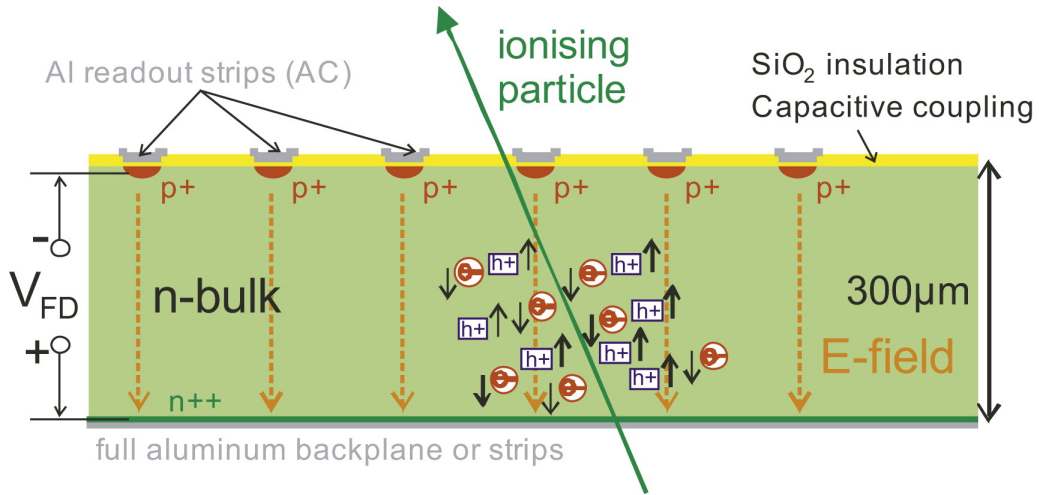
Figure 2.7: Working principle of a silicon detector. Electro-hole pairs, produced via ionisation by a charged particle, travel towards the electrodes on the two sides of the sensor [51].

Silicon sensors for tracking detectors are generally installed as close as possible to the interaction point and can therefore suffer because of the harsh radiation environment. For this reason, it is important to ensure operations with adequate stability for many years. Silicon detectors can be damaged by high dose of radiation: light particles, such as electrons, positron and photons are mainly responsible of surface defects, e.g. the creation of permanent charges, while heavier particles such as protons, neutrons and pions, because of their relatively large energy transfer, can also dislocate silicon atoms form the original locations in the crystal structure. The detector parameters are influenced by the presence of these defects; they can induce, e.g. the increase of the leakage current, the modification of the doping concentration, the creation of trapping centres that reduce the charge collection efficiency. In particular these parameters are very strongly correlated with irradiation and among them selves: the effective doping concentration determines the required operating voltage, which depends as well on the irradiation and the subsequent temperature-sensitive annealing; the leakage current of the sensor grows linearly with the integrated radiation dose; the effective doping concentration then increases with time in a temperature-dependent way. To contain this annealing and to reduce the leakage current, the sensors have to run at low temperature. This implies the integration of a cooling system in the detector which is also used to keep the power-supply services and the read-out electronics well below the temperature at which heat-induced failures occur. The sensor electronics must be as well sufficiently radiation hard.

Recently, several sensor technologies and configurations have been studied and developed to further improve the radiation tolerance of sensors and electronics. 3D silicon sensors have been proposed to overcome the limitations of traditional planar silicon sensors after exposure to high fluences of non-ionizing particles [50]. Here the implants are represented by columns etched into the bulk which cause the depletion to develop laterally. Since the space between columns is typically smaller than the thickness of the wafer, for 3D sensors the depletion voltage can be drastically reduced with respect to planar sensors. Moreover, as shown in Figure 2.8, the charge collection distance could be much shorter in 3D sensors. High electric fields can be achieved at low voltages so that the charge collection can be much faster. This property can mitigate charge trapping effects due to high levels of radiation.
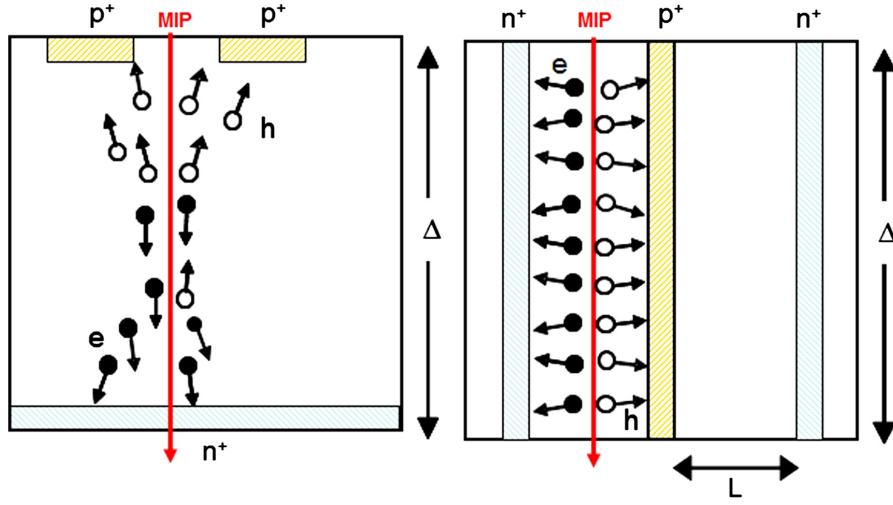
Figure 2.8: Schematic cross-sections of (left) planar sensor, and (right) 3D sensor, emphasizing the decoupling in 3D sensors of active thickness (Δ) and collection distance (L) [52].

2.2.3.2 Silicon Pixel and Strip Sensors

Strips are used as implants in silicon strip detectors (typically around 20 μm wide with an inter-strip distance of 50-100 μm). They can be single-sided or double-sided depending on how many sides of the sensors are structured into strips. The strips reach the end of the sensor where the smaller electronic chip is wire bonded. Double-sided strip sensors provide a two-dimensional readout with strips on two sides of the sensor orientated with an angle with respect to each other. Common strip orientations are 90° or a small stereo angle of the order of few degrees.

The distance between the strip implants, the so-called pitch, is the dominant parameter to determine the position resolution of the detector. The position of the penetration is calculated as the "centre of gravity" of the fired strips and, without further refinement, the position resolution is given by

$$\sigma \approx \text{pitch}/\sqrt{12} \tag{2.8}$$

as arises from geometrical considerations:

$$\sigma = \sqrt{\overline{x^2} - \bar{x}^2} = \sqrt{\frac{1}{\text{pitch}} \int_{-\frac{1}{2}\text{pitch}}^{+\frac{1}{2}\text{pitch}} x^2 dx} = \frac{\text{pitch}}{\sqrt{12}} \tag{2.9}$$

If two or more strips are traversed by the particle and hence clustered together, the resolution can be improved through geometrical constraints, such as the strip pitches.

Further refinement can be done using the information on the charge deposited in the strips. Profiting of readout electronics able to measure the charge collected on two neighbouring strips, charge interpolation becomes possible, which provides for improved resolution depending on sensor charge collection efficiency and the electronics threshold. The two readout version are after referred as digital and analog, respectively.

Equivalent resolutions, albeit in 2 dimensions, can be achieved with a pixellated readout structure. For pixel sensors the implants are small pixels rather than strips, with dimensions such as 100×150 μm^2. One complication of these devices is the big number of electrical connections: each pixel of the sensor has to be electrically connected to the corresponding electronic channel on the chip. The readout covers the full sensor area with readout cells of about the same dimension of the pixel sensor cells. A

process called bump bonding is used to make the connections in hybrid pixel detectors.

Beside hybrid pixel and strip detectors, other sensor structures have been recently developed to mainly reduce the complexity of hybrid pixel detectors, especially due to the large number of connections. Several groups have indeed developed monolithic pixel detectors which combine within one device both the sensitive volume and the electronics.

2.2.3.3 Basic strategies of Large Systems

In the course of silicon detector developments, the area of the detectors increased while the electronic circuits underwent several miniaturisation processes. This allowed the detectors to be equipped with several detection layers in the barrel and several wheels in the forward regions to provide a uniform η coverage with the minimum amount of material [51].

The main purpose of such detectors is to precisely measure tracks of charged particles in a magnetic field to allow:

- the measurement of the transverse component of the particle's momentum, p_T;

- the identification of primary and secondary vertices;

- the capability of resolving nearby tracks.

Strong design criteria are imposed to tracking devices to provide optimal p_T and impact parameter resolutions.

p_T **resolution** − The track momentum is measured by the estimation of the bending of the trajectory in a magnetic field, i.e. measuring the sagitta[7].

The transverse momentum resolution is composed by two terms in the following way:

$$\left(\frac{\sigma(p_\mathrm{T})}{p_\mathrm{T}}\right)^2 = \left(\frac{\sigma_\mathrm{MS}(p_\mathrm{T})}{p_\mathrm{T}}\right)^2 + \left(\frac{\sigma_\mathrm{geom}(p_\mathrm{T})}{p_\mathrm{T}}\right)^2. \tag{2.10}$$

The first term represents the multiple scattering (MS) contribution. It is a constant term and dominates at low p_T:

$$\frac{\sigma_\mathrm{MS}(p_\mathrm{T})}{p_\mathrm{T}} = \text{constant}. \tag{2.11}$$

The second term, with some approximation, is expressed in terms of the layout parameters via

$$\frac{\sigma_\mathrm{geom}(p_\mathrm{T})}{p_\mathrm{T}} = \frac{\sigma(S)[\mu\mathrm{m}]}{(L[\mathrm{cm}])^2 \, B[\mathrm{T}]} p_\mathrm{T}[\mathrm{GeV}] \tag{2.12}$$

where S is the sagitta, L is the lever arm, B is the magnetic field and R is the curvature radius (see Figure 2.9). Assuming a constant magnetic field, the trajectory in the transverse plane is described by a circumference. Equation 2.12 shows that the transverse momentum resolution can be improved if the resolution on the sagitta is improved. The uncertainty $\sigma(S)$ depends on the number of measurements and the space among them; assuming a large number of track points ($N \gtrsim 10$) and equal spacing it is approximated by:

$$\sigma(S) = \frac{\sigma(r-\phi)}{8}\sqrt{\frac{720}{N+4}} \tag{2.13}$$

---

[7] For an arc of circumference of radius R and a chord L, the sagitta is given by $S \simeq L^2/8R$, see Figure 2.9.

where N is the number of measurements and $\sigma(r - \phi)$ is the intrinsic position resolution in the transverse plane [53]. Moreover, a linear and quadratic improvement in the transverse momentum resolution can be achieved increasing the B field strength and the lever arm, respectively. However, because of the proportionality with the transverse momentum itself, increasing the p_T results into a worse resolution until the limit when not even the charge of the particle can be correctly identified. Moreover, Equation 2.12 shows that in a confined tracker volume there is a limit on the momentum resolution given the limitation in the lever arm. For high-momentum leptons it is thus important to supplement the ID measurement in order to not lose the measurement quality desired for physics analyses. For electrons, this is usually done by a highly precise calorimeter while for muons with a dedicated muon detector.

Impact parameter resolution – The accuracy in the reconstruction of primary and secondary vertices can be expressed in terms of the resolutions on the impact parameters. Respectively referred with d_0 and z_0, the transverse and longitudinal track parameters define the shortest distance between the reconstructed track and the nominal beam line in the transverse and in the longitudinal planes, as shown in Figure 2.10. They can be used to associate tracks to vertices and to identify decay vertices when they result to be very large compared to the corresponding experimental resolution.

The detector design strongly affects $\sigma(d_0)$ and $\sigma(z_0)$. In a simplified, but still rather accurate parametrization, the impact parameter resolution can be writted as a combination of a geometrical term, function of the intrinsic resolutions and the radii of the first two measurements, and a component of the first multiple scattering parameter. This model is based on a two layer approximation and is often referred to as $A \oplus B$-model [54]. The impact parameter resolution for a simplified two layer system, with radii r_1 and r_2, is expressed as [7]:

$$\sigma^2 = \sigma^2_{\text{geom}} + \sigma^2_{\text{MS}} \tag{2.14}$$

with

$$\sigma^2_{\text{geom}} = \left(\frac{\sigma_1 r_2}{r_2 - r_1}\right)^2 + \left(\frac{\sigma_2 r_1}{r_2 - r_1}\right)^2 \quad \text{and} \quad \sigma^2_{\text{MS}} = \sum_{j=1}^{n_{\text{scatt}}} (r_j \Delta\Theta_j)^2 \tag{2.15}$$

where σ_1 and σ_2 are the intrinsic position resolution on the two layers, $\Delta\Theta \simeq (0.0136/p_T[\text{GeV}]) \sqrt{\Delta X/X_0} [1 + 0.038 \cdot \ln(\Delta X_j/X_0)]$ is the average multiple scattering angle of a particle with transverse momentum p_T through the material of thickness ΔX_j (expressed in fractions of radiation lengths X_0) located at r_j and n_{scatt} is the number of measurements before the last sensitive element. It is clear that σ_{geom} is a constant value dependent on the layout configuration, while σ_{MS} is inversely proportional to the p_T:

$$\sigma = A \oplus \frac{B}{p_T}. \tag{2.16}$$

The above considerations lead to specific design properties:

- Light beam pipe and vertex detector, including support structures and cables to minimize the multiple scattering especially in front of the very first measurement layer, e.g. moving all electronic components outside the tracking volume;

- First measurement as close as possible to the primary interaction point to minimize the uncertainty on the tracking extrapolation. This is crucial for an optimal impact parameter resolution;
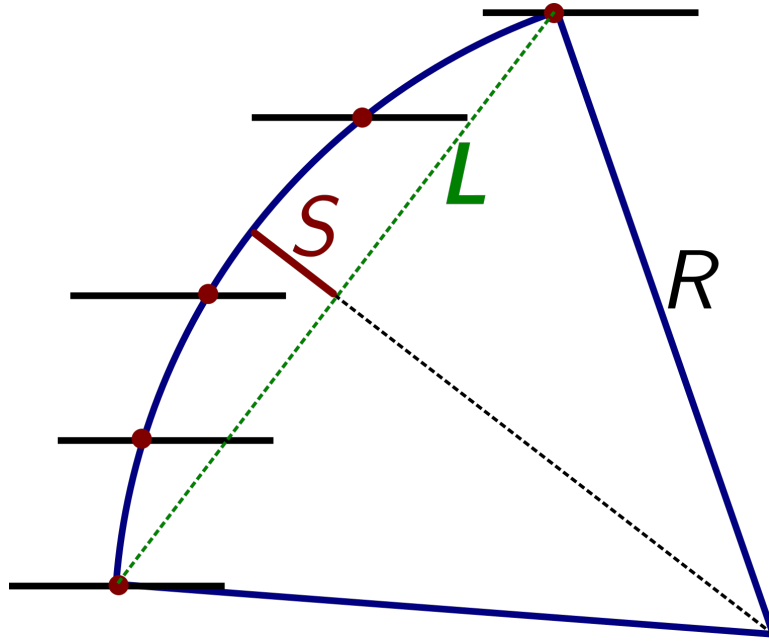
Figure 2.9: Definition of the sagitta S in the curvature plane of the track. L is the chord length and R is the curvature radius assuming a uniform magnetic field perpendicular to the plane and hence a circular trajectory in absence of energy loss.

- Outermost measurement layer placed at the largest possible radius to maximise the lever arm and the integrated magnetic field and hence improve the transverse momentum resolution;

- High intrinsic detector resolution, using for example silicon sensors with small pitch and analog readout;

- Provide enough overlap between sensors to help with hermeticity and to correct for misalignment when evaluating the position of the sensitive elements in the detector volume.

To complete the list of requirements, also considerations on the environment have to be taken into account. The following characteristics are therefore important:

- Position of layers and disks, to operate below the maximum sensor occupancy required;

- Sensor technology able to operate at very high levels of radiation with efficiency as stable as possible over several years;

- High sensor granularity to resolve nearby tracks.

Nevertheless, it is crucial to establish good pattern recognition and tracking reconstruction algorithms to fully benefit from all the layout characteristics to provide high tracking reconstruction efficiency and good ability to tag b-hadrons and τ leptons from the reconstruction of secondary vertices.

Taking in mind all the requirements listed here, the configuration of ATLAS ID has been carefully defined. The three sub-systems are described in the next sections highlighting the choices made to provide excellent tracking performance and operate in a very high radiation environment for ten years of data taking.

(a)

(b)
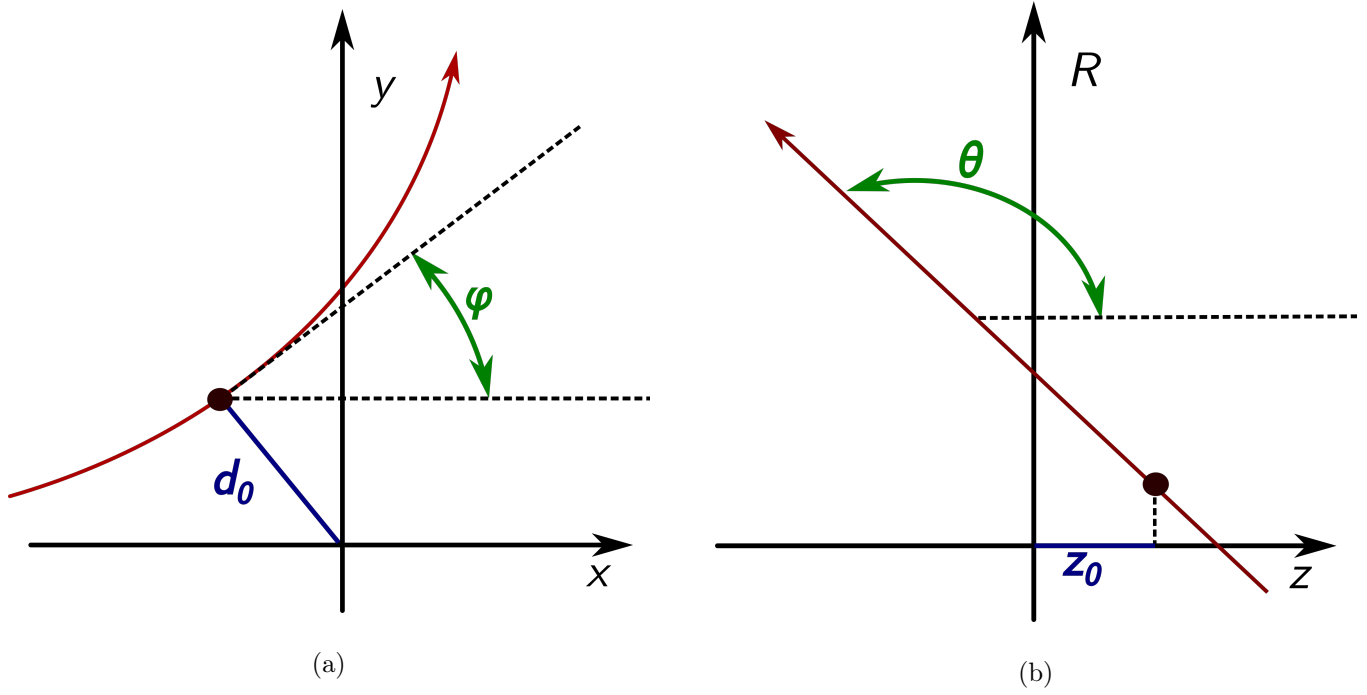
Figure 2.10: The perigee parameters (a) d_0 and (b) z_0, which define the track at its point of closest approach to the z-axis. The transverse impact parameter d_0 is defined as the distance of the perigee to the beam line, i.e. distance of the point of the track closest approach from the origin in the $x - y$ plane. The longitudinal impact parameter z_0 is defined as the value of z of the point on the track that determines d_0. The magnetic field direction is along the z axis. The figures are also showing the other track parameters φ and θ.

2.2.3.4   Pixel Detector

The Pixel Detector is the innermost part of the ID and has been designed to guarantee good pattern recognition performance in a very dense particle environment. It is composed of four cylindrical barrel layers and three disk layers in each of the end-cap regions. As shown in Figure 2.6, the Insertable B-Layer (IBL), inserted during the Long Shutdown (LS) 1 when also the size of the beam-pipe was reduced, is 62 cm long and sits at a radius 33.25 mm. The other layers are approximatively 80 cm long and have radii of 50.5, 88.5 and 122.5 mm. The three discs in each end-cap are placed at $|z| = 495.0$, 580.0 and 650.0 mm from the centre of the detector. They have a minimum radius of 340 cm. In this configuration the pixel detector provides at least four precise hits for the track reconstruction in the proximity of the interaction point. Anyway, more than four hits are provided on average thanks to the additional ϕ and z overlaps of the pixel sensors.

The basic unit of the detector is the module that contains the sensor and the required electronics. The IBL has been instrumented with planar and 3D silicon pixel sensor technology while the other three layers have silicon planar sensors. The pixel matrix is composed of 80×336 pixels for the IBL modules and 144×328 pixels for the modules belonging to the other layers and to the disks, for a total of about 2500 modules and 92 million channels. The dimension of the single pixel is $50~\mu m(r - \phi) \times 250~\mu m(z)$ and $50~\mu m(r - \phi) \times 400~\mu m(z)$ respectively for the IBL and the other layers. Thanks to the time over threshold (ToT) information, which can be directly translated into a representative measurement of the charge produced in the pixel channels, an average position resolution better than 10 μm in the $r - \phi$ direction and 65 μm (115 μm) in z for the IBL (the three outer layers) is achieved. The combination

of the higher granularity of the IBL sensors and the shorter distance to the interaction point with respect to the other pixel layers, produced an improvement by more than 40% [55] the transverse and longitudinal impact parameter resolutions with respect to the previous detector configuration. The very high granularity of the IBL also gave an excellent two-track resolution, which has an important impact for the pattern recognition.

2.2.3.5 Semiconductor Tracker

The Semiconductor Tracker (SCT) has been designed to provide at least eight precise measurements per track. It consists of four radial layers in the barrel covering the pseudo-rapidity range $|\eta| \lesssim 1.4$ and nine end-cap discs, with three rings each, on either side covering $1.4 < |\eta| < 2.5$.

Unlike the pixel detector, the SCT uses different sensor shapes for the barrel and the end-cap regions to provide enough sensor overlap while minimising the silicon area: barrel modules are rectangular, end-cap modules are trapezoidal with radial strips. The module is the basic unit of this detector and consists of two wire-bonded microstrip sensors mounted back-to-back with a stereo angle of 40 mrad. The microstrip sensors contain 768 read-out strips with a mean pitch of 80 μm and 6.4 cm length. Two sensors are wire-bonded together to have an active length of 12.8 cm. The binary readout of the SCT modules limits the spatial resolution per sensor to about 23 μm. Exploiting the stereoscopic effect, a spatial measurement is created by the two-dimensional strip position, in order to form the space-point position. About 800 μm is the resolution achievable on this second coordinate. Composed 988 modules in each of the two end-caps and 2112 in the barrel, the SCT counts ~ 6.2 million readout channels.

The SCT contributes to the resolution of the impact parameter, the momentum, and the z-position of the vertex. Thanks to its granularity, it covers a decisive role for the pattern recognition.

Due to their proximity to the beam-pipe, the pixel and SCT detectors are exposed to a very high radiation dose resulting in a decrease of their performance. The complete replacement of the tracker will be necessary for the Phase-II Upgrade and will be treated extensively from Chapter 6.

2.2.3.6 Transition Radiation Tracker

The Transition Radiation Tracker (TRT) is the outermost part of the three tracking sub-systems of the ID. It consists of about 300'000 straw tubes, 4 mm in diameter, which are filled with a gas mixture of 70 % Xe, 27 % CO_2 and 3% O_2. Due to large irreparable gas leaks that developed in the gas system during the LS1, part of the TRT detector is now flushed with a gas mixture composed primarily of the much cheaper 80 % Ar and 20 % CO_2 mixture. The gas inside the straws is ionised when a particle traverses it: the large potential difference applied between the surface of the straw and the wire allows the collection of the ionization clusters. The measurement of the time needed by the cluster to reach the wire can be then translated into the distance between the track and the wire, i.e. the drift radius, which is characterised by a spatial resolution of about 170 μm.

In the barrel, the straws are 144 cm long and aligned parallel to the beam-axis, thus they don't provide information on the z position of the traversing particle. In the end-caps, the straws are arranged radially in wheels with a length of 37 cm. With more than 30 hits per track, the TRT allows for continuous tracking within $|\eta| < 1.0$ for the barrel region and $1.0 < |\eta| < 2.0$ in the end-caps. The TRT not only provides a measurement of the trajectory of traversing particle but can be also used to distinguish between electrons and pions. For this purpose, the space between the straws is filled with polymer fibres (barrel) and foils (end-cap) to allow charged particles to emit transition radiation when traversing the boundary between materials with different dielectric constants. This effect depends on
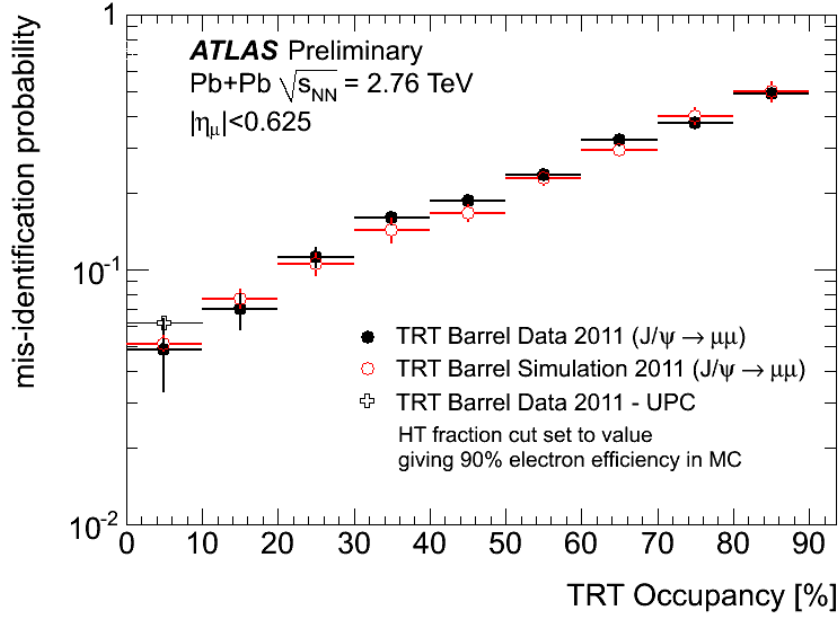
Figure 2.11: The probability of misidentifying a muon as an electron as a function of the TRT hit occupancy in Pb+Pb collisions. The TRT hit occupancy reaches very high values [56].

the Lorentz boost γ, and electrons tend to produce a larger amount of emitted photons compared to heavier particles such as pions, hence giving the detector the capability to discriminate between the two kind of particles.

In the TRT, the occupancy is much higher than in the pixel and SCT detectors because of the larger size of the straws compared to pixels and strips. Indeed, a 50% occupancy is reached when LHC is running at its design luminosity, while almost 100% is obtained in lead-lead collisions (see Figure 2.11).

From the track reconstruction point of view, the TRT plays an important role in the momentum resolution thanks to its long lever arm and helps in the identification of electrons allowing an electron track model to be applied in the track fit. However, the very high occupancy can degrade the pattern recognition performance Figure 2.11.

2.2.3.7   Material Budget of the ATLAS ID

Particles that traverse the inner detector interact with its material, i.e. with sensors, cables, support structures, cooling lines, etc. In particular, they can undergo several processes:

- Multiple scattering deflects charged particles from their trajectories;

- Hadrons can interact with the detector material through hadronic interaction and produce a stream of secondary particles.

- Interacting electromagnetically with the detector material, electrons emit photons via energy loss which can convert into e^+e^- pairs.

Interactions with the detector material lead to deterioration of the tracking reconstruction performance, which can be corrected up to a certain extent. For this reason, the amount of material should be as little as possible, preferring light-weight, low-Z material for the support structures and moving the end of services outside the tracking acceptance. Moreover, the material distribution in the ID
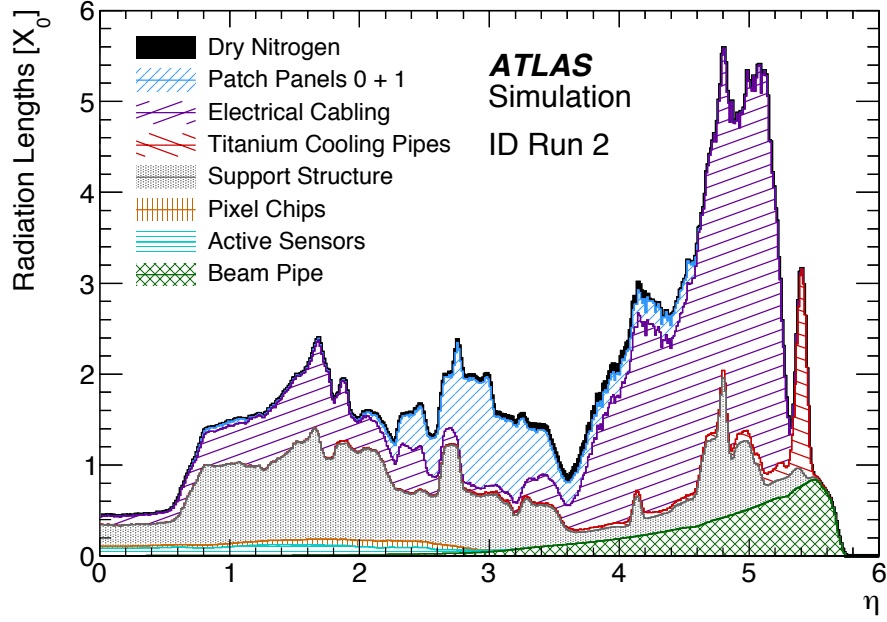
Figure 2.12: Radiation length X_0 versus the pseudo-rapidity η of the material of the current ATLAS Inner Detector (pixels, strips, TRT) [58].

volume affects strongly the calorimetry performance in particular at high pseudo-rapidity values. Although precise tables of the material content of a detector exist, there are – as experience shows – always small deviation when actually constructing the detector. Using photon conversions and hadronic interaction it is possible to estimate the amount of material within the tracking detector [57], which is usually expressed in terms of radiation lengths X_0 and nuclear interaction lengths λ_I. The radiation length X_0 is the mean distance over which a high-energy ($E \gg 2m_e$) electron loses all but $1/e$ of its energy due by bremsstrahlung. Equivalently, λ_I is the mean distance to reduce the number of relativistic primary hadrons to a fraction $1/e$. The amount of material associated with electromagnetic or nuclear hadronic interactions along a particular trajectory is expressed by dimensionless numbers, respectively N_{X_0} and N_{λ_I}, calculated as line integrals:

$$N_{X_0} = \int ds \frac{1}{X_0(s)}, \quad N_{\lambda_I} = \int ds \frac{1}{\lambda_I(s)}. \tag{2.17}$$

The ID material, expressed in terms of number of X_0 as a function of pseudo-rapidity, is shown in Figure 2.12. Figure 2.13 shows the distribution of hadronic-interaction vertices in data: the high resolution in the radial position of the vertices allows or the identification of all the details of the pixel detector.

2.2.4 Calorimeters

The ATLAS calorimeter system [41] surrounds the ID and is placed between the solenoid and toroid magnets. It consist of an inner electromagnetic calorimeter and an outer hadronic calorimeter, as shown in Figure 2.14, designed to contain all particles and measure their energy.

Both calorimeters are sampling calorimeters with layers of absorber alternated with layers of active medium material to perform energy measurements. When particles traverse the calorimeter, the dense absorbing material induce the particle to interact and create a cascade of secondary, less energetic particles, referred to as showers. The type of interaction and shower depends on the initial particle.
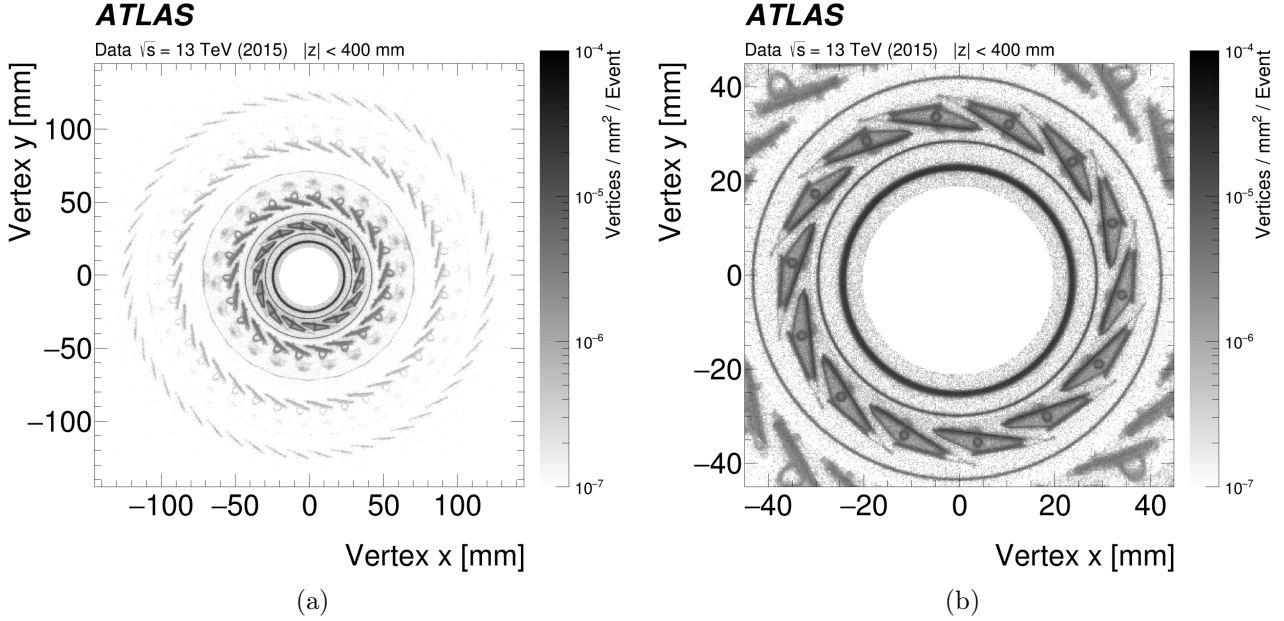
Figure 2.13: Distribution of hadronic-interaction vertex candidates for $|\eta| < 2.4$ and $|z| < 400$ mm in collision events: (a) $x - y$ view of the pixel detector; (b) $x - y$ view zomming into the beam pipe and IBL region [57].

In the electromagnetic calorimeter, mostly electrons and photons induce electromagnetic showers via bremsstrahlung and e^+e^- pair-production at high energies, and via ionisation and photoelectric effect at low energies. Hadronic showers, initiated by hadrons, from e.g. hadronic τ-lepton decays, are usually spatially more extended than electromagnetic showers and more complex. The energy of the initial particle is then obtained by summing up all the energy deposits within the active material of the calorimeter. The calorimeters have been designed to provide full coverage in ϕ and to measure a wide range of energy deposits from both charged and neutral particles over the pseudo-rapidity range $|\eta| < 4.9$. Moreover, to allow for a precise measurement, it is important that the hadronic showers are fully contained in the calorimeters and the amount of energy escaping the detection[8] is minimised. The most used figure of merit to define the calorimeter performance is the energy resolution, which is parametrised as:

$$\frac{\sigma_E}{E} = \frac{S}{\sqrt{E}} \oplus \frac{N}{E} \oplus C. \tag{2.18}$$

where S, N and C are respectively the so-called stochastic, noise and constant terms. The stochastic term accounts for the intrinsic fluctuations of the number of particles in the shower evolution; N describes the effect of pile-up noise and noise from readout electronics and is independent of the deposited energy; the constant term accounts for systematic effects due to mis-calibration of the detector as well as detector inactive material. At low energies, the resolution is limited by the pile-up noise, whereas at high energy, it is the constant term that limits the performance. The electromagnetic (hadronic) calorimeter has been designed to achieve an energy resolution with $N = 10\%$ (50%) and $C = 0.7\%$ (3%).

---

[8]Showers produced by very energetic hadrons may not be entirely absorbed by the calorimeter. Some of the particles in the shower can reach the muon spectrometer. This process is called punch-through.
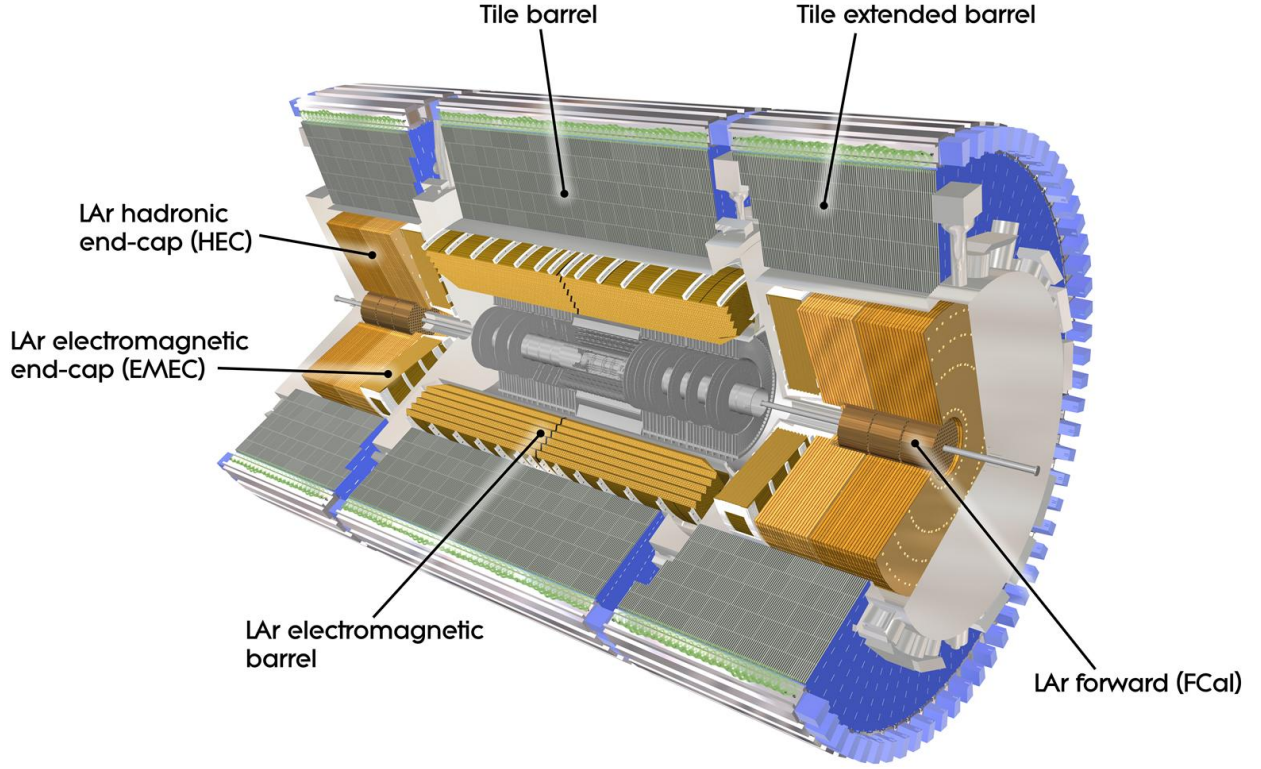
Figure 2.14: Schematic overview of the components of the electromagnetic and hadronic calorimeter in ATLAS [41]

2.2.4.1 Electromagnetic Calorimeter

The Electromagnetic Calorimeter (ECAL) is divided into a barrel region (EMB) and two end-caps (EMEC) covering $|\eta| < 1.475$ and $1.375 < |\eta| < 3.2$ respectively. The EMB consists of two identical half-barrels separated at $z = 0$ and each of the EMEC is mechanically divided into two coaxial wheels: an outer wheel covering the pseudo-rapidity range $1.375 < |\eta| < 2.5$ and an inner wheel that covers the remaining region up to $|\eta| = 3.2$. The transition region between EMB and EMEC ($1.375 < |\eta| < 1.52$), known as crack region, contains non-sensitive material in the form of services from the ID and are thus removed from most physics analyses using electrons and photons.

The ECAL uses liquid Argon (LAr) as active material with accordion-shaped Kapton electrodes and lead absorber plates over its full coverage. The LAr was chosen because of its intrinsic linear behaviour, high ionisation yield and stability. Moreover, it doesn't suffer from radiation damage making it preferable in the region close to the interaction point, as well as in the very forward region. The accordion geometry provides full ϕ coverage avoiding azimuthal cracks. The ECAL has a total thickness of at least 22 and 24 X_0 in the barrel and in the end-cap sectors respectively. This ensures the absorption of electron and photon showers up to a few TeV of energy and around 2/3 of typical hadronic showers. Over the region devoted to precision physics, i.e. $|\eta| < 2.5$, the ECAL is segmented into three longitudinal layers as shown in Figure 2.15a. The first layer is characterised by an excellent granularity in the η direction providing a precise position measurement in η of the electromagnetic shower and

(a)   (b)
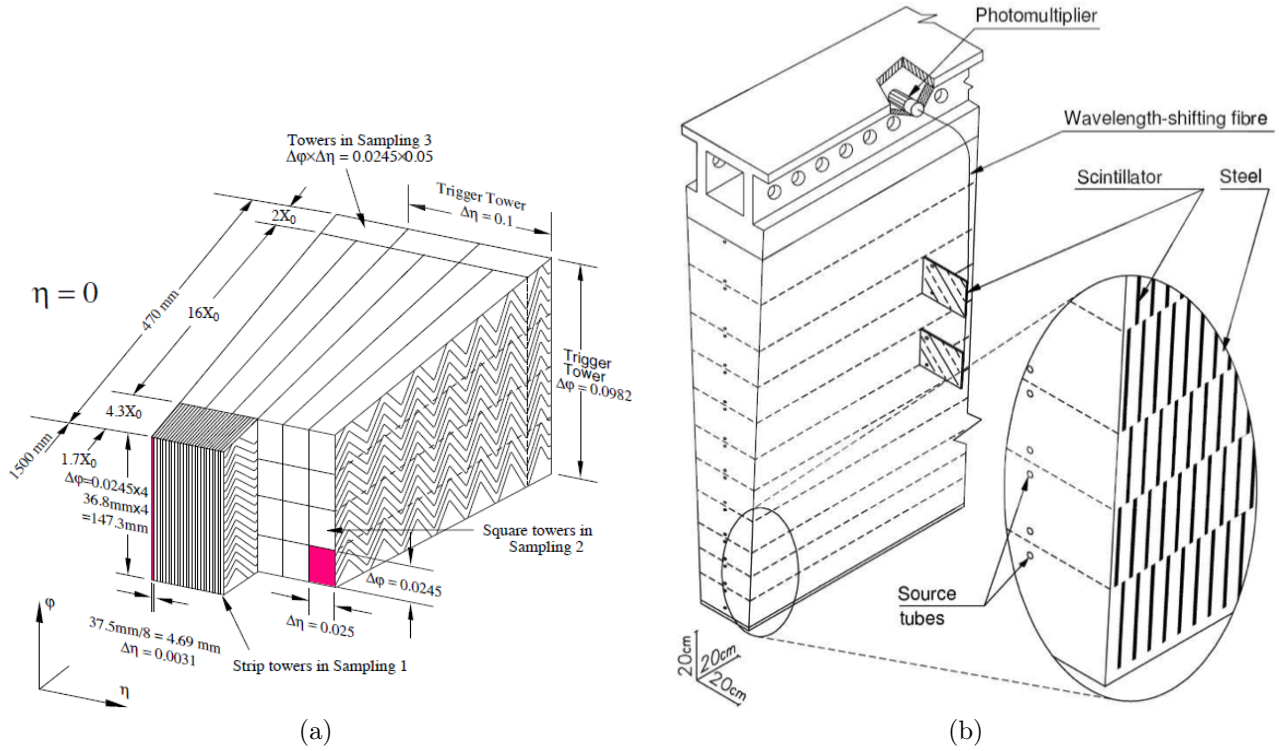
Figure 2.15: Schema of the different modules of the ATLAS calorimeters: electromagnetic calorimeter (a) and hadronic calorimeter (b).

enhancing particle identification (γ/π^0, e/π, etc.). The third layer is supposed to measure only the tails of the electromagnetic shower and therefore a coarser granularity was chosen. For $|\eta| > 2.5$, i.e. for the inner wheels of the EMEC, the detector is segmented in two layers and has a coarser granularity than for the rest of the acceptance. Where the amount of material exceeds $\sim 2~X_0$, in particular in $1.5 < |\eta| < 1.8$, a presampler, consisting of an active LAr layer of thickness 1.1 cm (0.5 cm) in the barrel (end-cap) region, is used to improve the energy measurement and correct for the energy loss of electrons and photons upstream of the calorimeter.

2.2.4.2 Hadronic Calorimeter

The ATLAS Hadronic Calorimeter consists of four different sub-systems that cover the entire pseudo-rapidity range up to $|\eta| = 4.9$. It uses different techniques as best suited for the widely-varying requirements and radiation environment over the large η range. They are the Tile Barrel, the Tile Extended Barrel, the LAr Hadronic End-caps (HEC) and the Forward Calorimeter (FCAL) (Figure 2.14). The main parameter in the design of the hadronic calorimeter is its thickness: with more than eleven interaction length λ_I, it provides good containment of hadronic showers minimising punch-through into the muon spectrometer.

Covering respectively the ranges $|\eta| < 1.0$ and $0.8 < |\eta| < 1.7$, the Tile Barrel and the Tile Extended Barrel calorimeters consist of sampling calorimeters that use scintillating tiles as active material and steel as absorber, arranged in three layers. The scintillation light induced in a tile upon the passage of radiation is read out by optical fibres and sent into two separate photomultiplier tubes.

The region $1.5 < |\eta| < 3.2$ is covered by the HEC which consists of two cylindrical wheels, each with different granularities, placed behind the electromagnetic calorimeter. Here, copper plates are used as

absorbers and LAr as active material. The HEC extends from $|\eta| = 1.5$ up to 3.2 and thus overlaps with the Tile Extended Barrel and the FCAL.

2.2.4.3 Forward Calorimeter

Finally, in the most forward part ($3.1 < |\eta| < 4.9$) the Forward Calorimeter (FCAL) is present. Its high density has been dictated by the very high particle flux it is exposed. The FCAL is characterised by a depth of approximately 10 λ_I, and consists of three layers in each end-cap: the first, made of copper, is used as electromagnetic calorimeter, while the remaining two, made of tungsten, are used as hadronic calorimeters. The structure of the three layers consists of a metal matrix of concentric rods and tubes parallel to the beam axis. The gaps between rods and tubes is filled with LAr which was chosen as active material.

2.2.5 Muon Spectrometer

Traversing the calorimeters, muons lose only a small fraction of their energy so that they can be detected in the Muon Spectrometer (MS), that provides high-resolution measurements of their momentum up to very high energies (few TeV) within $|\eta| < 2.7$. The muon momentum measurement is based on the track deflection in the toroid magnet (see § 2.2.2). The MS can perform stand-alone measurements being independent from the other sub-detectors: this feature is important for fast event triggering as well as for redundancy in the pattern recognition.

Muon tracks are measured in two types of precision tracking chambers, the Monitored Drift Tubes (MDTs) in the barrel and the Cathode Strip Chambers (CSCs) in the end-caps. Furthermore, Resistive Plate Chambers (RPCs) and Thin Gap Chambers (TGCs) are used in the barrel and in the end-caps respectively to allow for fast triggering of muon events within $|\eta| < 2.4$. In the barrel region, detectors are arranged in three layers around the beam axis, one layer being inside the magnet. In the end-caps the three layers are placed on four wheels perpendicular to the beam axis.

The MDTs are proportional chambers based on drift tube technology. The 30 mm diameter tubes are made of aluminium and are filled with an Ar/CO_2 gas mixture. Due to their reliability, mechanical robustness and simple operation, MDT chambers are employed to cover the larger area of the spectrometer.

Due to the large particle flux at large $|\eta|$, the innermost layer of the end-caps ($2.0 < |\eta| < 2.7$) uses the CSCs which are radially oriented multi-wire proportional chambers. A fast readout gives them the possibility to achieve higher acquisition rates.

The RPCs are used in the barrel region to trigger on muons exploiting their good spatial and time resolution, which allows for the discrimination of muons from different bunch crossings. The basic RPC unit is a narrow gas gap filled with a gas mixture, formed by two parallel resistive bakelite plates. They cover the pseudo-rapidity region $|\eta| < 1.05$.

Finally, in the end-cap wheels, $1.05 < |\eta| < 2.7$ ($1.05 < |\eta| < 2.4$ for the trigger), TGCs provide good time resolution and high rate capability. They rely on the same principle as multi-wire proportional chambers operating with a highly-quenching gas mixture of 55% CO_2 and 45% n-pentane (n-C_5H_{12}) and with wires arranged parallel to the MDT wires in order to provide the trigger information. The TGCs are also used to measure the ϕ coordinate of the track to complement the measurements performed by the MDTs.

2.2.6 Trigger System

Not every LHC collision can be recorded by the ATLAS detector: when the LHC operates at an instantaneous luminosity of 10^{34} cm^{-2} s^{-1}, about a billion proton-proton events are produced per second. Considering the size of each event to be approximately 1.3 MB, the resulting total data to be recorded exceed quickly the amount of data that can be stored permanently. Moreover, many of the events just contain well-known low-p_T proton scattering events. The goal of the ATLAS trigger and data acquisition (DAQ) system is therefore to select in real time and record efficiently events with interesting characteristics for physics, such as high-p_T leptons, photons, jets or large amount of missing transverse momentum, while discarding minimum-bias events[9].

The ATLAS trigger system is composed of a hardware-based Level-1 (L1) trigger and a single software-based High Level Trigger (HLT). They are able to reduce the event rate from the bunch-crossing rate of 40 MHz to 100 kHz at L1 and to an average recording rate of 1 kHz at the HLT. During the LS1 of the LHC, the ATLAS trigger system has undergone major changes to cope with the approximately 5 times larger event rates due to the decrease in bunch spacing and the increase of the peak luminosity expected for Run-2 data taking.

Only a subset of the detector information from the calorimeters with coarser granularity and the MS is used for the L1 trigger to accept or reject the event within a latency of 2.5 μs. No information from the ID is considered due to the huge amount of channels and hence long readout time. If the event is accepted at L1, the event information is read out from the pipeline memories of the detectors and stored in read-out buffers until they are further processed by the HLT. The information about the geographical coordinates in η and ϕ of the trigger objects is used to define one or more Regions-of-Interest (RoI's), in which interesting activity has been detected together with a rough estimate of the transverse momentum of the candidate object and the event energy sums.

The HLT can investigate the RoI using the full granularity of all sub-detectors and reconstructs the full event using fast offline-like algorithms. Furthermore, objects are calibrated and alignment corrections are applied. The HLT average processing time is 0.2 s/event. Commissioning in ongoing for a hardware track finder (FTK) to provide tracks to the HLT at L1 rates.

2.3 Upgrades of LHC and ATLAS

The LHC has worked in an excellent way so far: during the LS1, from 2013 to 2014, the machine has already been subject of a series of upgrades: the centre-of-mass energy was increased from 8 to 13 TeV, the number of bunches per beam was increased from 1380 to 2808 and the bunch spacing was reduced from 50 to 25 ns. With these modifications, the instantaneous luminosity reached the nominal value of 10^{34} cm^{-2} s^{-1} from 2015, which will allow for an integrated luminosity delivered until the next LS in 2019 of about 150 fb^{-1}. At the same time, some of the LHC experiments performed upgrade work on some of the sub-systems. In the case of ATLAS, the IBL was inserted (§ 2.2.3.4), which required the replacement of the beam-pipe, and a complete revision of the pixel detector was performed in order to recover the full functionality.

Over the next 10 years, a series of ambitious upgrades are part of the LHC scientific program that will ultimately result in an integrated luminosity for proton-proton collisions of 3000 fb^{-1} by 2035. The necessary improvements will be realised in two LSs, each of two to three years duration (see Figure 2.16).

During the LS2, in 2019 and 2020, LHC will be prepared to double the nominal instantaneous lu-

---

[9]Minimum-bias events are characterised by parton interactions with very low transferred momentum. The name comes from the fact that to record them a minimal set of trigger conditions is required at data taking.

minosity, reaching $\mathcal{L} = 2 - 3 \times 10^{34}$ cm^{-2} s^{-1}, with to 55 to 80 interactions per crossing and 25 ns bunch spacing. This will be possible thanks to the integration of the Linac4 into the injector complex, the increased energy of the PS Booster to reduce the beam emittance, and the upgrade of the LHC collimator system. ATLAS Phase-I Upgrades [59] will primarily involve the trigger system, both in the muon spectrometer (the New Small Wheel [60] will replace the first end-cap station of the MS) and the electromagnetic and forward calorimeters, to cope with luminosities beyond the LHC nominal design value, while retaining the same physics performance. Moreover, the FTK (see § 2.2.6) will perform on-line track finding and fitting in the full geometrical coverage using dedicated massive parallel processing: track parameters with resolution close to the off-line one will be provided at the HLT for a more advanced event selection.

In its ten-years operations period, ending in the early 2020s, the LHC will deliver between 300 and 400 fb^{-1}. By that time, accelerator and experiments will be facing the degradation of their components because of the accumulated radiation damage [61].

The Phase-II Upgrade, during the LS3 between 2024 and 2026, is the final step towards the High Luminosity LHC (HL-LHC). Thanks to upgrades of the accelerating cavities and bending magnets, the HL-LHC will be able to deliver very high peak instantaneous luminosities levelled down to typically 5.0 - 7.5 $\times 10^{34}$ cm^{-2} s^{-1} in the detector with up to 200 interaction per beam crossing every 25 ns, allowing the collection of a large dataset of up to 3000 fb^{-1}.

In order to cope with these extreme data rates, the ATLAS Phase-II Upgrade Program [62] foresees important changes for both tracking and trigger systems and further upgrades of other detector components. A complete replacement of the detector readout electronics is foreseen to accommodate a new two-steps Level-0/Level-1 trigger architecture with both higher acceptance rates and extended latencies. The 1 MHz accept rate at Level-0 will be reduced down to ~ 200 kHz thanks to the integration of a new Level-1 track trigger which will provide accurate tracking information to accompany the calorimeter and muon triggers. Moreover, an increased bandwidth of the tracking sub-system readout will be needed to cope with the higher occupancy and provide input to the new Level-1. The current tracking system will be completely replaced by an entirely new all-silicon tracker consisting of pixel layers to provide pattern recognition and precision measurements as close as possible to the interaction point complemented by a microstrip system for accurate tracking at larger radii.

The upgrades of the Inner Detector during the ATLAS Phase-II Upgrade is the one of the subjects of this thesis and will be described in detail in Chapter 6.
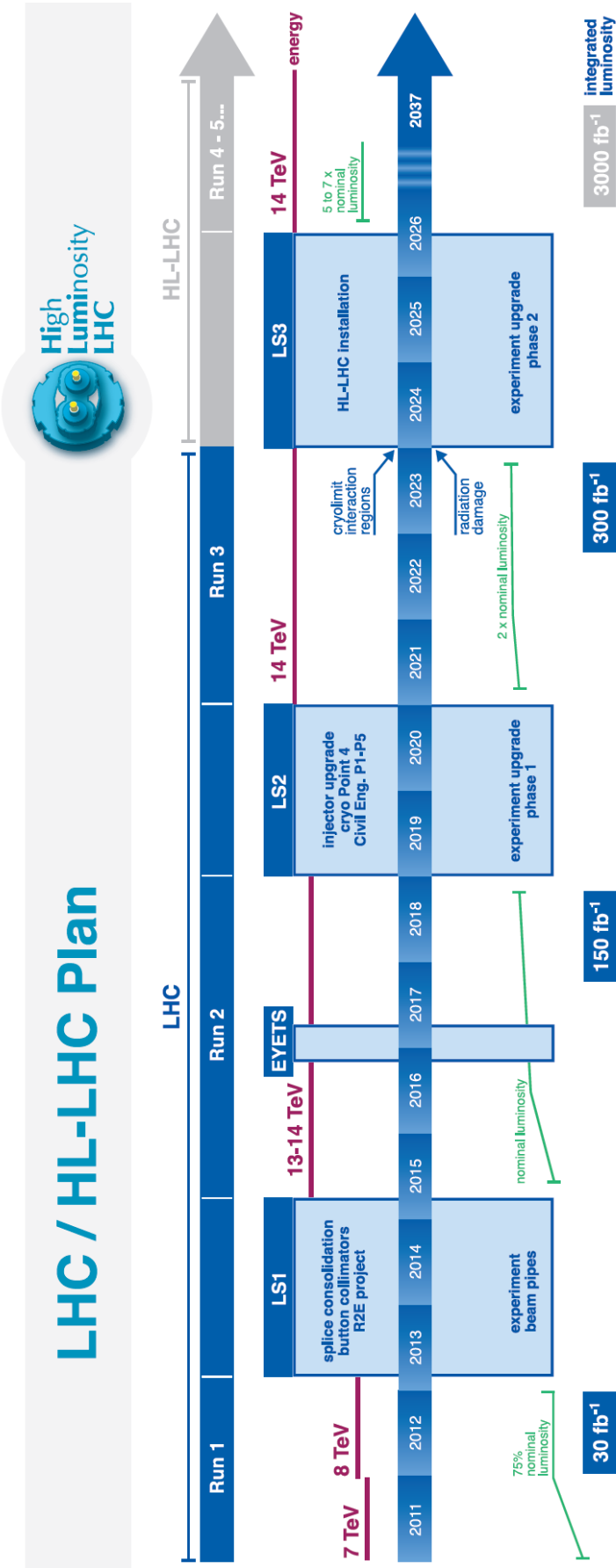
Figure 2.16: Updated status of the LHC baseline programme including the HL-LHC run. The picture shows the time slots dedicated to the Long Shutdowns (LSs) and to the End of Year Extended Technical Stop (EYETS). The increase of the centre-of-mass energy and instantaneous luminosity are indicated as well as the expected integrated luminosity after each Run [63].

Part II

Improving Jet Substructure Techniques for Searching for Resonances with Boson-Tagged Jets

3

Jet Reconstruction

Contents

3.1 Introduction

Unlike other particles in the Standard Model, e.g. electrons and muons, gluons and quarks, generally called partons, cannot be observed as individual particles in the detector. Due to the properties of the strong interaction, i.e. asymptotic freedom and color confinement, partons undergo fragmentation and hadronisation during which additional partons are radiated and final state hadrons are formed. The ensemble of the produced charged and neutral hadrons forms a stream of particles, a so-called jet, moving in a direction that is strongly correlated with that of the initial parton.

At hadron colliders like the LHC, jets are very commonly produced in the hard-scattering process in a proton-(anti)proton collision and in the hadronic decays of particles. Understanding of the properties of jets is therefore extremely important to correctly reconstruct events at the LHC and to improve our comprehension of hard-scattering processes.

This thesis focuses on the development of a boosted boson tagging technique which will be applied to the search for hadronic decays of boosted vector boson pairs. In such events, the vector bosons are produced with a transverse momentum which is generally much larger than their mass. For this reason, the two-quark system produced in the decay of the vector boson is collimated along the boson momentum direction. In particular, the angular separation between the decay products can be expressed in terms of the mass, m, and the transverse momentum, p_T, of the vector boson as follows:

$$\Delta R_{q\bar{q}} \simeq \frac{1}{\sqrt{x(1-x)}} \frac{m}{p_{\mathrm{T}}} \tag{3.1}$$

where x and $(1-x)$ are the fractions of the vector boson momentum carried by the two quarks. For W and Z boson decays, it is possible to simplify Equation 3.1 assuming that the two quarks have approximately the same momentum, leading to:

$$\Delta R_{q\bar{q}} \simeq 2\frac{m}{p_{\mathrm{T}}}. \tag{3.2}$$

Figure 3.1 shows the angular distance, $\Delta R_{q\bar{q}} = \sqrt{(\Delta\eta)^2 + (\Delta\phi)^2}$, between the two quarks from the W boson decay from $t \to Wb$ events as a function of the p_{T} of the W boson. At high p_{T}, i.e. $p_{\mathrm{T}} >$ 500 GeV, the parton showers generated by the two quarks significantly overlap and can no longer be resolved. Boosted vector bosons which decay hadronically can therefore be reconstructed as large-radius (large-R) jets with a size of $R = 1.0$ to fully contain all of the energy deposits from the hadronic decay. At this point, advanced substructure techniques can be used to exploit the differences between large and small-R jets: in the hadronic boson decay, two independent energy substructures can be identified within the larger-R jets. Further confidence on the provenance of the two jets from a W or a Z decay can be achieved by introducing additional requirements on other kinematic variables, i.e. the energy split between the sub-jets [64]. Substructure techniques play a central role in the developments of boosted boson tagging algorithms, as will be described in Chapter 5.

However, due to the high-luminosity environment (see § 2.1 and Figure 2.3), large-R jets at the LHC suffer from the contamination of soft particles unrelated to the hard-scattering process, which leads to mis-measured jet observables, such as mass and energy. Jet grooming techniques have been developed to mitigate the effect of pile-up and the underlying event, and will be discussed in § 3.4.

The description of the inputs to the jet reconstruction is presented in § 3.2 while § 3.3 describes how they are used in jet reconstruction algorithms. Jet grooming and jet calibration are discussed respectively in § 3.4 and § 3.5. Finally, § 3.6 and § 3.7 provide more information on some of the substructure variables.

In the following, jets originating from the hadronic decay of a vector boson will be referred to as W/Z-jets, while jets initiated by light quarks or gluons will will be referred to as QCD-jets.

3.2   Inputs to Jet reconstruction

Any set of four-vectors can be used as inputs to the jet reconstruction: topo-clusters, i.e. calorimeter energy deposits, lead to topo-cluster jets; tracks from the primary vertex are the inputs to track jets; and truth particles result in truth jets. By construction, the jet reconstruction process does not depend on the input type, although calibration factors and uncertainties have to be derived for the different objects in different manners. Recent developments have resulted in a new object, the Track-CaloCluster, which contains information from both tracks and calorimeter clusters to improve the precision of jet substructure techniques. This will be the main topic of Chapter 4.

In this section, the topo-cluster formation and calibration will be discussed, as topo-cluster jets will be used in the following chapters.

3.2.1   Topo-cluster Formation and Calibration

Topologically connected calorimeter cells are grouped together to form topo-clusters. The purpose is to recreate the three-dimensional energy deposit representing the shower development of a single particle entering the calorimeter while suppressing noise. The grouping procedure is based on the cell
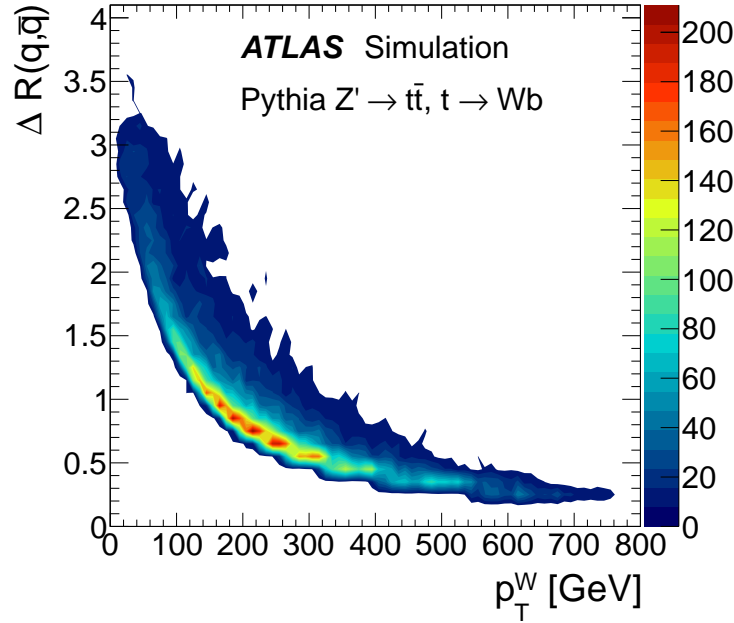
Figure 3.1: Distribution of the angular separation $\Delta R_{q\bar{q}} = \sqrt{(\Delta\eta)^2 + (\Delta\phi)^2}$ between the two quarks from the W boson decay from $t \to Wb$ events as a function of the p_T of the W boson [64].

signal-to-noise ratio, also referred as cell significance:

$$\zeta_{\text{cell}}^{\text{EM}} = \frac{E_{\text{cell}}^{\text{EM}}}{\sigma_{\text{cell}}^{\text{noise}}} \tag{3.3}$$

where $E_{\text{cell}}^{\text{EM}}$ is the cell signal measured at the electromagnetic scale and $\sigma_{\text{cell}}^{\text{noise}}$ is a noise term which includes the expected electronic noise and calorimeter activity due to pile-up energy deposits.

First the cluster is seeded by a cell having $\zeta_{\text{cell}}^{\text{EM}} > 4$. Iteratively, neighbour cells (and neighbours of the neighbours) are added if $\zeta_{\text{cell}}^{\text{EM}} > 2$, following the natural profile of the energy deposits. Finally, a contour of cells with $\zeta_{\text{cell}}^{\text{EM}} > 0$ is added to the cluster. The three steps are repeated for each seed cell until no seed cells remain. A splitting procedure is then used to split clusters in case multiple local energy maxima are found within it. The mass of the resulting topo-clusters is set to be zero while their energy corresponds to the weighted sum of the energies of the constituent cells.

Before being passed to the jet reconstruction algorithms, a Local Calibration Weighting (LCW or LC) scheme is used to calibrate clusters individually based on their properties, such as their energy density, isolation and depth in the calorimeter. This calibration scheme is designed to correct for the non-compensating character of the calorimeter and signal losses due to energy deposited in inactive material or outside of the topo-clusters. Correction factors compensating for these effects calibrate topo-clusters from the raw electromagnetic (EM) scale to the LC scale.

An additional correction is then applied to the topo-cluster angles. So far they have been assumed to point towards the nominal interaction point of $(0, 0, 0)$. Each calorimeter cluster is therefore corrected to point back to the reconstructed primary vertex (the beam spot is used in case no primary vertex is reconstructed) and all of the cluster kinematics are redefined accordingly. This correction provides a significant improvement in the resulting jet angular resolution.

Topo-clusters are now ready to be used as input to jet reconstruction algorithms.
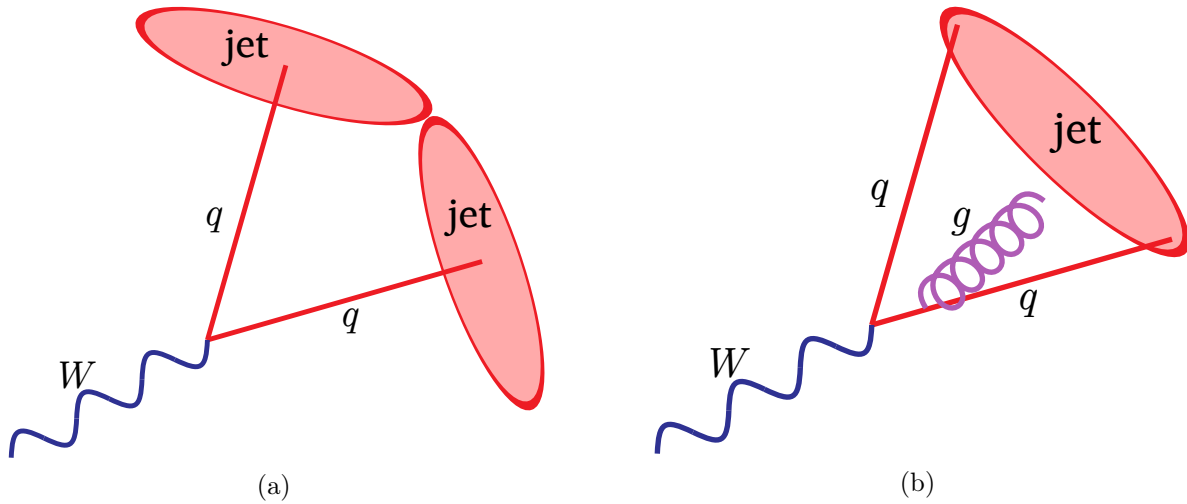
Figure 3.2: Configurations illustrating infra-red unsafety of a jet algorithm in events with a W boson decaying into two hard partons. In (b) the emission of the soft gluon causes one single jet to be reconstructed instead of two separate ones (a) [66].

3.3 Jet Reconstruction Algorithms

Jet algorithms are used to group energy deposits in three dimentional space into a jet. This process is governed by a distance parameter R which establishes how far an input can be from the primary jet axis and still be included in the jet. Jet reconstruction algorithms must have the following properties [65]:

- For practical reasons, they have to be simple to implement both in an experimental analyses and in theoretical calculations;

- The algorithms should be robust in the presence of pile-up and underlying event in the collision;

- The algorithms must be defined at any order of the perturbation theory providing finite cross-sections which should be relatively insensitive to hadronisation.

The last criterion is summarised in the definition of infra-red and collinear safe algorithms. In an infra-red safe algorithm, the emission of soft partons in the final state doesn't affect the topology nor the number of jets found by the algorithm, whereas collinear safety implying that the same jets are reconstructed independently on the collinear splitting of a hard particle. As an example, Figure 3.2 shows the effect of the radiation of a soft gluon on the number of jets that can be reconstructed: instead of being reconstructed as two separate jets, the two decay products of a vector boson can be merged into a single jet due to soft gluon emission.

In collinear safe algorithms, the number of reconstructed jets does not depend on the split of a particle carrying a certain fraction of the jet p_T into two collinear particles. In case a different number of reconstructed jets occurs, divergences in the calculation of the tree-level matrix element are not cancelled.

Sequential recombination algorithms, the most widespread class of jet algorithms in ATLAS, will now be described.

3.3.1 Sequential Recombination Algorithms

Sequential recombination algorithms are based on the combination of pairs of inputs, which could be either topo-clusters, tracks, truth particles or any other four-vector, into a single object if they satisfy a minimum distance criterion. Pair merging is repeated until no further combinations are possible. Given a pair of inputs ij, their combination depends on the the distance parameter defined as:

$$d_{ij} = \min\left(p_{\mathrm{T},i}^{2p}, p_{\mathrm{T},j}^{2p}\right) \frac{\Delta R_{ij}^2}{R^2} \tag{3.4}$$

where $p_{\mathrm{T},i}$ and $p_{\mathrm{T},j}$ are the transverse momenta of the inputs, $\Delta R_{ij}^2 = \Delta \eta_{ij}^2 + \Delta \phi_{ij}^2$ their angular distance and R a free parameter that controls the size of the jet. Subsequently, it is possible to define a "beam" distance

$$d_{iB} = p_{\mathrm{T},i}^{2p}. \tag{3.5}$$

For each pair of inputs, if $d_{ij} < d_{iB}$, i and j are merged into a new pseudo-particle. If $d_{iB} < d_{ij}$, then i is removed from the input collection and called a jet if its transverse momentum is above a given threshold $p_{\mathrm{T,min}}$[(1)].

The parameter p in Equations (3.4) and (3.5) determines the kind of algorithm: the k_t algorithm [67,68] corresponds to $p = 1$, the Cambridge-Aachen algorithm [69] to $p = 0$ and the anti-k_t algorithm [70] to $p = -1$. All of these jet algorithm variants are infra-red and collinear safe to all orders of perturbation theory. The main difference between the three jet algorithms lies in the shape of the boundaries of the reconstructed jet: while the k_t and the Cambridge-Aachen algorithms lead to irregularly shaped jet boundaries, the anti-k_t algorithm results in cone-like boundaries, as shown in Figure 3.3. This behaviour depends on the how the constituents are combined together and, in particular, if the clustering process starts from low or high-p_{T} inputs. The combination of low-p_{T} constituents can be very problematic in the high pile-up environment where additional jet can be reconstructed from random constituents not associated with real jets. Unlike the k_t and the Cambridge-Aachen algorithms, the anti-k_t algorithm merges first high p_{T} inputs. By construction, the anti-k_t algorithm is much less affected by pile-up, as it starts building the jet from the hard constituents and gives the jets a regular area.

The anti-k_t algorithm is generally used in ATLAS with a typical radius of $R = 0.4$. However, the shape of jets obtained using the Cambridge-Aachen and k_t algorithms support studies into the parton shower development of the initial particle.

The large-R jets studied in the following chapters are reconstructed using the anti-k_t algorithm using a radius parameter $R = 1.0$.

3.4 Jet Grooming Algorithms

As mentioned in § 3.1, effects due to pile-up can contaminate large-R jets leading to wrongly measured jet observables. As an example consider the jet mass from simulated W boson and QCD di-jet events, as shown in Figure 3.4a. For W-jets, the jet mass is far from being close to the mass of its originating boson. To remove the pile-up contamination, several grooming techniques have been studied by the ATLAS collaboration, including trimming [71], split-filtering [72] and pruning [73].

In the following a brief description of the trimming technique will be presented, since trimmed jets will be used later on.

[(1)]The limit on the transverse momentum avoids arbitrarily soft entity without any other object in $\Delta R_{ij} < R$ to be reconstructed as a jet.

(a)

(b)

(c)
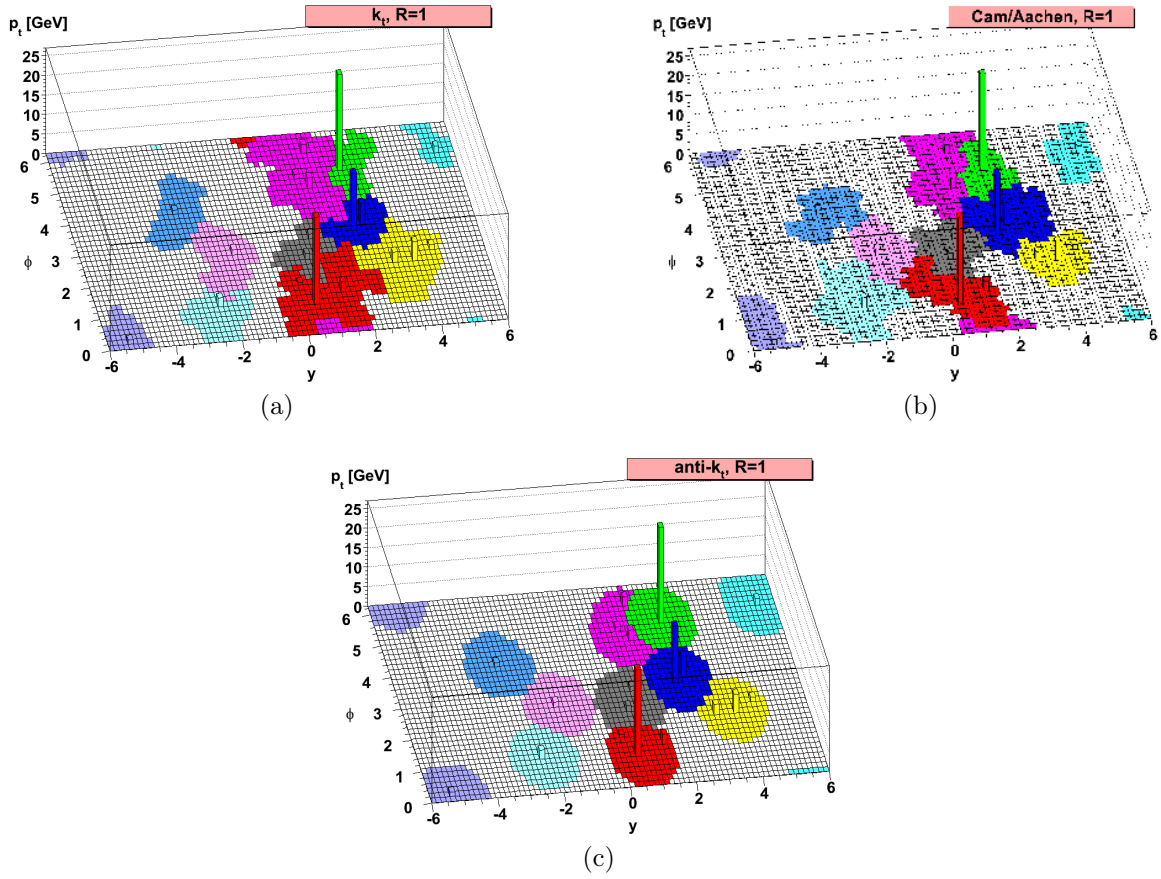
Figure 3.3: Example of clustering particles in the same event to form jets using the k_t algorithm (a), the Cambridge-Aachen algorithm (b) and the anti-k_t algorithm (c). The main difference between the three jet algorithms lies in the shape of the boundaries of the reconstructed jet: while the k_t and the Cambridge-Aachen algorithms lead to irregularly shaped jet boundaries, the anti-k_t algorithm results in cone-like boundaries [70].
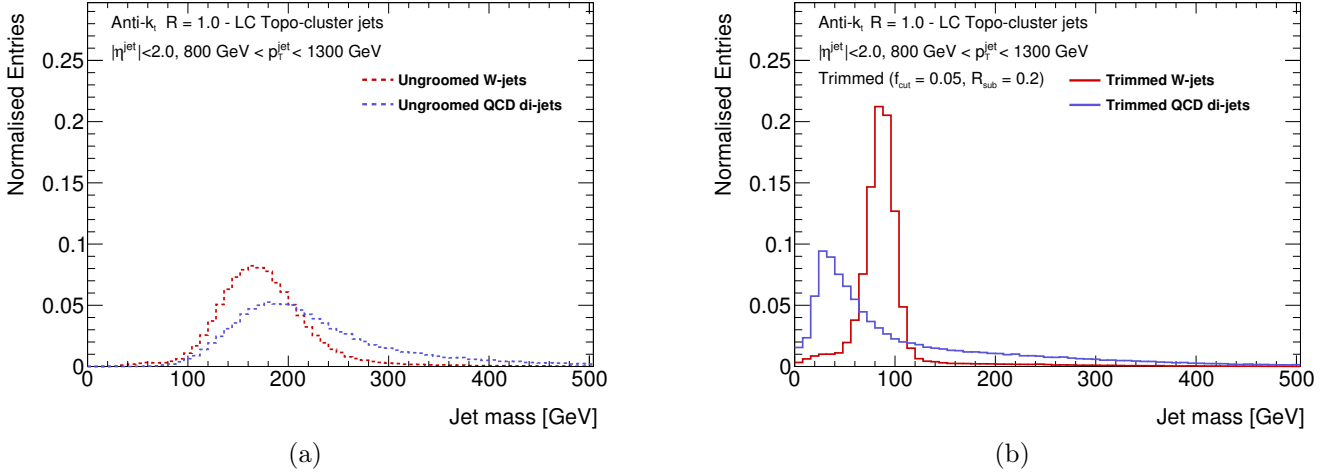
Figure 3.4: Comparison of the mass distribution for W and QCD di-jets reconstructed with the anti-k_t algorithm with $R = 1.0$ before (a) and after (b) trimming ($f_{\text{cut}} = 0.05$ and $R_{\text{sub}} = 0.2$). The discrimination between the two jet topologies as well as the mass resolution of the W/Z-jets is significantly improved after trimming.

3.4.1 Trimming

The trimming technique can be summarised in the following steps:

1. the constituents of the large-R jet are re-clustered into sub-jets, using the k_t algorithm, with a typical size of $R_{sub} = 0.2$[(2)];

2. sub-jets are removed from the large-R jet if their transverse momentum (p_T^{sub}) is below a certain fraction of the large-R jet p_T: $p_T^{\text{sub}} < f_{\text{cut}} \cdot p_T$, typically $f_{\text{cut}} \approx 0.05$;

3. the remaining sub-jets are combined to form the trimmed large-R jet.

By construction, this grooming technique is able to remove many constituents corresponding to pile-up and initial-state radiation, which produce sub-jets that are relatively soft with respect to sub-jets from the hard scattering process. Figure 3.4b shows the mass distribution for W-jets and QCD di-jet events after trimming is applied to the jets: the discrimination between the two jet topologies as well as the mass resolution of the W/Z-jets is significantly improved.

3.5 Large-R Jet Calibration

Jets reconstructed with the algorithm presented in § 3.1 cannot yet be used in an analysis. This is due to detector and reconstruction effects, such as the non-compensating behaviour of the ATLAS calorimeter, presence of dead material, and shower leakage. QCD di-jet Monte Carlo simulations are therefore used to derive calibration constants to correct the reconstructed jets to the truth jet energy and mass scale [74]. The same calibration factors are then applied to both data and Monte Carlo events. Further differences between data and Monte Carlo are accounted for later.

Truth jets and reconstructed jets are built using the same jet algorithm and the same grooming technique. A truth jet is then matched to a reconstructed jet if their angular distance in the $\eta - \phi$

[(2)]$R_{sub} = 0.2$ is used is Run-2 while $R_{sub} = 0.3$ was used during Run-1.

space is below 0.75 times the jet size, i.e. $\Delta R < 0.75\ R$. Once the matching is done, the jet energy response and the jet mass response are evaluated:

$$\mathcal{R}_E = \frac{E_{\text{reco}}}{E_{\text{true}}}, \qquad \mathcal{R}_m = \frac{m_{\text{reco}}}{m_{\text{true}}}. \tag{3.6}$$

Starting with the jet energy scale correction, the calibration factors are then evaluated in bins of E_{true}[3] and η_{det}, i.e. the jet η pointing from the geometric centre of the detector[4]. In each $(E_{\text{true}}, \eta_{\text{det}})$ bin, the response is fitted assuming a Gaussian distribution and converted into an average response as a function of E_{true} for each η_{det} bin. A numerical inversion technique is then used to transform the average E_{true} into the corresponding E_{reco}. The resulting jets are calibrated at the LC+JES scale.

At this point, the mass scale correction is performed starting from the mass response distribution as a function of m_{true} and η_{det} and using the same procedure as described above for the energy calibration. Figure 3.5 and Figure 3.6 show respectively the jet energy response and the jet mass response as a function of the η_{det} in different jet energy bins before and after calibration. After calibration, the η-dependent effects are reduced and the two responses show a uniform behaviour across the entire detector. In addition to the jet energy and mass calibration, the jet η is also corrected to obtaining the final calibrated jet four-vector.

However, after calibration is applied, some inconvenient behaviours appear mainly due to the incorrect behaviour of the numerical inversion technique for high-p_T and low truth mass jets. To address these difficulties and improve the jet mass resolution, especially at high-p_T, the track-assisted jet mass was introduced.

3.6   Jet Mass Definitions

One of the most important and powerful variables to differentiate jets from the decay of a boosted vector boson from QCD-jets is the mass of the jet. For W and Z-jets, the mass of the reconstructed jet is close to the mass of the vector boson, while for QCD-jets the mass distribution generally peaks at low values since they originate from approximately massless partons. The jet mass is evaluated starting from the energy and the momentum of the constituents, C, of the jet as follows:

$$m^2 = \left(\sum_{i\,\in\,C} E_i \right)^2 - \left(\sum_{i\,\in\,C} \vec{p}_i \right)^2. \tag{3.7}$$

Typically, for calorimeter jets composed of topo-clusters, this definition of the jet mass leads to the so-called calorimeter-based jet mass denoted m_{calo}.

Although the calorimeters offer an excellent energy resolution (see § 2.2.4), in highly collimated environments, such as the ones originating from highly boosted vector bosons, the spatial granularity can become a limiting factor. In these scenarios, the spatial separation of the decay products reaches the calorimeter granularity, affecting the measurement of the jet kinematics. In the extreme case where the reconstructed jet consist of a single calorimeter cluster, Equation 3.7 returns zero as a value for the jet mass.

The track-assisted jet mass [75] has been implemented to improve the mass resolution at high p_T profiting from the excellent angular resolution of the tracker. Reconstructed tracks are therefore included in the jet reconstruction if they satisfy the following selection criteria [76]:

---

[3]The true quantity is preferred to the reconstructed one to remove the dependence on the underlying p_T distribution and thus allow the responses to result in Gaussian distribution.

[4]Using η_{det} removes any ambiguity as to which region of the detector is measuring the jet.
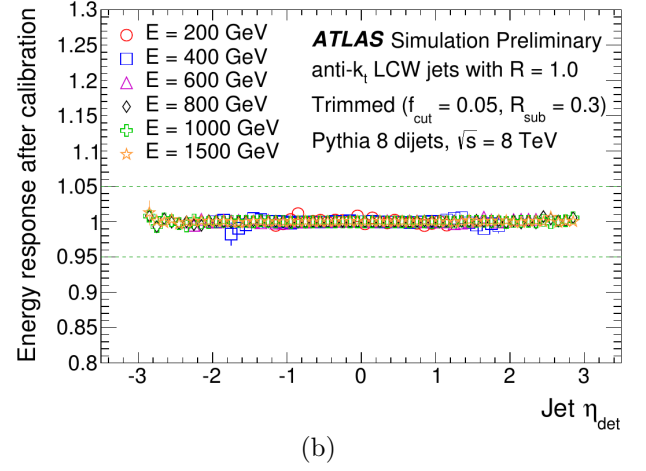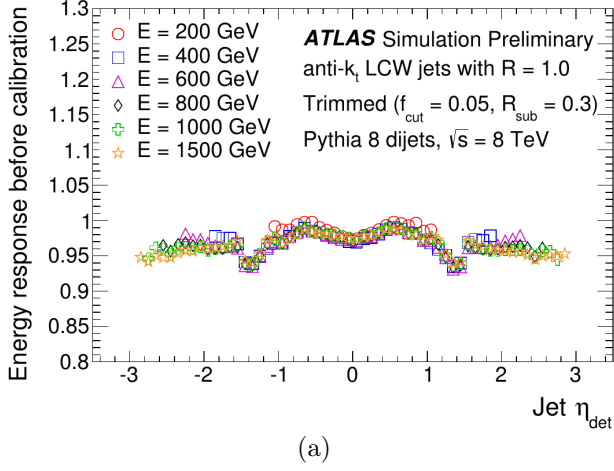
Figure 3.5: Jet energy response as a function of jet η_{det} before (a) and after (b) jet energy calibration. After calibration, the η-dependent effects are reduced and the two responses show a uniform behaviour across the entire detector [74].
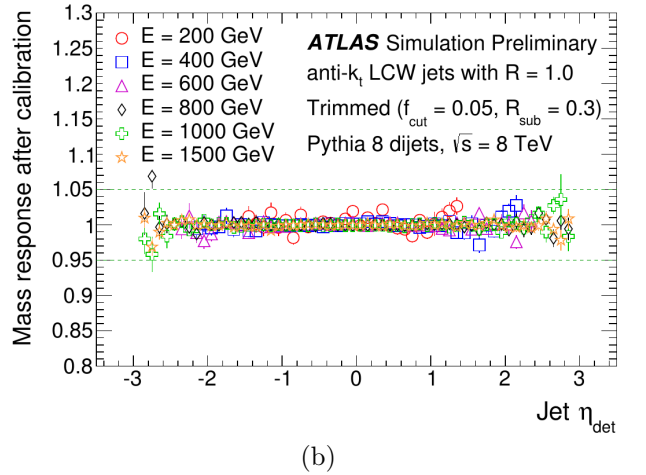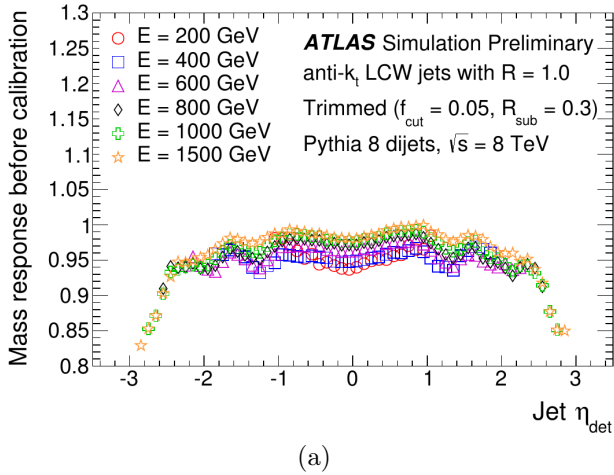

Figure 3.6: Jet mass response as a function of jet η_{det} after the jet energy calibration and before (a) and after (b) jet mass calibration. After calibration, the η-dependent effects are reduced and the two responses show a uniform behaviour across the entire detector [74].

- Originate from the primary vertex, defined as the vertex with the highest $\left(\sum p_T^{\text{trk}}\right)^2$;

- $p_T^{\text{trk}} > 500$ MeV;

- $|\eta| < 2.5$;

- $|d_0| < 1.5$ mm;

- $|z_0 \sin\theta| < 1.5$ mm;

- pixel measurements ≥ 1;

- SCT measurements ≥ 6;

Reconstructed tracks passing the selection mentioned above are then "ghost associated" to the calorimeter jets, i.e. are added to the inputs of the jet reconstruction algorithms with infinitesimally small p_T. A track is then associated to a jet if it is clustered into it. It is possible to evaluate the mass of the jet considering only the ghost associated tracks. This definition of the jet mass is called the track-based jet mass and is denoted m_{trk}. Since the ID can only reconstruct trajectories from charged particles, m_{trk} neglects the contribution of the neutral component of the jet and hence doesn't provide an accurate description of the mass of the jet. The track-assisted mass definition can be expressed as follows, where the ratio of the transverse momenta $p_T^{\text{calo}}/p_T^{\text{trk}}$ is introduced to correct for the missing neutral component:

$$m_{\text{TA}} = \frac{p_T^{\text{calo}}}{p_T^{\text{trk}}} \times m_{\text{trk}}. \tag{3.8}$$

Figure 3.7 shows the three different jet mass definitions obtained for jets with 1.6 TeV $< p_T <$ 1.8 TeV: the track-assisted jet mass is comparable to the calorimeter-based jet mass and superior in resolution to the track-based jet mass.

To further improve the mass resolution it is possible to combine the information coming from the calorimeter-based mass and the track-assisted mass. This is supported by the fact that the correlation between the two masses is small [75] assuming a Gaussian distribution for the individual jet mass responses. The combined mass is then obtained as:

$$m_{\text{comb}} = \frac{\sigma_{\text{calo}}^{-2}}{\sigma_{\text{calo}}^{-2} + \sigma_{\text{TA}}^{-2}} \times m_{\text{calo}} + \frac{\sigma_{\text{TA}}^{-2}}{\sigma_{\text{calo}}^{-2} + \sigma_{\text{TA}}^{-2}} \times m_{\text{TA}} \tag{3.9}$$

where the calorimeter-based mass and the track-assisted mass are linearly combined with weights proportional to their corresponding inverse mass resolution squared.

Figure 3.8 shows the resolution of the calorimeter-based jet mass and the track-assisted jet mass with an additional curve depicting the resolution of the combined jet mass for W-jets. To more accurately account for outliers in case of a non-Gaussian response distribution, the mass resolution is defined as:

$$\sigma(m) = \frac{1}{2} \times \frac{68\% \text{ IQnR}\,[R(m)]}{\text{median}\,[R(m)]} \tag{3.10}$$

where 68% IQnR $[R(m)]$ is 68% interquantile range (IQnR)[5] of the mass response distribution $R(m)$ and median $[R(m)]$ its median. The combined jet mass smoothly interpolates between $m_{\text{comb}} \sim m_{\text{calo}}$ at low p_T and $m_{\text{comb}} \sim m_{\text{TA}}$ at high p_T giving a better mass resolution over the full p_T range than for the calorimeter-based or track-assisted jet mass.

---

[5]The $x\%$ interquantile range (IQnR) is defined as $q_{50\%+x\%} - q_{50\%-x\%}$, whereby $q_{50\%+x\%}$ and $q_{50\%-x\%}$ are the $(50+x)^{\text{th}}$ and $(50-x)^{\text{th}}$ percentiles of the given distribution, respectively.
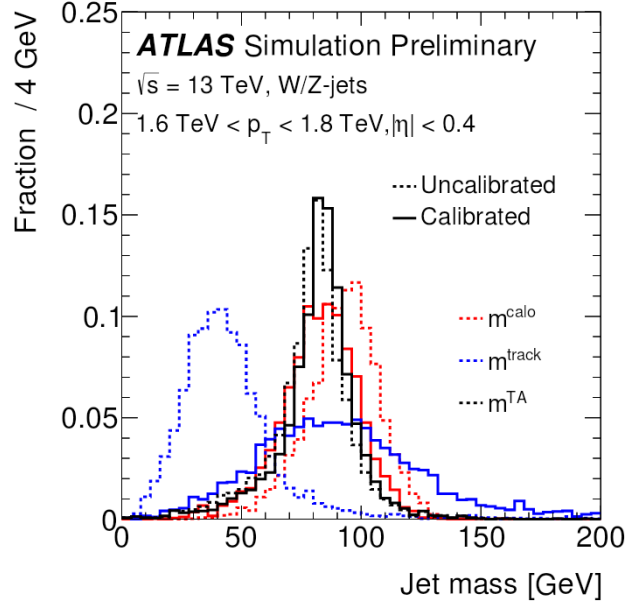
Figure 3.7: Distribution of the jet mass for different jet mass definitions for uncalibrated (dashed line) and calibrated (solid lines) jets with 1.6 TeV $< p_{\mathrm{T}} <$ 1.8 TeV: calorimeter-based jet mass (red), track-based jet mass (blues) and the track-assisted mass (black). The track-assisted jet mass is comparable to the calorimeter-based jet mass and superior in resolution to the track-based jet mass [75].
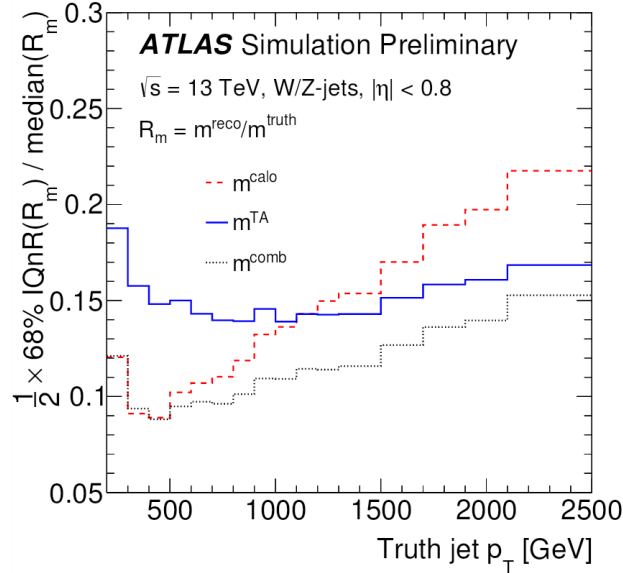
Figure 3.8: Jet mass resolution as a function of the truth jet p_{T} for three different mass definitions: calorimeter-base jet mass (red), track-assisted jet mass (blue) and the combined jet mass (black). The mass resolution is defined as the ratio of the 68% interquantile range (IQnR) to twice the median of the mass response [75].

3.7 Substructure Variables

As introduced already in § 3.1, substructure variables can distinguish between the two-prong structure of W/Z-jets from the one-prong structure of QCD-jets. The many jet substructure techniques can be categorised as follows [77]:

- Jet shapes make use of the relative positions and momenta of jet constituents with respect to each other;

- Splitting scales use the clustering history of the jet to define discriminating variables;

- Subjettiness variables evaluate the compatibility of a given jet with the hypothesis of consisting of a certain number of subjet axes;

- Centre-of-mass jet shapes use the constituent position with respect to the jet axis;

- Quantum-jet variables.

This section will describe in detail the energy correlation variables, which belong to the jet shape family. They have been shown to be among the most powerful variables at discriminating between QCD-jets and W/Z jets.

3.7.1 Energy Correlation

Energy correlation variables [78] have the advantage of not relying on reconstructing subjets inside the given jet and therefore can better handle emission of soft quarks and gluons at large angles.
First define the N-point energy correlation functions, labelled ECF, which are evaluated from the p_{T} and the pair-wise angular separation ΔR_{ij} of all the constituents of any given jet J:

$$\mathrm{ECF}(0, \beta) = 1, \tag{3.11a}$$

$$\mathrm{ECF}(1, \beta) = \sum_i p_{\mathrm{T}_i}, \tag{3.11b}$$

$$\mathrm{ECF}(2, \beta) = \sum_{i<j \in J} p_{\mathrm{T}_i} p_{\mathrm{T}_j} \left(\Delta R_{ij}\right)^\beta, \tag{3.11c}$$

$$\mathrm{ECF}(3, \beta) = \sum_{i<j<k \in J} p_{\mathrm{T}_i} p_{\mathrm{T}_j} p_{\mathrm{T}_k} \left(\Delta R_{ij} \Delta R_{jk} \Delta R_{ki}\right)^\beta, \tag{3.11d}$$

where β is a free parameter whose optimisation is based on the mass of the resonance under study [78]. If a jet contains N subjets, the $N+1$-point energy correlation function will be significantly smaller than the N-point energy correlation function, i.e. $\mathrm{ECF}(N+1, \beta) \ll \mathrm{ECF}(N, \beta)$. From the hadronic decay of boosted vector boson, $N = 2$ dense energy cores of energies are expected within the jets and the two dimensionless ratios, C_2^β [78] and D_2^β [79, 80], are generally considered:

$$C_2^\beta = \frac{\mathrm{ECF}(3, \beta)\mathrm{ECF}(1, \beta)}{\mathrm{ECF}(2, \beta)^2}, \tag{3.12}$$

$$D_2^\beta = \frac{\mathrm{ECF}(3, \beta)\mathrm{ECF}(1, \beta)^3}{\mathrm{ECF}(2, \beta)^3}. \tag{3.13}$$

However C_2^β and D_2^β are neither infra-red nor collinear safe unless a mass window requirement is imposed on the jet, e.g. around the mass of the vector boson.
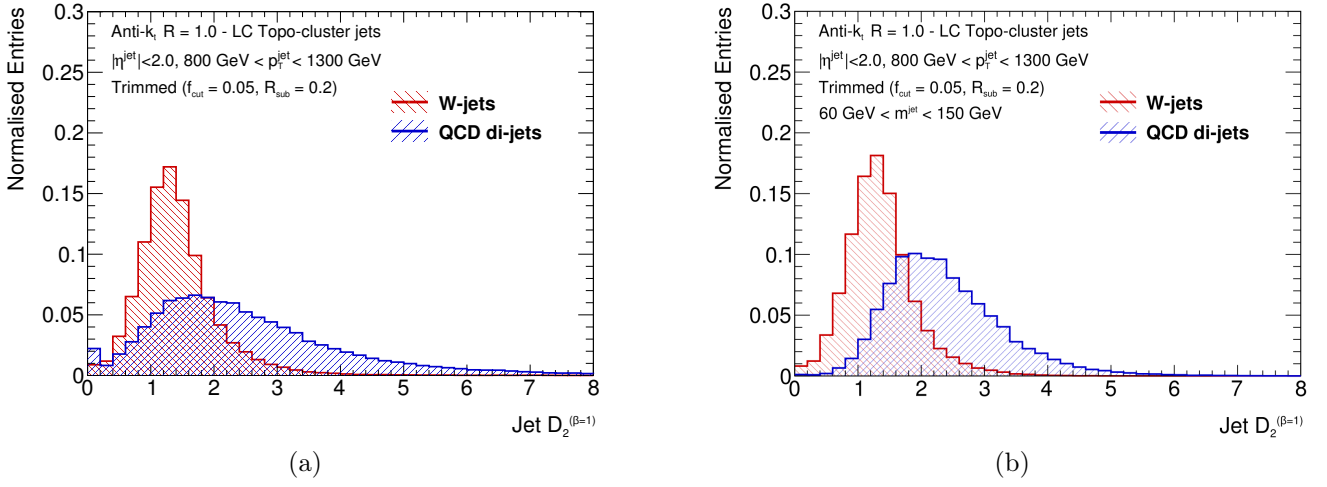
Figure 3.9: Energy correlation variable $D_2^{\beta=1}$ for the two leading anti-k_t $R = 1.0$ trimmed jets in W and QCD di-jet events with (a) and without (b) a mass window (60 GeV $< m^{\text{jet}} <$ 150 GeV) requirement. Because of the correlation between the jet mass and $D_2^{\beta=1}$, the application of the mass cut improves the discrimination between signal and background.

Figure 3.9 shows the $D_2^{\beta=1(6)}$ distribution for signal and background jets with and without a mass window requirement around the W boson mass (50 GeV $< m^{\text{jet}} <$ 150 GeV). Figure 3.9b shows that $D_2^{\beta=1}$ is correlated to the jet mass and that after the mass cut the discrimination between signal and background is improved.

$D_2^{\beta=1}$ will be used in the next chapters of this thesis. Its resolution will be considered as the metric to evaluate the jet substructure performance improvement obtained using a new input type to jet reconstruction, the Track-CaloCluster, as described in Chapter 4. Moreover, it will be used, together with the jet mass, to develop and optimise a two-variable boosted boson tagging technique.

---

[6]Both $\beta = 1$ and $\beta = 2$ have been studied by the ATLAS Collaboration. However, $\beta = 1$ has shown better discrimination between W/Z-jets and QCD jets [77].

4

Developments of Track-CaloCluster Objects as Inputs to Jet Reconstruction

Contents

4.1 Introduction

As introduced in § 3.7, jet substructure is used to study energy structures within a jet and represent a powerful tool to identify hadronically decaying vector bosons [81], boosted $H \rightarrow b\bar{b}$ [82] and top quarks [83], as well as to distinguish between light quark and gluon initiated jets [84]. All these tagging methods and more have been subsequently adopted in searches for new physics, e.g. searches for diboson resonances [28, 33], and in measurements of Standard Model processes [85].

This thesis mainly discusses the discrimination between W/Z-jets and QCD-jets. As the momentum of the vector boson increases, the decay system is increasingly boosted with increasingly small angular separation between the quarks (see Equation 3.2) until they are reconstructed into a single large-R jet. The ability to identify the source of the large-R jet and distinguish between vector boson initiated jets and the overwhelming multi-jet background, relies on both the energy and angular resolutions of the detector used to reconstruct the jets. The ATLAS calorimeter has an excellent energy resolution (see § 2.2.4) but, because of its granularity, its angular resolution is insufficient to resolve the boosted products of hadronically decaying vector bosons. On the other hand, the tracking system has an excellent angular resolution (see § 2.2.3) and very good track reconstruction efficiency at high energy [86]. As charged particles become more energetic, they are less bent by the magnetic field, and thus their extrapolation to the calorimeter can be evaluated with great precision while the p_T measurement deteriorates. Figure 4.1 shows a comparison between the uncertainty on the extrapolation of good quality tracks [86] to the calorimeter and the width of topo-clusters using a $W' \rightarrow WZ \rightarrow qqqq$ sample with $M_{W'} = 1$ TeV. The track extrapolation uncertainty at the calorimeter entrance, σ_track, has

been evaluated using the full ATLAS detector material model and the entire magnetic field description. The width of topo-clusters is defined as follows [87]:

$$\sigma_{\text{cluster}} = \sqrt{\sigma_\eta^2 + \sigma_\phi^2} \quad \text{with} \quad \sigma_\eta \approx \sigma_\phi \approx \text{atan}\left(\frac{\sqrt{\langle r^2 \rangle}}{|\vec{c}|}\right) \times \cosh(\eta) \tag{4.1}$$

where $|\vec{c}|$ is the distance between the center of gravity of the cluster and the origin of the ATLAS reference frame and $\langle r^2 \rangle^{(1)}$ describes the radial extension of the cluster with respect to the axis of the shower. Figure 4.1 shows that the typical track uncertainty is smaller than the average topo-cluster size across the entire detector and for $p_{\text{T}} \gtrsim 5$ GeV.

Based on these considerations, the superior angular resolution of the tracking system can be combined with the calorimeter information in order to mitigate its resolution limitations: this has been shown to provide superior performance in previous techniques such as the combined mass (see § 3.6).

This chapter will focus on the development of a new object, the Track-CaloCluster (TCC), which unifies track and topo-cluster information to benefit at high p_{T} from the energy resolution of the calorimeter and the spatial resolution of the inner detector. § 4.2 will introduce the Monte Carlo simulation samples used to perform the performance studies described in this chapter. The TCC reconstruction and performance will be discussed in § 4.3 while § 4.4 will cover the jet substructure performance for jets built from TCCs. Finally, the most recent developments on TCC-jets, including the derivation of energy and mass calibration scale factors, are described in § 4.5

Most of the content in this chapter has been previously presented in [88], with leading contributions from the author of this thesis.

4.2 Monte Carlo Simulation Samples

The results presented in this chapter have been obtained using dedicated samples of hadronic decays of boosted vector bosons. Events of $W' \to WZ \to qqqq$ have been simulated varying the mass of the W' boson from 0.8 TeV to 5 TeV to probe different regions in transverse momentum p_{T}. Z and W bosons produced in the decay of the W' are longitudinally polarised. These samples have been generated with PYTHIA8 [89] as Monte Carlo generator with the A14 event tune [90] and the NNPDF2.3 leading order parton distribution function [91]. The effect of additional proton-proton collisions has been simulated by overlaying an average of 24 minimum-bias events.

4.3 Track-CaloClusters

Profiting from the complementary behaviour of the tracking system and the calorimeter, TCC 4-vectors are built by combining the energy scale components of topo-cluster 4-vectors and the angular coordinates from track parameters.

The TCC reconstruction procedure is a type of particle flow, but very different in many aspects from the standard ATLAS particle flow implementation [92]. Although both techniques aim to improve the understanding of hadronic showers combining tracker and calorimeter information, they have been developed using different track-cluster matching criteria, 4-vector construction algorithms and energy sharing procedures to optimally perform in two very different kinematic regions.

In the next sections the two key elements of the TCC reconstruction will be discussed: § 4.3.1 will present the track-cluster matching criterion used to associate tracks and topo-clusters, while the object

---

$^{(1)}\langle r^2 \rangle$ is the second moment of radial distance of the cells from the axis of the shower.

(a) Topo-clusters, vs η

(b) Tracks, vs η

(c) Topo-clusters, vs Energy

(d) Topo-clusters, vs p_{T}
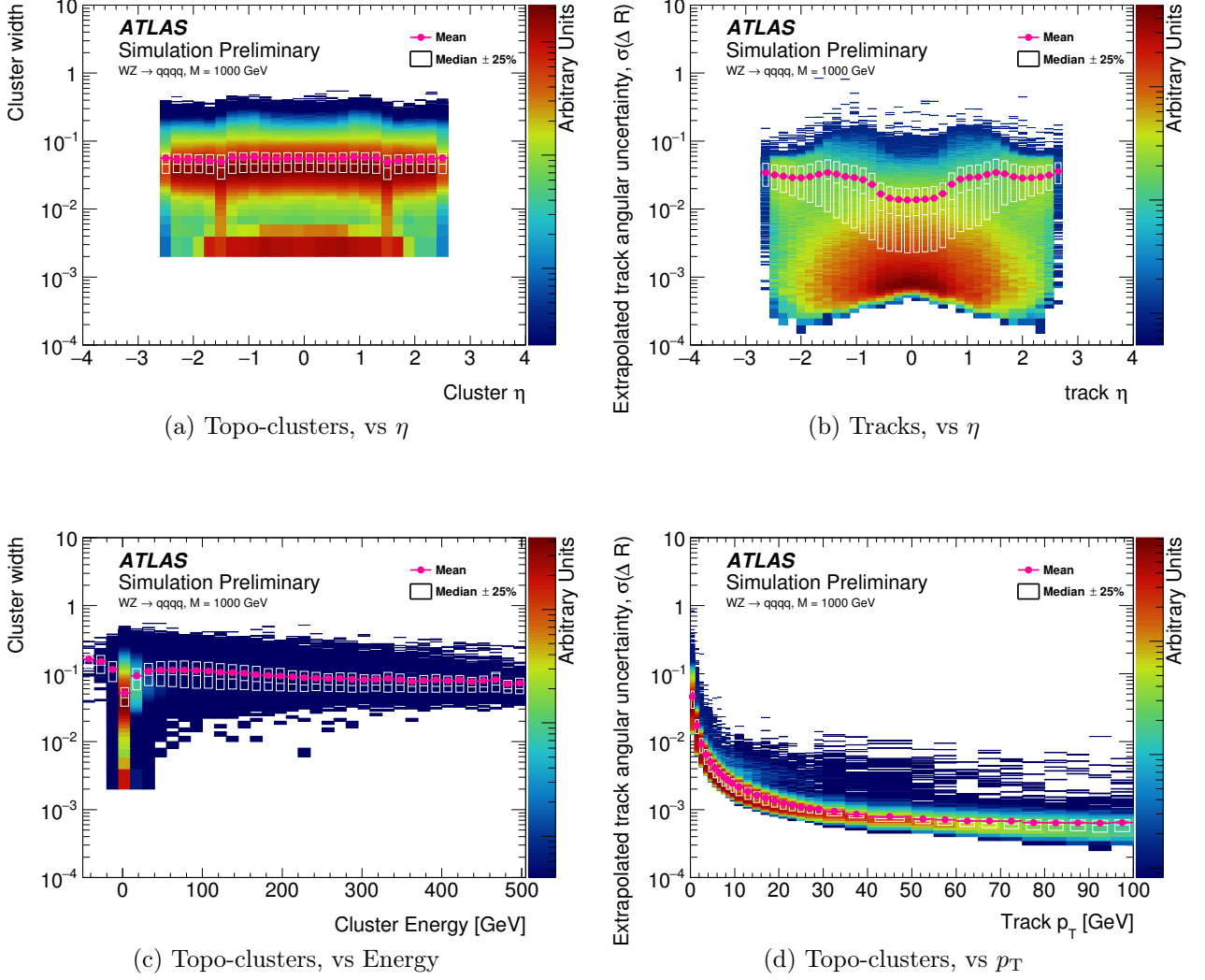
Figure 4.1: Comparison of the topo-cluster width and track uncertainty at the calorimeter entrance in $W' \to WZ \to qqqq$ events with $M_{W'} = 1$ TeV. In (a) and (c) the cluster width is shown as a function of η and of the cluster energy, respectively, while (b) and (d) show the track uncertainty at the calorimeter entrance as a function of the track η and p_{T}, respectively. Because of the non-Gaussian shape of some of the distributions, the mean (pink points) and the 50% median window (white boxes) are shown [88].

reconstruction will be discussed in § 4.3.2, placing particular emphasis on the energy sharing algorithm on which the energy-scale components evaluation of the TCC 4-vector relies.

4.3.1 Track-Cluster Matching

In order to reliably combine track and topo-cluster information, a robust track-cluster matching criterion has to be defined.

The TCC matching algorithm attempts to match every track to every topo-cluster in a two-step procedure. First, the track is extrapolated to the calorimeter and its extrapolation uncertainty σ_{track} is compared to the topo-cluster width σ_{cluster}, as defined in § 4.1. If the track extrapolation uncertainty is larger than the cluster width, $\sigma_{\text{track}} > \sigma_{\text{cluster}}$, the track is discarded from the matching procedure since no further precision is added to the cluster position. Otherwise, the matching procedure continues and the track matches a cluster if the angular separation between the two objects $\Delta R \, (\text{track}, \text{cluster}) < \sqrt{\sigma_{\text{cluster}}^2 + \sigma_{\text{track}}^2}$. As the track uncertainty reduces when increasing the transverse momentum of the track (see Figure 4.1d), at high p_{T} the matching criterion results into requiring the track to be within the cluster, i.e. $\Delta R \, (\text{track}, \text{cluster}) \lesssim \sigma_{\text{cluster}}$. The matching is performed using tracks from any primary vertex, as tracks from multiple proton-proton collision can match the same topo-cluster. They will contribute to the energy sharing as will be described in § 4.3.2.

Studies have been performed to understand how this matching criterion compares to fixed-cone matching strategies.

Figure 4.2 depicts the fraction of matched clusters as a function of η either using the matching criterion with the variable $\Delta R = \sqrt{\sigma_{\text{cluster}}^2 + \sigma_{\text{track}}^2}$ or fixed $\Delta R = 0.1$. In these Figures, clusters are weighted by their energy. Both matching criteria have a high efficiency in matching high-energy clusters and behave similarly as a function of η. The two strategies differ in $2.5 < |\eta| < 2.8$: including the track extrapolation uncertainty and the cluster width in the ΔR definition increases the number of matched clusters in this region. Clusters are not matched outside the tracking coverage, $|\eta| > 2.8$.

Figure 4.3 shows the fraction of matched tracks as a function of track η and p_{T} using the variable or fixed ΔR matching criteria. Figure 4.3a shows that the two matching strategies behave similar as a function of η but with less tracks matched using the variable ΔR. In particular, the two matching criteria differ in the low p_{T} region where $\sim 5\%$ less tracks are matched using the variable ΔR (Figure 4.3b). The low matching efficiency shown in Figure 4.3 is due to the contribution of pile-up tracks that participate in the matching procedure and are not matched to any topo-cluster.

The track-cluster matches are used to build TCC objects which can be divided into three categories. Tracks compatible with the primary vertex and matched to topo-clusters are used to build combined TCCs; tracks from the primary vertex not matched to topo-clusters and topo-clusters not matched to tracks are used to build charged and neutral TCCs, respectively.

Figure 4.4 presents the resulting fraction of charged, neutral and combined-TCC objects for $W' \to WZ \to qqqq$ events with $M_{W'} = 1$ TeV. Up to a p_{T} of 5 GeV the largest fraction consists of neutral TCCs which are mainly due to pile-up clusters. As the p_{T} increases, the contribution of combined TCCs rises as highly energetic topo-clusters are more likely to come from the hadronic decay of the vector bosons and thus close to tracks. In this highly boosted regime both charged and neutral decay products are collimated and contribute to the same topo-clusters.

4.3.2 Track-CaloCluster Reconstruction

After the matching between tracks and clusters has been performed, the TCC 4-vectors are built. Some of the possible configuration are depicted in Figure 4.5. Referring to the figure, ① indicates the
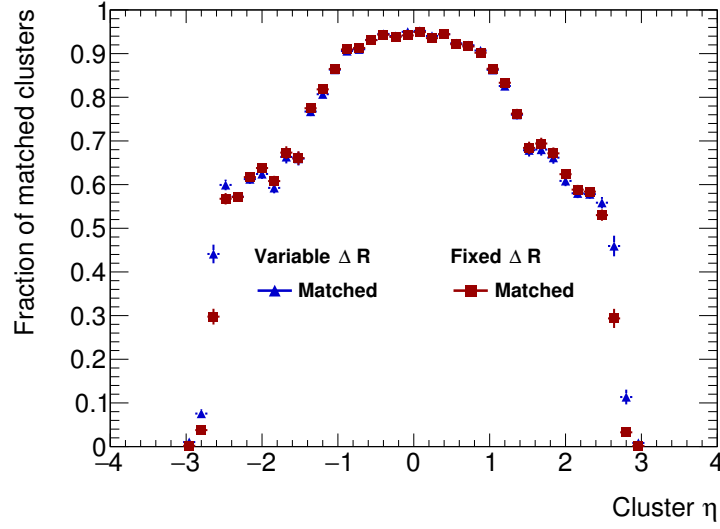
Figure 4.2: Comparison of the fraction of matched clusters as a function of the cluster η using a matching criterion with variable $\Delta R = \sqrt{\sigma_{\text{cluster}}^2 + \sigma_{\text{track}}^2}$ and fixed $\Delta R = 0.1$. The clusters are weighted by their energy contribution. Both matching criteria have a high efficiency in matching high-energy clusters and behave similar as a function of η. The two strategies differ for $2.5 < |\eta| < 2.8$: including the track extrapolation uncertainty and the cluster width in the ΔR definition allows for the variable ΔR matching criterion to increase the number of matched clusters.
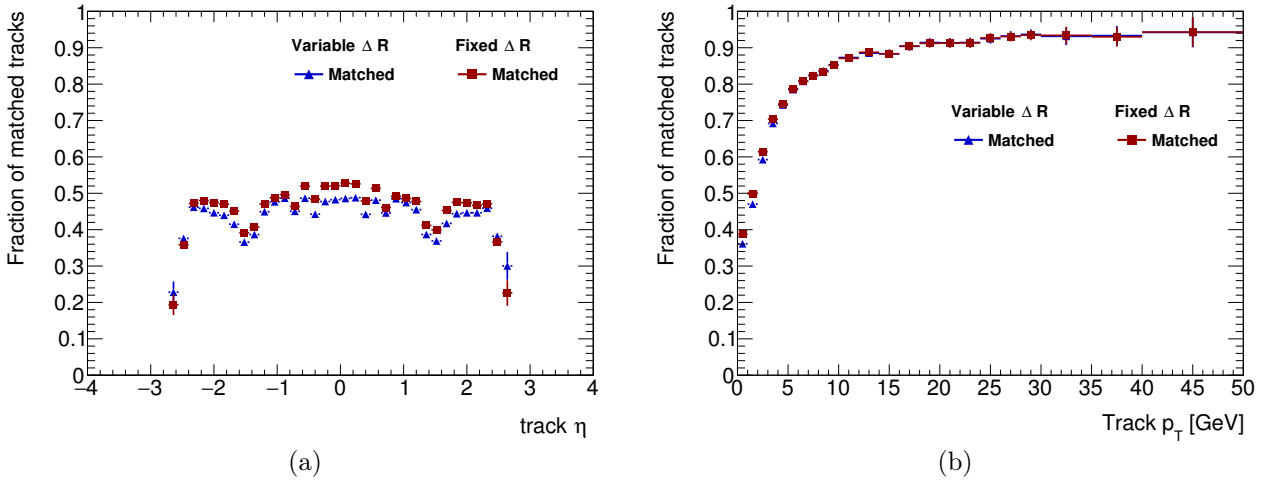
Figure 4.3: Comparison of the fraction of matched tracks as a function of (a) the track η and (b) track p_{T} using a matching criterion with variable $\Delta R = \sqrt{\sigma_{\text{cluster}}^2 + \sigma_{\text{track}}^2}$ and fixed $\Delta R = 0.1$. The two matching criteria differ for $p_{\text{T}} \lesssim 5$ GeV where $\sim 5\%$ less tracks are matched using the variable ΔR. The loss of matched tracks is uniform in η. The low matching efficiency is due to the contribution of pile-up tracks that participate to the matching procedure and are not matched to any topo-cluster.

(a)

(b)
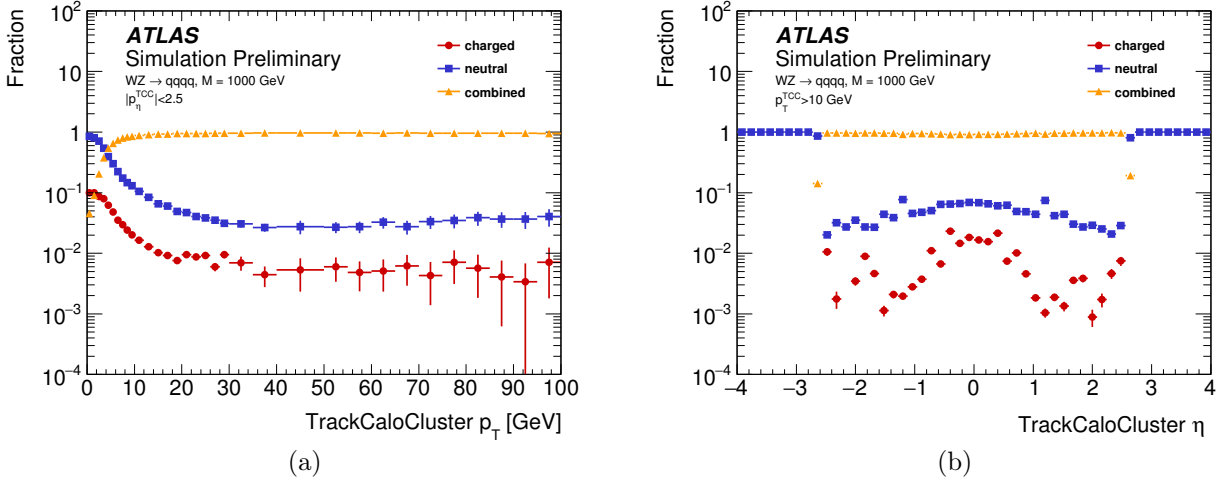
Figure 4.4: Comparison of the fraction of charged, neutral and combined-TCC objects as a function of (a) the TCC p_{T} and (b) TCC η in $W' \to WZ \to qqqq$ events with $M_{W'} = 1$ TeV. Tracks compatible with the primary vertex and matched to topo-clusters are used to build combined TCC; tracks from the primary vertex not matched to topo-clusters and topo-clusters not matched to tracks are used to build charged and neutral TCC, respectively [88].

TCC object 1, c_1 refers to the topo-cluster c_1 and t_1 to the track t_1.

In case the TCC is composed of a track matching only one cluster, such as ①, the TCC 4-vector is built from the track angular information and the topo-cluster energy scale in the following way:

$$\mathrm{TCC}_{①} = \left(p_{\mathrm{T}}^{c_1}, \eta^{t_1}, \phi^{t_1}, m^{c_1} = 0 \right). \tag{4.2}$$

In case of topo-clusters not matched to any track, as for ②, the topo-cluster 4-vector is directly used to obtain:

$$\mathrm{TCC}_{②} = \left(p_{\mathrm{T}}^{c_7}, \eta^{c_7}, \phi^{c_7}, m^{c_7} = 0 \right). \tag{4.3}$$

Tracks from the primary vertex not matching any topo-cluster, as shown in ③, are used to build the 4-vector of a charged TCC:

$$\mathrm{TCC}_{③} = \left(p_{\mathrm{T}}^{t_6}, \eta^{t_6}, \phi^{t_6}, m^{t_6} = 0 \right). \tag{4.4}$$

Except for the above mentioned simple cases, all other TCC objects are built from one seed track and multiple clusters. Moreover, each of the clusters can be shared by multiple tracks, as shown for ⑥ and ⑦. The 4-vector evaluation therefore becomes more complicated. The TCC reconstruction procedure still creates one TCC object for each track originating from the primary vertex. The angular information of the seed track is then used to define the angular quantities of the TCC 4-vector while the energy coordinates must be adapted to account for energy sharing between different matches.

For each track seeding a TCC, all matching topo-clusters are considered. Next, for each topo-cluster, the energy is divided between all tracks matching that cluster with a split factor defined by the ratio of the p_{T} of the given track and the sum of all p_{T} of other matching tracks. This strategy allows to split the topo-cluster energy between tracks without relying on the absolute scale of the track p_{T}. Only the ratio of individual track p_{T} to the p_{T} sum of all matched tracks is used. Moreover, in this approach, the energy measurements provided by the calorimeter and the tracker are never compared: the track p_{T} is only used to derive weights to redistribute the topo-cluster energy measurement.
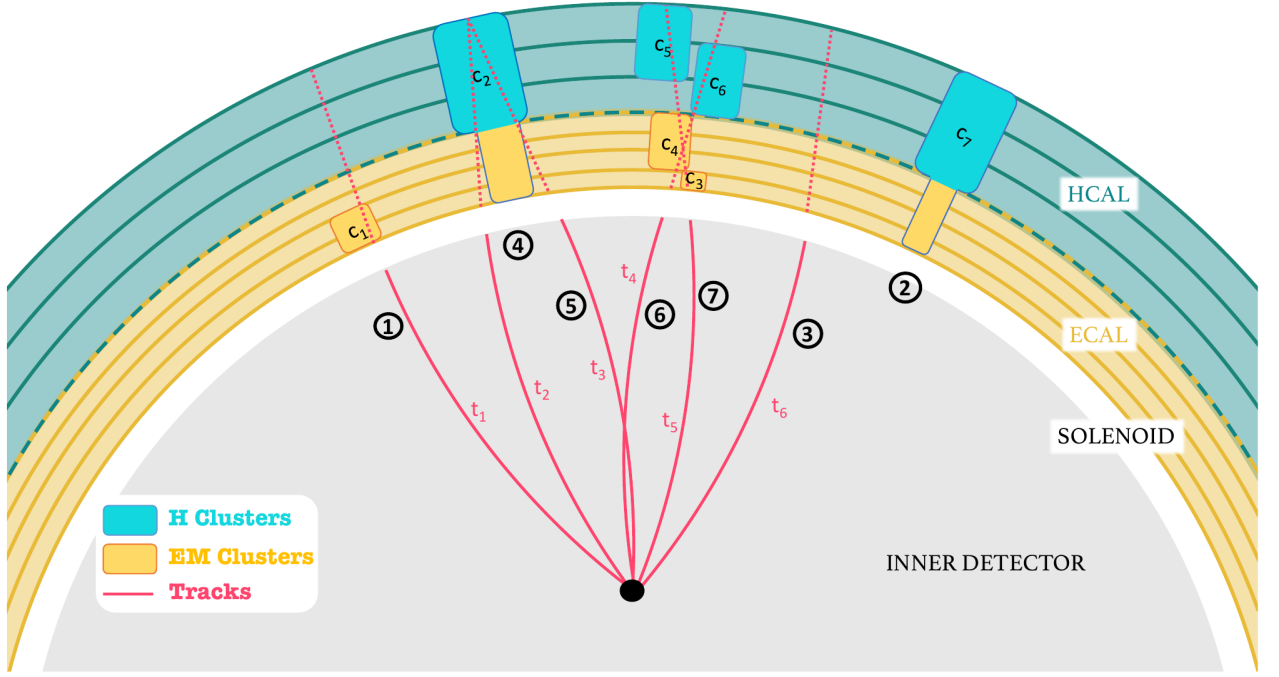
Figure 4.5: Drawing of seven possible TCC objects with: ① a simple track-cluster match, ② a topo-cluster without a matching track, ③ a track without a matching topo-cluster, ④ and ⑤ a single topo-cluster shared by two tracks, ⑥ and ⑦ multiple track-cluster matches [88].

Referring again to Figure 4.5, ④ and ⑤ correspond to two TCC objects whose tracks are matching the same topo-cluster. Following the above prescription, the 4-vector of the two TCCs is derived as:

$$\text{TCC}_{③} = \left(p_T^{c_2} \frac{p_T^{t_2}}{p_T[\mathbf{p}^{t_2} + \mathbf{p}^{t_3}]}, \eta^{t_2}, \phi^{t_2}, m^{c_2} \frac{p_T^{t_2}}{p_T[\mathbf{p}^{t_2} + \mathbf{p}^{t_3}]} = 0 \right), \tag{4.5}$$

$$\text{TCC}_{④} = \left(p_T^{c_2} \frac{p_T^{t_3}}{p_T[\mathbf{p}^{t_2} + \mathbf{p}^{t_3}]}, \eta^{t_3}, \phi^{t_3}, m^{c_2} \frac{p_T^{t_3}}{p_T[\mathbf{p}^{t_2} + \mathbf{p}^{t_3}]} = 0 \right), \tag{4.6}$$

where $p_T[\mathbf{p}^{t_2} + \mathbf{p}^{t_3}]$ is the p_T of the 4-vector sum of the two particles associated to t_2 and t_3.

The energy sharing equation can be generalised to include all possible scenarios with a seed track τ matched to a set of topo-clusters C_τ. As previously mentioned, each topo-cluster c in C_τ can be matched to multiple tracks T_c and each track t in the set of tracks T_c can match other clusters C_t. The general form of the energy-sharing equation makes use of two quantities:

- Considering a cluster c matched to a seed track τ, its contribution to the resulting TCC object is proportional to the fraction of its p_T and the p_T of the sum of all matched clusters. This is denoted f_τ^c:

$$f_\tau^c = \frac{p_T^c}{p_T\left[\sum_{k \in C_\tau} \mathbf{p}^k\right]}. \tag{4.7}$$

f_τ^c represents the relevance of the topo-cluster c compared to the other clusters matched to the seed track τ.

- The cluster c matched by a seed track τ can be matched by multiple tracks and hence contribute to different TCC objects. Its contribution per TCC object is weighted by the fraction of p_T required by the seed track τ compared to all other tracks t matched to the cluster. Then $F_{c,t}^\tau$ is:

$$F_{c,t}^\tau = \frac{p_T^\tau}{p_T \left[\sum_{t \in T_c} \mathbf{p}^t \cdot f_t^c \right]},\qquad(4.8)$$

where f_t^c represents the contribution of the track $t \in C_t$ to the topo-cluster c considering again the fraction of the energy of the cluster c compared to the other clusters matched by the track t:

$$f_t^c = \frac{p_T^c}{p_T \left[\sum_{k \in C_t} \mathbf{p}^k \right]}.\qquad(4.9)$$

Following the description reported above, $F_{c,t}^\tau$ can be interpreted as the relevance of the seed track τ when compared to all other tracks matching the cluster c, considering as well the contribution of the matched cluster to account for the energy shared with any other TCC based on the number of other objects it matches.

Using the quantities shown above, it is possible to construct the generalised energy sharing equation:

$$\mathbf{M}_\tau = \sum_{c \in C_\tau} \mathbf{p}^c \, f_\tau^c \, F_{c,t}^\tau = \sum_{c \in C_\tau} \mathbf{p}^c \, \frac{p_T^c}{p_T \left[\sum_{k \in C_\tau} \mathbf{p}^k \right]} \, \frac{p_T^\tau}{p_T \left[\sum_{t \in T_c} \mathbf{p}^t \frac{p_T^c}{p_T \left[\sum_{k \in C_t} \mathbf{p}^k \right]} \right]}.\qquad(4.10)$$

The scale components of the final TCC 4-vector are then obtained using the 4-vector $\mathbf{M}_\tau$ while the angular components come from the seed track τ:

$$\mathrm{TCC}_\tau = \left(p_T\left[\mathbf{M}_\tau\right], \eta^\tau, \phi^\tau, m\left[\mathbf{M}_\tau\right] \right).\qquad(4.11)$$

The general formulae in Equation 4.10 and Equation 4.11 handle all TCC cases where matches between tracks and clusters occur, including the simple cases previously reported in Equation 4.5 and Equation 4.6. Other examples of the use of the energy sharing equation are reported in Appendix A of Reference [88].

In the way Equation 4.11 is written, the p_T and mass of the TCC 4-vector are obtained considering the sum of the weighted 4-vectors of all the topo-clusters taking part in the matching accounting for their contribution to other TCCs. As a consequence, while combined TCCs with only one topo-cluster matching the seed track have mass equal to zero, two or more topo-clusters result in a non-zero TCC mass.

It is worth stressing again one important feature of Equation 4.10: the seed track τ used to reconstruct the combined-TCC object must originate from the primary vertex while tracks t contributing to the energy sharing scale factors can come from any vertex. This means that combined TCC are reconstructed if they originate from the hard-scatter process while pile-up activity is considered to handle energy overlaps in the calorimeters and hence correctly scale the TCC energy components.
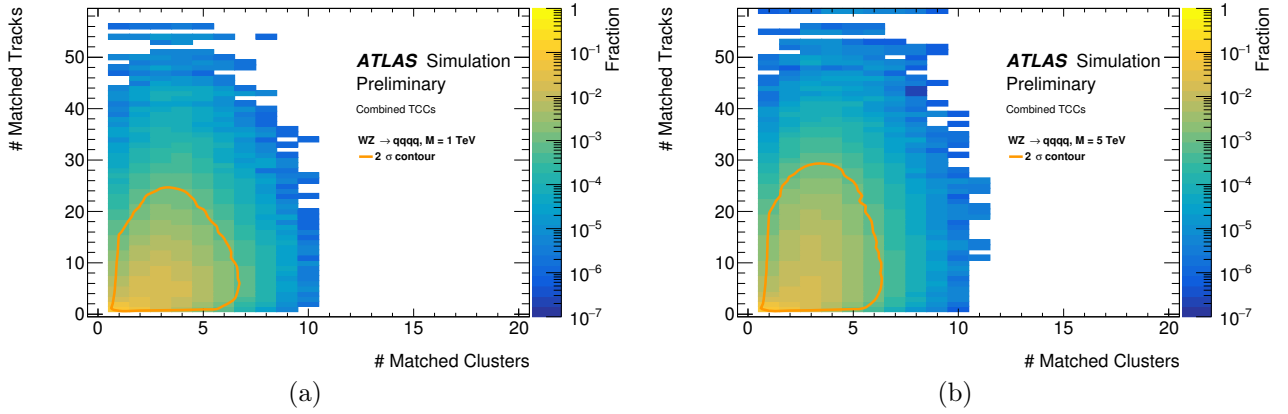
Figure 4.6: Comparison of the distribution of the number of clusters matched to the seed track when reconstructing combined-TCC objects and the number of tracks matched to each of those clusters in $W' \to WZ \to qqqq$ events with (a) $M_{W'} = 1$ TeV and (b) $M_{W'} = 5$ TeV. The plot is filled for each of the combined TCCs the number of clusters N_c matched to the seed track and for each of the cluster the number of tracks N_t it is matched to. The 2σ bulk of the distribution is also shown [88].

Figure 4.6 presents an estimate of the sizes of the sets C_τ and T_c for combined-TCC objects reconstructed in $W' \to WZ \to qqqq$ events with $M_{W'} = 1$ TeV and $M_{W'} = 5$ TeV. The plot is filled considering for each combined TCC the number of clusters N_c matched to the seed track τ and for each of the cluster $c \in C_\tau$ the number of tracks N_t it is matched to. The 2σ bulk of the distribution is contained in the region bounded by 6 topo-clusters and 25 to 30 tracks depending on the W' mass. In rare cases, which are which are approximately six orders of magnitude less compared to the bulk of the distribution, a single topo-cluster can be matched to a very high number of tracks. This is mainly due to two reasons. First, as mentioned already, tracks participating in the energy sharing equation originate from any vertex and correspond to a moderate fraction of those matches. Second, in rare cases the size of the clusters, which enters in the matching criterion, can be very wide resulting in an large number of tracks matching the given topo-cluster.

4.4   Jet Reconstruction for Track-CaloClusters

ATLAS uses the anti-k_t algorithm (see § 3.3) with a distance parameter $R = 1.0$ to reconstruct large-R jets which are subsequently trimmed (see § 3.4.1) to remove pile-up and underlying event contributions using the parameters $f_{\text{cut}} = 5\%$ and $R_{\text{sub}} = 0.2$.

The flexibility of the reconstruction algorithms allows for different objects to be used as input of the jet reconstruction. In particular, two interesting subsets of the TCC objects are considered as input: all TCCs or only combined TCCs. The former contains both the neutral and charged contributions and should provide the best representation of the energy flow in the event including the majority of the hard scatter energy. However, jets built from unmatched topo-clusters (neutral TCCs) are sensitive to pile-up effects, as already studied for topo-cluster jets. For this reason, using only combined TCC as input to the jet reconstruction is particularly interesting: the track-to-primary-vertex association significantly suppresses pile-up at the cost of missing some of the real scatter energy.

Trimming is applied to TCC jets using the same parameters as used for the LC topo-cluster jet collection. Moreover, jets can be calibrated using dedicated scale factors in order to account for detector and reconstruction effects (see § 3.5). However, for the preliminary studies presented in the this section

TCC jets are used at the uncalibrated scale since the comparisons are not strongly altered by calibrations. Unless clearly stated, LC topo-cluster jets are fully calibrated using the procedure explained in § 3.5. The difference between the uncalibrated and calibrated scale will be discussed when relevant. Energy and mass calibration for TCC jets will be discussed in § 4.4.

Truth jets are also used for performance evaluations. Trimmed truth jets are obtained using stable truth particle ($c\tau > 10$ mm) as input to jet reconstruction, excluding contributions from muons, neutrinos and particles from pile-up.

For each reconstructed jet collection, the main quantities used to quantify the performance of a given observable $\mathcal{O}$ are the response, defined as the ratio $R_r(\mathcal{O}) = \mathcal{O}_{\text{reco}}/\mathcal{O}_{\text{true}}$, and the residual, defined as $R_d(\mathcal{O}) = \mathcal{O}_{\text{reco}} - \mathcal{O}_{\text{true}}$. The response is used to discuss observables which have a scale, e.g. mass and energy, while in all other cases, especially when the true value can be zero, the residual is taken into account. In the definition of $R_r(\mathcal{O})$ and $R_d(\mathcal{O})$, the true value of the observable $\mathcal{O}_{\text{true}}$ is retrieved from the truth jet matched to the reconstructed one. In some cases, the pseudo-response R_{pr} is used to compare two reconstructed jet definitions: $R_{pr}(\mathcal{O}) = \mathcal{O}_{\text{reco,1}}/\mathcal{O}_{\text{reco,2}}$, where the reconstructed jets are required to match.

The mass response for three TCC jet collections is shown in Figure 4.7. The effect of trimming is visible comparing the mass response distribution for the untrimmed and trimmed jet collections built using all-TCC objects. Jets built using only combined TCCs already have a well-behaved mass response without trimming.

Figure 4.8a shows the p_{T} pseudo-response obtained for three TCC jet collections compared to the trimmed uncalibrated LC topo-cluster jet definition. For the trimmed all-TCCs jet collection, the distribution is expected to peak at approximately unity because of the numerator and denominator being at the same scale. Moreover, the removal of pile-up topo-clusters matched with tracks from pile-up primary vertices produces a small shift towards smaller p_{T}. The combined-TCC jet collection behaves similarly to the trimmed all-TCC jets suggesting that the pile-up contribution is well controlled despite the lack of grooming. Finally, the third distribution shows the untrimmed all-TCC jet collection. In this case, the contribution of pile-up is more pronounced and increases the jet p_{T} as expected.

The comparison of the η residual distributions for LC topo-cluster jets, all-TCC jets and combined-TCC jets is shown in Figure 4.8b. The calibrated LC topo-cluster jets have the best performance, consistent with the fact that the centroid position of high energy topo-clusters is very well known. Although TCCs are built from track spatial coordinates, the inclusion of charged and neutral components degrades the resolution on the jet direction.

Rather than improving the jet angular resolution, the power of TCC jets lies in the ability to resolve substructure below the topo-cluster size scale by improving the constituent angular resolution. Figure 4.9 shows the reconstruction of a single $W' \to WZ \to qqqq$ simulated event using LC topo-cluster jets, all-TCC jets and combined-TCC jets. Compared to LC topo-cluster jets, both TCC-jet collections are able to resolve the two separated subjets (grey regions) within both large-R jets.

4.4.1 Jet Substructure Performance with Track-CaloCluster Jets

The most intuitive jet substructure variable, which is also extremely powerful when identifying hadronic decays of massive particles, is the jet mass. As described in § 3.6, LC topo-cluster jets make use of the combined mass, m_{comb}, that maximally exploits the calorimeter at low p_{T} and the tracker at high p_{T} and therefore provides an improved mass resolution. However, the track-assisted mass, that is integrated in the definition of the combined mass, assumes a uniform fraction of the charged to neutral energy components and hence doesn't account for local fluctuations. These can be very large in large-R jets and affect substructure variables. On the contrary, local fluctuations are by construction
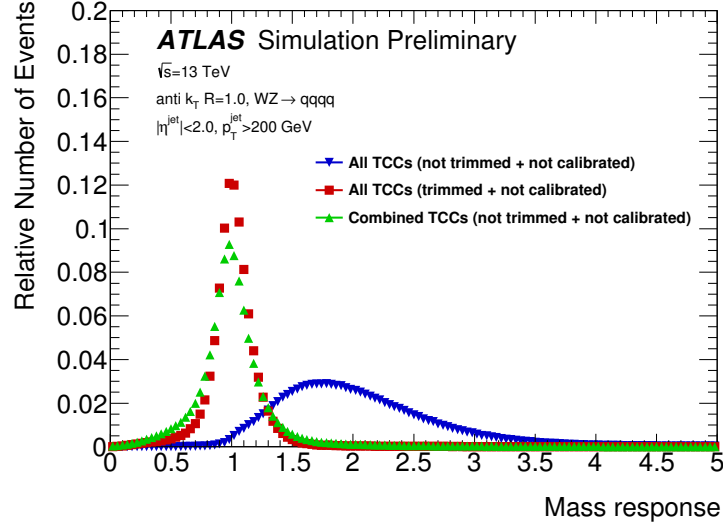
Figure 4.7: Comparison of the mass response for three TCC jet collections: jets built using all TCCs and not trimmed (blue upside-down triangles), jets built using all TCCs and trimmed (red squares) and jets built using only combined TCCs (green triangles). The effect of trimming is visible comparing the mass response distribution for untrimmed and trimmed jet collections built using all-TCC objects. Jets built using only combined TCC present a well-behaved mass response without the need for trimming [88].
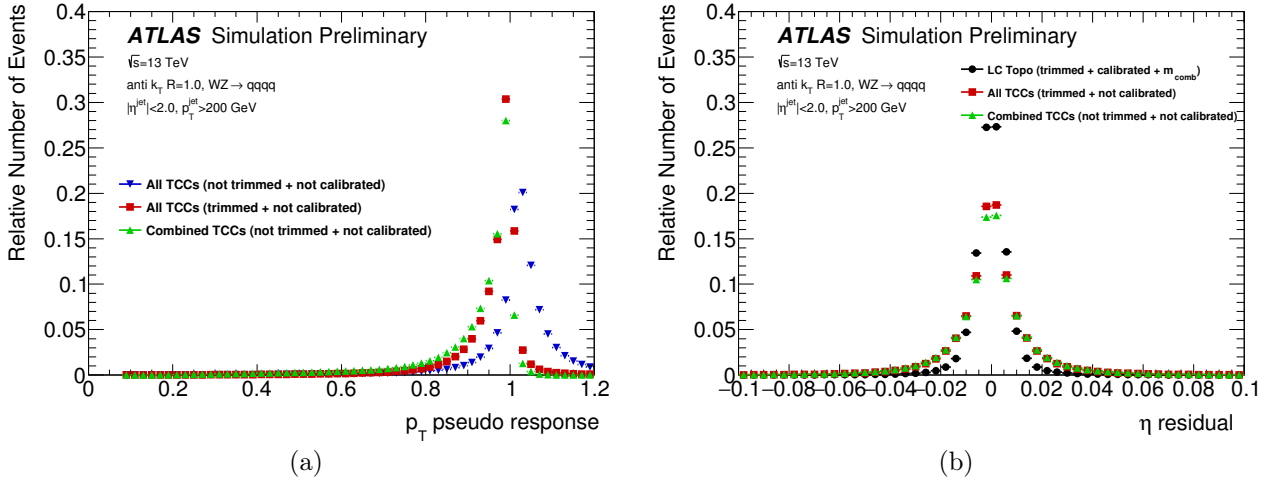
Figure 4.8: (a) Comparison of the p_T pseudo-response for the three TCC jet collections compared to the trimmed uncalibrated LC topo-cluster jet definition: jets built using all TCCs and not trimmed (blue upside-down triangles), jets built using all TCCs and trimmed (red squares) and jets built using only combined TCCs (green triangles). The distribution peaks at approximately one for the trimmed all-TCC and the combined-TCC jet collections. The effect of pile-up is more pronounced for the untrimmed all-TCC jet collection. (b) Comparison of the η residual distributions for trimmed LC topo-cluster jets (black dots), trimmed all-TCC jets (red squares) and untrimmed combined-TCC jets (green triangles). The calibrated LC topo-cluster jets are shown to have the best performance [88].
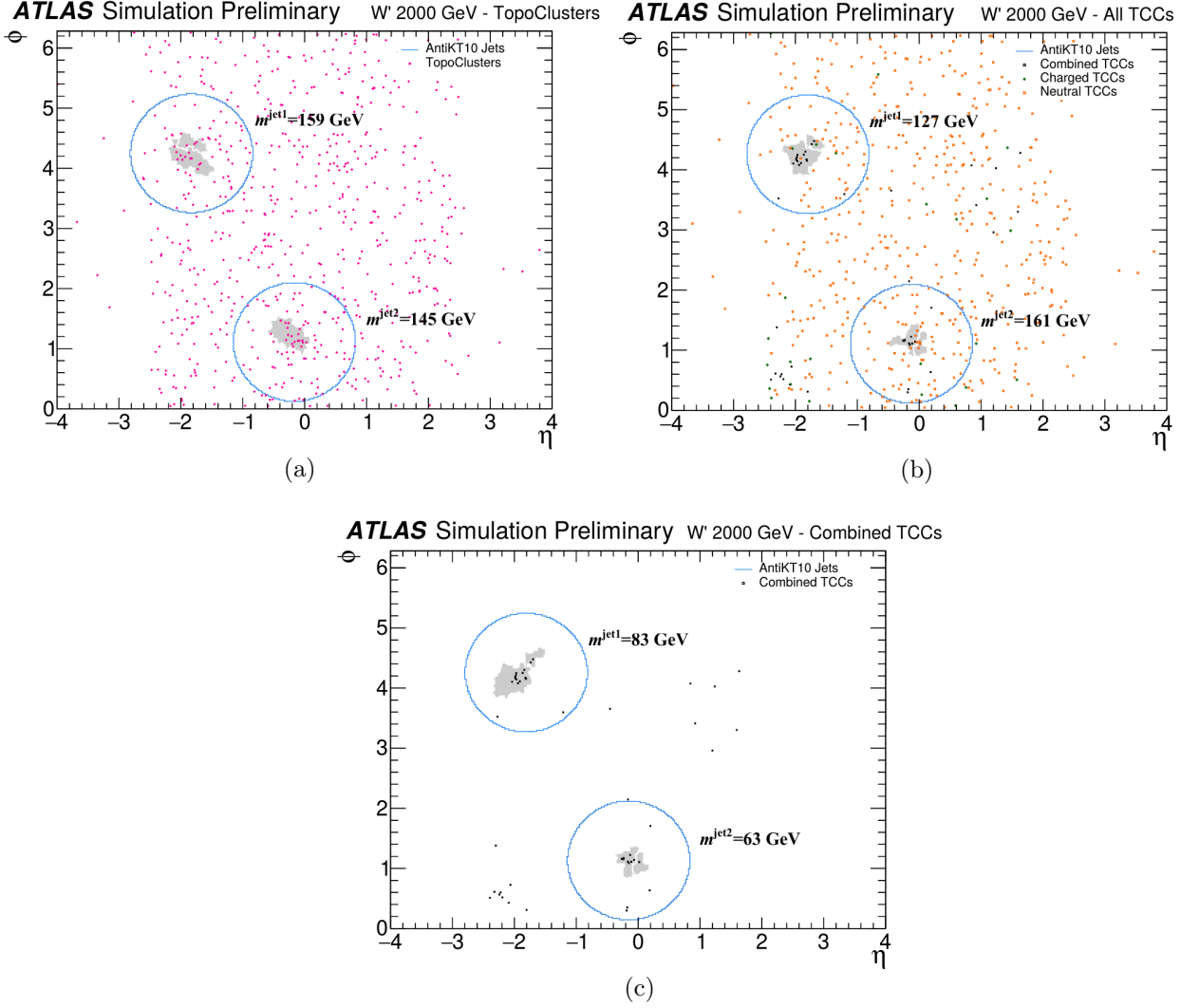
Figure 4.9: Reconstruction of a single $W' \to WZ \to qqqq$ simulated event using (a) LC topo-cluster jets, (b) all-TCC jets and (c) combined-TCC jets. Anti-k_t jets with $R = 1.0$ are considered before trimming and at the uncalibrated scale to show the raw detector view of the event. Blue circles envelope the jets, while the grey regions denote the anti-k_t subjets with $R_{\text{sub}} = 0.2$ and $f_{\text{cut}} = 5\%$. Compared to the LC topo-cluster jets, both TCC-jet collections are able to resolve the two separated subjets within both large-R jets [88].

considered in the TCC technique and therefore jets built from TCC objects are expected to provide a mass resolution superior to that of topo-cluster jets using m_{comb} at high p_{T}. A comparison of the mass response for different jet collections for 700 GeV $< p_{\mathrm{T}} < 800$ GeV and for 2.1 TeV $< p_{\mathrm{T}} < 2.5$ TeV is shown in Figure 4.10a and Figure 4.10b, respectively. The performance for the different jet collections is shown to be very similar. At high p_{T}, as expected, the responses of TCC jets peak at values larger than one because of their uncalibrated scale.

Another particularly useful substructure variable for the identification of hadronically decaying vector bosons is $D_2^{\beta=1}$ (see § 3.7), hereafter referred to as D_2. The particularity of this variable is its dependence on the angular resolution of the inputs used to build the jets. For this reason, two considerations have to be made. First, the better angular resolution of TCCs compared to topo-clusters is expected to improve the D_2 calculation when using TCC jet collections. Second, since D_2 is evaluated from the inputs of the jets, the jet calibration doesn't change the results, and thus allowing LC topo-cluster jets to be directly compared to TCC jets. The comparison of the D_2 residual for different jet collections for 700 GeV $< p_{\mathrm{T}} < 800$ GeV and for 2.1 TeV $< p_{\mathrm{T}} < 2.5$ TeV is shown in Figure 4.11a and Figure 4.11b, respectively. The D_2 residual is shown to be very stable for TCC jets when varying the p_{T} by an order of magnitude, while it changes dramatically for LC topo-cluster jets broadening at high p_{T} where it is no longer Gaussian. Moreover, the LC topo-cluster jets are extremely biased towards large values of D_2 while TCC jets remain centred around zero. In addition, a long tail is shown by the combined-TCC jet collection suggesting that part of the relevant energy contribution is missed when considering only track-cluster matches.

In order to understand the evolution of the mass response and D_2 residual and to compare mass responses centred at different values, a resolution metric must be defined. As already shown in Equation 3.10 and discussed in § 3.6, the mass resolution is defined as:

$$\sigma(m) = \frac{1}{2} \times \frac{68\% \ \mathrm{IQnR} \left[R_r(m) \right]}{\mathrm{median} \left[R_r(m) \right]}. \tag{4.12}$$

Alternatively, the D_2 resolution is obtained as:

$$\sigma(D_2) = \frac{1}{2} \times 50\% \ \mathrm{IQnR} \left[R_d(D_2) \right]. \tag{4.13}$$

The respective $\sigma(m)$ and $\sigma(D_2)$ are shown in Figure 4.12. The mass resolution for all-TCC jets is superior to LC topo-cluster jets m_{comb} for $p_{\mathrm{T}}^{\mathrm{truth}} > 2$ TeV and slightly worse for $p_{\mathrm{T}}^{\mathrm{truth}}$ below that value. For the D_2 resolution the situation is very different. All-TCC jets significantly outperform the LC topo-cluster jets in the entire $p_{\mathrm{T}}^{\mathrm{truth}}$ spectrum reaching a factor two improvement at the high bound of the considered range. For both variables, combined-TCC jets present a degraded resolution compared to the other collection due to the high tails as seen in Figures 4.10 and 4.11. For the three jet collection $\sigma(m)$ and $\sigma(D_2)$ degrades with increasing $p_{\mathrm{T}}^{\mathrm{truth}}$. For the D_2 resolution, this effect is less pronounced for all-TCC jets.

Another important aspect that has to be considered is the pile-up robustness of the TCC procedure compared to jets built from topo-clusters. In order to address it, the median of the mass response and its resolution for high p_{T} jets as a function of the number of reconstructed primary vertices is shown in Figure 4.13. All the distributions present relatively stable central values and widths across the entire considered range. A small positive slope characterises the combined-TCC jets both in Figure 4.13a and Figure 4.13b where $W' \rightarrow WZ \rightarrow qqqq$ events with $M_{W'} = 1$ TeV and with $M_{W'} = 5$ TeV are considered, respectively. Therefore, the three jet definition considered are reasonably stable against pile-up, with combined-TCC jets being slightly more sensitive because of the lack of grooming.
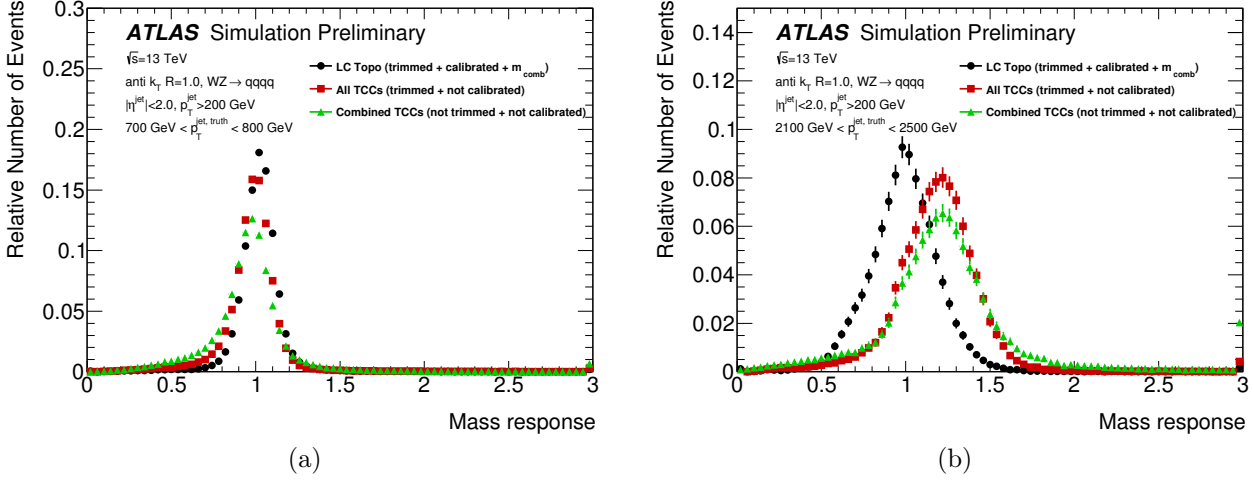
Figure 4.10: Comparison of the mass response for different jet collections for (a) 700 GeV $< p_T <$ 800 GeV and (a) 2.1 TeV $< p_T <$ 2.5 TeV: trimmed LC topo-cluster jets (black dots), trimmed all-TCC jets (red squares) and untrimmed combined-TCC jets (green triangles). The last bin in each plot is the overflow for all entries beyond the considered range which results to be relevant only for combined-TCC jets. The performance for the different jet collections are shown to be very similar. At high p_T, as expected, the responses of TCC jets peak at values larger than one because of their uncalibrated scale. The witdth of the distributions cannot be directly compared. A quantitative comparison of the mass response is shown in Figure 4.12a [88].
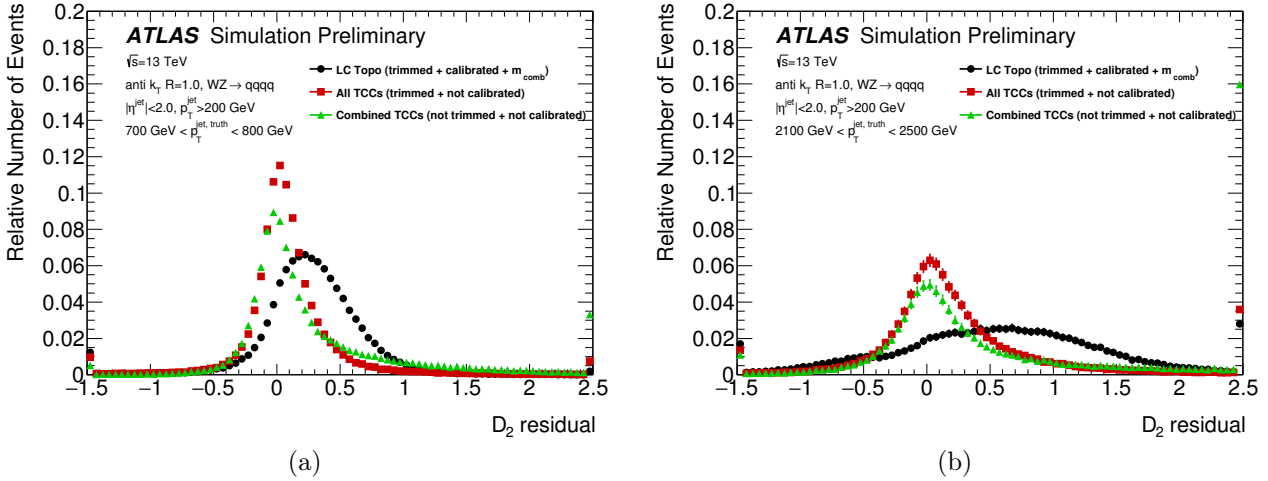
Figure 4.11: Comparison of the D_2 residual for different jet collections for (a) 700 GeV $< p_T <$ 800 GeV and (a) 2.1 TeV $< p_T <$ 2.5 TeV: trimmed LC topo-cluster jets (black dots), trimmed all-TCC jets (red squares) and untrimmed combined-TCC jets (green triangles). The first (last) bin in each plot is the underflow (overflow) for all entries before (beyond) the considered range which results to be very relevant for combined-TCC jets at high p_T. The D_2 residual is shown to be very stable for TCC jets when varying the p_T by an order of magnitude, while it changes dramatically for LC topo-cluster jets broadening at high p_T where it is no longer Gaussian. [88].
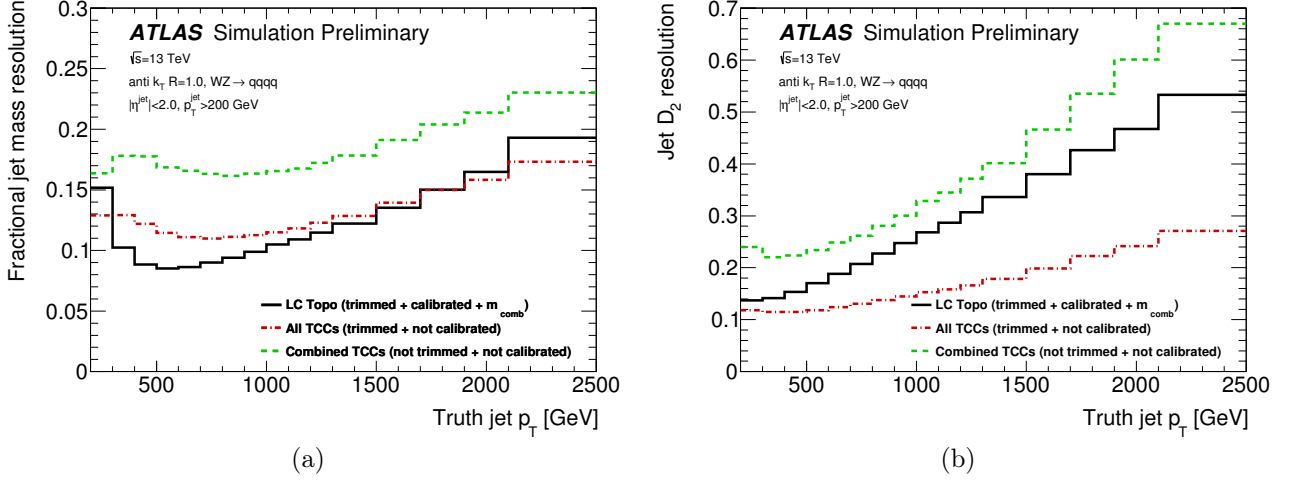
Figure 4.12: Comparison of the fractional jet (a) mass and (b) D_2 resolutions as a function of p_T^{truth} for trimmed LC topo-cluster jets (black), trimmed all-TCC jets (red) and untrimmed combined-TCC jets (green). All-TCC jets outperform the LC topo-cluster jets at high p_T^{truth}, particularly for D_2 [88].
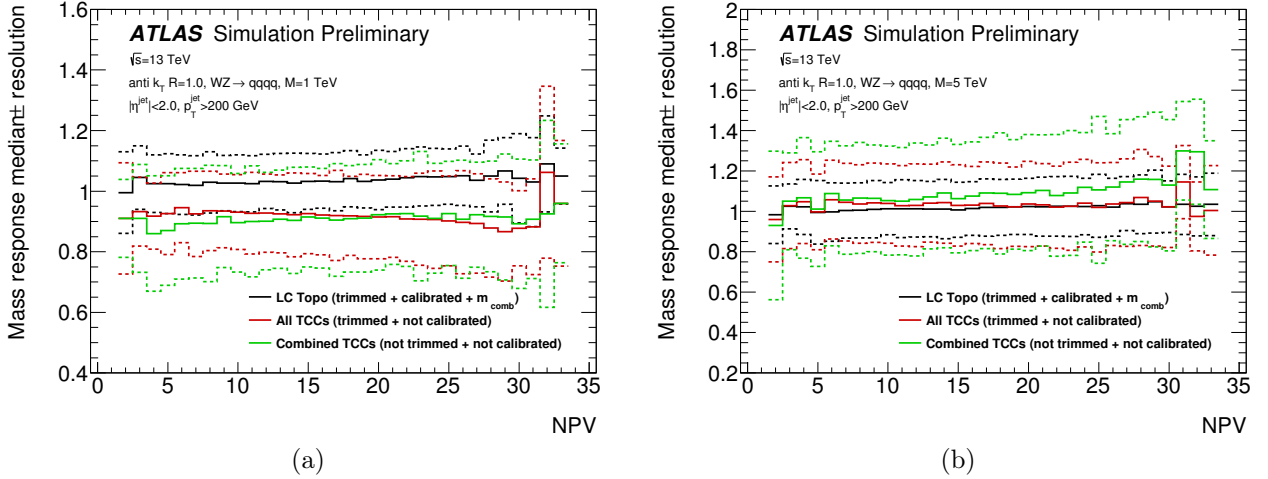
Figure 4.13: Mass response as a function of the number of reconstructed primary vertices for trimmed LC topo-cluster jets (black), trimmed all-TCC jets (red) and untrimmed combined-TCC jets (green) in $W' \to WZ \to qqqq$ events with (a) $M_{W'} = 1$ TeV and (b) $M_{W'} = 5$ TeV. For each distribution, the median is indicated with a solid line while the resolution window around the median is delimited by two dashed lines. A small positive slope characterises the combined-TCC jets in both plots [88].

4.5 Further Improvements

This chapter has focused on preliminary studies of jet substructure performance using jet built from TCCs. Jets built from all the TCC categories, i.e. combined, charged and neutral, are seen to outperform the topo-cluster jet combined mass for $p_T > 2$ TeV with a worse resolution for most of the lower p_T range. Moreover, they perform significantly better than LC topo-cluster jets for the D_2 resolution across the full p_T range. In addition, combined-TCC jets results are very interesting for their pile-up resilience without the use of grooming, but further studies are needed to improve their performance.

All the results presented in this chapter have shown the great potential of TCCs to increase sensitivity of the ATLAS physics program, especially in analyses where jet substructure techniques play a critical role.

The crucial step before actually using TCC-jets in an analysis it to derive correction constants to calibrate the reconstructed jets to the truth jet energy and mass scale following the procedure discussed in § 3.5. While this process was ongoing, further studies have shown that mis-measured tracks with excessively high p_T can strongly affect the energy scale of charged TCCs leading to wrongly estimated jet kinematics. Therefore, it was decided to neglect the charged objects and build TCC jets from combined and neutral components. The combined+neutral-TCC jet collection has been considered the baseline for all further developments and will be referred from now on simply as TCC jets.

Calibration factors have been derived to calibrate TCC jets to the truth energy and mass scale, using for the derivation of the mass scale correction factors a parameterisation of the mass response in bins of $\ln(m/p_T)$ and η_{det}. Figure 4.14 and Figure 4.15 show the jet energy response and the jet mass response as a function of the truth jet p_T before and after calibration. After calibration, detector effects are reduced and the mean and median of the energy and mass response move towards unity showing a uniform behaviour across the considered p_T spectrum.

The mass and D_2 resolutions have been re-evaluated for the fully calibrated TCC-jet collection and are shown in Figure 4.16a and Figure 4.16b. The results are shown to be consistent with what has been presented in Figure 4.12a and Figure 4.12b.
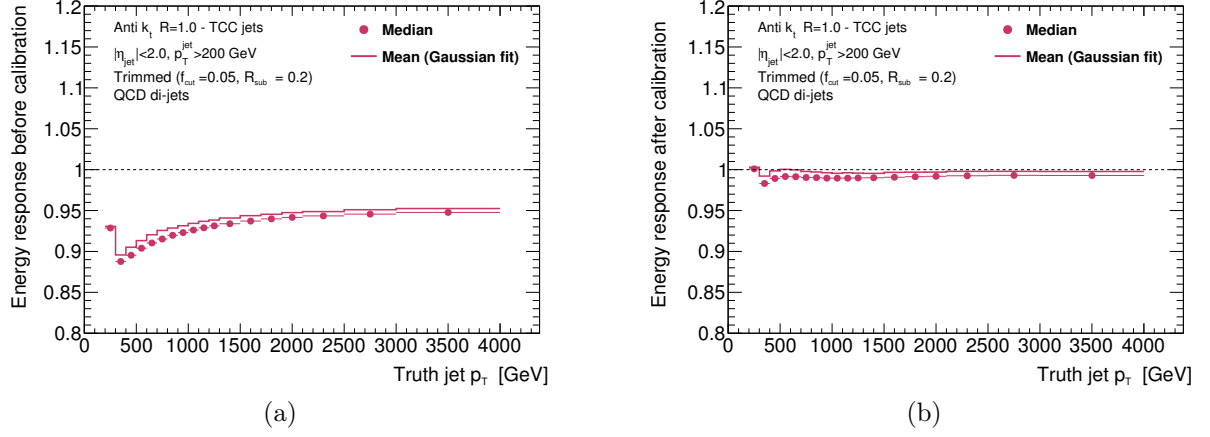
Figure 4.14: Jet energy response for TCC jets as a function of the truth jet p_T before (a) and after (b) jet energy calibration. The median and the mean of the energy response as a function of the truth jet p_T are shown. The mean is obtained fitting iteratively the core of the distribution with a Gaussian function. After calibration, detector effects are reduced and the mean and median of the energy and mass response move towards one showing a uniform behaviour across the considered p_T spectrum.
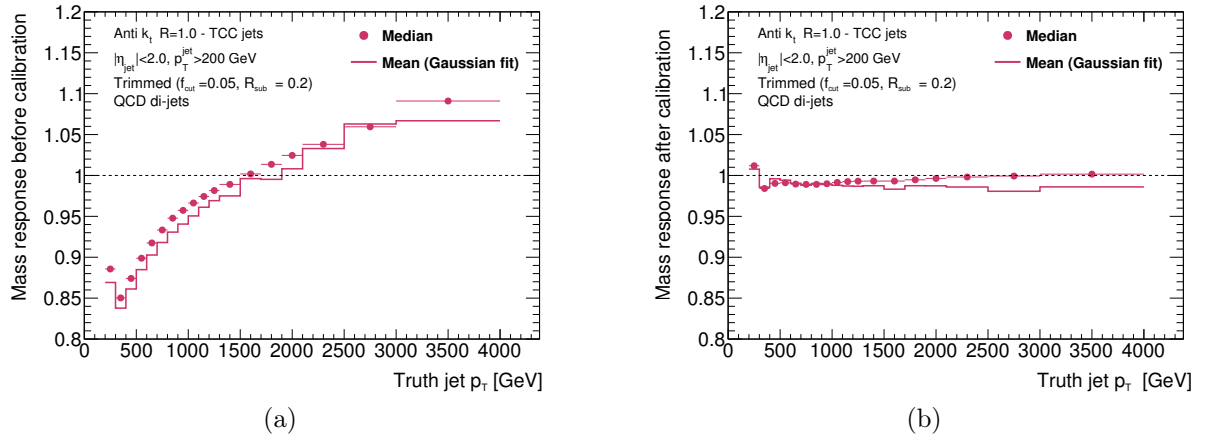
Figure 4.15: Jet mass response for TCC jets as a function of the truth jet p_T after the jet energy calibration and before (a) and after (b) jet mass calibration. The median and the mean of the mass response as a function of the truth jet p_T are shown. The mean is obtained fitting iteratively the core of the distribution with a Gaussian function. After calibration, detector effects are reduced and the mean and median of the energy and mass response move towards one showing a uniform behaviour across the considered p_T spectrum.

(a)   (b)
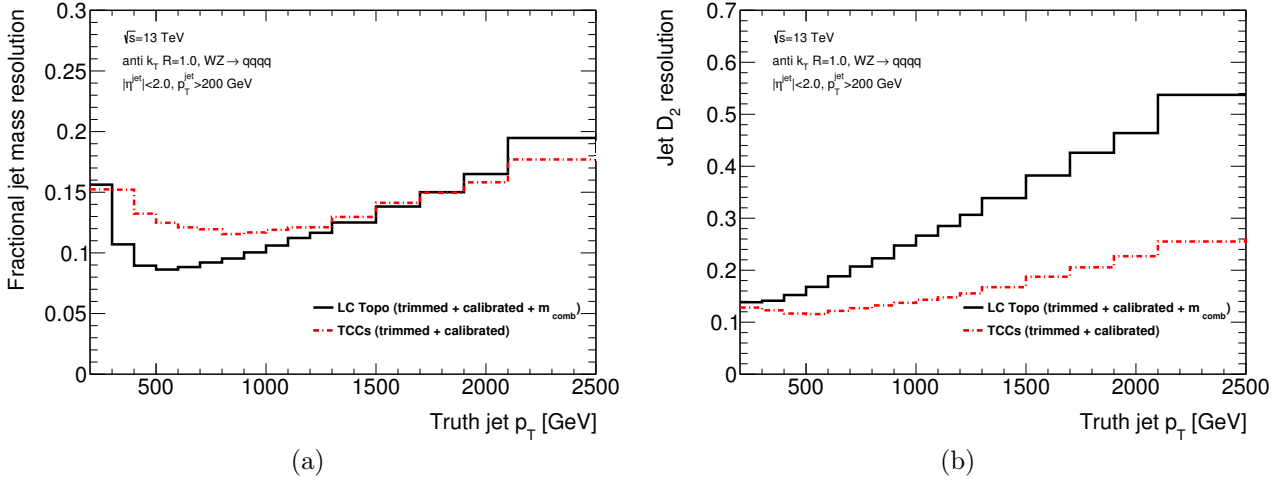
Figure 4.16: Comparison of the fractional jet (a) mass and (b) D_2 resolutions as a function of p_T^{truth} for trimmed LC topo-cluster jets (black) and trimmed TCC jets (red). The two jet collections are fully calibrated.

<div align="right"># 5</div>

Identification of Boosted Vector Bosons

Contents

5.1   Introduction

As described in § 1.2.1, several extension of the Standard Model predict heavy resonances decaying to pairs of vector bosons. Fully hadronic signatures enhance the sensitivity of searches looking for these extensions in a high energy regime. It is therefore crucial to efficiently identify such hadronic decays and distinguish them from QCD multi-jet events.

The identification of boosted hadronic decays of vector bosons makes use of grooming techniques (see § 3.4), to remove pile-up and underlying event contamination, initial- and final-state radiation from the reconstructed large-R jets, and a tagging algorithm that exploits jet substructure variables to separate boson jets and background QCD jets.

This chapter will focus on the development and optimisation of a new vector boson tagger. Unlike previous techniques [28, 33], optimised for maximising the background rejection for fixed signal efficiencies, this novel approach is designed to provide the maximum significance for boosted W/Z-jets with respect to QCD-jets. It has been optimised to identify W and Z bosons for both TCC and LC topo-cluster jets in order to provide a quantitative comparison of the physics reach when profiting from the improved jet substructure performance of TCC jets.

The algorithm described in this chapter is adopted in the search for narrow diboson resonances decaying to fully hadronic final states in 79.4 fb^{-1} of proton-proton collision data collected by the ATLAS experiment between 2015 and 2017 at $\sqrt{s} = 13$ TeV [93].

The chapter is organised as follows: simulated samples and event selection definitions will be presented in § 5.2; § 5.3 will describe in detail the implementation and optimisation of the boson tagger, while performance evaluations of the identification technique for diboson resonance searches will be discussed in § 5.4 and § 5.5.

5.2 Monte Carlo Simulation Samples

The $W' \to WZ \to qqqq$ process has been generated using PYTHIA8 [89] with the NNPDF2.3 leading order parton distribution function (PDF) and the A14 tune [90] of the underlying event. Additional contributions from multiple proton-proton interactions were simulated by overlaying the event with minimum-bias events generated with PYTHIA8. The W' mass has been varied from 0.4 TeV to 5 TeV. QCD multi-jet background samples are simulated using PYTHIA8 with the A14 tune and NNPDF2.3 leading order PDF set. These samples are generated in several bins of transverse momentum and weighted to produce a smoothly falling jet p_T spectrum when combined.

For these studies, signal and background samples are reweighted to correspond to a dataset of 120 fb^{-1}. Events are required to contain at least two large-R jets with $|\eta| < 2.0$ to guarantee a good overlap with the tracker acceptance. Only the two jets with the highest p_T are considered and are required to have $p_T > 200$ GeV. Trimming is applied to TCC jets using the same parameters as used for the LC topo-cluster jet collection, $f_{cut} = 5\%$ and $R_{sub} = 0.2$. The jet energy and mass are calibrated for both TCC and LC topo-cluster jet definitions. Moreover, a p_T-dependent optimisation of the boson identification algorithm is provided based on the trimmed anti-k_t $R = 1.0$ truth jet p_T. Using the information of truth particles matched to reconstructed jets, boson jets can be truth labelled. The classification as W/Z-jets allows for the optimisation of the identification of W and Z bosons separately.

5.3 Identification of Hadronically Decaying Vector Bosons

In the last years, many grooming techniques and substructure variables have been studied and used in previous fully-hadronic diboson resonance searches [28, 33]. Many studies have been performed to identify jet substructure variables able to provide the highest discrimination power between boosted bosons and QCD jets [77, 81]. To date, the largest sensitivity gain comes from the use of the jet mass (see § 3.6) and D_2 (see § 3.7.1).

- **Jet Mass:** as shown in Figure 3.4b, the mass of QCD jets is lower than the W- and Z-jet masses, peaking in the region of 30-40 GeV (with a p_T dependence). Boson jets, on the other hand, peak at the mass of the initial boson. Requiring that the jet mass of a W candidate roughly matches the mass of the W boson, and the jet mass of a Z candidate roughly matches the mass of the Z boson, therefore provides significant discrimination against QCD jets.

- **D_2:** resolving the energy structure(s) within a jet distinguishes between W/Z-jets, characterised by a two-prong structure, and QCD-jets which are mainly one-prong.

This section is dedicated to the description of the boson identification technique and its optimisation based on the two substructure variables.

5.3.1 Jet Mass and Substructure Tagging

The general idea of the procedure is to optimise, based on MC simulation, p_T dependent cuts on the jet mass and D_2 in order to maximise the sensitivity to boson decays. A metric has to be therefore

introduced to define the optimal working point.

The sensitivity definition used in these studies is

$$\mathcal{S} = \frac{\varepsilon}{\frac{a}{2} + \sqrt{B}} \tag{5.1}$$

where ε indicates the efficiency of the chosen cuts on the signal, a is the number of sigmas corresponding to one-sided Gaussian significance and B is the number of expected QCD background events after selection [94]. The value $a = 3$ is used. Compared to other expressions that are commonly used ($\mathcal{S} = S/\sqrt{B}$ and $\mathcal{S} = S/\sqrt{S+B}$, where S is the number of expected signal events after selection), the definition shown in Equation 5.1 depends on the signal efficiency after the selection cuts, ε, instead of the absolute number of events selected, S, and therefore has the advantage of not depending on the cross-section of the desired signal, thus is more suitable for optimisation, allowing for the determination of a single set of cuts that is optimal both for setting limits and for making a discovery. Moreover, the often used $\mathcal{S} = S/\sqrt{B}$ has the additional disadvantage of breaking down at small values of B, pushing down the experiment efficiency. As an example, it prefers an expectation of 0.1 signal events with a background of 10^{-5} over 10 signal events and 1 background event, while the proposed definition prefers the inverse.

For each truth p_T bin, all possible pairs of (jet mass, D_2)-cuts with a signal efficiency between 5 and 100% are considered in the following way: first, the mass cut is varied in steps of 1% in signal efficiency as a symmetric window around the median of the W/Z-jet mass distribution. For a given mass cut, the corresponding jet D_2 distribution is evaluated and the one-sided D_2 cut is varied in steps of 1% in signal efficiency. The significance is then calculated for each (jet mass, D_2)-cut combination. An example distribution of the significance $\mathcal{S}$ as a function of jet mass and D_2 efficiency cuts for TCC W-jets in the truth jet p_T bin [1000, 1100) GeV is shown in Figure 5.1a. Three different working points can be defined:

- **Maximum-significance working point:** the central value of the plateau of highest significance in each truth jet p_T bin was selected as (jet mass, D_2)-cut of the boson-tagger, as shown in Figure 5.1b;

- **Fixed-signal-efficiency working point:** the tagger is optimised to provide $(50 \pm 1)\%$ signal efficiency. The (jet mass, D_2)-cut is selected to provide the highest significance in each truth jet p_T bin (see Figure 5.1c);

- **Fixed-background-rejection working point:** as shown in Figure 5.1d the requirement on fixed background rejection, $1/\varepsilon_{\text{bkg}} = 10^2$ (corresponding to a background efficiency $\varepsilon_{\text{bkg}} = (1.00 \pm 0.05)\%$), is used to define the set of (jet mass, D_2) cuts. The highest significance value is then chosen to obtain the (jet mass, D_2)-cut in each truth jet p_T bin.

The (jet mass, D_2)-cut for the three working points is shown in Figure 5.2 for the same truth p_T bin [1000, 1100) GeV for TCC jets.

In the following, results will be shown only for the maximum significance working point as this will be considered as the benchmark configuration of the boson identification algorithm. In fact, the new approach has been seen to improve sensitivity for all jets compared to fixed-signal-efficiency or fixed-background-rejection taggers.

After selecting the initial cut values for each truth jet p_T bin, parametric functions are used to fit the p_T dependence of the jet mass window and the jet D_2 cut. This is done mainly to avoid bin-edge effects that may result from the use of discrete selection criteria.

The mass window parameterisation has a physically motivated approach considering two factors:

(a)

(b) Maximum-signficance working point

(c) Fixed-signal-efficiency working point

(d) Fixed-background-rejection working point
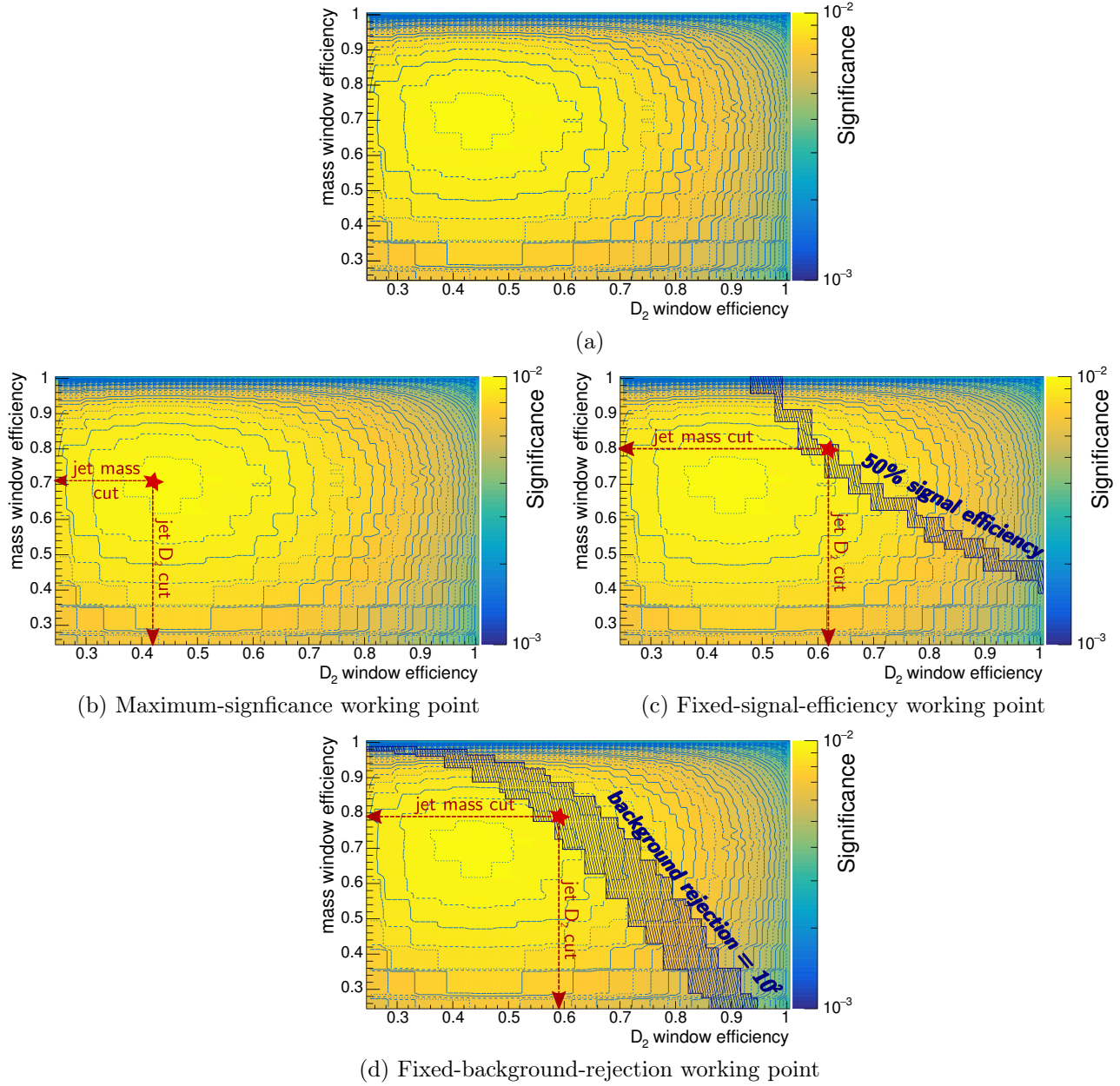
Figure 5.1: (a) Significance, defined as $\mathcal{S} = \frac{\varepsilon}{\frac{3}{2}+\sqrt{B}}$, for W and Z jets from HVT $W' \to WZ \to qqqq$ events with respect to QCD background jets for truth jet $p_T \in [1000, 1100)$ GeV. It is shown as a function of the signal efficiencies corresponding to the jet mass and D_2 cuts. (b), (c) and (d) depict the evaluation of the three working points selecting the pairs of (jet mass, D_2) values corresponding to (b) the highest significance value, (c) the highest significance value requiring a fixed 50% signal efficiency and (d) the highest significance value for a fixed background rejection. The blue lines in (c) and (d) represent the significance values corresponding to the fixed signal efficiency and background rejection requirements, respectively. The line corresponding to a fixed background rejection of 10^2, i.e. background efficiency $\varepsilon_{\text{bkg}} = (1.00 \pm 0.05)\%$, has been extracted from a background rejection map as a function of the signal efficiencies for the jet mass and D_2 cuts.
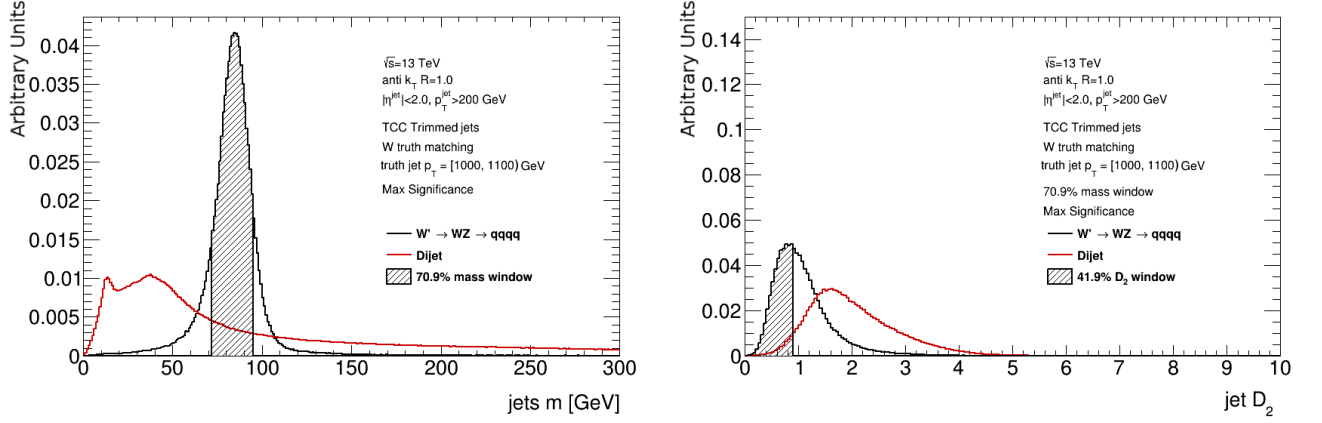
(a) Mass cut and D_2 cut for the maximum-signficance working point
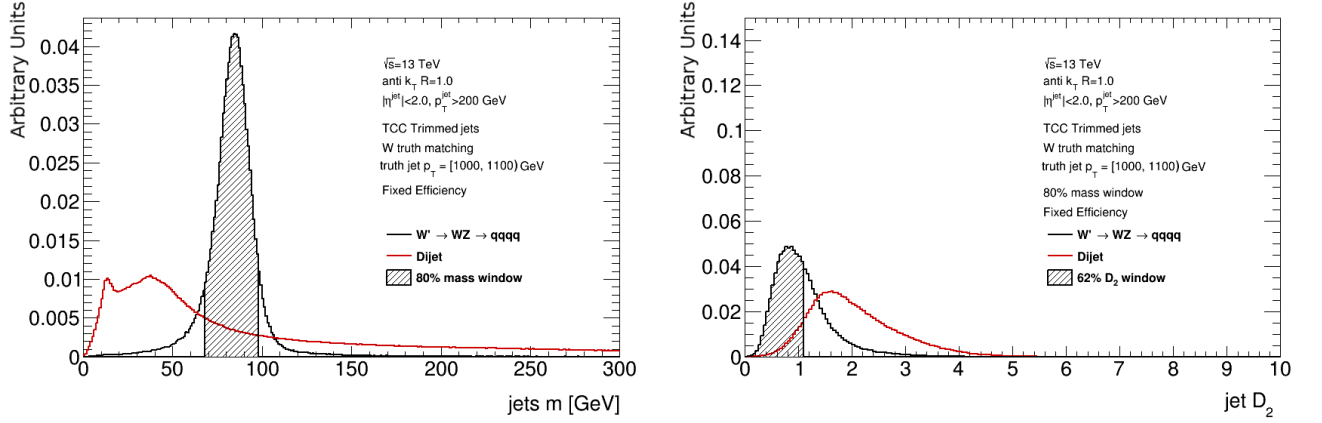
(b) Mass cut and D_2 cut for the fixed-signal-efficiency working point
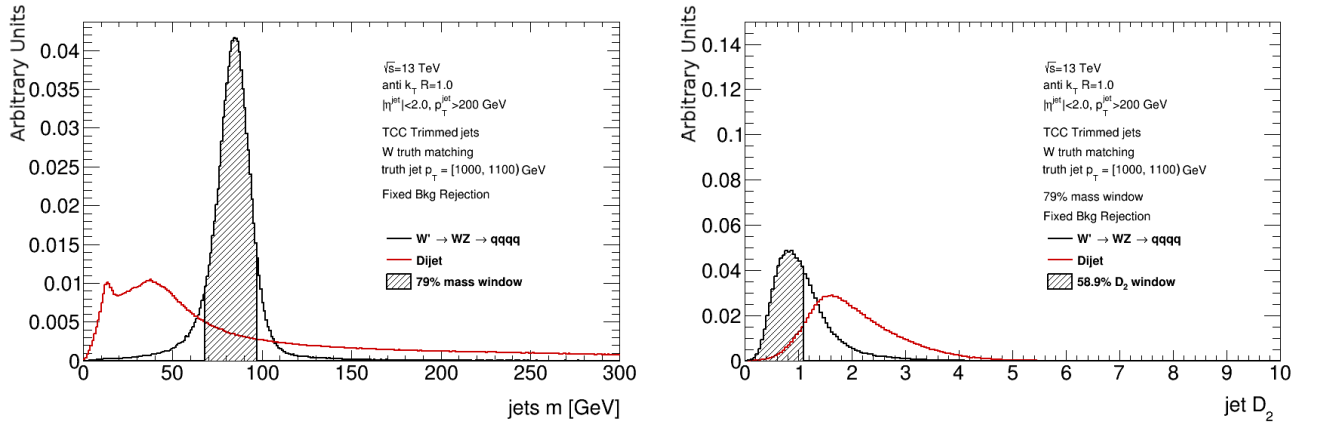
(c) Mass cut and D_2 cut for the fixed-background-rejection working point

Figure 5.2: Visualisation of the (jet mass, D_2) cuts for W-jets with truth jet $p_T \in [1000, 1100)$ GeV for the three working points. The D_2 distribution is obtained after the jet mass cut is applied.

- **Energy resolution:** at low p_T, there is a significant contribution to the mass resolution from the jet energy resolution of $R = 1.0$ jets. To first order, the energy resolution improves (i.e. decreases) with $1/p_T$ as more energy is contained within the jet. This resolution contribution can be defined by two parameters: $\sigma_E \propto A/(p_T - B)$;

- **Angular resolution:** at high p_T, the calorimeter spatial granularity becomes too coarse to resolve fine jet substructure and increases the resolution of the jet mass. This is counterbalanced by the use of tracks in TCC jets. At the same time however, the efficiency and resolution for tracks in the ID is also slightly degraded at higher p_T. As these effects will depend on the collimation, and the collimation depends on p_T, two additional terms are added to the resolution: $\sigma_A \propto C \cdot (p_T - D)$;

The current mass paramatererisation sums in quadrature the two contributions into a 4-parameter function:

$$\mathcal{F}_{\text{mass}} = \sqrt{\sigma_E^2 + \sigma_A^2} = \sqrt{\frac{A^2}{(p_T - B)^2} + C^2 \cdot (p_T - D)^2}. \tag{5.2}$$

which was observed to fit well the bounds of the mass window cut. The D_2 parameterisation is a third-order polynomial. Figures 5.3a and 5.3b show the mass window and D_2 cut parameterisation for TCC and LC topo-cluster W-jets.

Contrary to previous taggers, the new approach does not enforce a fixed signal efficiency nor a fixed background rejection, but rather creates a smooth behaviour which maximizes the analysis sensitivity. The resulting signal efficiencies and background rejections for W-jets are shown in Figure 5.4 for the two jet collections. The results for Z-jets are not shown here as they are very similar to those of W-jets. A rather loose cut is applied on the jet mass accepting about $80 - 90\%$ of the signal. Because of the slightly worse mass resolution for $p_T < 1.5$ TeV (see Figure 4.16a), a loser cut on the mass is obtained using TCC jets with respect to LC topo-cluster jets. This is also visible comparing the two jet collections in Figures 5.3a and 5.3b. The D_2 selection cuts much harder for both jet collections, and retains about 30% efficiency for both W and Z-boson jets with $p_T = 500$ GeV. At higher jet p_T, the signal efficiency increases reaching 60% efficiency for jets with a p_T of 2500 GeV. This is well motivated by the behaviour of the background, which does decrease rapidly for high di-jet masses, and thus higher jet p_T. At the regime of high di-jet masses above 3.0 TeV, background rejection through boson-tagging is not the main concern of the analysis, but rather maintaining a reasonable acceptance for signals with small cross-sections. This is also reflected in the background rejection as a function of jet p_T. The main difference between the two jet collections lies, as expected, in the discrimination power based on D_2 resolution. Figure 5.3 shows that the maximum D_2 selection criteria increases approximately linearly with truth jet p_T using LC topo-cluster jets while it is more stable for TCC jets. The improved D_2 resolution of TCC jets (see Figure 4.16b) allows for higher discriminating power between boson- and QCD-jets, which also translates into a higher background rejection for $p_T \gtrsim 1000$ GeV for TCC jets with respect to LC topo-cluster jets.

5.4   Performance Evaluation for Diboson Resonance Searches

A first application of the new identification approach will be used in the search for narrow diboson resonances (WW, WZ and ZZ) decaying to fully hadronic final states.

As explained in § 1.2.1.4 this search profits from larger branching ratios of the vector bosons decaying to quarks, but is dominated by the enormous background of Standard Model QCD di-jet production.
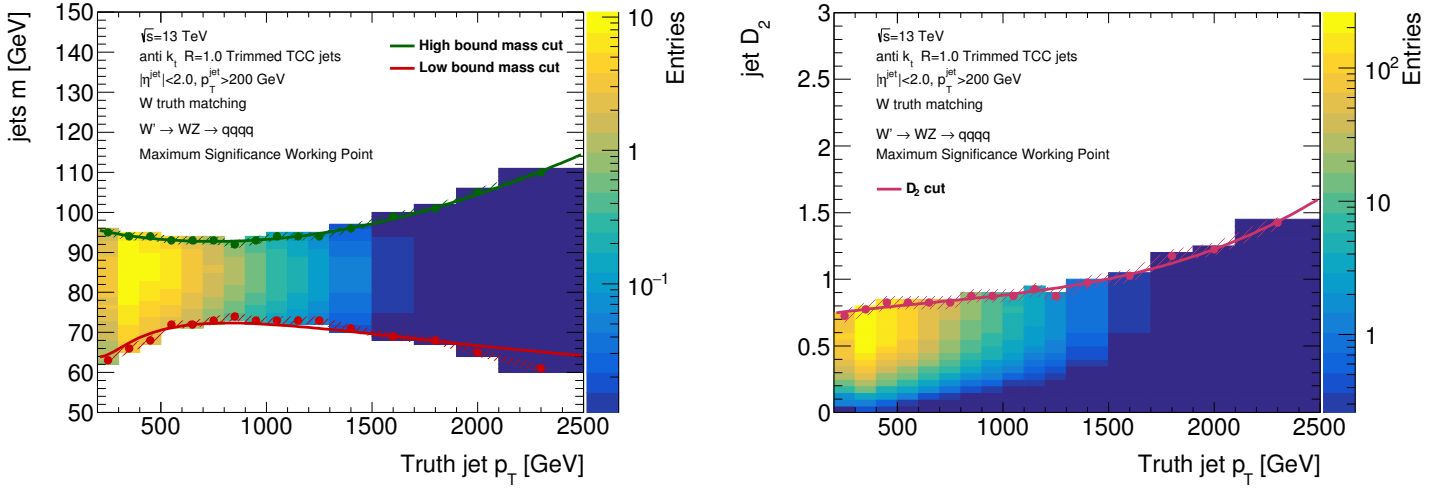
(a) Mass cut (left) and D_2 cut (right) for W-truth-labelled TCC jets
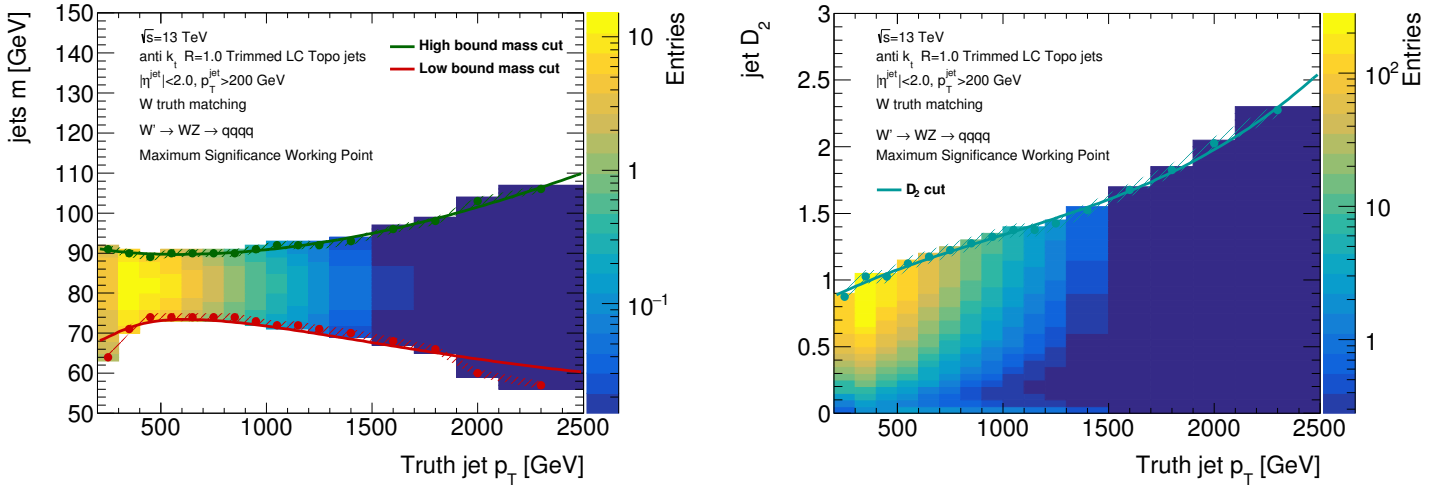
(b) Mass cut (left) and D_2 cut (right) for W-truth-labelled LC topo-cluster jets

Figure 5.3: Jet mass window (left) and D_2 cut (right) of the W-tagger as a function of truth jet p_T for (a) TCC jets and (b) LC topo-cluster jets. Both the initial cut values for maximum significance and the fitted parametrization are shown. The tagger is only valid for jets up to 2500 GeV.

(a)

(b)

(c)
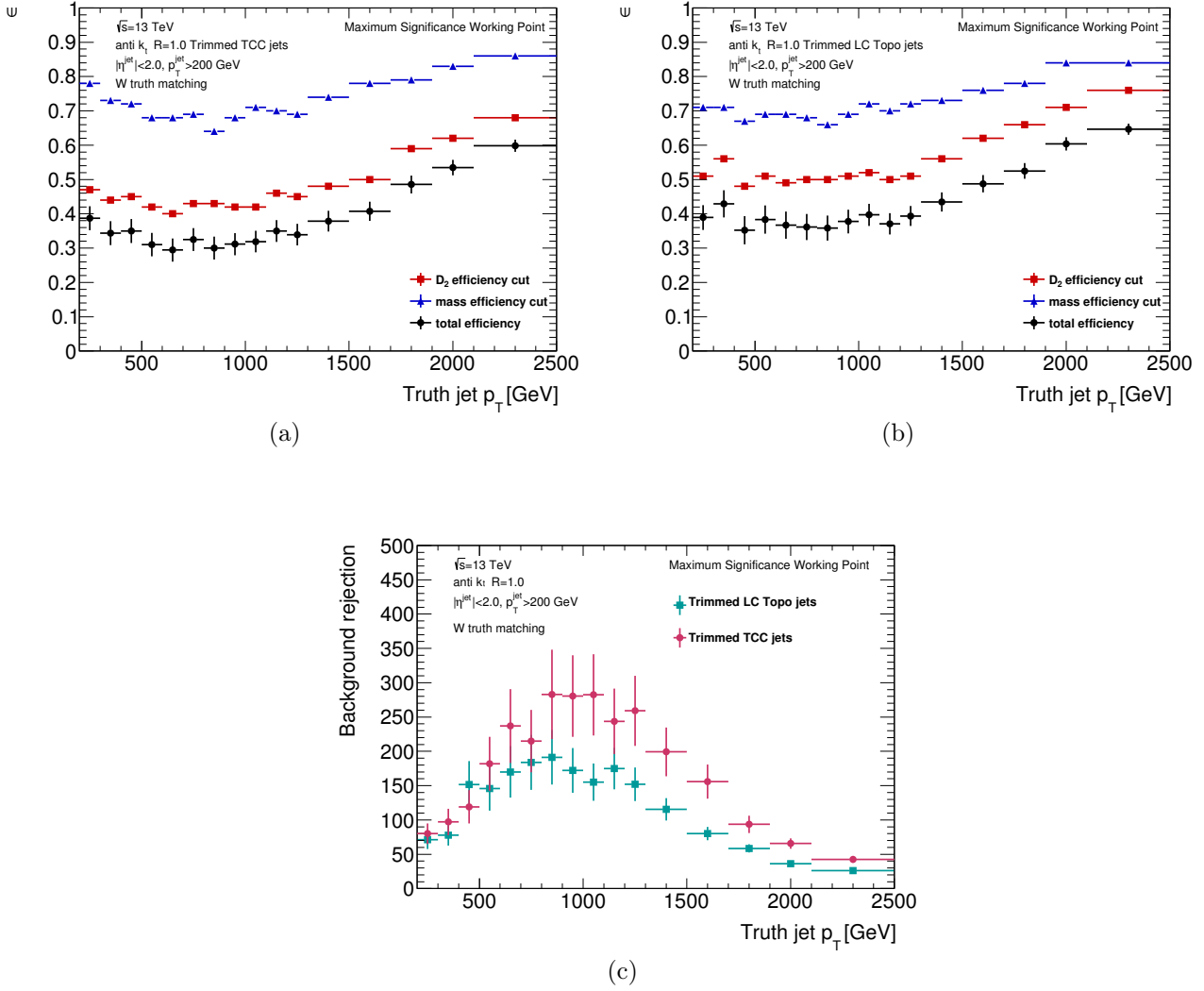
Figure 5.4: Signal efficiency as a function of the truth jet p_T for the W-tagger for HVT $W' \to WZ \to qqqq$ events for (a) TCC and (b) LC topo-cluster jets. (c) Background rejection of the W-tagger for QCD di-jet events as a function of the truth jet p_T.

Other Standard Model processes, such as W/Z+jets, diboson, top-quark pairs and single-top production, can be neglected at high p_T due to their much smaller magnitude. The decay of a heavy particle will appear as a narrow resonant structure in the invariant di-jet mass on top of the smoothly falling QCD background distribution (see Figure 5.6).

The same event selection as in [28] is imposed to evaluate the performance of the boosted vector boson identification. Events pass the pre-selection stage if they contain at least two reconstructed large-R jets within $|\eta| < 2.0$ with a mass bigger than 50 GeV; the leading jet is required to have $p_T > 450$ GeV and the subleading jet $p_T > 200$ GeV, respectively. Moreover, the invariant mass of the system formed by these two jets, m_{JJ}, must be larger than 1.1 TeV. Additional kinematic requirements are imposed to suppress the QCD di-jet background.

- The rapidity separation between the leading and subleading jet (indicated with subscripts 1 and 2) is required to be $|\Delta y_{1,2}| = |y_1 - y_2| < 1.2$ to suppress t-channel di-jet production, since signal is s-channel.

- To remove events with poorly-reconstructed jets, the p_T asymmetry between the leading and subleading jets is required to be $A = (p_{\mathrm{T},1} - p_{\mathrm{T},2})/(p_{\mathrm{T},1} + p_{\mathrm{T},2}) < 0.15$.

The boosted boson tagger is used for the identification of boson-jets. Each of the two leading jets are required to pass either the W boson or Z boson tagging criteria. Events are categorised in WW, WZ or ZZ signal regions. It is worth mentioning at this point that the mass and D_2 windows for the identification of W- and Z-jet overlap and thus the signal regions are not independent.

Preliminary studies of the boson tagger have been conducted using $W' \to WZ \to qqqq$ Monte Carlo simulation with three different W' mass points, $M_{W'} = 2, 3, 4$ TeV. Figure 5.5 and Figure 5.6 show the di-jet mass distributions, m_{JJ}, for the $WW + WZ$ and $WW + ZZ$ signal regions using either TCC or LC topo-cluster jets. Compared to LC topo-cluster jets, TCC jets boost the sensitivity at high p_T where the background contribution is reduced by a factor of two in integrated luminosity. The significance, defined as $\mathcal{S} = S/\sqrt{B}$, is evaluated in a $\pm 10\%$ mass window around each mass value. TCC jets provide higher significance: the values are improved from $\sim 10\%$ at 2 TeV to $\sim 45\%$ at 4 TeV with respect to LC topo-cluster jets. Moreover, compared to previous taggers optimised for a fixed signal efficiency, the new definition provides a less steeply-falling di-jet mass distribution. The uncertainty shown on the plots in Figure 5.5 and Figure 5.6 is only statistical. The limited statistics available in the Monte Carlo samples[1] after boson tagging is applied is strongly affecting the bin-by-bin fluctuation.

The selection efficiency, defined as the number of selected events at different stages of the analysis divided by the number of generated events, is shown in Figure 5.7 as a function of the resonance mass for HVT Z' and W' signals and for the bulk G_{RS} decaying to WW and ZZ. The signal efficiencies are shown after the pre-selection stage, after the rapidity separation and p_T asymmetry requirements and after requiring the two leading large-R jets to be boson-tagged, separating the contributions of the jet mass and D_2 cuts. The signal selection efficiency after all cuts are applied shows the same shape as in Figure 5.4a. The corresponding values of the selection efficiency for the di-jet QCD background are shown in Figure 5.8.

---

[1]Monte Carlo samples are scaled to 120 fb^{-1}, but the number of simulated events is less than 120 fb^{-1} the in some areas.

(a)   (b)
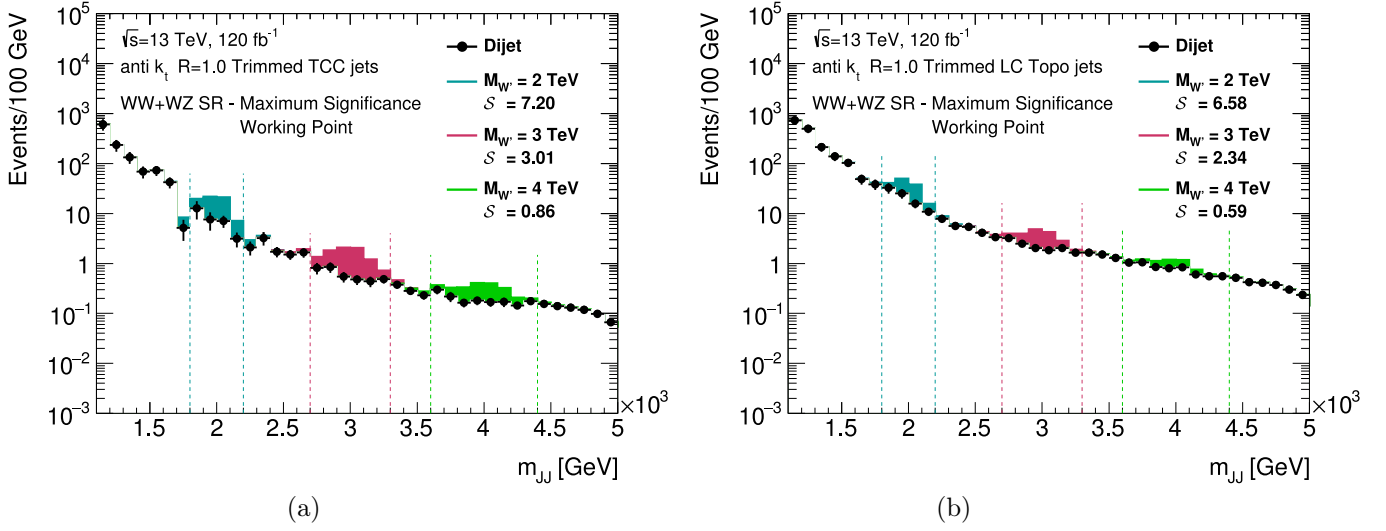
Figure 5.5: Di-jet mass distributions, m_{JJ}, for the $WW + WZ$ signal region using (a) TCC and (b) LC topo-cluster jets. The signal from $W' \rightarrow WZ \rightarrow qqqq$ events with three different W' mass points, $M_{W'} = 2, 3, 4$ TeV, is added on top of the smoothly falling background di-jet mass spectrum. The significance $\mathcal{S} = S/\sqrt{B}$ is evaluated in a $\pm 10\%$ mass window around each mass value and is reported on the plot. The uncertainty shown on the points is only statistical and bin-by-bin fluctuation exist due to the limited statistics available after boson-tagging is required. TCC jets provide higher significance: the values are improved from $\sim 10\%$ at 2 TeV to $\sim 45\%$ at 4 TeV with respect to LC topo-cluster jets.

(a)   (b)

Figure 5.6: Di-jet mass distributions, m_{JJ}, for the $WW + ZZ$ signal region using (a) TCC and (b) LC topo-cluster jets. The signal from $W' \rightarrow WZ \rightarrow qqqq$ events with three different W' mass points, $M_{W'} = 2, 3, 4$ TeV, is added on top of the smoothly falling background di-jet mass spectrum. The significance $\mathcal{S} = S/\sqrt{B}$ is evaluated in a $\pm 10\%$ mass window around each mass value and is reported on the plot. The uncertainty shown on the points is only statistical and bin-by-bin fluctuation exist due to the limited statistics available after boson-tagging is required. TCC jets provide higher significance: the values are improved from $\sim 20\%$ at 2 TeV to $\sim 45\%$ at 4 TeV with respect to LC topo-cluster jets.
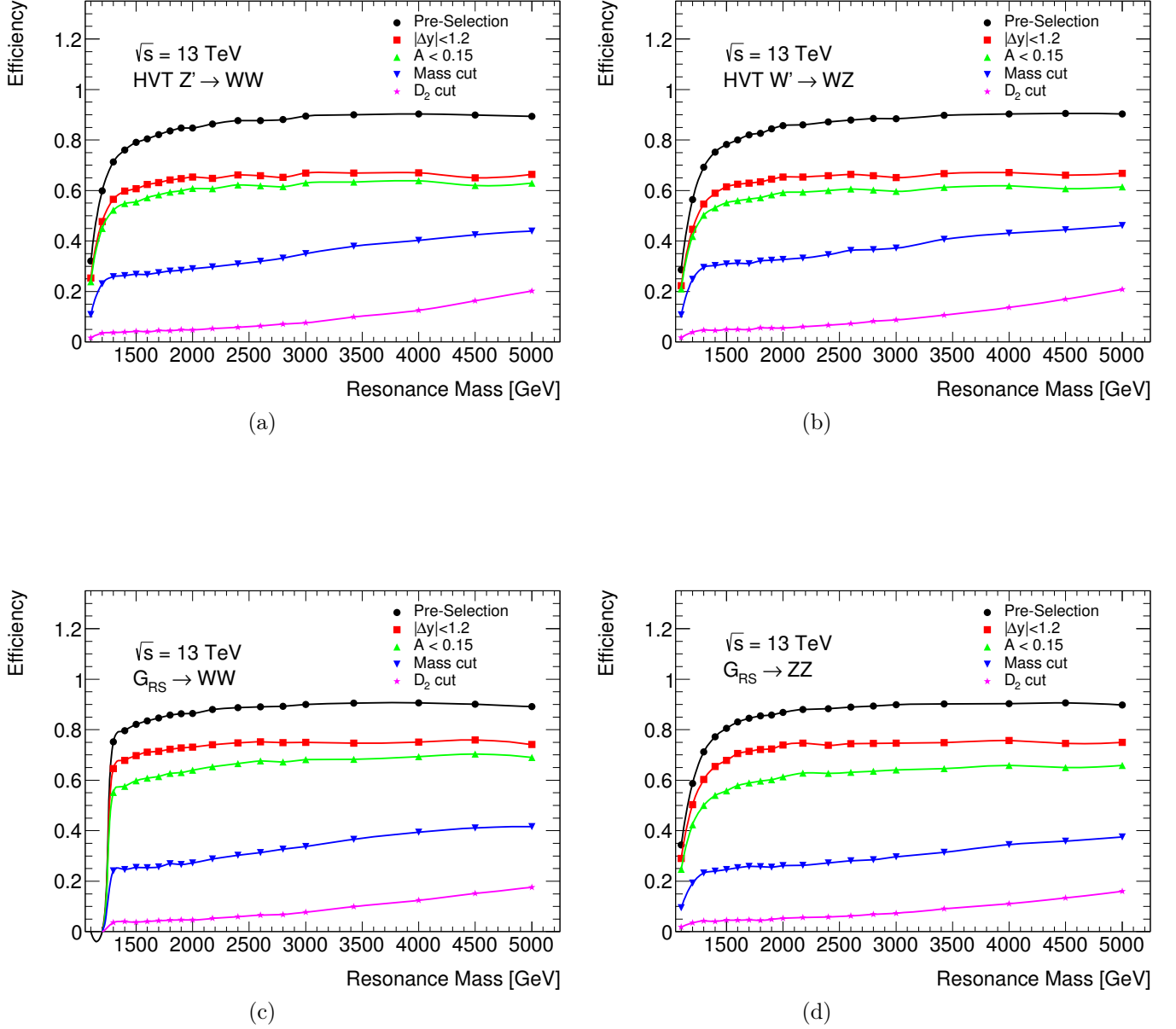
Figure 5.7: The efficiency for the selection, defined as the number of selected events at different stages of the analysis divided by the number of generated events, for (a) HVT $Z' \to WW$, (b) HVT $W' \to WZ$, (c) bulk $G_{RS} \to WW$ and (d) bulk $G_{RS} \to ZZ$ as a function of the resonance mass. The selections considered include sequentially pre-selections, topological cuts on $|\Delta y_{1,2}|$, p_T asymmetry, and boson-tagging using jet mass and D_2 (e.g. $|\Delta y_{1,2}|$ also includes preselection cuts) [95].

(a)

(b)

(c)
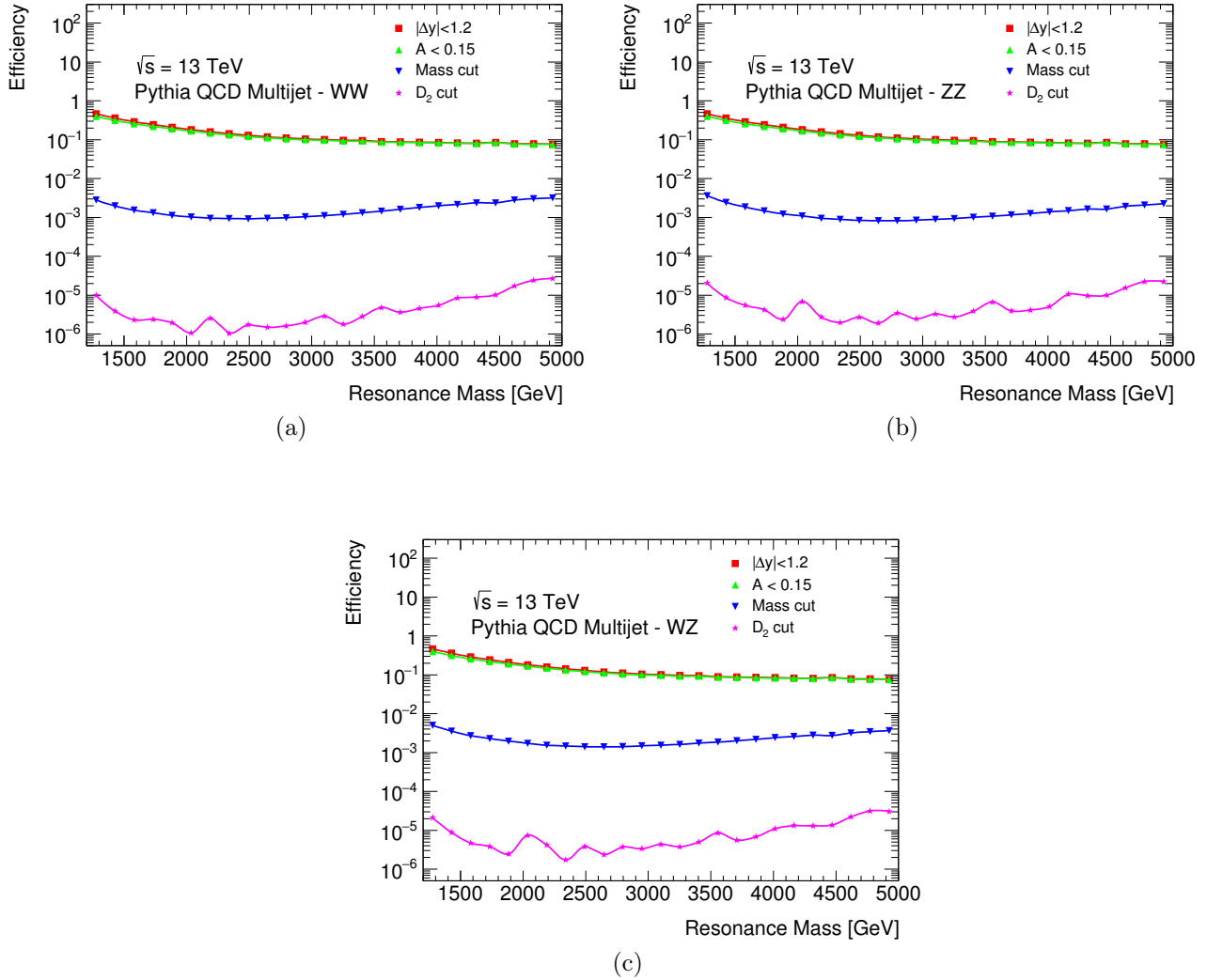
Figure 5.8: The efficiency for the selection, defined as the number of selected events at different stages of the analysis divided by the number of generated events, for the QCD di-jet background as a function of the resonance mass. The selections considered include sequentially pre-selections, topological cuts on $|\Delta y_{1,2}|$, p_T asymmetry, and boson-tagging using jet mass and D_2 (e.g. $|\Delta y_{1,2}|$ also includes preselection cuts) [95].

5.5 Vector-Boson Identification Studies Using Data

The efficiency of the vector boson tagger is measured in data using a sample enriched in final states with a vector boson plus jets.

Data collected in 2015, 2016, and 2017 from $\sqrt{s} = 13$ TeV LHC proton-proton collisions in the 25 ns running period is used. Events are selected with the lowest un-prescaled single large-R-jet trigger with the leading ungroomed anti-k_t $R = 1.0$ jet $p_T \geq 360$ GeV in 2015, $p_T \geq 420$ GeV in 2016, and leading trimmed anti-k_t $R = 1.0$ jet $p_T \geq 440$ GeV in 2017. After requiring good beam and detector conditions, the integrated luminosity corresponds to 3.2 fb^{-1} in 2015, 32.9 fb^{-1} in 2016, and 43.3 fb^{-1} in 2017.

For these studies W+jets and Z+jets samples, generated with SHERPA [96] interfaced with the CT10 [97] PDF set, and QCD di-jet background samples, simulated with PYTHIA8 with the A14 tune and NNPDF2.3LO PDF set, are used. Monte Carlo samples are scaled to correspond to the same integrated luminosities and reproduce the same machine and detector conditions.

Events are selected requiring two jets in $|\eta| < 2$ and requesting that the leading jet has a p_T larger than 600 GeV. One of the selected jet is required to pass the D_2 selection for either a W or a Z while the other is required to fail it in order to provide an orthogonal selection with respect to the diboson search and reduce Standard Model diboson backgrounds. The selected jets should be representative of the jets selected in the signal region for the diboson resonance search. The mass distribution of the selected jets, m_J is fitted by a signal-plus-background function, allowing to measure the rate of V+ jets events.

First, the background mass distribution is parameterised by the exponential:

$$\mathcal{F}_{\text{bkg}} = A \cdot \exp\left[B \cdot (m_J - 100) + C \cdot (m_J - 100)^2 + D \cdot (m_J - 100)^3 + E \cdot (m_J - 100)^4\right] \quad (5.3)$$

where A, B, C, D and E are fit parameters.

The W+jets and Z+jets Monte Carlo samples are used to estimate the signal parameters. The signal mass distributions for the vector-boson jets are described by the following functional form:

$$\mathcal{F}_V = \mathcal{F}_{\text{signal}}^V + \mathcal{F}_{\text{bkg}} \quad (5.4)$$

with

$$\mathcal{F}_{\text{signal}}^V = A' \cdot \left\{\exp\left[-\frac{1}{2}\left(\frac{m_J - m_V - B'}{C'}\right)^2\right] + D' \cdot \exp\left[-\frac{1}{2}\left(\frac{m_J - m_V - B'}{E'}\right)^2\right]\right\} \quad (5.5)$$

where m_V is the mass of the vector boson V and A', B', C', D' and E' are fit parameters. Among the defined parameters, A' measures the scale of the signal function and B' represents the offset of the double Gaussian with respect to the mass of the vector boson. Figure 5.9 shows the fits to the background, W and Z jet mass distribution performed in the range [55, 180] GeV.

The fits to the signal jet mass are used to extract the number of W and Z boson candidates. The W and Z templates are added together with the appropriate scale factors to reproduce the ratio of the W and Z rates. The $W + Z$ template is fitted to data together with the background using the following functions for the signal-plus-background and background-only fits:

$$\mathcal{F}_{\text{data}}^{\text{sig+bkg}} = \mathcal{F}_{\text{signal}}^W + \mathcal{F}_{\text{signal}}^Z + \mathcal{F}_{\text{bkg}} \quad (5.6)$$

$$\mathcal{F}_{\text{data}}^{\text{bkg}} = \mathcal{F}_{\text{bkg}} \quad (5.7)$$

To fit the data only the normalisation of the $W + Z$ template, the offset of the mean of the double Gaussian functions and the background parameters are allowed to float.

A background-only and signal-plus-background fit is then performed to the mass distribution in data in the range [55, 180] GeV, as shown in Figure 5.10a. The number of W/Z events is evaluated from the integral of the fitted $W + Z$ template. The boson tagging signal efficiency after preselection in data is $\varepsilon_{\mathrm{data}} = (89 \pm 8)\%$. The closure of the fitting procedure has been probed on simulation. The W and Z templates are scaled to reproduce the efficiency in data and the sum of the simulated samples is treated as if it were data and fitted to exactly the same functions. The closure fit returns a scaling parameter of 1.04 ± 0.10 as shown in Figure 5.10b. Finally, the scale factor S to correct the signal efficiency in Monte Carlo simulation, $\varepsilon_{\mathrm{MC}}$, to that in data, $\varepsilon_{\mathrm{data}} = S \cdot \varepsilon_{\mathrm{MC}}$, is derived. The resulting value is $S = 0.78 \pm 0.10$. The scale factor on the W/Z-tagging efficiency is used to scale the overall Monte Carlo signal yield which allows the evaluation of the uncertainties in the large-R jet tagging efficiency (see § 5.7.3).
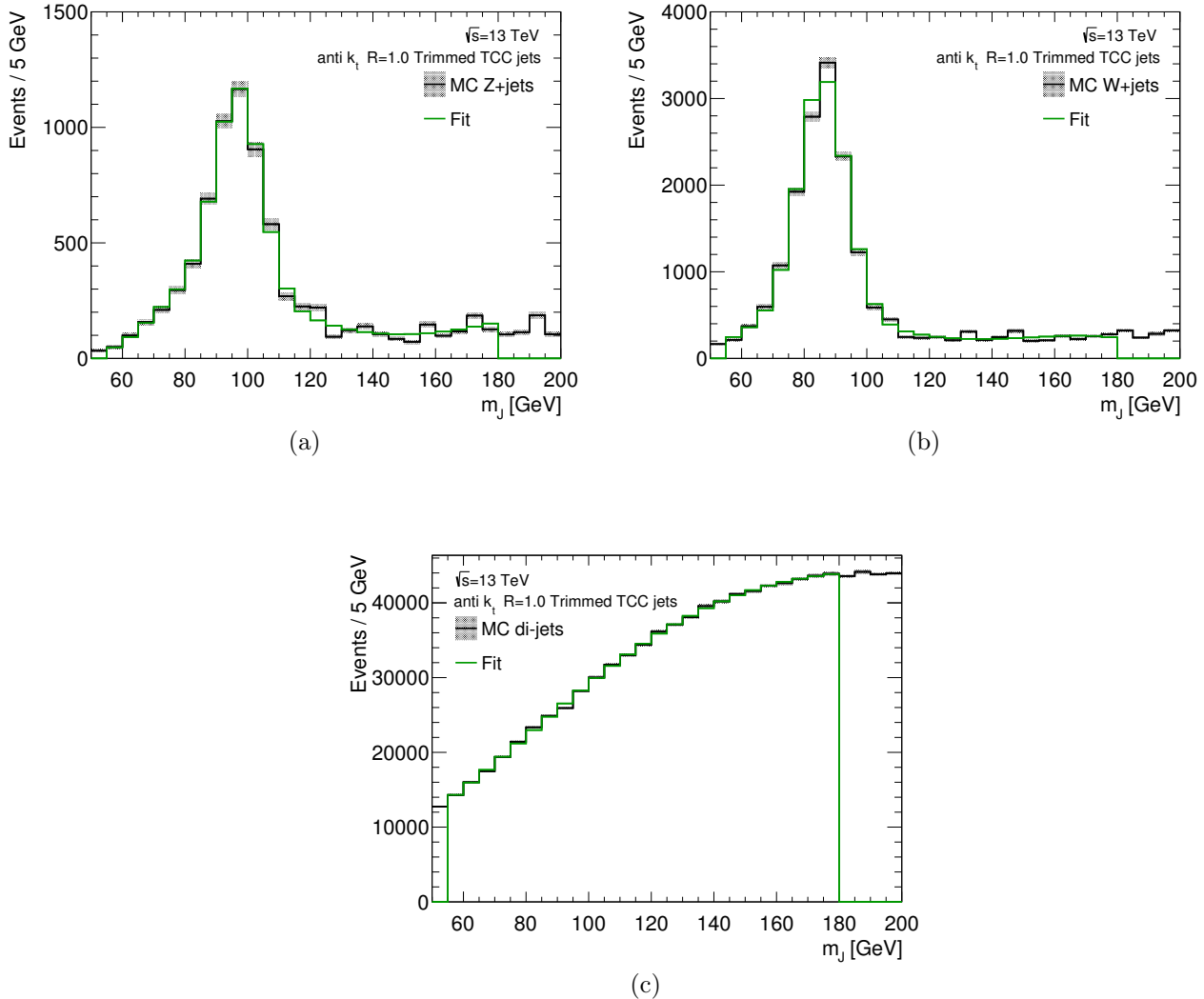

Figure 5.9: Fit to the jet mass distribution for (a) Z, (b) W and (c) di-jet events using the fit functions described in the text. The fits to the W and Z jet mass are used to extract the number of vector boson candidates.
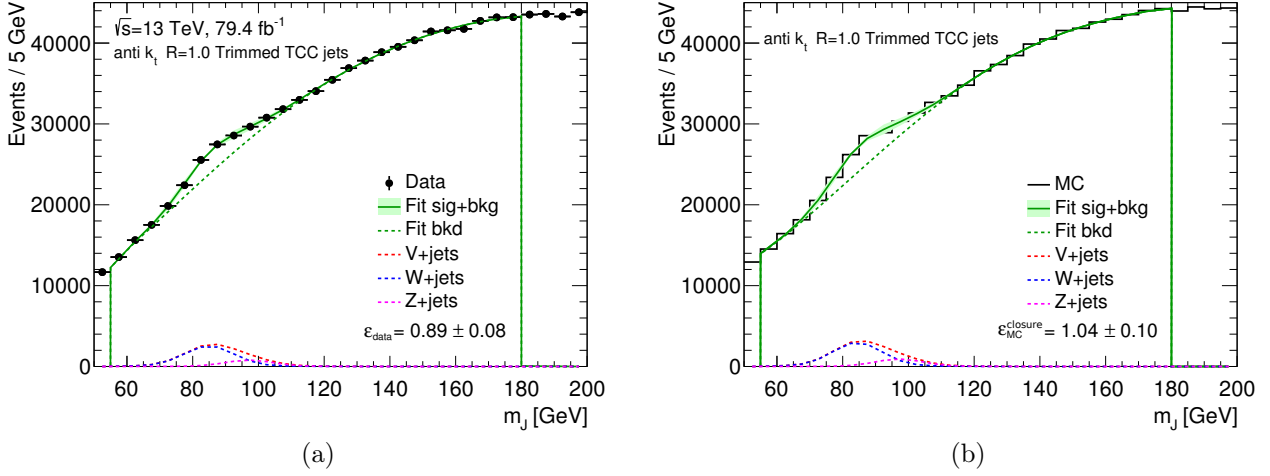
Figure 5.10: (a) Fit to the jet mass distribution in a V+jet enriched sample in data corresponding to 79.4 fb^{-1} proton-proton collisions at $\sqrt{s} = 13$ TeV. (b) Closure of the fitting procedure treating simulated samples as data. Both plots show the background-only and signal-plus-background fits using the functions described in the text.

5.6 Conclusions

This chapter describes in detail the implementation of a novel tagging technique optimised for boosted vector boson identification as developed for the search for diboson resonances in the fully hadronic channel.

The influence of pile-up effects can be mitigated using trimmed jets. Jet mass and D_2 are the best jet substructure variables to provide the largest discrimination between boson- and QCD-jets. TCC jets provide an improved capability to resolve two separated structures within a large-R jet and motivate the use of this new jet collection. The identification algorithm is optimised using the figure of merit described in § 5.3.1, which is independent of any a-priori assumption on the cross section of known signals. Parametric functions are then used to fit the p_T dependence of the jet mass window and the jet D_2 cut.

The new implementation of the tagger boosts sensitivity at high p_{T}. Compared to LC topo-cluster jets, TCC jets provide a reduction of the background contribution up to a factor two in integrated luminosity and approximatively 45% higher significance for 4 TeV resonances. The efficiency for the selection, defined as the number of selected events at different stages of the selection divided by the number of generated events, is obtained for different signal and background samples.

The efficiency of the vector boson tagger is measured in a data sample enriched in final states with a vector boson plus jets. The value obtained is $\varepsilon_{\mathrm{data}} = (89 \pm 8)\%$. Using simulated samples, a closure procedure is performed. Excellent closure is observed, with a scale parameter on the boson-tagging efficiency of 1.04 ± 0.10. The scale factor S to correct for the signal efficiency in Monte Carlo simulation, $\varepsilon_{\mathrm{MC}}$, to that in data, $\varepsilon_{\mathrm{data}} = S \cdot \varepsilon_{\mathrm{MC}}$, is $S = 0.78 \pm 0.10$.

5.7 Diboson Resonance Search at $\sqrt{s} = 13$ TeV with 79 fb^{-1}

The vector boson identification algorithm described in this chapter is used in the search for WW, WZ and ZZ resonances with 79 fb^{-1} of proton-proton collisions collected at the LHC with the ATLAS detector in 2015-2017 [93]. In the following, a brief discussion on the strategy of this analysis is

provided. The results shown in § 5.7.4 demonstrate that the analysis is able to largely improve on past results mostly thanks to the use of the novel techniques developed by the author of this thesis.

5.7.1 Event Selection

Events are selected with the lowest un-prescaled single large-R-jet trigger with the leading ungroomed anti-k_t $R = 1.0$ jet $p_T \geq 360$ GeV in 2015, $p_T \geq 420$ GeV in 2016, and leading trimmed anti-k_t $R = 1.0$ jet $p_T \geq 440$ GeV in 2017. After requiring good beam and detector conditions, the integrated luminosity corresponds to 3.2 fb^{-1} in 2015, 32.9 fb^{-1} in 2016, and 43.3 fb^{-1} in 2017.

Events with electrons or muons in $|\eta| < 2.5$ with $p_T > 25$ GeV are vetoed in order to ensure orthogonality with other diboson searches with leptons in the final state. Events are selected if they contain at least two trimmed anti-k_t $R = 1.0$ TCC jets with the leading and subleading of these being within $|\eta| < 2.0$ and having $p_T > 500$ GeV and $p_T > 200$ GeV, respectively. Their mass must be bigger than 50 GeV and their invariant mass, m_{JJ}, larger than 1.2 TeV. As described in § 5.4, the pair of jets is required to have a small separation in rapidity, $|\Delta y_{12}| < 1.2$, and a p_T asymmetry smaller than 0.15. After boson-tagging, the data is categorised in five non-exclusive signal region: events with two jets identified as WW, ZZ, and WZ, and events with two jets identified as either WZ or WW, and either WW or ZZ.

5.7.2 Background Parameterisation

As previously mentioned, this search is performed looking for a narrow resonance on the smoothly falling m_{JJ} distribution expected by the Standard Model. The background to the search is estimated empirically based on a binned maximum-likelihood fit of a parametrised form to the observed m_{JJ} spectrum. The modelling of the parametric form has been tested in a dedicated control region in data using the ABCD-like method. Four different orthogonal regions are obtained requiring or not events to be boson-tagged and reverting the requirement on the separation in rapidity of the two leading jets. Explicitly, region A contains events with both jets boson-tagged and $|\Delta y_{12}| > 1.2$, region B (that is the nominal signal region) contains events with both jets boson-tagged and $|\Delta y_{12}| < 1.2$, region C contains events not boson-tagged and jets with $|\Delta y_{12}| > 1.2$ and region D contains events not boson-tagged and jets with $|\Delta y_{12}| < 1.2$. Regions A and C are used to derive per-event transfer factors to go from the region D to the fit control region B. The already unblinded data-set is used to verify that the control region obtained is able to reproduce the expected background distribution in the signal region in both shape and statistics. Additional studies are performed to confirm the ability of the chosen background fit function to describe the expected di-jet mass spectra in the five signal regions.

5.7.3 Systematic Uncertainties

The uncertainty on the background modelling is directly taken from the errors on the fit parameters of the background estimation. It reaches values up to 40%.

Signal Monte Carlo samples, over the search region $1.2 < m_{JJ} < 5.0$ TeV, are used to evaluate systematic uncertainties arising from detector effects and Monte Carlo mis-modelling on the expected signal yield and shapes. Uncertainties due to the large-R jet calibrations affect the large-R jet p_T, mass and D_2.

- One important effect is due to the uncertainty on the jet p_T scale, that shifts the expected signal mass spectrum, in particular the peak of the resonance, and thus affects the significance of an

excess if observed. It is evaluated measuring the track-to-calorimeter double ratio between data and Monte Carlo. For TCC jets, the total p_T of the jet is derived from calorimeter information and is independent of the track-based jet p_T. Since the jet p_T scale uncertainty is not limiting the sensitivity of this search, the correlation between calorimeter p_T and track-based p_T is not studied explicitly. Instead, the obtained uncertainties is increased by a conservative factor of two to cover any correlation between the two observables. Additional uncertainties due to the track reconstruction efficiency, track impact parameter resolution, track fake rate are taken into account. The size of the total jet p_T scale uncertainty varies with jet p_T and is between 5% and 10% for the full mass range.

- Uncertainties in the measurement of the jet p_T resolution would lead to a mis-measurement of the width of any observed signal and affect the signal selection efficiency. It is evaluated event-by-event by rerunning the analysis applying a Gaussian smearing on the input jet p_T. The width of the Gaussian is an absolute 2% per jet and is symmetrised.

- The boson tagging efficiency is affected by the uncertainty in the jet mass scale and resolution. The selection efficiency is also affected by any uncertainty on the value of the boson tagging discriminant D_2. The overall yield obtained after boson tagging is corrected using the scale factor on the W/Z-tagging efficiency evaluated in § 5.5. The uncertainty on the scale factor is also assigned as a two-sided variation on the yields. The uncertainty on the tagging efficiency is measured to be of the order of 20% per-jet.

Other sources of uncertainty are less relevant. The uncertainty from the trigger is found to be negligible thanks to the offline requirements on the leading jet p_T and m_{JJ} that ensure the trigger to be fully efficient. Uncertainties related to the behaviour or PDFs and the choice of Monte Carlo tune depend on the signal model. A constant PDF uncertainty of 1% is applied for the RS model while the HVT model requires a pole-mass dependent uncertainty ranging from 1% to 12%. Constant 5% (3%) Monte Carlo tune uncertainty is applied for the RS (HVT) model.

5.7.4 Results

The di-jet mass distribution of the selected events in the $WZ + WW$ and $WW + ZZ$ signal regions are shown in Figure 5.11. The expected background distributions are obtained using the background-only fits to the data. The fit is performed in the range $1.2 < m_{JJ} < 6.0$ TeV. No events are observed beyond 5 TeV. In the absence of a significant excess, 95% confidence level (CL) upper limits on the production cross-section times branching ratio of the different benchmark models are set considering all the systematic uncertainties. The cross-section limits are extracted for the different benchmark models and are shown in Figure 5.12. A spin-1 vector triplet with couplings predicted by the HVT model A (B) (see § 1.2.1.2) is excluded in the range 1.20 TeV$< m(V') < 3.40$ TeV (1.20 TeV$< m(V') < 4.15$ TeV), at the 95% CL. Production of a G_{KK} in the bulk RS model (see § 1.2.1.3) is excluded in the ranges 1.20 TeV$< m(G_{KK}) < 1.90$ TeV and 2.1 TeV$< m(G_{KK}) < 2.3$ TeV, at the 95% CL.

This analysis is able to largely improve on past results mostly due to the use of novel techniques described in this thesis. Figure 5.13 shows the extrapolation of the expected limits from the previous results [28] to the current dataset size, assuming no change to the previous analysis strategy or its uncertainties. The expected limits on cross section times branching fraction would roughly improve by a factor of $\sqrt{L_{2015-2017}/L_{2015-2016}}$ for the m_{JJ} range which was not statistically limited, and $L_{2015-2017}/L_{2015-2016}$ for the high mass range where no events were observed, where L is the integrated luminosity of the respective data sets. The improvement in expected limits for the $WW + WZ$ channel

at 3 TeV (5 TeV) is about a factor two (four) larger than expected just from the increased size of the dataset.
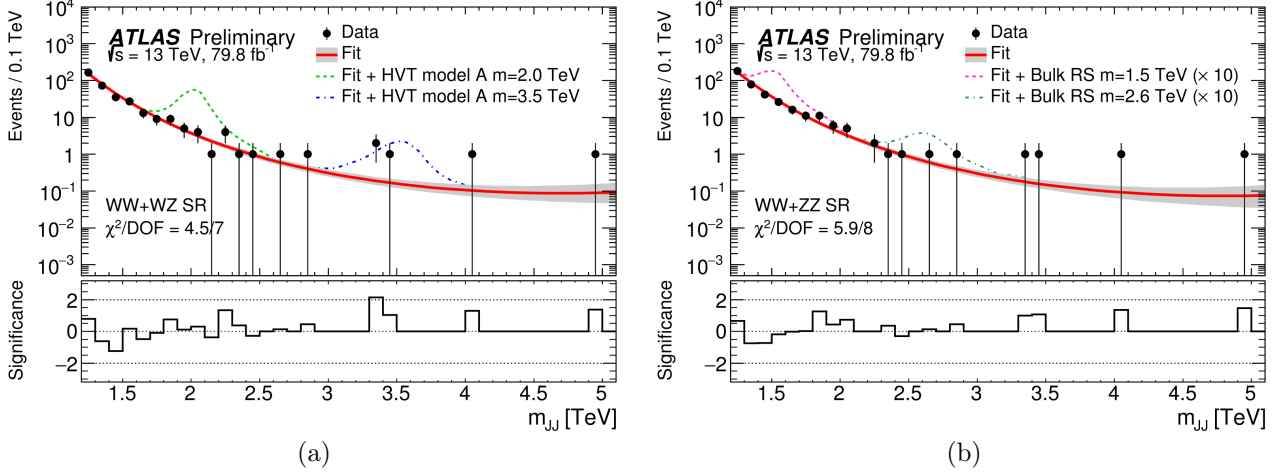
Figure 5.11: Background-only fits to the di-jet mass distributions in data after tagging in the combined (a) $WZ + WW$ and (b) $WW + ZZ$ signal region. The significance shown in the bottom plot is the difference between the data and the fit in units of the uncertainty on this difference [93].
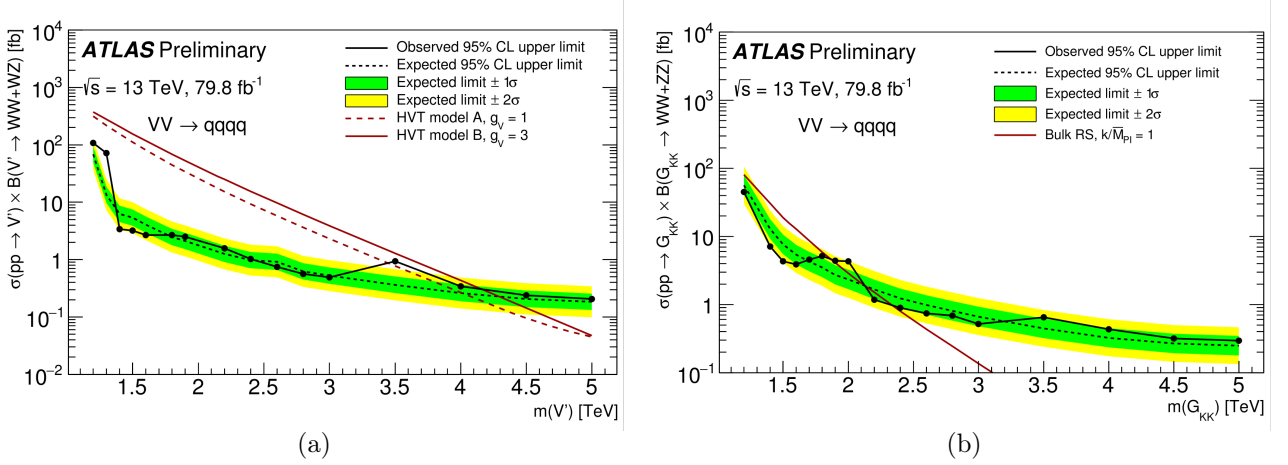
Figure 5.12: Background-only fits to the di-jet mass distributions in data after tagging in the combined (a) $WZ + WW$ and (b) $WW + ZZ$ signal region. The significance shown in the bottom plot is the difference between the data and the fit in units of the uncertainty on this difference. The plots show the observed and expected limits at 95% CL on cross section times branching ratio for (a) $WW + WZ$ production as a function of mass of the HVT V', $m(V')$, and (b) $WW + ZZ$ production as a function of the mass of the bulk RS graviton, $m(G_{KK})$ [93].
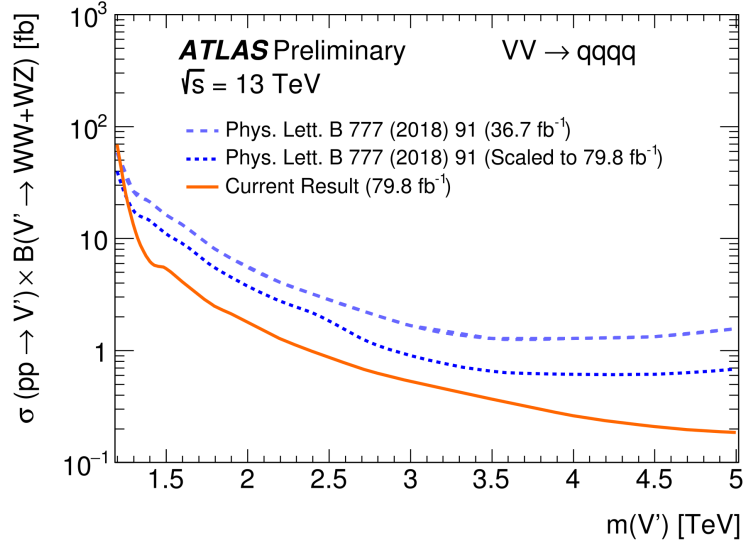
Figure 5.13: Comparison between the current and previous (Reference [28]) expected limits at 95% CL on cross section times branching ratio for $WW + WZ$ production as a function of $m(V')$. An extrapolation of the expected limits from the previous results to the current dataset size, assuming no change to the previous analysis strategy or its uncertainties, is also shown [93].

Part III

The ATLAS Tracking System Towards High-Luminosity LHC

6

The ATLAS Phase-II Inner Tracker: Motivations and Requirements

Contents

6.1 Introduction

On July 2012, the ATLAS and CMS Collaborations have announced the discovery of the Higgs boson [10, 11], resulting in a major step forward in our understanding of the universe. Beside the Higgs boson discovery, the dataset collected in the last years allowed for high precision measurement of several Standard Model parameters, such as the W-boson mass provided by the ATLAS Collaboration [98], the coupling of the Higgs boson to bottom quarks measured by the CMS Collaboration [14] and the measurement of the decay of $B_s^0 \to \mu\mu$ performed at the LHCb and CMS experiments [99, 100]. Although great progress was achieved so far in understanding the Standard Model (see Figure 1.2), the LHC experiments haven't found yet any convincing sign of physics beyond it. Moreover, considering the accelerator configuration at the beginning of 2019, i.e. before the LS2, more than 10 years will be needed to half the statistical uncertainty in the measurements and even including extrapolations to the expected number of events to be collected until the end of 2023 do not leave a large margin of sensitivity for such new findings. One way to increase sensitivity is to upgrade the accelerator to explore higher-mass ranges. However, the current dipole magnets do not allow for delivering proton-proton collisions at higher energy in the center-of-mass. The only possibility in the next decade is therefore to increase the size of the dataset by increasing the accelerator luminosity and extending the data-taking periods. This will allow to increase statistical sensitivity to new physics and further improve precision on Standard Model measurements.

Larger dataset extends the energy scales that can be studied in high energy, e.g. through boson-boson scattering, to further improve our knowledge on the electroweak symmetry breaking mechanism and to probe for signatures of new physics processes predicted by models such as supersymmetry and extra dimensions well into the multi-TeV region. Moreover, it will consent to probe rare Higgs decay and production modes to a high precision: $H \to \mu\mu$, vector boson fusion Higgs production (with $H \to \gamma\gamma$ and $H \to \tau\tau$), and associated production with a top-pair ($t\bar{t}H$ with $H \to \gamma\gamma$) or vector bosons (VH

with $H \to \gamma\gamma$ and $H \to bb$). The expected precision for the fermion coupling measurements will improve the limits on physics beyond the Standard Model that can be set from loops in, for example, $gg \to H$ and $H \to \gamma\gamma$. The full luminosity will also allow the Higgs self-coupling to be studied for the first time in channels such as $HH \to \tau\tau bb$ and $HH \to \gamma\gamma bb$. The luminosity upgrade will substantially increase the exotics discovery potential.

The first part of this document has demonstrated that the combination of the strengths of both the calorimeter and the tracker into Track-CaloCluster jets provides the most performant method currently available in ATLAS to resolve energy deposits in large-R jets, significantly improving, up to a factor two, the D_2 resolution in a wide p_T spectrum. This can be directly translated into a boost in sensitivity of the ATLAS physics program, especially in analyses where jet substructure techniques play a critical role. At the HL-LHC conditions, the usage of the tracking system information will become even more fundamental to minimise the pile-up dependence of jet substructure variables [101]. Additionally, high-p_T leptons, photons, jets, and missing E_T characterise the final states of several BSM models. It is crucial that the detector design maintains sensitivity to such signatures while improving and extending existing techniques to further expand the experiment physics reach.

One of the main requirement of the ATLAS Phase-II Upgrade Program is the complete replacement of the ID with an entirely new tracking system with equal or better performance to that provided by the current ID. It is imperative to grant high reconstruction efficiency for the different physics objects, provide good vertex definition and pile-up mitigation extending the track-to-vertex matching to the currently-uncovered very-forward region in pseudo-rapidity, improve tracking in dense environment and b-tagging performance.

The design of the ATLAS Phase-II Inner Tracker (ITk) and the evaluation of the performance of the candidate layouts are described in detail in the second part of this document.

This chapter is dedicated to the presentation of the major limitation of the current ATLAS ID and the list of performance requirements that are driving the ITk layout optimisation process, presented in § 6.2 and § 6.3, respectively. Finally, the historical overview on the evolution of the ITk layout design is described in § 6.4.

6.2   Limitations of the current ATLAS Inner Detector

The ATLAS ID was carefully designed to successfully work during the first 10 years of the ATLAS data-taking under the design LHC operating conditions: instantaneous luminosity $\mathcal{L} = 1.0 \times 10^{34}$ cm^{-2} s^{-1}, with beam crossing every 25 ns providing collisions at 14 TeV in the centre-of-mass and an average of 23 proton-proton interactions per bunch crossing. Already in 2016 the LHC design parameters have been exceeded: the instantaneous luminosity reached peak values of $\mathcal{L} = 1.37 \times 10^{34}$ cm^{-2} s^{-1}, with average pile-up of $\langle\mu\rangle = 24.9$ (see Figure 2.3) and peaks of the order of ~ 40 proton-proton interactions per bunch crossing, usually at the beginning of the run. Thanks to the choice of the detector technology and design parameters (such as segmentation, space-point precision, distribution and amount of material, occupancy) the ATLAS ID has been able to perform reasonably well despite the anticipated pile-up configuration. Nevertheless, it was not designed to meet the very stringent requirements of the Phase-II Upgrade (see § 2.3): while proton-proton collisions will be still happening every 25 ns at 14 TeV in the centre-of-mass, the instantaneous luminosity will reach $\mathcal{L} = 7.5 \times 10^{34}$ cm^{-2} s^{-1} (after levelling), $\langle\mu\rangle = 200$ and an integrated luminosity 4000 fb^{-1}.

The current pixel detector has been constructed using radiation-hard sensors and electronics able to resist up to an integrated luminosity of 400 fb^{-1} that will be collected until the end of 2023. The IBL itself was designed to operate up to an integrated luminosity of 850 fb^{-1}. At the same time, the SCT will be able to withstand an integrated luminosity of 700 fb^{-1}. Above these values, the detector will

start to experience performance degradation: pattern recognition will suffer because of the reduced hit efficiency while the progressive increment of the leakage current will put a strain on the cooling system and power supplies.

For what concerns the software, the foreseen increase in pile-up will strongly affect the track reconstruction: the additional hits will make the events more chaotic resulting in a very challenging environment for pattern recognition and track-finding. Moreover, the granularity of the current SCT and TRT sub-detectors will not be sufficient to resolve close-by particles in the jet cores, which would limit the HL-LHC physics reach.

The front-end electronics of both pixel and SCT sub-detectors have been designed to accommodate occupancies produced by up to 50 pile-up events [62]. Limitation in the buffers and in the links between the front-end chips and the read-out drivers will lead to major data losses above $\mathcal{L} \sim 3.0 \times 10^{34}$ cm^{-2} s^{-1}.

The limitations listed above make clear the need of the complete replacement of the ATLAS tracking system to deliver equal or better tracking performance to that provided by the current ID during the present data-taking, even with the more severe HL-LHC conditions.

6.3 Performance Requirements of the ATLAS Phase-II Inner Tracker

As explained in the ATLAS Phase-II Letter of Intent [62], performance requirements of the ITk are justified by the physics program of Phase-II and are driving the layout optimisation process of the future tracker described in Chapter 7. Of course, the main requirement is not to degrade the tracking performance with respect to the current ATLAS ID despite the very challenging pile-up scenario.

The general performance requirements for the future tracking system are listed below and will be developed in the next chapter where the layout optimisation process is described.

Pseudo-rapidity Acceptance – One of the key characteristic of the ITk layout is the possibility to reconstruct tracks from the primary vertex with pseudo-rapidity values up to $|\eta| = 4.0$. The extended tracking acceptance, compared to the current ID, has been already shown to be beneficial [58,62,102] since it improves the performance in track-to-vertex association, E_T^{miss} resolution, pile-up jet rejection. As an example, the acceptance for the VBF channel $H \rightarrow WW \rightarrow l\nu l\nu$ improves by a factor two with respect to tracking in $|\eta| = 2.0$ [103].

Amount of Material – One of the crucial points of the layout definition is how the material is distributed and where it is located within the tracking-system volume. This indeed affects the detector reconstruction performance for pions, electrons and photons, influencing as well the reconstruction efficiency, the momentum resolution and the amount of fake tracks reconstructed. Moreover, the amount of material affects as well the calorimetry performance and the minimisation of the non-active services is one of the main requirements especially at higher values in pseudo-rapidity. For the ITk the goal will be to provide $< 2.5\% \ X_0$ per pixel layer including services and support structures. A further reduction is particularly welcome for the innermost system.

Hermeticity – To maintain pattern recognition capabilities in a high pile-up environment and to allow for robustness against limited detector defects, the ITk layout is required to provide at least 13 hits over the full pseudo-rapidity range for all tracks with transverse momenta above 1 GeV originating from primary vertices in ±150 mm along the beam direction and in ±2 mm along the radial direction. In the following chapters, layout concepts that fulfil this requirements are referred as "hermetic".

Detector Occupancy and System Redundancy – The detector layout is required to have an occupancy level that doesn't undermine the pattern recognition. Based on the experience with the current ATLAS ID, the occupancy is required to be less than 1% in the strips and 0.1% for pixels. Moreover, the layout has to provide enough redundancy so that the pattern recognition and tracking performance are not compromised in case of inactive modules and/or inactive channels in the detector volume. Typical values of module and channel inefficiencies of 10% are then taken into account.

Track Reconstruction Efficiency and Fake Rate – The future inner tracker has to reconstruct different types of charged particles with high efficiency and low fake rate up to 200 proton-proton interactions per bunch crossing. Muons provide the optimal track reconstruction efficiency: they indeed are minimum ionising particles, don't interact strongly with the detector material and, because of the relatively higher mass, they radiate less than electrons. The muon track reconstruction efficiency is therefore required to be close to 100% for all pile-up scenarios, with an expected degradation of the order of few percent for low transverse momenta ($p_\mathrm{T} \sim$ 1 GeV) at 200 overlaid pile-up events. For other types of particles, such as pions and electrons, the track reconstruction efficiency is limited by the amount of material in the detector volume. It is anyway required to be as high and stable as possible when increasing pile-up. Both electrons and pions, with respectively $p_T > 5$ GeV and $p_T > 1$ GeV, have to achieve a track reconstruction efficiency $> 90\%$ within $|\eta| \leq 1.0$ and $> 85\%$ in $1.0 < |\eta| < 2.7$.
The new tracking detector has to be able to reconstruct tracks in the core of very energetic jets very efficiently: this can be achieved if the detector has good resolution to resolve close-by tracks. Very low inefficiency is required when reconstructing tracks within a jet ($\sim 1\%$): it should not increase by more than 5%(10%) moving towards the jet axis for light (b-)jets.

Track Resolution – When reconstructing the trajectories of charged particles it is important to measure the track parameters with good precision to associate the reconstructed track to the correct vertex. The transverse and the longitudinal impact parameters (d_0, z_0) give information of the point of origin of the track while the measurement of signed particle momentum enables to derive the electrical charge, the transverse momentum component p_T and the polar and azimuthal angles (θ, ϕ). Performance requirements for the track parameter resolutions are listed in Table 6.1 and Table 6.2.
The rate of charge misidentification is required to be smaller than 0.5% (10%) for muons with $p_\mathrm{T} = 500$ GeV ($p_\mathrm{T} = 2$ TeV) while the fraction of tracks with an estimated transverse momentum $|p_\mathrm{T}^\mathrm{reco} - p_\mathrm{T}^\mathrm{true}|/p_\mathrm{T}^\mathrm{true} > 0.5$ has to stay below a rate of 1% over the entire detector coverage for particles following the p_T-spectrum of the underlying minimum-bias events.

b-Tagging, Vertex Reconstruction and Photon Conversion – Even in presence of 200 overlaid pile-up events, the performance for the reconstruction and identification of the primary vertex is required to be compatible with the current one, providing high efficiency in associating the reconstructed objects (muons, electrons, tracks in high-p_T jets) to the correct reconstructed vertex. In the case of top pairs production events the probability to reconstruct the $t\bar{t}$ vertex has to be larger than 0.95. In addition, the probability of $t\bar{t}$-decay charged particles being associated to the correct reconstructed vertex should be larger than 0.90.
Good efficiency, at least as the one corresponding to the current detector, is also required for the reconstruction and identification of b-jets, maximising at the same time the rejection of light jets, as well as for the reconstruction of electrons from photon conversions in the entire detector volume.

Track Parameter	Required Values	η Range
Inverse Transverse Momentum		
$\sigma(q/p_{\mathrm{T}})(p_{\mathrm{T}} = 1 \text{ GeV})$	$< 0.15 \text{ TeV}^{-1}$	$|\eta| < 2.0$
$\sigma(q/p_{\mathrm{T}})(p_{\mathrm{T}} = 10 \text{ GeV})$	$< 0.15 \text{ TeV}^{-1}$	$|\eta| < 2.0$
$\sigma(q/p_{\mathrm{T}})(\infty)$	$< 0.3 \text{ TeV}^{-1}$	$|\eta| < 2.0$
Transverse Impact Parameter		
$\sigma(d_0)(p_{\mathrm{T}} = 1 \text{ GeV})$	$< 100 \ \mu\text{m}$	$|\eta| < 0.5$
$\sigma(d_0)(\infty)$	$< 8 \ \mu\text{m}$	$|\eta| < 0.5$
Longitudinal Impact Parameter		
$\sigma(z_0)(p_{\mathrm{T}} = 1 \text{ GeV})$	$< 100 \ \mu\text{m}$	$|\eta| < 0.5$
$\sigma(z_0)(\infty)$	$< 50 \ \mu\text{m}$	$|\eta| < 0.5$

Table 6.1: Required ITk track parameter resolutions in presence of 200 overlaid pile-up events.

Accuracy of centroid position	$\eta = 0.0$	$|\eta| \sim 2.5$
$\sigma(\eta)$	0.2×10^{-3}	0.35×10^{-3}
$\sigma(\phi)$	0.4×10^{-3}	0.7×10^{-3}

Table 6.2: The precision achievable for the reconstruction of the centroid of electromagnetic clusters using track extrapolation.

Sensor granularity, distribution of layers and disks both in the pixel and strip sub-detectors, material amount and distribution, minimum number of hits and maximum number of holes[1] and many other parameters need optimisation to best fulfil the requirements listed above. For this reason an accurate and careful optimisation process of the candidate layouts has been in place whose outcome provided the basis for the decision of the layout presented in the Phase-II Strip and Pixel Technical Design Reports (TDRs) [58, 104].

6.4   From the Letter-of-Intent to the ITk layouts

The ITk layout design process started from the ATLAS Phase-II Letter of Intent (LoI) proposal [62]. In there, an all-silicon-detector tracker is proposed composed of four pixel and five strip barrel layers (three with shorter strips and two with longer ones) and sets of pixel and strip end-caps disks covering up to $|\eta| = 2.7$. As shown in Figure 6.1 the LoI Strip detector hosts as well a so-called "stub" layer to maintain the coverage and avoid performance degradation in the strip barrel to end-cap transition region ($1.0 < |\eta| < 1.1$).

Since the LoI, studies have shown that the physics program is significantly enhanced with an increased pseudo-rapidity coverage. A further evolution of the LoI layout was therefore presented in the ATLAS Phase-II Scoping Document [102], extending the tracking capability up to $|\eta| = 4.0$ (see Figure 6.2). In order to extend the tracking coverage, the LoI included more pixel disks in the end-cap region giving birth to its very-forward extension, referred as LoI-VF layout. The exact pseudo-rapidity cut-off was defined taking into account the combined effects of the decreased magnetic field at large z and small radius and the effects of increased material due to services located in front of the calorimeter. In particular, additional material at high pseudo-rapidity has to be carefully monitored, since it degrades

---

[1] A hole is an intersection of the predicted particle's trajectory with an active sensor element from which no measurement is assigned to the track (inactive sensors are not taken into account).
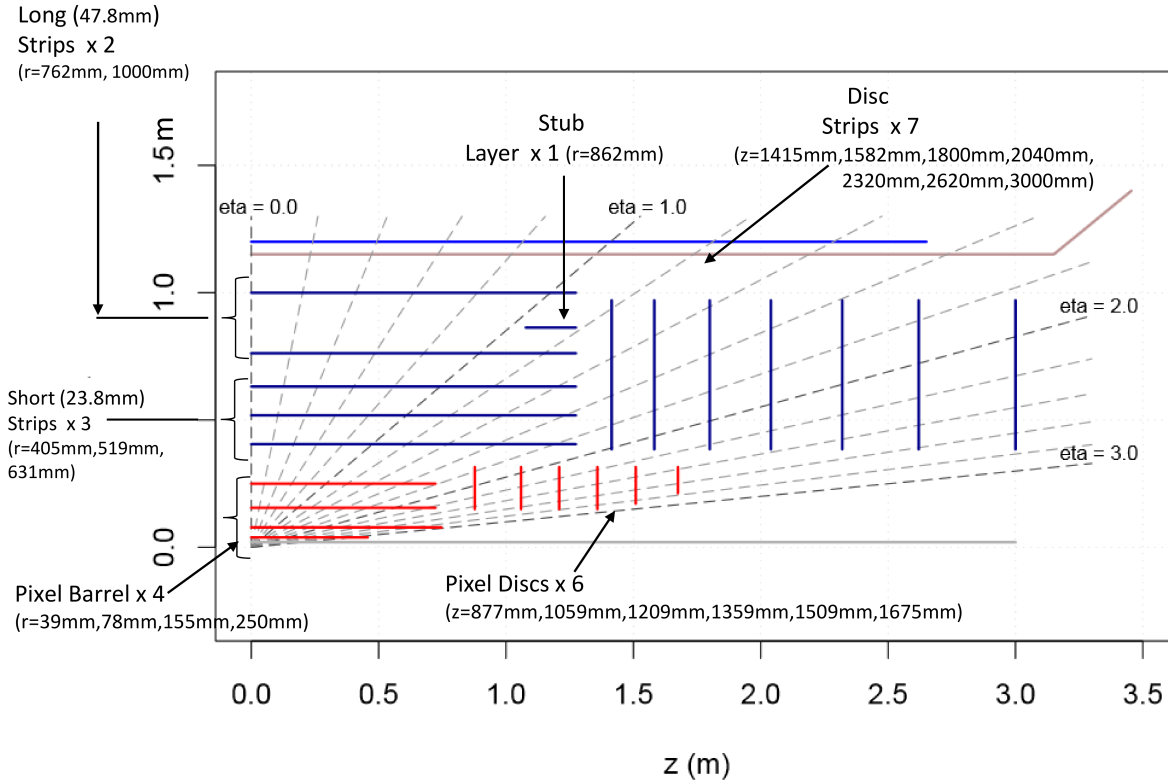
Figure 6.1: The LoI baseline layout showing the coverage of the pixel (red) and strip detectors (blue). The tracking system covers up to $|\eta| = 2.7$ and matches the coverage of the muon system. The blue line outside the ITk volume represents the coil of the solenoid magnet.

the resolution of the forward calorimetry, increases the flux of secondary particles into the forward regions of the ITk, which in turn increases the neutron fluence throughout the tracker volume.

Recently, an optimisation process has been ongoing to review the general requirements for the ITk layout to further optimise the pixel and the strip layouts beyond the LoI and the LoI-VF designs. Several variations have been examined, including detailed engineering considerations for the local, global supports and services.

During the optimization of the ITk layouts, different aspects have been considered: tracking performance and its ultimate effect on the ATLAS physics reach, impact on other sub-systems, detector buildability, mechanics properties, etc. Such a complex problematic, with heterogeneous inputs, cannot be trivially put into a simple metric that ranks different design concepts accordingly. For this reason, a process has been defined to study and illustrate the list of strengths and potential weaknesses with different approaches towards a better and robust understanding of the layout choices and features to guide the community towards a final ITk layout.

This entire process builds the next part of this PhD thesis and will be described in the following chapters. Its outcome laid the groundwork for the ITk layout design described in the ITk Pixel and Strip TDRs [58, 104].

The next chapter gives a description of the ITk candidate layouts and their optimisation. It is followed by an immersion in the software environment needed to implement and study them.
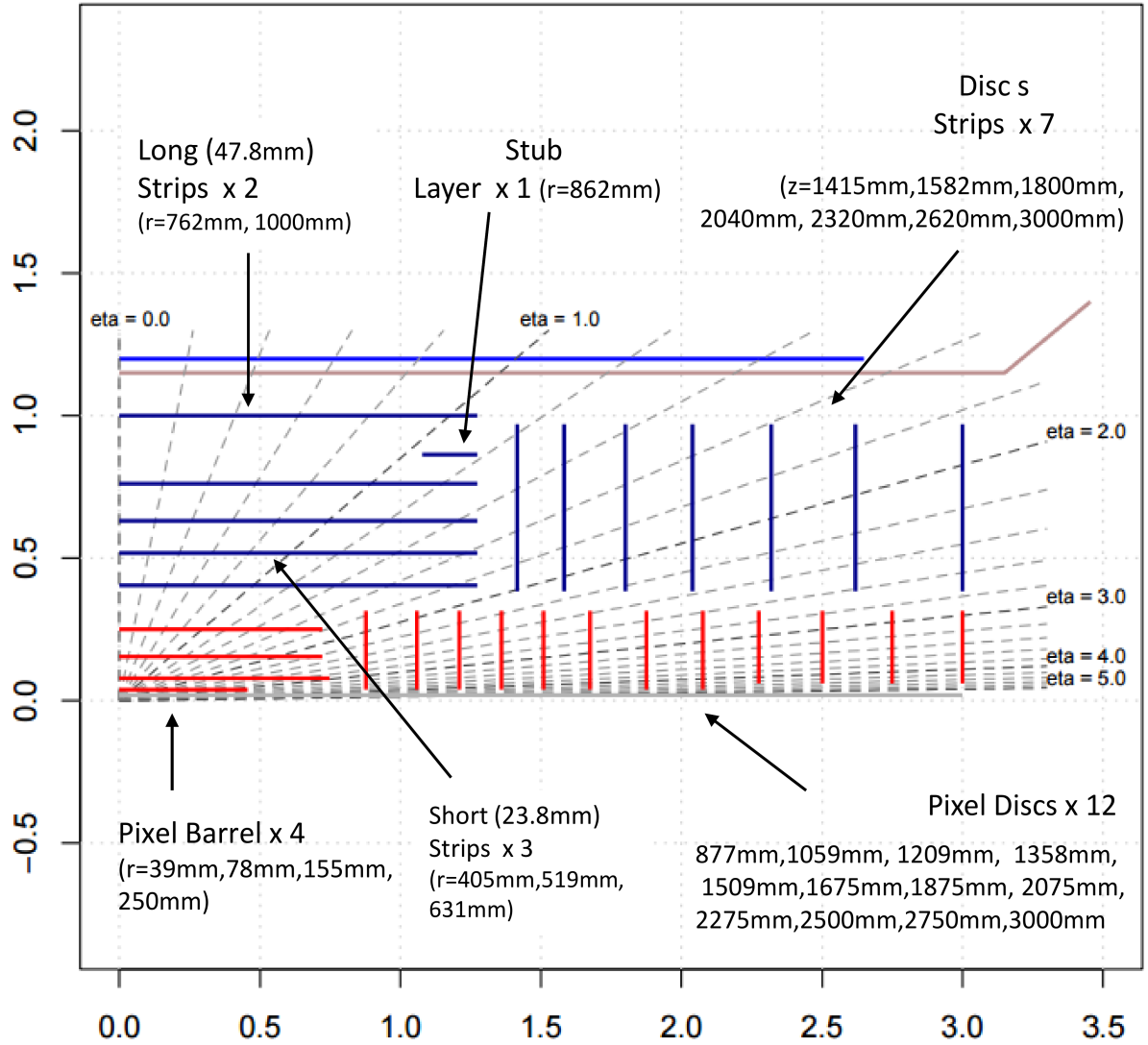
Figure 6.2: The LoI-VF layout showing the coverage of the pixel (red) and strip detectors (blue). The tracking system covers up to $|\eta| = 4.0$. The blue line outside the ITk volume represents the coil of the solenoid magnet.

7 Optimisation process of the ATLAS ITk Layout

7.1 Overview on the Layout Optimisation Process

The design process for the ITk layout started few years ago and followed the list of requirements documented in § 6.3. The main parameters underpinning the optimisation procedure were: extended η coverage, hermeticity, system redundancy, amount of material in the tracking volume, impact parameter and momentum resolutions as well as track reconstruction efficiency and fake rate. The general idea was to derive a robust tracking system which will provide excellent performance even in presence of 200 overlaid pile-up events.

The optimisation process has progressed in multiple steps during which specific software and routines allowed the evaluation of the performance of the proposed layout candidates.

At a first stage, performance estimates have been performed using the semi-analytical IdRes program [105] which allows for a quick evaluation of track resolutions and hit statistics of the layouts. The inputs to this tool are sensor resolutions, positions and material as well as rough estimates of inactive material for services and supports. Processing these inputs, the program derives the main effects they have on momentum and impact parameter resolutions. However, IdRes fails to accurately

describe efficiencies, details about layout hermeticity (e.g. module overlapping regions) and has no concept about the effects from pile-up and dense environments.

A more realistic but still fast simulation of the layouts is obtained using a fast track extrapolation engine based on the ATLAS fast tracker simulation, FATRAS [106]. Thanks to the more detailed geometry description, accurate studies on coverage, hermeticity and system redundancy can be performed. Results obtained with this tool are shown in Chapter 9.

Finally, using the GEANT4 [107] tool kit, embedded in the ATLAS full simulation software, the layout can be described with extreme accuracy. The usage of the ATLAS full simulation framework provide a deeper and more complete understanding of the layout performance, including effects from pile-up, which allows for further fine-tuning towards the ITk design proposal as presented in the two ITk TDRs [58, 104].

This chapter will mainly focus on the first step of the optimisation process. It will develop as follows: § 7.2 provides details on the general characteristic of the ITk layout and its differences with respect to the LoI design; the detailed description and the optimisation procedure of the Strip and Pixel detector layouts are given in § 7.3 and § 7.4, respectively; § 7.5 provides an overview on the layout variations.

7.2 General Layout Characteristics

The starting point for the optimisation of the ITk layout was the LoI detector design presented in [62]. At the time the LoI layout was defined, some general decision regarding the pixel and strip volumes and envelopes needed to be taken. The same geometrical constraints apply as well on the most recent evolutions of the LoI layout.

In general, the tracker has to fit in the current ATLAS tracking volume, including the space occupied nowadays by the TRT (see § 2.2.3.6). For this reason, the nominal radius of the outer strip barrel layer has to take into account the radius of the cryostat bore, services, moderator and clearance needed for the insertion. Similarly, the longitudinal extension is limited by the position of the end-cap electromagnetic calorimeters (EMEC, see § 2.2.4.1). The innermost radius is defined by the beam pipe envelope. Given the available knowledge on the HL-LHC conditions, the outer radius of the beam pipe is set to 33 mm, determining a minimum radius for the innermost pixel layer of 39 mm when taking into account the needed clearance for the insertion[1]. Figure 7.1 shows the distribution of ITk layers and disks in the available space and compares it to the current ATLAS ID using the same scale.

The Pixel Support Tube (PST, inner envelope at $r_{\mathrm{PST}} = 345$ mm) separates the pixel from the strip detector, while the Inner Support Tube (IST, inner envelope at $r_{\mathrm{IST}} = 145$ mm) is situated between the second and the third pixel layers to allow the replacement of the innermost ones.

Two of the most relevant changes between the most recent layouts and the LoI layout are the number of layers and disks in the two sub-systems and the complete re-organisation of the pixel end-cap region. The system was changed to host in the same volume five pixel and four strip barrel layers; moreover, in the strip detector the barrel length was enlarged by increasing the number of barrel modules arranged longitudinally from 13 to 14, which led to a reduction of disks from seven to six on each side. The consequences on tracking performance due to these updates were evaluated using fast simulation and showed that the new configurations allowed a better control of the fakes than in the LoI layout, while maintaining similar tracking performance.

For the end-cap region, a solution based on independent rings of different sizes attached to cylindrical

---

[1]A re-use of the Run-2/3 beam pipe with an outer radius of 28.3 mm is in consideration. In this configuration, a slightly smaller radius is possible. A detailed discussion can be found in § 7.5 and § 10.2.2.2.

Figure 7.1: Distribution of ITk layers and disks (negative z values) compared to the current ATLAS ID (positive z values). The tracking volume is shown using the same scale.

supports was considered the most appropriate, being extremely flexible in terms of module positioning along the beam axis and permitting at the same time a reasonable service routing.

7.3 The Strip Layout

7.3.1 Description of the Strip Layout

The ITk strip layout, presented in the ATLAS ITk Strip TDR [58], is shown in Figure 7.2. It is situated around the pixel detector with a silicon area of ~ 165 m^2. It consists of a central barrel region between $z = \pm 1.4$ m and two end-caps that extend the length of the detector to $z = \pm 3$ m. The barrel and the end-caps hold respectively four cylinders and six disks to provide optimal coverage up to ± 2.7 units of rapidity. All the modules are double sided with stereo angles implemented giving the second coordinate measurement (see § 2.2.3.5). The distance between the centres of the active sensors on the two sides of a barrel layer (end-cap disk) is 6.42 mm (15.0 mm), mainly driven by mechanical and technical constraints.

The basic mechanical building blocks of barrel and end-caps are staves and petals, respectively. They ensure mechanical rigidity, support the modules, host the common electrical, optical and cooling services and provide accurate alignment and fixation points.
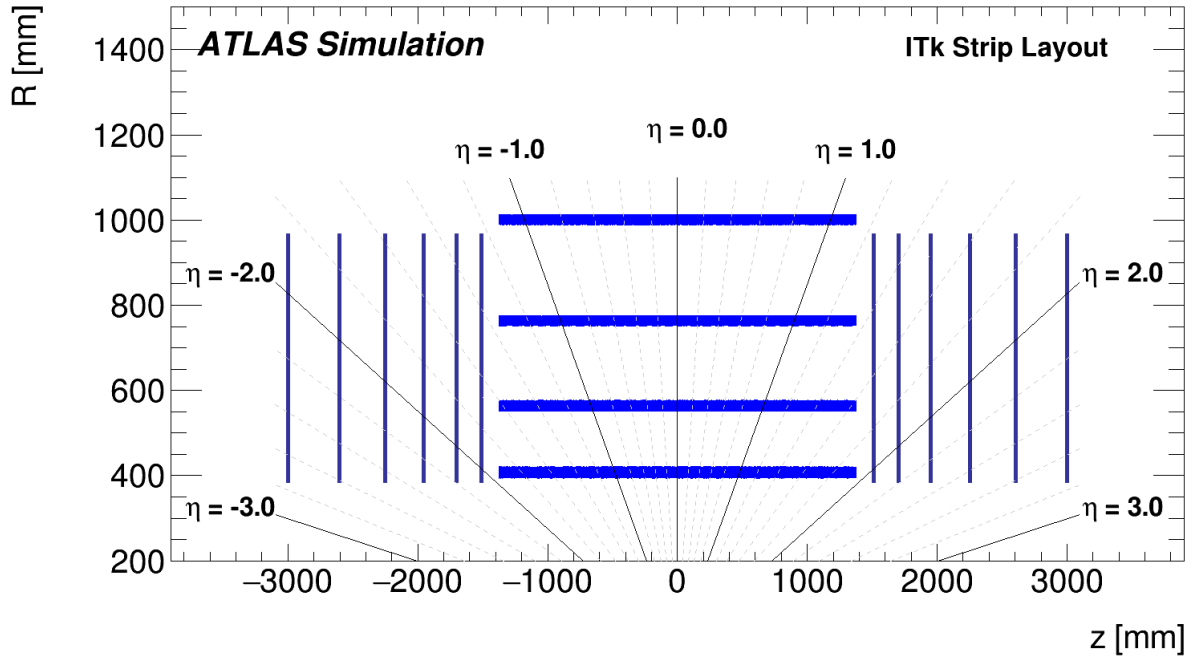
Figure 7.2: The Layout of the ITk Strip Detector. Only the upper half of the Strip Detector is shown. The horizontal axis is the axis along the beam line with zero being the interaction point [58].

An overview of the geometry with the location of the sensing elements in the strip barrel and end-cap sections is given in Table 7.1 and Table 7.2.

The two inner layers of the barrel are equipped with short strips of 24.1 mm length. The two outer layers have longer strips of 48.2 mm. All strips in the barrel section have a pitch of 75.5 μm. In the end-cap the strips are radially distributed pointing to the centre of the beam line. The strip lengths varies from 19.0 mm in the region closest to the beam axis to 60.1 mm in the outermost region to keep the strip occupancy below 1%. The strip pitch, as stated in Table 7.2, is averaged over the strip length for the wedge shaped strip segments.

The stereo angles for the barrel section and the end-caps are different in value due to technical constraints and are optimised separately for the two systems. In the barrel, a total stereo angle of 52 mrad is allowed in the barrel by tilting the strips by 26 mrad on each side of a layer with respect to the beam axis. In addition, the barrel sensors are tilted in the $R\phi$ plane to allow the overlap of neighbouring sensors to be hermetic for tracks down to $p_{\mathrm{T}} = 1$ GeV.

In the end-caps a 40 mrad stereo angle is achieved by rotating the strips by ± 20 mrad with respect to the radial orientation in each disk. Moreover the stereo angle is directly implemented in the sensor design to minimise the dead space between sensors. The result is a very peculiar sensor shape referred to as "Stereo Annulus": the outer and the inner edges are arcs of concentric circles, centred on the beam line, while the straight edges are rotated with respect to the centre of the disk to implement the needed stereo angle. Figure 7.3 shows how the sensor is designed to have the stereo angle built in. The use of the annulus needed the implementation of a new type of shape in the reconstruction set up which required a more elaborate parameterisation of the contour.

The radii at which the barrel layers are located and the z-positions of the end-cap disks are chosen to optimise the number of hits on a track and the p_{T}-resolution, as described in the next section.

Layer	Radius [mm]	Number of Staves	Sensors on 1/2 Stave	Strip Pitch [μm]	Strip Length [mm]	Tilt Angle [°]
0	405	28	14	75.5	24.1	11.5
1	562	40	14	75.5	24.1	11.0
2	762	56	14	75.5	48.2	10.0
3	1000	72	14	75.5	48.2	10.0

Table 7.1: Layout parameters for barrel region of the ITk Strip Detector. Each strip barrel layer is 2.8 m long extending from -1400 mm to +1400 mm along the z-axis [58].

Ring/Row	z-position [mm]	Inner Radius [mm]	Strip Pitch [μm]	Strip Length [mm]
0/0	1512	384.5	75.0	19.0
0/1		403.5	79.2	24.0
0/2		427.5	74.9	29.0
0/3		456.4	80.2	32.0
1/0	1702	489.8	69.9	18.1
1/1		507.9	72.9	27.1
1/2		535.0	75.6	24.1
1/3		559.1	78.6	15.1
2/0	1952	575.6	75.7	30.8
2/1		606.4	79.8	30.8
3/0	2252	638.6	71.1	32.2
3/1		670.8	74.3	26.2
3/2		697.1	77.5	26.2
3/3		723.3	80.7	32.2
4/0	2602	756.9	75.0	54.6
4/1		811.5	80.3	54.6
5/0	3000	867.5	76.2	40.2
5/1		907.6	80.5	60.2

Table 7.2: Main layout parameters for the strip end-cap disks. The "Rows" are counted from the innermost position to larger radii. A number of rows is then grouped into a "Ring" as they are combined in sensors [58].

(a)

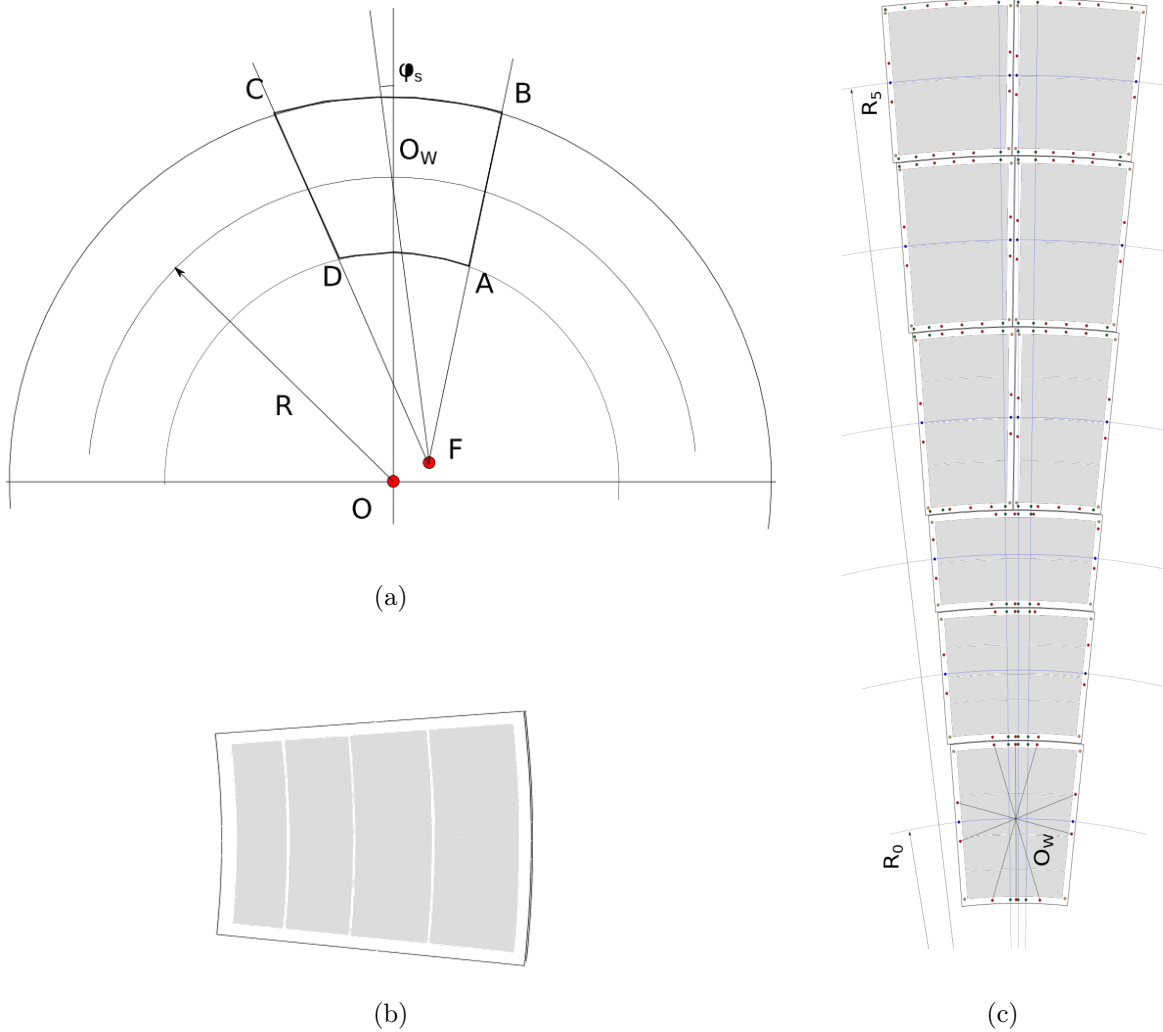(b)   (c)

Figure 7.3: (a) Sketch showing the Stereo Annulus sensor geometry: ABCD delimitate the sensor with the arcs CB and DA centred at the centre of the beam pipe O. The implementation of the stereo angle moves the strips to point to F which is slightly displaced from O. (b) A drawing of one of the sensor on a etal (Ring 0). (c) Modules assembled on a petal. [58].

7.3.2 Optimisation of the Strip Layout

The strip layout has been optimised first with respect to the pixel layout following two main considerations: to provide a tracker with the best possible momentum resolution and to extend as much as possible the barrel section, being the most interesting region for physics at LHC. These considerations have been developed as follows:

- Benefiting from the best momentum resolution translates into maximising the track lever arm (see Equation 2.12), and hence moving the last hit as far out as possible in the solenoidal magnitic field. Here the major constraints are geometrical: the polymoderator in front of the cryostat bore limits the radius of the outermost layer in the barrel, set at $r = 1000$ mm; the last strip disk can be placed at ± 3000 mm giving the position of the EMEC; the outer radius is limited by the space for the polymoderator, the end-cap support and service routing as well as by the additional space for the routing of the barrel services. The number of strip disks has been decided to maximally benefit from the lever arm in between the barrel and the last disk taking into account the total barrel length, the additional cost for more strip disks and the effect of more hits and more material on the overall tracking performance. The innermost barrel layer is placed as close as possible to the PST, at 405 mm in radius, to correspond in coverage to the last strip disks position at $z = \pm 3000$ mm.

- Most of the interesting physics at the LHC are s-channel processes that lead predominantly to high-p_T objects in the central part of the detector. The most problematic region for physics is therefore the transition between the barrel and the end-cap systems where the measured track length is reduced and fewer hits are produced, resulting in a poorer momentum resolution and less robust track reconstruction in general. As shown in Figure 7.1, in the current ATLAS ID the barrel/end-cap gap at the outer radius is at $|\eta| \sim 0.7$. For the ITk, preference was given to maximally extend the barrel region and profit of the longest possible barrel stave. This allowed to move the transition region further out in pseudo-rapidity, significantly extending the best tracking region for s-channel processes up to $|\eta| \sim 1.1$. As a consequence, the number of disks in each of the end-cap was fixed to 6, enough to provide the needed coverage and good momentum resolution.

- The distance between the barrel and the end-cap region is driven by engineering constraints. Services and supports have to fit in that region, allowing the first end-cap disks to sit at ± 1512 mm in z. This is causing a drop in the hit distribution as shown in Figure 7.4b, since the first disk is not providing the needed coverage when dropping out of the last barrel layer. To solve this, the LoI layout was enriched of "stub" layers (see § 6.4 and Figure 6.1). However, they were subsequently removed to reduce the layout engineering complexity. At the time these studies have been conducted, no practical solution was in place to cover the barrel/end-cap gap in the baseline layouts.

- To complete the strip layout, the remaining 2 barrel layers and the additional 4 end-cap disks have to be placed. The hermeticity requirement is now driving the placement procedure, as it couples the radius of a barrel layer to the z position of the end-cap disk that takes over the coverage when leaving the barrel layer in η. As mentioned already, hermetic coverage should be given for tracks from any primary vertex position within ± 150 mm in z. The position of the disks was calculated from the radial position of the barrel assuming $z_{vertex} = 150$ mm which represents the limiting case for tracks at positive η. This choice allows for a small additional overlap in η between the barrel and the disk top end (layers and disks are in reality extended

complex objects). Pattern recognition aspects are also taken into account: when adjacent layers and disks are placed, large distances among them are indeed avoided to not lead to harder combinatorial problems.

The procedure described returns the placement of the strip layers and disks as listed in Table 7.1 and Table 7.2. The optimised layout is shown in Figure 7.4a and the obtained strip hit distribution as a function of pseudo-rapidity η is shown is Figure 7.4b for particles with transverse momentum of 1 GeV[2]. These results are obtained using the IdRes program.

7.4 The Pixel Layout

The decision to increase to five the number of pixel layers and to explore the possibility of extending the tracker coverage to $|\eta| = 4.0$ required to develop new mechanical supports concepts, providing both an excellent central performance as well as the desired extended pseudo-rapidity coverage.

During the layout development process, the candidate layouts for the barrel region have been divided into two families: a design based on longitudinal structures (staves) oriented along the beam axis and eventually extended in z for the inner layers to provide sampling at high $|\eta|$, and an inclined design, in which modules at the end of the staves are inclined with respect to the beam axis, to reduce the track incidence angle on the sensor. For both types of layouts, the innovative stave concepts developed allow to push the material of barrel services and stave supports to larger z.

For the end-cap regions, a ring system has been designed independently of the pixel barrel layout choice.

7.4.1 Description of the Pixel Barrel Layouts

#### 7.4.1.1 The Extended Barrel Layout Concept

The *Extended* Layout evolves from a traditional pixel detector concept as currently implemented in the ATLAS detector. The barrel section is made of staves, longitudinal structures on which the modules are mounted in order to be maintained parallel to the beam direction. In addition, a tilt angle implemented in the $R - \phi$ plane allows the overlap of adjacent sensors. This design solution uses I-beam structures [62, 102] (see Figure 7.5) to support silicon modules from two adjacent layers. In these beams, the construction of each flange resembles that of a traditional stave: a titanium pipe is embedded in a foam block stiffened with a thin carbon fibre laminate which serves as bonding platform for the sensors. To create the I-beam, the two flanges are joined together through a thin carbon fibre web resulting in a structure with a greater moment of inertia and thus mechanically more stable than the equivalent individual staves. Furthermore, the web geometry leaves an internal space which could be used to route the electrical services. The height of the web can also be varied together with the width of the flanges to allow for certain design flexibility.

This novel stave concept allows to extend the structure up to 3.5-4.0 in pseudo-rapidity while traditional barrel staves extend usually up to $|\eta| = 1.5 - 2.0$. In this way, a track at large $|\eta|$ is expected to produce a long cluster on the crossed module firing an amount of pixel given by $N_{pixel} = t/(p \tan \theta) + 1$, where t is the sensor thickness, p is the pixel pitch along the beam direction and θ is the incident angle. As shown in Figure 7.6, from the long cluster we can derive the information about the impact position but also a continuous measurement along the path in the sensor, including precision measurement of the dE/dx and track direction. Using the long cluster can also be beneficial during pattern recognition:

---

[2]High tracnverse momentum tracks are in general easier to hermetically contain, as bending effects are less strong.
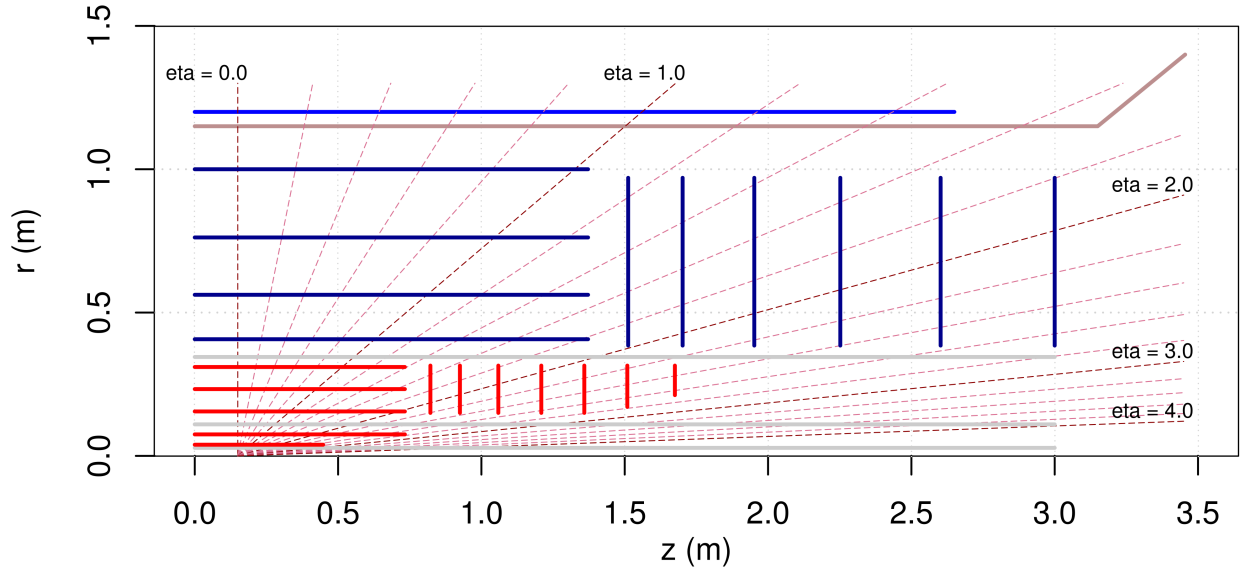
(a)
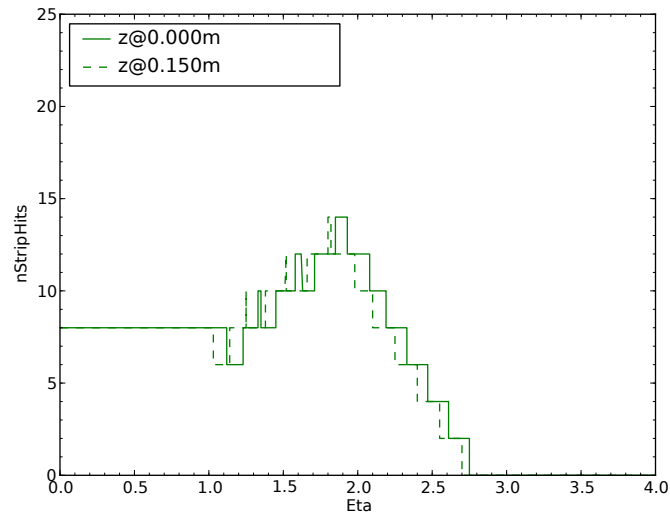
(b)

Figure 7.4: (a) Layout of the ITk strip detector. The pseudo-rapidity lines are evaluated at z_{vertex} = 150 mm. (b) Number of strip hits as a function of η for particles with p_{T} = 1 GeV and vertex position z_{vertex} = 0 mm and z_{vertex} = 150 mm. These results are obtained using the IdRes program [105].
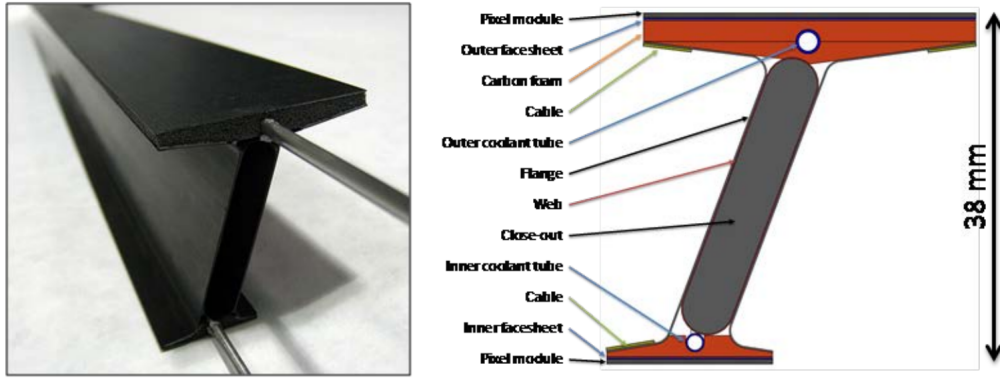
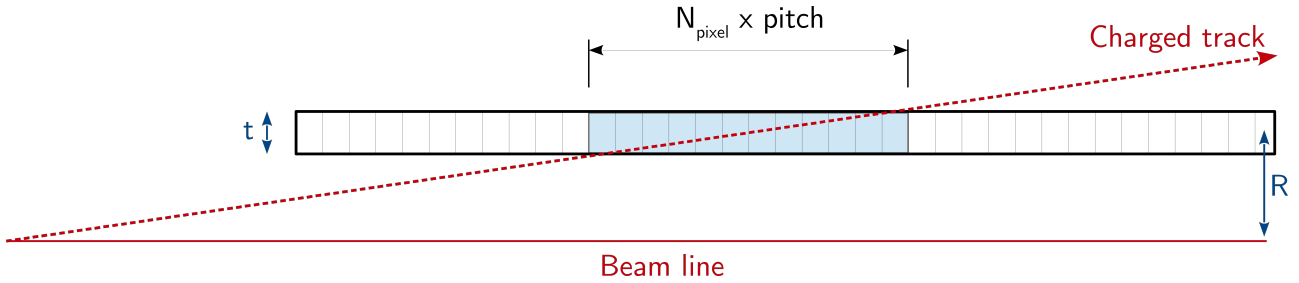Figure 7.5: I-beam concept prototype and cross-section diagram.

Figure 7.6: Use of large clusters produced by tracks at high $|\eta|$ in the *Extended* Layout. Information on the track direction can be extracted from the length of the cluster.

the entry and the exit points on the sensor are precise measurements and can provide extra information on the track direction used to reject wrong cluster assignment not compatible with it. However, other effects, such as pixel inefficiencies, signal under threshold or overlap between clusters generated by different tracks, can separate long clusters in multiple parts attenuating the advantages deriving from the extra information available. Moreover, non trivial changes were needed in order to make the current reconstruction algorithms properly work with the new layout concept. They will be discussed in § 8.2.3.

The arrangement of sensors placed horizontally with respect to the beam line has however some potential drawbacks. Most critically, this is the amount of material traversed by the particles[3], which could be particularly harmful at low momenta, and the increase in channel occupancy due to the large number of pixels crossed per track, which could lead to a saturation of the readout bandwidth, especially for the inner layer.

7.4.1.2   The Inclined Barrel Layout Concept

Alternative ideas to traditional stave designs have been investigated in the last ten years [62, 102], and converged into a second family of layouts called *Inclined*. The base concept is to maintain, as much as possible, the sensors perpendicular to the direction of the particles in order to minimise the traversed material by keeping a close to normal incident angle to each module. There are some advantages of this approach: small clusters can reduce the channel occupancy in the detector, hence the use of the

---

[3] The shallow incident angle at large η renders a thinly constructed layer as significant traversed material.

readout bandwidth, and minimise the probability of overlap between tracks. Most prominently, the material crossed by the tracks is reduced, as well as the silicon surface needed to obtain an hermetic surface at a given radius, with positive implications in terms of cost and services. In addition, an *Inclined* layout allows multiple hits per barrel layer at relatively low traversed material for the particle, reducing the impact of material in between the measurements.

The first mechanical structure to implement this solution was originally proposed by Teddy Todorov[†] in the Alpine Layout, in which modified horizontal staves are used to maintain foam blocks (machined to match the desired tilt angle) to support the silicon modules inclined with respect to the beam direction. Figure 7.7 shows a prototype of the Alpine stave structure. Recently this concept has been evolved by different mechanics groups allowing a deeper understanding of the complexity of engineering and installation. This is, indeed, one of the main disadvantages of this layout: inclined staves are mechanically more complicated than longitudinal ones, both in terms of fabrication and module loading. Furthermore, the most critical aspect is perhaps the thermal management: heat extraction capability may be reduced by the limited surface contact between the sensor support structure and the cooling pipe.

Based on the idea of the Alpine layout, another concept for the local support was conceived to accommodate tilted modules. The SLIM (A Stiff Longeron for ITk Modules) concept relies on module cells to achieve the desired thermal performance. In these cells the silicon module is supported by a pyrolytic graphite plate used as a heat spreader, which is bonded to a cooling block made of a highly conductive, light material. As shown in Figure 7.8a, each individual cell is then connected to the cooling line through a base block soldered to the titanium pipe. The cooling lines loaded with the module cells are attached to carbon composite structures known as "longerons". The truss construction of the longeron is shown in Figure 7.8b.

### 7.4.2 Description of the Pixel End-cap Ring System

At the time the LoI-VF Layout was proposed (see Figure 6.2) the extended coverage up to $|\eta| = 4.0$ was provided by a forward pixel system made of 12 disks. This resulted in an average of 20 available hits at $|\eta| > 2.0$, a large silicon surface and hence a large number of modules to compose the disks. Moreover, no detailed mechanical design or service routing considerations were taken into account [102]. In order to realistically evaluate the performance of such an extended detector coverage, a new end-cap concept based on rings of sensors instead of disks was developed. As shown in Figure 7.9, independent rings of different sizes are placed at different radii and different positions along the beam axis, providing an optimal coverage and a reduction of the required silicon area. The active elements can hereby be placed only where needed instead of building full disk structures. Indeed, the minimisation of the sensor surface is obtained preferring the extra hits to be in the inner ring layers than in the outer ring layers. Moreover, the ring design gives the possibility to create radial gaps that can be used to route the services, without compromising the detector hermeticity. The ring positions in z can also be easily adapted to the coverage needs of different barrel layouts. The concept itself is thus not dependent on the particular choice of the pixel barrel layout.

The rings have modules mounted on both faces (6 mm are considered in between the two faces), giving to each ring the needed hermeticity in $R - \phi$, and are supported by cylindrical structures, coaxial with the beam pipe, that serve as support for the services.
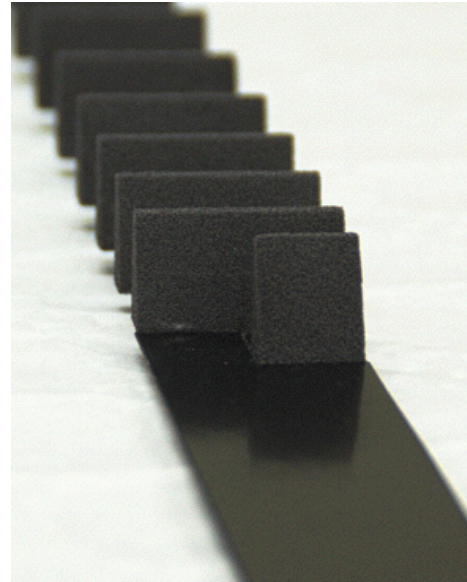
7.4.3 Optimisation of the Pixel Layouts

The smallest entity for the pixel detector is the chip. Several chips are connected together to define the different flavours of modules used. Figure 7.10 shows the pixel module sizes used simulation based
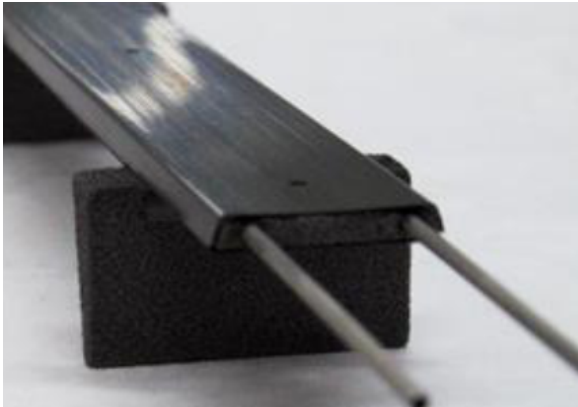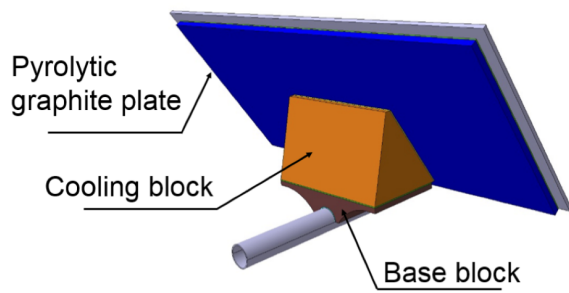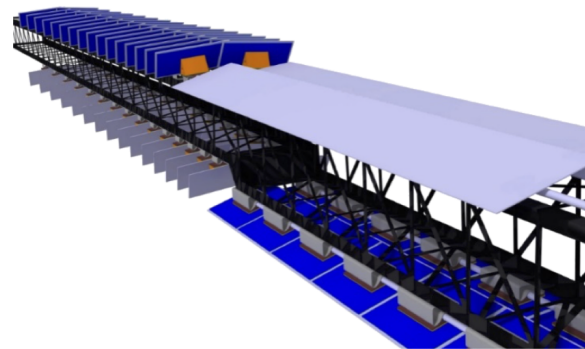
(a)

(b)

Figure 7.7: Prototype of an Alpine stave featuring several foam "mountains".

(a)

(b)

Figure 7.8: Schematic representation of (a) a tilted module cell used in the SLIM concept and (b) a typical SLIM longeron (truss construction) supporting four cooling lines.
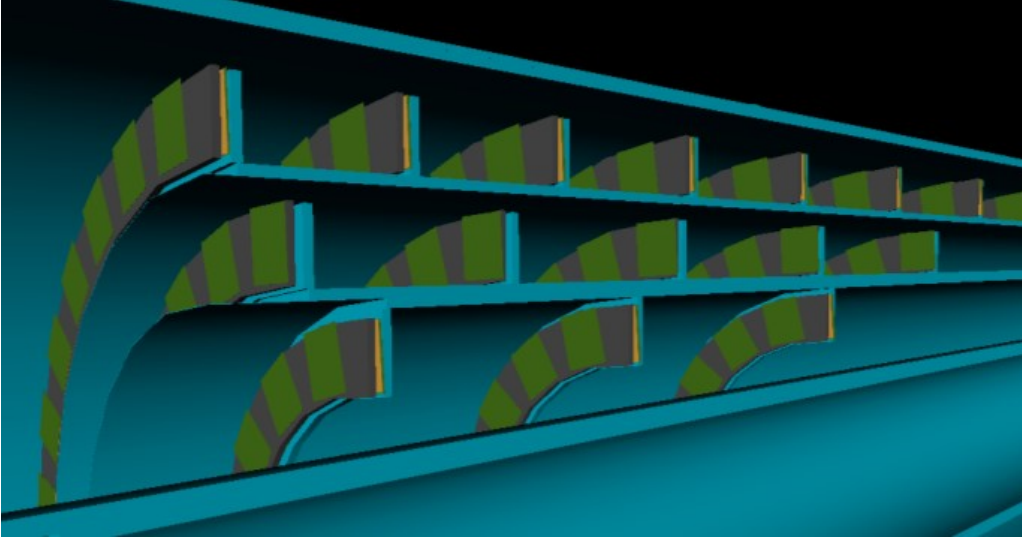
Figure 7.9: Pixel end-cap structure made of rings of different sizes attached to cylindrical support structures.

on the RD53 chip. The definition of the module size has been one of the main ingredient in the optimisation procedure of the pixel layouts. More details on the modules and their implementation will be given in § 8.2.2.

Further iterations have led to different module sizes (see § 11.2) and will not be discussed in this document.

7.4.3.1 Optimisation of the Pixel End-cap Ring System

The pixel end-cap ring system is composed of 3 ring layers corresponding to the 3 outer pixel barrel layers in between the IST and the PST and an inner ring layer placed inside the IST to reach the needed coverage up to $|\eta| = 4.0$. Each ring layer is constructed of so-called quad modules with 4 readout chips on a sensor, giving the rings a radial extent of 4.04 cm. The end-cap services are routed directly outwards along z for each layer in between the rings, while the outer barrel services run higher on the inside of the PST. Therefore, leaving enough radial space for services to run constrains the radial positions of outer pixel ring layers (see Table 7.4).

Moving to high z, it is beneficial not to put detectors too close to the beam line for various reasons, in particular for the impact any material in this region has on the radiation levels in the tracker. For the same reason it has been asked to run the barrel services outside the innermost ring layer along the IST, which allows at the same time to minimise the material in front of the forward calorimeter. As a consequence, the outer radius of this ring layer has been set to 120 mm.

Geometrical and engineering constraints define the position of the first and last rings on the layers. For the outer region, it has been decided that the maximal extension for a barrel layer is 731 mm and considering a gap of 92 mm between the last barrel module and the first end-cap ring, the first pixel ring in each end-cap layer is placed at $z = \pm 823$ mm. Similar considerations are valid for the innermost ring layer: once the radius and the half-length of the innermost barrel layer are fixed, respectively to 39 mm and 1218 mm, the latter to cover up to $|\eta| = 4.0$, the first ring of the innermost ring layer can be placed at $z = \pm 1308$ mm. As the strip disks, the last rings are placed at $z = \pm 3000$ mm at the end of the tracker volume.

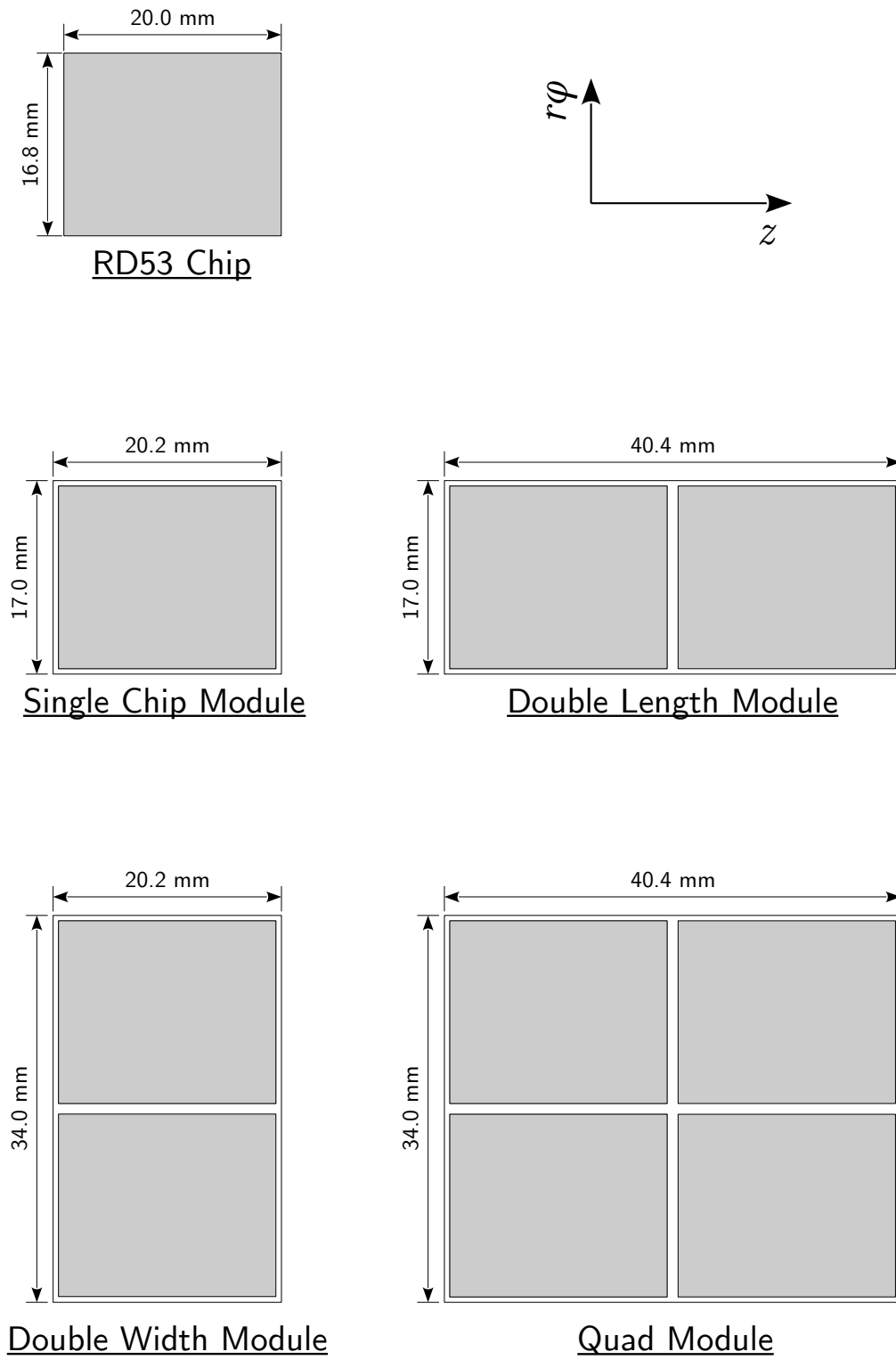The position of the remaining rings along the beam line is defined to provide an hermetic layout and is

Figure 7.10: Pixel module sizes as described in the simulation. The first row shows the RD53 chip.

strongly correlated with the choice of the barrel system as will be described in the next two sections.

7.4.3.2 Optimisation of the Extended Barrel Layout

Starting from the outer region, the design of the *Extended* Layout proceeded as follows:

- The most important engineering design constraint is the length of the stave. It should be indeed long enough to avoid lining up the barrel to end-cap transition region of the outer pixel system with the strip barrel/end-cap gap around $|\eta| \sim 1.1$. Moreover, supports and end-of-barrel services are moved as far as possible in z to extend the best tracking region. Adding to the evaluation other considerations concerning the stave stability, cooling capabilities and the required amount of services, at the time these studies were carried out, the maximal barrel stave length for the outer region was set to 731 mm.

- In order to provide a hit multiplicity bigger than 5 pixel hits at all η, the radius of the pixel barrel layer has to be adjusted to provide at least one hit either on the last barrel sensor or on the first ring sensor when the vertex is at $z_{\text{vertex}} = 150$ mm[4]. Following this criterion, the radii of the outer barrel layers are set as shown in Table 7.3. All the modules in this region are quads.

- The design of the outer pixel ring system is mainly driven by hermeticity requirements. First, in each ring layer the intermediate ring positions where chosen such that from $z_{\text{vertex}} = 150$ mm all layers are crossed, allowing for some overlaps between neighbouring rings in η. The size of the overlap is then increased to make the last ring be exactly at $z = 3000$ mm. As a result one obtains an outer pixel end-cap system with at least 3 measurements plus overlaps within its η coverage and the z-distance between neighbouring rings slowly increasing with z. In a second step, to provide the required coverage it is needed to add additional measurements into the pixel ring system whenever one additional strip disk drops out as a function of η. Since the silicon surface of the rings scale quadratically with the ring radius, it is preferable to introduce additional rings starting from the inner part.

This procedure gives an hermetic layout up to $|\eta| = 3.2$ made of an outer *Extended* barrel layout complemented with its end-cap ring system. The inner pixel system, that sits inside the IST, allows to extend the pseudo-rapidity coverage up to $|\eta| = 4.0$. Same engineering constraints and hermeticity requirements apply for its optimisation:

- The radius of the innermost pixel barrel layer has been set to $r = 39$ mm. Unlike other pixel barrel layers which are composed of quad modules introduced above, the innermost layer requires dual modules with two chips along the beam pipe and only one chip in ϕ (see Figure 7.10). With the I-beam stave, the two layers inside the IST are coupled together. An outer radius of 75 mm was then chosen, such that with dual modules and quad modules respectively for the first and the second layer, an hermetic coverage with reasonable overlaps is obtained. In order for the detector to cover up to $|\eta| = 4.0$ from vertices within ± 150 mm along the beam line with the best possible impact parameter resolution, the length of the active layers, and therefore of the staves, has to be from -1218 mm to $+1218$ mm. This extended barrel arrangement provides one precision long cluster up to $|\eta| = 4.0$ in the closest possible position to the beam line, and a second long cluster on the second layer covering up to $|\eta| = 3.4$.

- The barrel system inside the IST is accompanied by a ring layer that likewise sits inside the IST. The entire system has to provide at least 9 pixel hits for $|\eta| > 2.7$: the rings on the innermost

---

[4] $z_{\text{vertex}} = 150$ mm represents the limiting case for tracks at positive η, as already explained in § 7.3.2

Layer	Radius [mm]	Number of Staves	Sensors on 1/2 Stave	1/2 Stave Length [mm]	Sensor Size [mm^2]
0	39	16	30	1218	40.2×16.8
1	75	16	30	1218	40.2×33.8
2	155	32	18	731	40.2×33.8
3	213	44	18	731	40.2×33.8
4	271	54	18	731	40.2×33.8

Table 7.3: Layout parameters for the *Extended* Pixel Barrel Layout.

Ring Layer	Inner Radius [mm]	Sensors per Ring	Sensor Size [mm^2]	Position [mm]
0	80.0	24	40.2×33.8	1308 1391 1501 1620 1750 1830 1910 1997 2088 2188 2292 2397 2503 2618 2740 2867 3000
1	150.0	36	40.2×33.8	823 899 986 1082 1189 1308 1394 1486 1598 1685 1778 1876 1980 2090 2246 2414 2596 2793 3000
2	212.5	48	40.2×33.8	823 944 1088 1258 1349 1448 1554 1669 1794 1929 2075 2233 2404 2589 2790 3000
3	275.0	60	40.2×33.8	823 918 1027 1151 1294 1456 1642 1854 1968 2089 2217 2355 2502 2658 2825 3000

Table 7.4: Layout parameters for the Ring End-cap Layout.

row are placed along the beam line following the same procedure as outlined above contributing with 5 to 8 hits increasing with η.

Figure 7.11 shows the full ITk *Extended* Layout and the η dependence of the pixel and total hit coverage obtained using the IdRes program.
Table 7.3 summarise the main parameters of the *Extended* Layout as simulated for the studies shown in this document.The radii and the positions of the rings forming the end-cap system coupled with the *Extended* Layout are shown in Table 7.4.

### 7.4.3.3   Optimisation of the Inclined Barrel Layout

In order to allow for a fairer comparison among the two layout candidates, the *Inclined* Layout has been designed to be as similar as possible to the *Extended* Layout in terms of layer positions, not revisiting the decision about the barrel stave radii and lengths that have been determined for the *Extended* barrel. Similarly, the end-cap system derived for *Extended* Layout has been coupled to the *Inclined* Layout as well.
The optimisation procedure for the outer and inner barrel systems follows two different strategies:

- For the outer pixel barrel, inclining the sensors at the end of the staves is primarily a way to reduce the sensor surface needed. Sensors are therefore tilted on the stave as soon as the incidence angle becomes smaller after inclining the module. Fixing the tilt angle to 56° results in tilting them from $|\eta| \sim 1.1$ at $z_{\text{vertex}} = +150$ mm. The barrel-like section of the stave is set to be at the same radius as the corresponding *Extended* barrel layer while the inclined modules have their lower tip at this same radius and extend further outwards. It is required as well that the
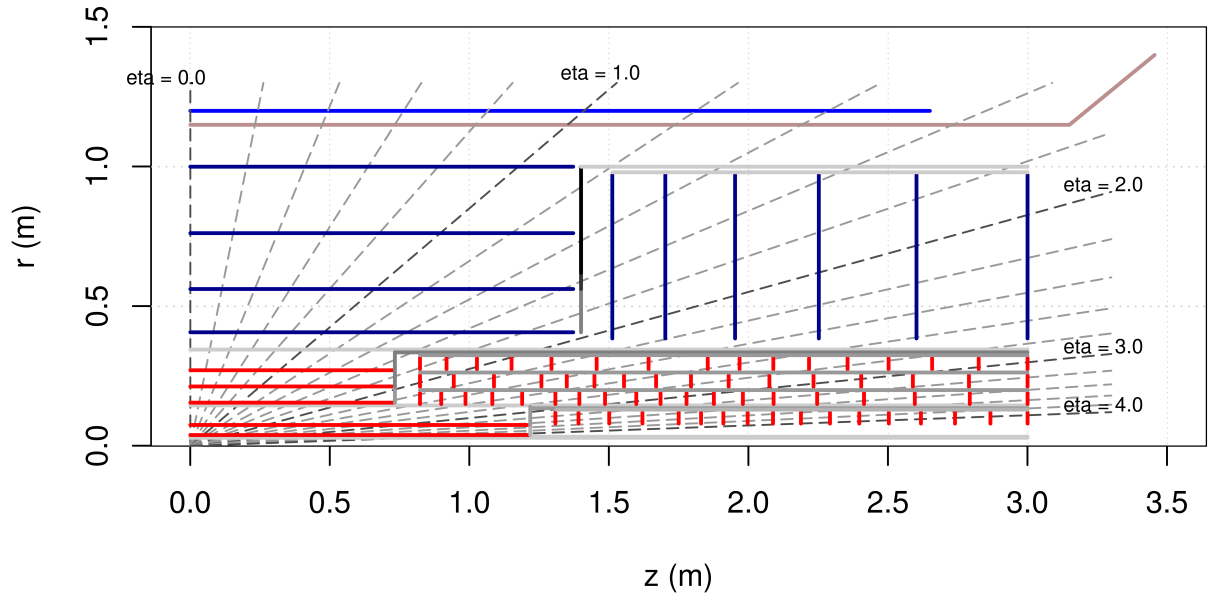
(a)
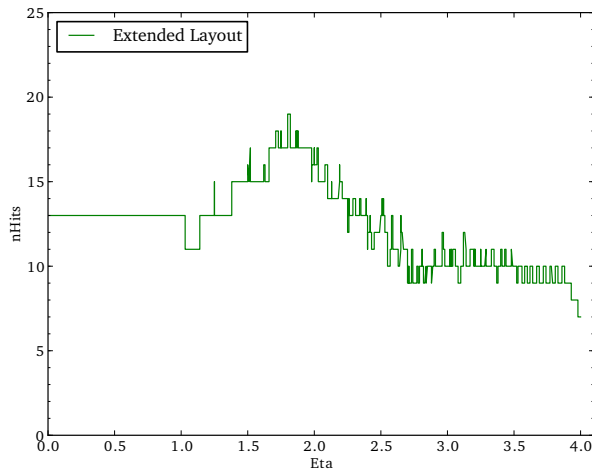
(b)
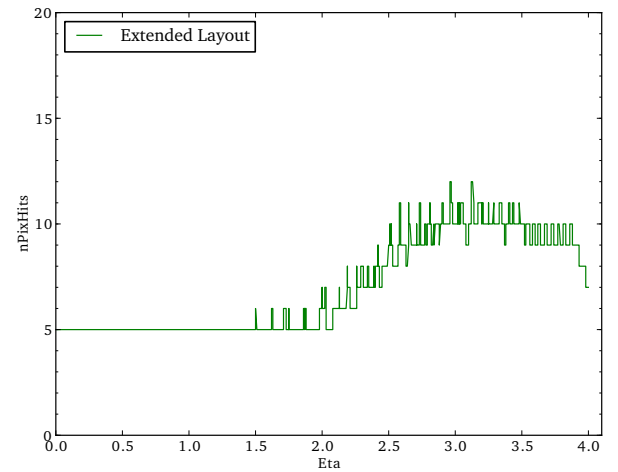
(c)

Figure 7.11: (a) Final design of the ITk *Extended* Layout. Number of (b) total hits (pixel+strip) and (c) pixel hits as a function of η are evaluated for particles with $p_\mathrm{T} = 1$ GeV and vertex position $z_\mathrm{vertex} = 150.0$ mm. These results are obtained using the IdRes program [105].
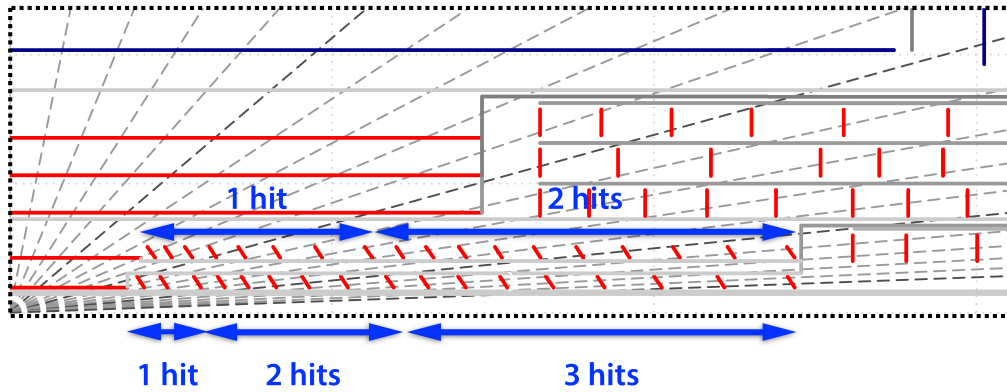
Figure 7.12: Hit arrangement for the inner barrel section of the *Inclined* Layout.

cooling lines are bent when moving from the straight to the inclined section of the stave together with moving the services outwards at the transition point. For this reason, a higher material concentration is expected which can degrade the tracking performance in the straight to inclined transition region. To mitigate this effect, a shorter extrapolation distance is required between the last hit on the flat region of the barrel and the hit on the first inclined module, i.e. before and after the material in the transition region is crossed: the first inclined module is therefore placed as close as possible to the last barrel sensor. The remaining inclined modules are placed following the same procedure as described for the ring system: the overlap in η of the inclined modules was adjusted such that the last module is placed at the end of the stave reaching the same active length as the corresponding layer in the *Extended* Layout ensuring hermeticity when moving from the barrel to the end-cap pixel region.

- While the *Extended* Layout is characterised by long clusters at small incident angles, that can be used to associate hits to track candidates (see § 8.2.3), the *Inclined* inner pixel system design aims for a detector set-up that allows for track finding with several hits close to the interaction region to improve the impact parameter resolution for forward jets, while preserving as much as possible a low overall material budget. The stave dimensions are given by the radius of the innermost barrel layer, set at 39 mm and constrained by the beam pipe, and a length driven by the requirement to cover up to $|\eta| = 4.0$. For the *Inclined* Layout the second inner layer needs to be at 85 mm, in order to ensure the hermeticity coverage from inclined sensors in this layer. The design starts requiring 1 measurement per layer, with $z_{\mathrm{vertex}} = 150$ mm, adding additional hits to increase the coverage, up to 3 measurements in the innermost layer after dropping out of the second layer in η. This arrangement allows for 3 or more measurements in the most difficult region at large η to facilitate track finding. The hit arrangement for the inner barrel section is shown in Figure 7.12.

- When coupling the *Inclined* barrel layout with the ring system optimised for the *Extended* Layout, an excess of measurements is expected in the forward region, compared to the minimum requirement of 9. Of course, the ring system can be re-optimized to remove the excess of hits from the different ring layers, while preserving at least 1 hit in each ring layer at all η covered.
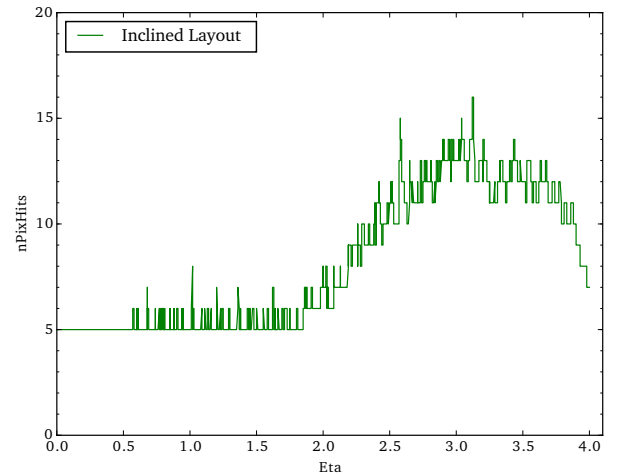
Figure 7.13a shows the full ITk *Inclined* Layout and the η dependence of the pixel and total hit coverage. The excess of hits is visible in Figure 7.13c. The main layout parameters are summarised in Table 7.5 and Table 7.6.
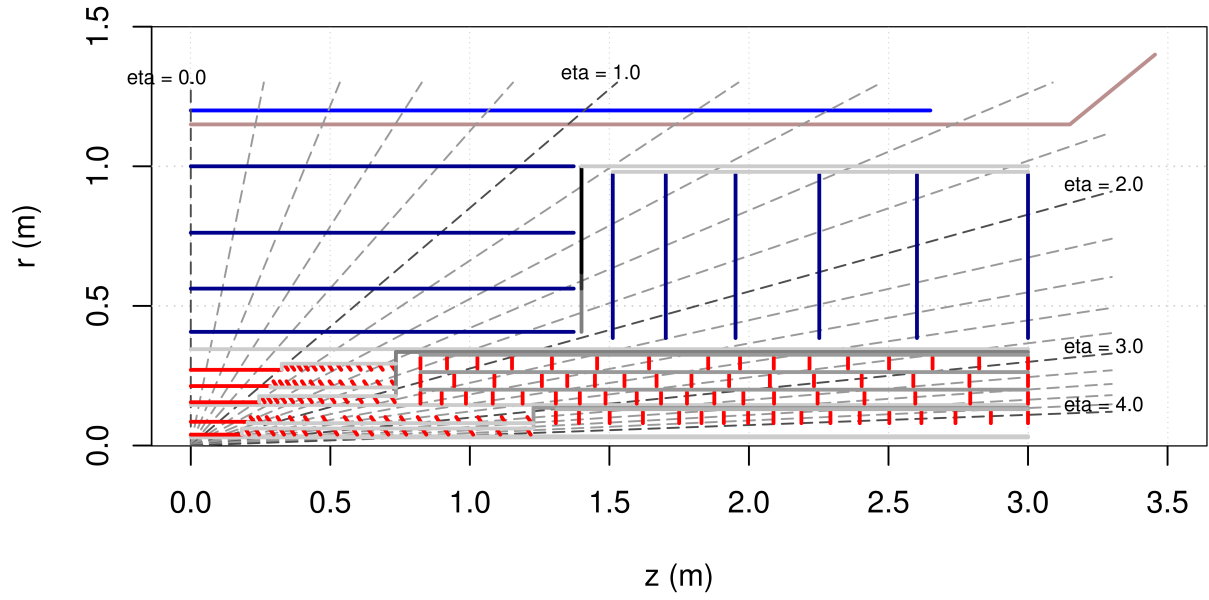
(a)
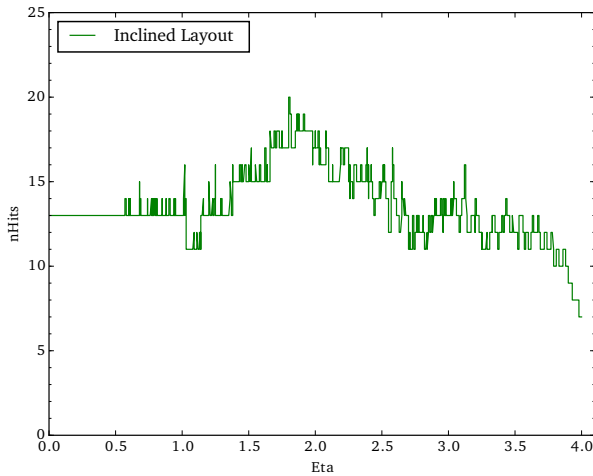
(b)

(c)

Figure 7.13: (a) Final design of the ITk *Inclined* Layout. Number of (b)) total hits (pixel+strip) and (c)) pixel hits as a function of η are evaluated for particles with $p_{\mathrm{T}} = 1$ GeV and vertex position $z_{\mathrm{vertex}} = 150.0$ mm. These results are obtained using the IdRes program [105].

Layer	Radius [mm]	Number of Staves	1/2 Stave Length [mm]	Sensors on 1/2 Stave		Sensor Size [mm²]	
				Straight Region	Inclined Region	Straight Region	Inclined Region
0	39	18	1250	4.5	17	40.2 × 16.8	20.0 × 16.8
1	85	18	1250	5	18	40.2 × 33.8	20.0 × 33.8
2	155	32	780	6	13	40.2 × 33.8	20.0 × 33.8
3	213	44	780	7	13	40.2 × 33.8	20.0 × 33.8
4	271	54	780	8	13	40.2 × 33.8	20.0 × 33.8

Table 7.5: Layout parameters for the barrel-like region of the *Inclined* Pixel Barrel Layout.

Layer	Positions of the Inclined Modules on the Stave [mm]
0	197.8 234.1 285.8 322.8 359.7 403.1 454.0 513.9 584.2 638.4 696.4 760.9 832.4 911.9 1000.2 1098.1 1206.9
1	214.4 240.7 272.2 309.9 355.1 409.2 473.9 551.5 599.9 646.5 697.3 752.7 813.0 878.8 950.5 1028.6 1113.7 1206.5
2	254.1 275.9 300.0 326.4 355.4 387.3 422.4 461.0 503.4 550.0 601.3 657.6 719.6
3	295.7 318.6 343.2 369.7 398.1 428.8 461.8 497.2 535.4 576.5 620.7 668.3 719.5
4	336.7 359.5 383.5 409.1 436.1 464.8 495.1 527.3 561.4 597.5 635.8 676.4 719.4

Table 7.6: Layout parameters for the inclined region of the *Inclined* Pixel Barrel Layout.

7.5   Overview on the layout under study

The studies presented in this document are using two main layouts, an *Extended* and an *Inclined* Layout, both of them coupled with the same pixel ring system in the end-cap and a common strip layout. For some specific studies, different flavours of the already mentioned layout have been considered.

- A special version of the *Extended* Layout, labelled *Extended@33mm*, characterised by an inner-most barrel layer lowered down at 33 mm, has been implemented to test eventual improvement deriving from the first measurement being closer to the interaction point. For this layout, the beam pipe radius is reduced accordingly: it is moved to 28.3 mm with respect to the default 32.1 mm, while keeping the same amount of material.

- Two different pixel sizes are considered: the nominal simulated pixel channel size is $50 \times 50 \ \mu\text{m}^2$, with some studies exploring an alternative size of $25 \times 100 \ \mu\text{m}^2$.

The $R - z$ hit distribution for the two main layouts is shown in Figure 7.14, while Figure 7.15 provides a zoom in their pixel detectors.
Table 7.7 and Table 7.8 are comparing respectively the pixel surface and the number of pixel modules for the different layouts. For comparison also the *Inclined* Layout with an optimized ring system (as introduced in § 7.4.3.3) is reported.
As a first result, the *Inclined* Layouts presents a reduction of the surface required: the total barrel *Inclined* surface is $\sim 30\%$ less than that of the *Extended* Layout. Anyway, a smaller total sensor surface does not immediately imply lower construction costs, because a large fraction of the pixel module cost is due to bump-bonding, which scales as the number of modules and not their area. As shown in Table 7.8, the *Inclined* Layout has a higher number of smaller modules with respect to the *Extended* Layout since modules are smaller by a factor two in the inclined region.

	Surface [m²]		
	Extended Layout	*Inclined* Layout	*Inclined* Layout with optimised ring system
Inner Barrel Straight	1.95	0.35	0.35
Inner Barrel Inclined	–	0.64	0.64
Inner Barrel Total	1.95	1.00	1.00
Inner Rings	1.11	1.11	0.98
Outer Barrel Straight	6.36	2.53	2.53
Outer Barrel Inclined	–	2.28	2.28
Outer Barrel Total	6.36	4.82	4.82
Endcap Outer Rings	6.55	6.55	4.53
Barrel Total	8.31	5.82	5.82
Endcap Rings Total	7.66	7.66	5.51
Total	15.97	13.48	11.33

Table 7.7: Summary of Pixel surface in the different layouts. The last column reports surface for the *Inclined* Layout with an optimized ring system.
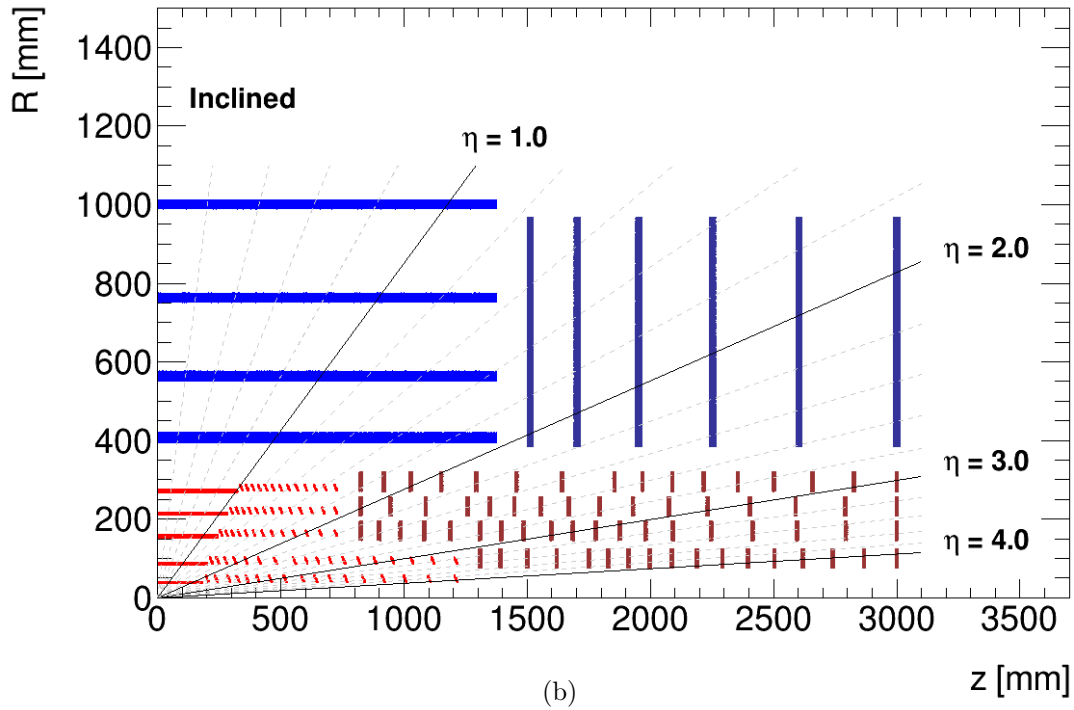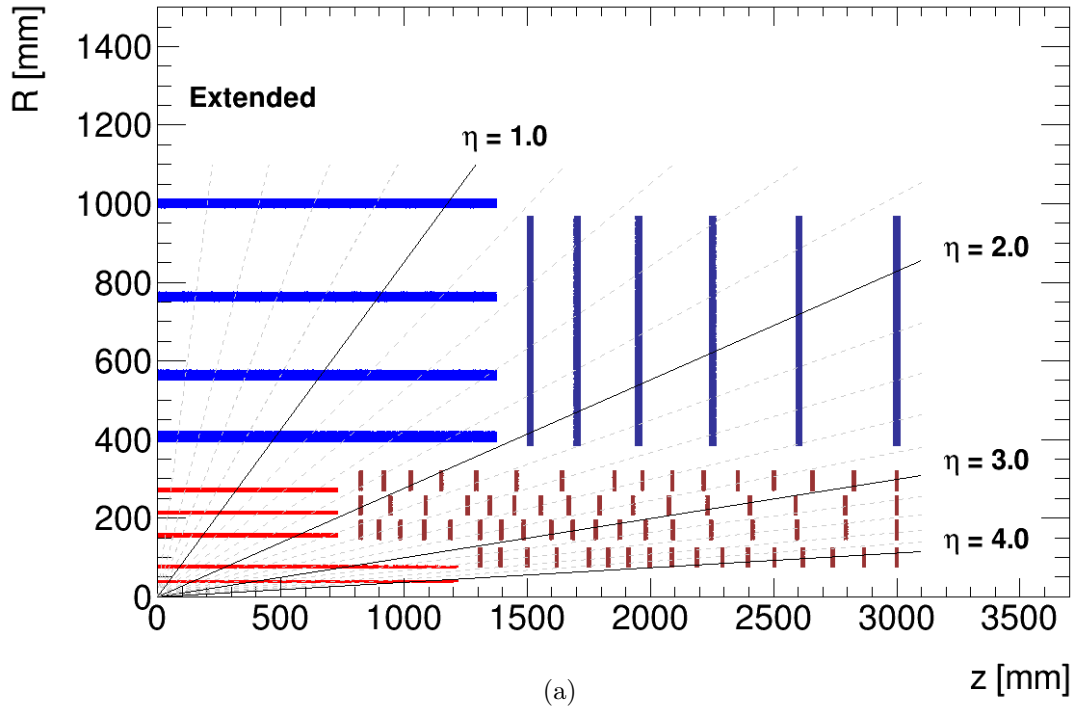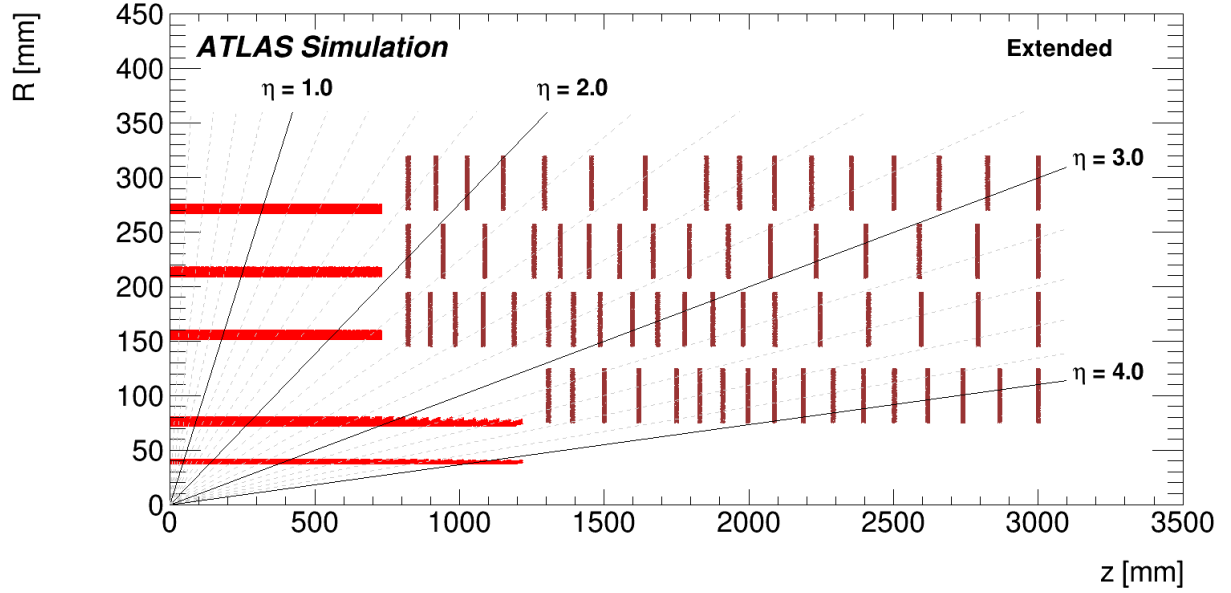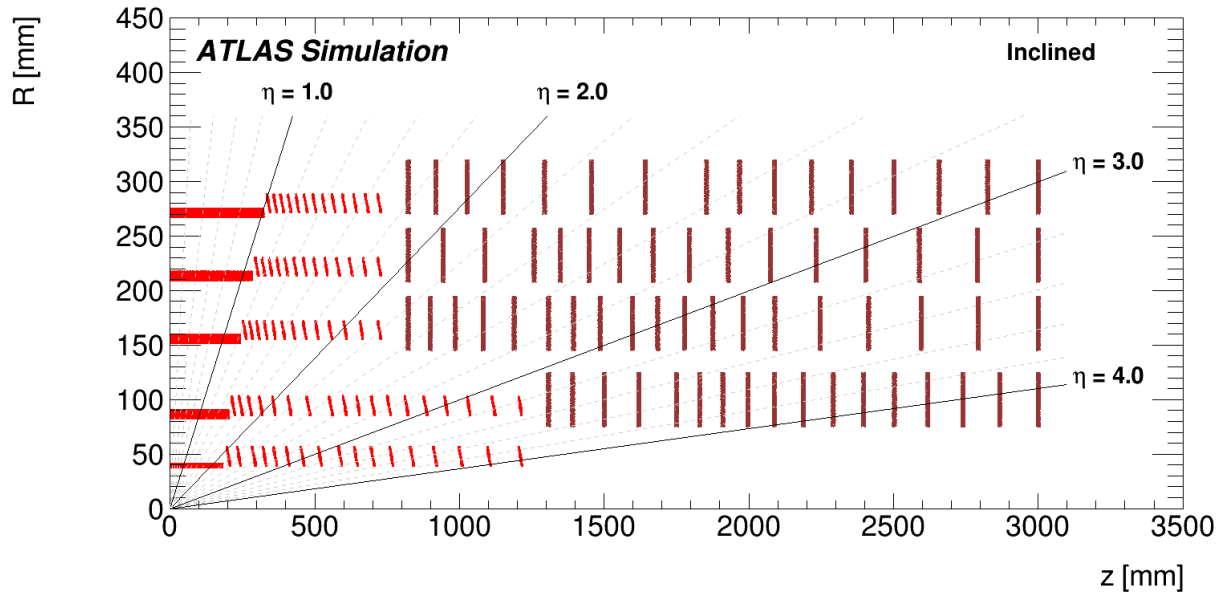
(a)

(b)

Figure 7.14: $R - z$ hit distribution for the pixel and strip sub-systems for the ITk layouts under considerations: (a) *Extended* Layout and (b) *Inclined* Layout. Only the positive pseudo-rapidity region is shown.

(a)

(b)

Figure 7.15: $R - z$ hit distribution for the pixel detectors of the (a) *Extended* and (b) *Inclined* Pixel Barrel Layouts. Only the positive pseudo-rapidity region is shown. They are completed by the same end-cap ring system [58].

	Number of Pixel modules		
	Extended Layout	*Inclined* Layout	*Inclined* Layout with optimised ring system
Inner Barrel	1920	1602	1602
Outer Barrel	4680	5244	5244
Barrel Total	6600	6846	6846
Endcap Rings	5640	5640	4056
Total	12240	12486	10902

Table 7.8: Summary of the number of Pixel modules in the different layouts. The last column reports modules for the *Inclined* Layout with an optimized ring system.

8

Software Implementation: From Simulation to Reconstruction

Contents

8.1 Introduction

The project the author of this thesis has been working on during the author qualification period has to be considered the first step towards the ITk layout simulation.

ATLAS uses a common geometry description, based on the GeoModel [108] library, for all stages of simulation and reconstruction. The geometry is then converted, via dedicated tools, into a GEANT4 [107] or a reconstruction geometry depending on the production step. Implementing such a geometry model is a time consuming operation. Is is thus useful to proceed with fast simulation approaches for layout development and prototyping. Those fast simulation techniques are in general less precise, but can be used for many decision. In ATLAS, one of this program is IdRes [105] that allows for quick evaluation of track resolution studies and hit statistics. However, it fails in describing the details of the geometry as well as efficiencies and effects due to pile-up. A more complex fast simulation approach is the fast ATLAS track simulation, FATRAS [106]. FATRAS uses the reconstruction geometry and the offline reconstruction tools and performs a full tracking through this geometry. Hence, it allows to precisely perform coverage studies including module overlaps and supports a more precise material model than IdRes. By creating a script-based input for the geometry builders of the reconstruction geometry, it is thus possible to perform accurate geometry studies without the necessity of GeoModel implementations. The goal of the project was indeed the implementation of a new toolkit to build customised
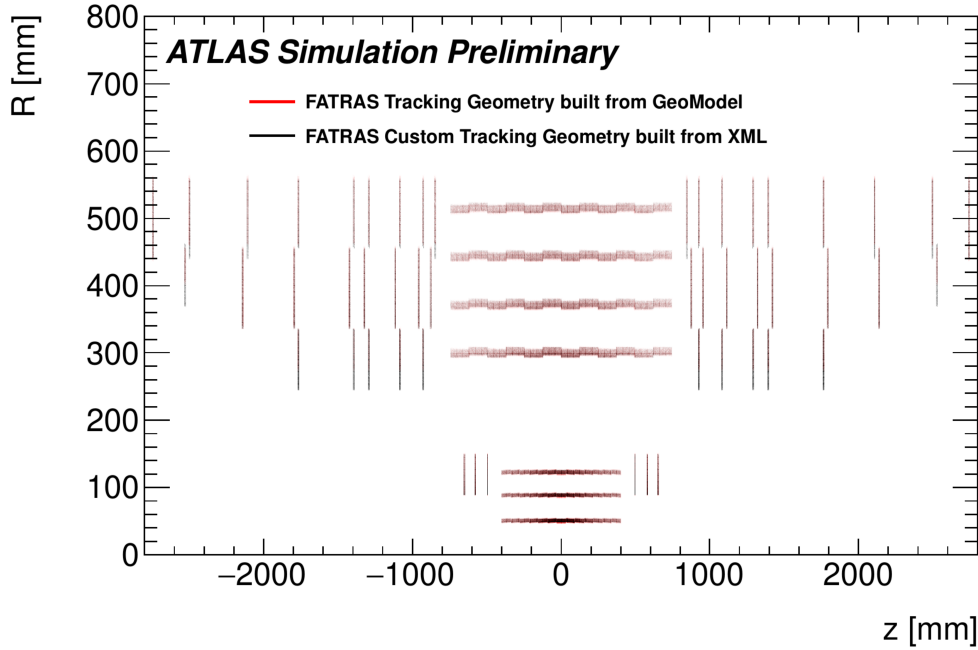
Figure 8.1: Hit distribution of single μ tracks in the ATLAS Pixel and SCT detectors using FATRAS tracking geometry from GeoModel (red) and from XML configuration file (black) [109].

geometries reading the detector descriptions from python or XML configuration files [109]. This allowed to facilitate the detector description guaranteeing at the same time a good level of accuracy during simulation.

A first demonstration consisted in the emulation the ATLAS pixel and SCT detectors: the description of the layout has been read from the configuration file and translated into the ATLAS geometry. Figure 8.1 shows the comparison of the hit distributions for single muon tracks using the reconstruction geometry built from GeoModel and from XML configuration files. In the context of the Phase-II Upgrade, the new builder has been used to perform coverage evaluations for the ITk layout candidates (see Chapter 9).

During the development of the project, the needs of a more flexible geometry description and implementation has become evident. Based on this initial implementation, a new ITk simulation framework was implemented to build a GeoModel description of the candidate layouts from XML configuration files: this additional step allowed to combine the flexibility needed in the implementation of the diverse ITk detector layouts with the usage of the full simulation framework and GEANT4. Thanks to this new approach, many layouts have been implemented through the several iterations necessary to optimise and correct some of the characteristics of the proposed geometries. The usage of one common geometry description has been recently included in a wider project supported by the ATLAS core software group.

8.2   Simulation, Digitisation, Reconstruction

Full simulation of the ITk layouts has been performed using Athena release 20.20, dedicated to the ATLAS Phase-II Upgrade Program. A full simulation campaign in ATLAS consists of:
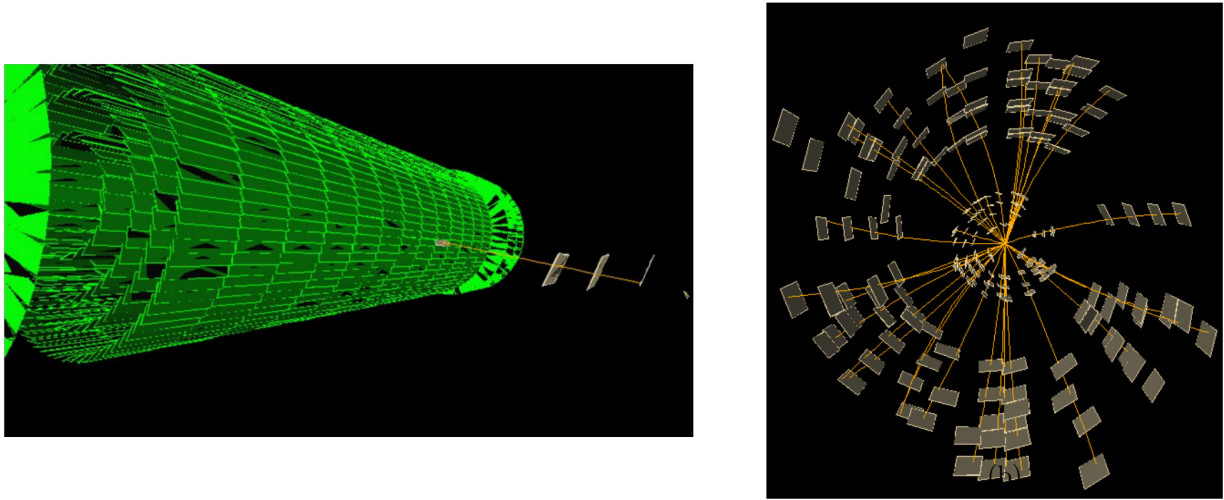
- Event generation;

Figure 8.2: A single muon event (a) and a top pair production event (b) visualized with the ATLAS Virtual Point 1 tool [110]. In (a) the entire custom tracking geometry is shown while (b) shows only the surfaces used in the track extrapolation. Extrapolated tracks are shown in both pictures.

- Detector simulation using GEANT4;

- Digitisation of simulated energy deposits into the actual detector readout data format;

- Event reconstruction starting from the digitised data.

8.2.1 Detector Simulation for ITk

The ATLAS full simulation is based on the GEANT4 toolkit. The ITk simulation uses dedicated GeoModel packages to implement the geometry from a description encoded in XML configuration files and, via dedicated tools, the precise geometry description is converted from GeoModel to GEANT4. Particles are propagated through this geometry and the various physics processes, caused by their interaction with the detector material, are simulated. In sensitive detector elements, processes ranging from energies of a few eV, such as the ionisation in gases, up to TeV energies are simulated to provide a detector-response model as realistically as possible.

The simulation step produces hits, i.e. small steps in the material with a starting point, an end point and the amount of energy deposited by the particle.

8.2.1.1 Material Description of the ITk layouts

One of the main concerns when optimising the tracker, is the impact of the material within the detector volume on the tracking performance, electron and photon measurements. The material also impacts fluence levels and total ionising doses. Particular care was therefore taken to describe the amount of material in the tracker volume and its distribution for the different ITk candidates. Figure 8.3a and Figure 8.3b show the material location in the detector volume as simulated. All components are placed carefully inside detector volume and described with their actual material components in terms if chemical compounds and density. The precise description was provided by the pixel and strip groups. In particular, the amount of services needed in the two sub-detectors is very crucial and is very much dependent on the geometry itself. Indeed, at any z-position along a stave the number of cables needed to operate the detector has to be evaluated.Moreover, the non-active material behind

and in front of the sensors has to be correctly modelled in both pixel barrel layouts, to account for the services along the stave structure inside the coupled layers (Layers 0-1 and 2-3). For the fifth layer, the corresponding cables are run behind the sensitive elements. Additional services have been added to route the cable out to the Patch-Panel 1 (PP1, shown in green in Figure 8.3a). Where the fine-granular structures are not relevant for the tracking performance, or simply not known yet due to missing detailed engineering layouts[1], the amount of material is usually averaged over the occupied space, such as e.g. averaged over the ϕ angle.

For the *Inclined* Layout, the modelling of inclined modules necessitated the correct simulation of the cooling blocks (see Figure 7.8a) and their position with respect to the sensitive elements. The inclined-sensor supports are individually modelled as 0.6 g/cm^3 carbon foam wedges. This density was chosen as it matched Alpine prototypes with the best thermal performance, accordingly to the results achieved before these studies were completed. These prototypes have a sensor angle of 74°, whereas simulation models use an angle of 56°, as a larger (steeper) inclined sensor angle is more challenging to cool. For this reason the inclined-sensor supports modelled in simulation represent a most-pessimistic scenario in terms of material budget.

The breakdown of the material components for the two main layouts in terms of radiation lengths (X_0) as a function of η is shown in Figure 8.4a and Figure 8.4b. The very central region, $0.0 \leq |\eta| < 1.0$, has very little material because of the light design of the support structures and the little contribution of cables and cooling. Moving to the forward direction, the incident angle into barrel-like modules and cylindrical support structures) increases dramatically. This is enhanced by the fact that the outer detector regions usually are equipped not only with the local services, but also with services and cables from the inner regions that are routed outwards. The effects of sensors, supports and services in the *Inclined* Layout results is a reduction of X_0 with respect to the *Extended* Layout when moving towards the forward region. In particular, in the intermediate region with $1.0 \leq |\eta| < 2.2$ there is a relative excess of material of about 5% with a narrow spike with a maximum of 10% in the *Inclined* Layout over the *Extended* Layout, as shown in Figure 8.4c. This is due to the presence of the carbon foam inclined-sensor supports, predominantly those in the outer three pixel barrel layers, in the barrel to inclined transition region. Moving in the forward region, $2.2 \leq |\eta| < 4.0$, the *Extended* Layout presents an excess of up to 30% in material budget when compared to the *Inclined* Layout. The two spikes at $|\eta| \sim 3.4$ and $|\eta| \sim 4.0$ in Figure 8.4c correspond to the end-of-stave material.

Figure 2.12 showed the material distribution in terms of X_0 as function of η for the current ATLAS ID. Compared to the current tracker, both ITk layouts achieve an incredible reduction of the material, as shown in Figure 8.5: the material is about 50% lower in the region $|\eta| < 4.0$ with even larger reduction at highest $|\eta|$ values.

8.2.2   Digitisation for ITk

The simulated hits are processed in a subsequent digitisation step in order to emulate the detector electronics output. During digitisation, the deposited energy for each GEANT4 step is used to evaluate the free charge and the drift time to the readout surface accordingly to the sensor thickness, carries mobility, depletion and bias voltage and Lorentz shift. Given the set of charges with different drift times, the response of the front-end electronics to these charge is simulated adding contributions due to noise and capacitive coupling to nearby pixels or strips. At this point the algorithm estimate the total signal in each device and checks if it is be above threshold. Pixels and strips above threshold are labelled as fired and are collected as output of the digitisation algorithms.

---

[1]It is worth mentioning that the ITk description in the simulation is in constant development to represent with the highest level of detail and accuracy the engineering layouts.
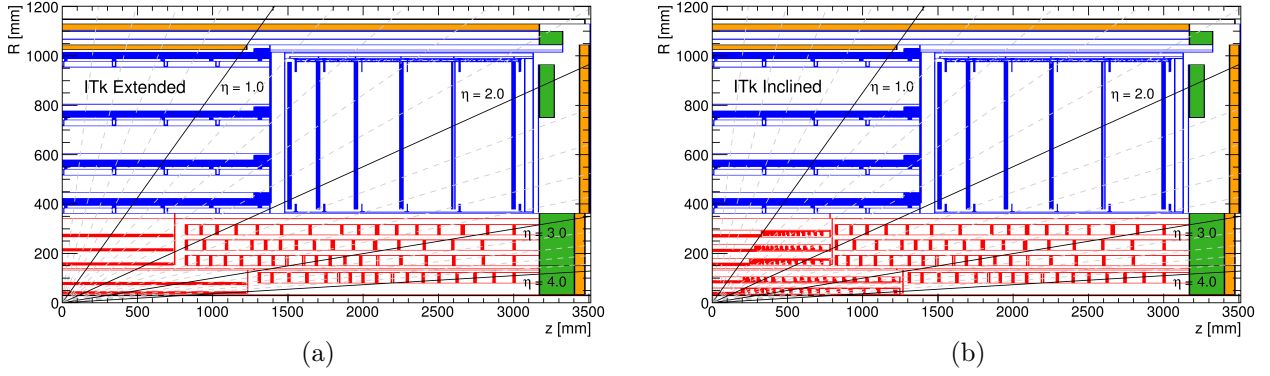
Figure 8.3: Location of the main materials for one quadrant of the ITk Layouts: (a) *Extended* Layout, (b) *Inclined* Layout. The pixel detector is shown in red, the strip detector is in blue; the polymoderator and the Patch-Panel 1 are highlighted respectively in orange and green [111].
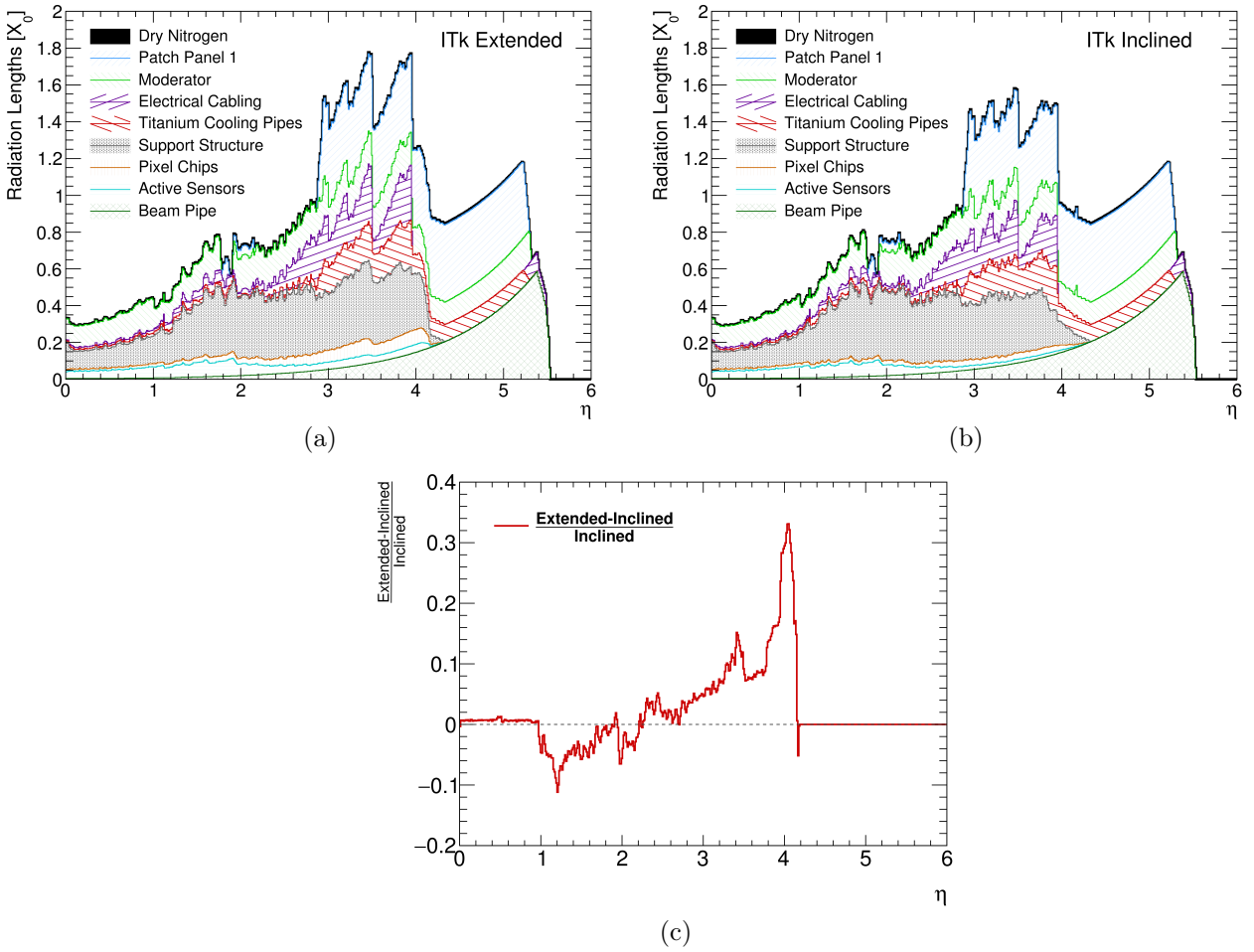

Figure 8.4: Material distribution in radiation lengths, X_0, versus pseudo-rapidity η for the (a) *Extended* Layout and (b) *Inclined* Layout. (c): Fractional difference of the total X_0 versus η for the *Extended* Layout with respect to the *Inclined* Layout [111].
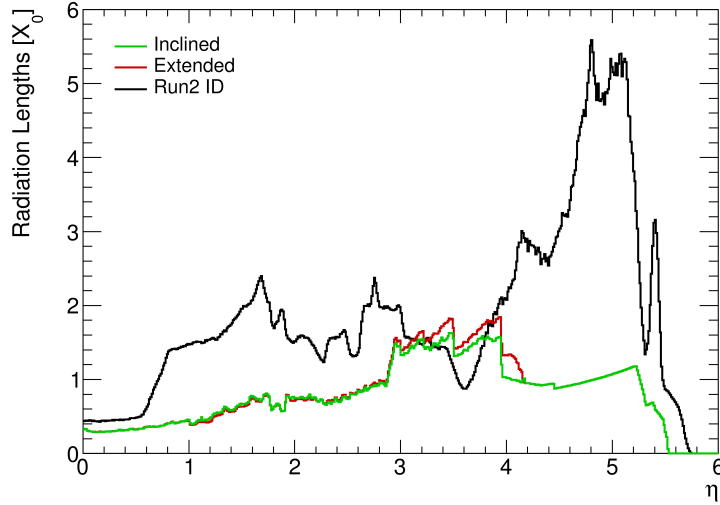
Figure 8.5: Total radiation length X_0 versus the pseudo-rapidity η for the current ATLAS Inner Detector (as reported in Figure 2.12) and the two ITk layouts. The ITk layouts are shown without the contribution from the moderator as the material distribution for the current ATLAS ID does not contain it [111].

The digitisation software of the ITk strips and pixels is based on the ATLAS SCT and IBL offline software respectively. Both strips and pixels are modelled as n-in-p sensors with electron carriers, without simulated defects. The sensor thickness for the strip detector is of 320 μm while the pixel sensors are simulated with a thickness of 100 μm for layers and rings inside the IST and 150 μm elsewhere. To allow for flexible studies of optimal readout segmentation, the readout segmentation for both sub-systems is defined in XML configuration files. Two pixel sizes are taken into account:

- For the nominal pixel size of 50×50 μm^2, the front-end electronics in-time threshold is set to 600 electrons, with an intrinsic standard deviation of 40 electrons added in quadrature with a noise standard deviation of 75 electrons.

- For 25×100 μm^2 pixels these values are multiplied by 1.5 owing to the larger capacitance of such rectangular pixels.

8.2.3 Reconstruction for ITk

The track reconstruction strategy used in the ITk reconstruction is based on the ATLAS Inner Detector track reconstruction [112] with adapted parameters that reflect the difference between the ITk detector layouts and the current ATLAS geometry. The different steps and algorithms are described in the following sections.

To account for the difference in number of modules crossed by the particles at a given direction of flight, the reconstruction requirements applied on the number of clusters, holes[2] and kinematic quantities depend on the pseudo-rapidity of the seed or track candidate. The requirements used in the reconstruction for the two layouts under study differ slightly and are shown in Table 8.1. In the case of the *Inclined* Layout, the higher expected number of pixel measurements in the forward region allows

---

[2]A hole is a missing measurement on a track where a hit on an active sensor is expected (inactive sensors are not taken into account).

Requirement	Extended Layout			Inclined Layout	
	$\lvert\eta\rvert < 2.7$	$2.7 < \lvert\eta\rvert < 3.4$	$3.4 < \lvert\eta\rvert < 4.0$	$\lvert\eta\rvert < 2.7$	$2.7 < \lvert\eta\rvert < 4.0$
pixel+strip measurements	≥ 9	≥ 7	≥ 6	≥ 9	≥ 9
pixel measurements	≥ 1	≥ 1	≥ 1	≥ 1	≥ 1
holes	< 2	< 2	< 2	< 2	< 2
double holes	≤ 1	≤ 1	≤ 1	≤ 1	≤ 1
pixel holes	< 1	< 1	< 1	< 1	< 1
strip holes	< 2	< 2	< 2	< 2	< 2
p_T [MeV]	> 900	> 400	> 400	> 900	> 400
$\lvert d_0 \rvert$ [mm]	≤ 2	≤ 10	≤ 10	≤ 2	≤ 10
$\lvert z_0 \rvert$ [cm]	≤ 25	≤ 25	≤ 25	≤ 20	≤ 20

Table 8.1: Set of requirements applied during the track reconstruction depending on the pseudo-rapidity interval for the *Extended* Layout and *Inclined* Layout.

for a constant requirement over the entire detector acceptance. For the *Extended* Layout, requirements are placed on the properties of the clusters, such as the minimum length, shape, and whether there is a cluster in the innermost pixel layer. For both layouts, a lower track p_T is required in the forward region to maintain an adequate tracking efficiency beside the degradation of the magnetic field.

8.2.3.1 Data Preparation and Space-Point Formation

The first step of event reconstruction is the formation of clusters from the individual channels of the strip and pixel detectors. For silicon-based detectors as present in the ITk, this is a local pattern recognition step where adjacent readout channels are grouped together in clusters, which represent single position measurement. This is done using a connected component analysis which is chosen to be based on eight-cell connectivity [113].

For the strip detector, a local cluster position is calculated and corrected for the Lorentz shift, and a measurement error is assigned..

For the pixel detector, additional algorithms have been implemented. A dedicate cluster merging step is needed in the forward pixel barrel for the *Extended* Layout, where incident particles cross the sensors at small incidence angles (see § 7.4.1.1). In such a case, because of charge deposition fluctuations it is possible that some pixels of the resulting long cluster are below threshold. To prevent this kind of situation which results in multiple clusters being reconstructed, pixel barrel clusters are merged into a single long cluster if all of the following conditions are satisfied:

- Only pixels on the same modules can be merged;

- The clusters are at most one channel apart in ϕ and satisfy a maximal gap length in z;

- None of the clusters are longer in ϕ than in z;

- The resulting long cluster is not longer than would be expected from a particle originating within ± 20 cm from the origin of the detector.

Two main clustering algorithms are available to evaluate the position of the cluster and its resolution.

Digital Clustering – The local position of the cluster is calculated by taking a simple center of gravity of all the pixels in the cluster. The position of the cluster is corrected for the Lorentz

shift, and a two dimensional covariance matrix is assigned to it:

$$\sigma = \begin{pmatrix} \left(\frac{\mathrm{pitch}_x}{\sqrt{12}}\right)^2 & 0 \\ 0 & \left(\frac{\mathrm{pitch}_y}{\sqrt{12}}\right)^2 \end{pmatrix}$$

where pitch_x and pitch_y are the pixel dimensions respectively in the ϕ direction and along the beam line.

However, for both layouts this method needs to be refined in the case of longer clusters, as otherwise missing pixels (e.g. under threshold) and extra pixels (e.g. originating from delta rays) cause large biases in local position determination. Thus barrel clusters above a certain length in z are reduced to their main two rows, defined as the longest line of channels hit along z with its longest neighbouring line. The local position in ϕ is then evaluated by averaging over the main two rows instead of the whole cluster, and the local position along z is simply taken as the middle of the cluster, neglecting the presence of holes. A final correction is applied to clusters across module edges: in this case clusters are reconstructed independently in each of the two modules and cannot be merged for technical reasons. The result of these corrections is shown in Figure 8.6 for a few selected long clusters. Figures 8.6a, 8.6c, 8.6e and 8.6g make clear the effect of delta rays on the evaluation on the cluster position.

Analog Clustering – If the time-over-threshold (ToT) information is available then a charge interpolation algorithm can also be used. The ToT information can be transformed to a representative charge measurement for the individual pixel channels and can be used to get a more accurate estimate of the position of the cluster and hence redefine its resolution using a charged sharing technique. The charge information can be used as an even more powerful tool for track reconstruction in dense environment: when the local track density gets so high that clusters from close-by particles merge or overlap, e.g. in the core of boosted jets or as a product of a decay of a boosted object, the charge pattern in such shared clusters can be used in order to flag or potentially even split them [114].

It is clear that the usage of analog charge information and an advanced algorithm to determine if a cluster might come from one or more particles is critical. When the studies reported in this document were performed no such algorithm for the ITk existed yet. Instead, the probability for a cluster to be identified as merged is modelled using truth information (see § 8.2.3.5).

Because of the missing implementation of the analog clustering algorithm for the ITk reconstruction, the digital clustering was used by default. Anyway, in absence of a reliable prediction of the ultimate intrinsic resolution and readout thresholds of the ITk pixel sensors and digitization models (in some cases not yet developed), additional methods have been developed to mitigate potential errors in the measurement estimation:

Geometrical Clustering – The geometrical clustering algorithm [115] is used to calculate the expected cluster shape and a centroid method using the path length in the individual pixels is used to reconstruct a cluster position. The geometric clustering is close to the analog clustering that is used in the ATLAS Run-2 setup. The cluster position is hereby calculated using the channels contributing to the cluster but weighted by the deposited charge in the individual channels.

Truth-based Clustering – The truth position of the particle intersection with the measurement plane is smeared with a normal distribution throughout the whole pixel detector. The smearing
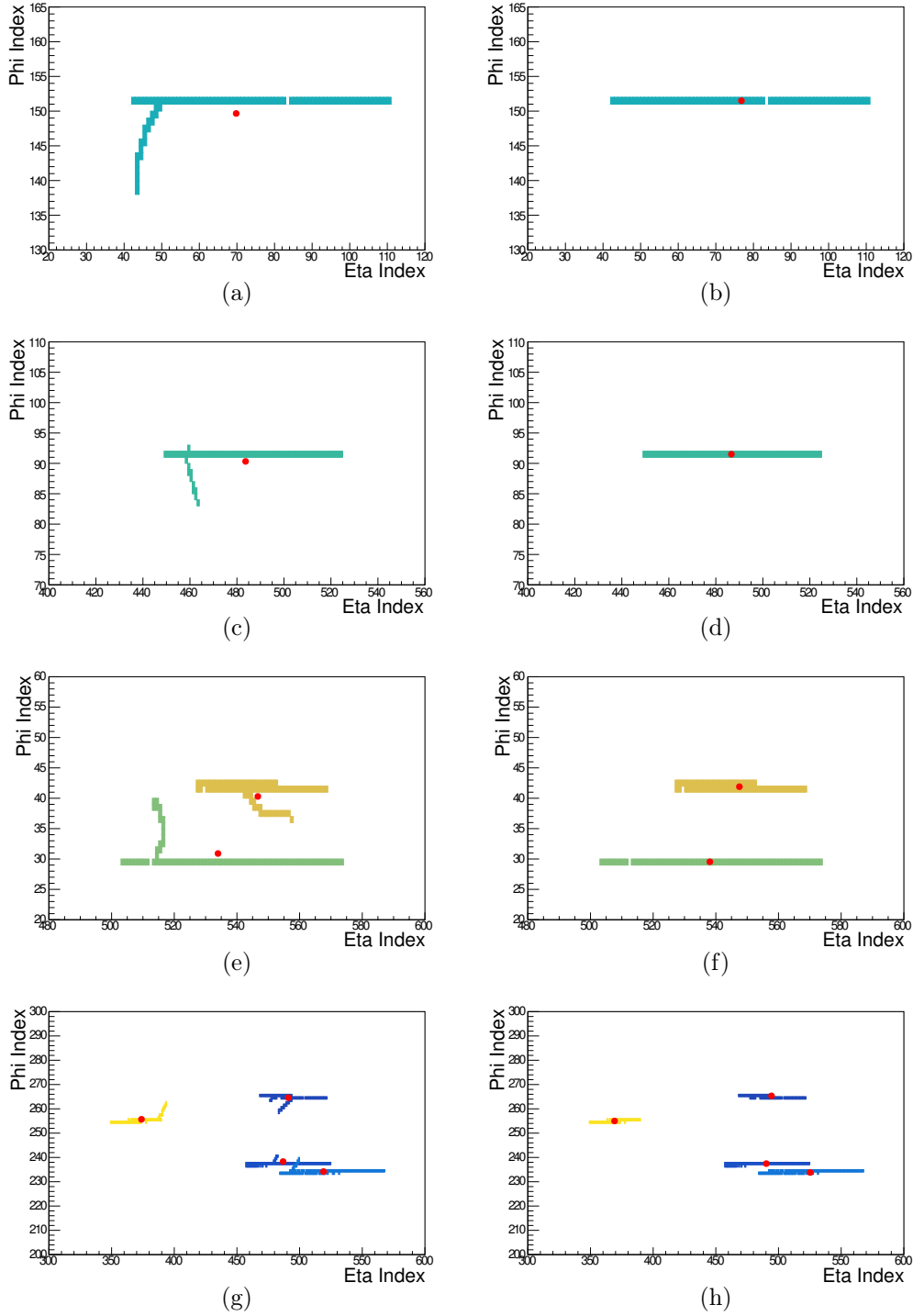
Figure 8.6: Examples of pixel cluster shapes before (a, c, e, g) and after (b, d, f, h) the correction procedure described in § 8.2.3.1. The selected clusters belong to the innermost layer of the *Extended* Layout. The indices of the pixels on the readout frame are indicated on the two axis, where η is along the beam line. The red circles correspond to the center of the clusters as evaluated by the digital clustering algorithm. The colors associated to the clusters have no meaning.

is applied as corresponding covariance in the measurement error matrix. Further information of the truth-based clustering algorithm is provided in § 10.1.

All the algorithms described above build a performance band in which the ultimate performance of the layouts is obtained using the truth-based clustering. These results are described in Chapter 10. Clusters are then transformed into three dimensional representations, in the following referred to as space-points, which build the input to the track finding stage.

For the strip detector, as only one dimension is measured with sufficient precision, clusters from both sides of the double-sided modules are used to build space-points, which requires the incorporation of the relative stereo angle between the strips on both sides and a constraint of track pointing to the interaction region. Some assumption about the track trajectory is therefore needed in order to transform strip clusters from the two sides of a module into a single two dimensional representation on one surface. For the standard collision reconstruction setup, space-points in the strip detector are built assuming a particle origin at (0,0,0) and using a straight line track model. This can lead to a wrong estimate of the space-point position for particles not originating from the nominal interaction point, e.g. from a shifted vertex position or even more for particles from cosmic rays. The space-point formation algorithm was developed starting from the current ATLAS SCT cluster to space-point conversion, which was designed for a smaller strip detector with a significant smaller gap between the sensors on each side. Updates were indeed needed in order to take the increased gap into account in the ITk strip layout during the space-points creation. At the time being, space-point formation from sensors that overlap in ϕ or z, which is expected to improve significantly the space-point creation efficiency, is not yet enabled.

In the pixel detector, clusters can be directly transformed into space-points starting from their evaluated local position.

8.2.3.2   Track Seeding

Track finding starts with the track seeding stage: triplets of space-points that are roughly compatible with being aligned on a helical track model are built and further investigated. This simple model applies loose cuts on the transverse and longitudinal impact parameters of the track seeds by simple geometrical extrapolation to the beam line. Seeds can be built from space-points that are entirely formed by pixel space-points (PPP), mixed space-points (PPS, PSS), and solely strip space-points (SSS). The different seed configuration show different purity and efficiency due to the different spatial resolution of the space-points in the different detector layers and given the largely differing hit density environment. A seed efficiency of close to 100% of reconstructable tracks in the tracker volume is desired, as failure of finding an appropriate track seed automatically turns into a failure of finding the particle's track. A high seed duplication rate, i.e. many seeds for one identical particle put pressure on upstream ambiguity solving methods and eventually could lead to track duplicates.

For the ITk reconstruction, only SSS and PPP seeds are used starting with SSS seeds. The number of seeds per event as a function of $|\eta|$ for the *Extended* and *Inclined* Layouts is shown in Figure 8.7a. The two candidate layouts behave very similarly in the region to $|\eta| < 2$ and because of the identical strip system evidently show the exact same ensemble for SSS seeds. In the region with $2 < |\eta| < 3.5$ significantly more PPP seed combinations are possible in the *Inclined* Layout, which is caused by the higher number of available pixel space-points due to the design choice of allowing multiple measurements per layer (Figure 7.12). In the region above $|\eta| > 3.5$ where the identical pixel ring system dominates, the seed numbers are again very similar for the two layouts.

For the *Extended* Layout, a seed filter was developed to improve the purity of track seeds, based on the fact that the size of pixel clusters corresponding to particles coming from the primary interaction
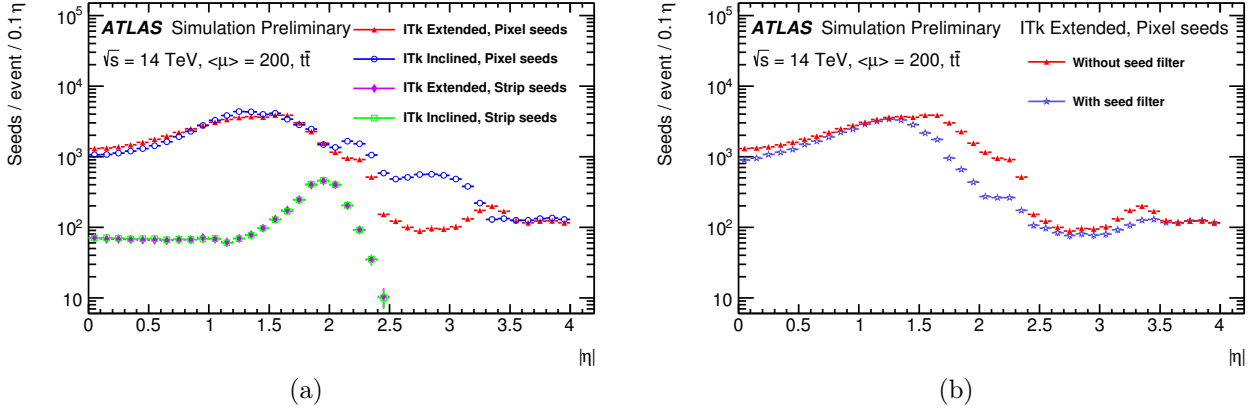
Figure 8.7: (a) Number of unfiltered pixel (PPP) and strip (SSS) seeds as a function of pseudo-rapidity for the *Extended* and *Inclined* Layouts. (b) Effect of the pixel seed filter on the number of pixel seeds for the *Extended* Layout [116].

is directly related to their incident angle in barrel sensors (see § 7.4.1.1). This is in contrast to clusters from secondary particles, which in this layout have much smaller cluster sizes. The seed filter was therefore implemented to reject seeds with a pixel barrel cluster of a length inconsistent with the seed θ angle. The effect of this filter is shown in Figure 8.7b: a reduction of the number of fake seeds using this filter was observed which leads to a reduction in the number of fake tracks. This comes at the cost of a small tracking efficiency loss. This implementation of the seed filter also led to no significant reduction in the computing time for reconstruction [116].

Seeds that pass the first set of cut requirements are further processed requiring a fourth space-point confirmation in the projected direction of the track seed before progressing to the combinatorial track finding.

8.2.3.3 Combinatorial Track Finding

Successfully formed seeds are used to builds roads for the combinatorial track finding. A combinatorial Kalman Filter [117] is the core of the algorithm: the track trajectory is propagated to detector modules along a road given by the seed direction and clusters on the detector modules within the road are tested for compatibility with the given track hypothesis. Multiple scattering and deterministic energy loss are approximately taken into account at this step considering a simplified model for the tracker material and the magnetic field for computing performance reasons. The output object of this process are called track candidates. Track candidates that do not pick up sufficient clusters are dropped and not considered further in the track reconstruction. A highest possible technical efficiency of track candidates is therefore required, as track candidates not found in the track finding stage can currently not be recuperated.

8.2.3.4 Track Candidates and Ambiguity Solving

Due to the combinatorial nature of the track finding, clusters can be wrongly assigned to track candidates. For this reason, an ambiguity solving algorithm is run during the final stage of the track reconstruction. A most accurate material model and magnetic field data in used now. Tracks are fitted using a global χ^2-minimization technique. At this stage, also holes are detected given the track trajectory, the detector geometry and its status. From past experience it has been shown that holes

and double holes, i.e. holes on both sides of double-sided sensors, build a very strong suppression of fake combinations. Another important aspect of the ambiguity solving, which gave rise to its name, is the final assignment of clusters to competing tracks in order to find the final track collection for further physics analyses. One after the other track candidates are processed and thanks to a scoring algorithm they are ranked according to their hit content and track fit quality. Ambiguities between multiple track candidates are solved comparing the corresponding scores and keeping the track with the highest one.

8.2.3.5 Dedicated Reconstruction Tools

Dedicated reconstruction tools are tailored to optimise reconstruction in specific environments or of specific particles.

A dedicated electron reconstruction configuration has been developed for ATLAS to account for energy loss through radiation when traversing the tracking volume. Two main effects must be taken into account: first, trajectories from electrons that have radiated sufficiently energetic photon appear to be kinked and not compatible with the track model any more; secondly, if additional angular deflections are allowed to recover the set of measurements that belong to an electron, they can also increase the possibility to wrongly associate hits to the track candidate and hence bias the results and increase the potential fake rate. Based on these consideration, the ATLAS electron reconstruction algorithms allow for additional angular deflections during the track finding only in regions compatible with an electromagnetic deposit in the calorimeter. The same requirement is then used during the track fit to allow for fitting the additional angle weighted by the traversed material in order to control the incremental χ^2 contribution. Finally, when a track candidate is associated to an electron object, a dedicated fitting technique, the Gaussian sum filter, which models the bremsstrahlung tail with multivariate Gaussian components, is used to improve the track resolution. Since the size of the bremsstrahlung effect is proportional to the traversed material, the reduction of the material within the tracker volume can improve the electron track reconstruction efficiency and the track resolutions.

A dedicated track reconstruction is also in place for dense environments. Tracks in boosted objects are characterised by a high local hit density and inter particle distances on the innermost measurement layers smaller than the channel size. Because of this, the measurements become merged and are common to multiple track candidates, which in general are penalized in the ambiguity solving method if the clusters are not correctly labelled as shared. As already discussed in § 8.2.3.1, the information on the charge deposited in the pixels is the essential ingredient to identify clusters created by more than one particle and hence improve the tracking performance in dense environments. In Run-1 and Run-2 of the ATLAS data taking, a dedicated trained set of neural networks has been successfully used to identify and eventually refine the cluster information from merged clusters [114,118]. For the first ITk studies that are reported in this document, as no final digitization model has been established, the performance of the neural network is emulated using truth information the assumption that it behaves similarly well as with the current ATLAS IBL (which has a 4-bit readout for the time over threshold information).

Results on the reconstruction of different objects are shown in Chapter 10.

9
Coverage Studies

Contents

9.1 Introduction

In order to capture the maximum number of particles stemming from each collision, hermetic coverage should be given for tracks from any primary vertex position within a cylinder around the nominal center of the detector with radius of 2 mm and length of 300 mm, i.e. ±150 mm along the beam direction, in the entire pseudo-rapidity acceptance $|\eta| < 4.0$.

Before running CPU expensive full simulation samples, dedicated studies have been performed to verify the hermeticity of the *Extended* and the *Inclined* Layouts. They are presented in this chapter and are based on the ATLAS reconstruction geometry and a fast simulation engine FATRAS [106] as described already in § 8.1 [109].

The detector description is read from XML configuration files and both the GeoModel and the corresponding tracking geometry are built. A fast tracker simulation based on the offline extrapolation engine allows to simulate different particles which are propagated through the tracking volume. The engine navigates through volumes and layers and propagates the trajectories accordingly to the magnetic field. Hits are produced where intersections of the tracks with sensitive surfaces occur. The extrapolation engine also updates the trajectories performing interactions with the detector material. For the studies proposed, average effects due to energy loss, via ionisation and radiation are taken into account. The hits provided by the extrapolation engine are then counted as measurements and used to study the coverage of the layouts.

9.1.1 Definitions

In this chapter, a hit is defined as the intersection of the track with any sensitive surface within readout boundaries (threshold effects are not taken into account). The sequence of hits provided by

the extrapolation engine per event is called track.

Tracks are labelled as selected if they fulfil the geometrical acceptance requirement:

- $|\eta| < 4.0$;

- $|z_{\text{vertex}}| < 150$ mm;

- $|R_{\text{vertex}}| < 2$ mm;

Selected tracks are said to be inside the detector if they satisfy the requirement on the minimum number of hits as follows:

★ Tracking cuts on hits:

    − *Extended* Layout:
         - $|\eta| \in [0.0;\ 2.7[$: 9 hits
         - $|\eta| \in [2.7;\ 3.4[$: 7 hits
         - $|\eta| \in [3.4;\ 4.0]$: 6 hits
    − *Inclined* Layout:
         - $|\eta| \in [0.0;\ 4.0]$: 9 hits

(η, ϕ) combinations of the selected tracks that don't satisfy the hit requirement mentioned above, are labelled as gaps for the layout. The geometrical tracking efficiency is then built taking into account the number of tracks meeting the hit requirement and the total number of tracks inside the geometrical acceptance. It is shown as a function of η, z_{vertex} and R_{vertex} of the tracks. Similar requirements on the number of measurements as for reconstruction are applied (see § 8.2.3).

A second set of requirements has been considered asking for 2 additional hits in order to have a first estimate of the weakness in the redundancy and in the ability of finding tracks from displaced vertices, such as e.g. tracks from photon conversions.

★ Requiring 2 additional hits:

    − *Extended* Layout:
         - $|\eta| \in [0.0;\ 2.7[$: 11 hits
         - $|\eta| \in [2.7;\ 3.4[$: 9 hits
         - $|\eta| \in [3.4;\ 4.0]$: 8 hits
    − *Inclined* Layout:
         - $|\eta| \in [0.0;\ 4.0]$: 11 hits

To prove that both layouts are fulfilling the coverage requirement under different LHC conditions, single muons are simulated and different vertex distributions are taken into account:

- Fixed vertex: vertex is set to $(0, 0, 0)$, i.e. $z_{\text{vertex}} = 0$ mm and $R_{\text{vertex}} = 0$ mm;

- Flat smearing of the vertex: z_{vertex} uniformly distributed in [-300 mm, 300 mm] and R_{vertex} uniformly distributed in [-3 mm, 3 mm]

- Gaussian smearing of the vertex: using $\sigma_{z_{\text{vertex}}} = 50$ mm, 60 mm, 70 mm, 80 mm and $3 \cdot \sigma_{R_{\text{vertex}}} = 2$ mm, in order to contain 99.7% of the simulated tracks in a cylinder with a radius of 2 mm.

η and ϕ of the simulated particles are uniformly distributed in [-4.0, 4.0] and [-π, π[, respectively. The different options will allow to understand the robustness of the two layouts against longer luminous regions and where the geometrical tracking efficiency starts to decrease. In the three scenarios, single muons with $p_{\text{T}} = 1, 10, 100$ GeV have been simulated.

9.2 Coverage Studies and Results

9.2.1 Coverage Studies with Fixed Vertex Position

Figure 9.1 shows the total number of pixel-plus-strip measurements on track, demonstrating that the number of hits is above the required value at all η for both layout except for $\eta = 0$ when passing in between sensitive sensors. The number of pixel measurements and strip measurements as a function of η is shown as well. The average number of hits exceeds the minimum requirement due to sensor overlaps.

Figure 9.2 shows the average number of hits as a function of the track parameters η and ϕ for the *Extended* and the *Inclined* Layout. Single muons with $p_T = 1$ GeV are used to point out the presence of potential holes when the bending effects due to the magnetic field are bigger. Given the fixed position of the vertex and the solenoidal magnetic field, the track η coincides with the detector η highlighting the layout features:

- The identical configuration of the central region implies the same hit distribution for $|\eta| < 1.0$ for both layouts.

- At $|\eta| \sim 1.1 - 1.2$, the strip barrel to end-cap transition region corresponds to a drop in the hit distribution.

- The striations in $1.2 < |\eta| < 2.7$ shown in Figure 9.2a correspond to the strip end-cap and pixel ring systems. For $|\eta| > 2.7$, full coverage is provided by the pixel end-cap system.

- The inclined section of the innermost layers of the *Inclined* Layout starts at $|\eta| \approx 1.5$ (see Figure 9.2b). The hit arrangement described in Figure 7.12 translates into an excess of hits compared to the *Extended* Layout.

- In the region above $|\eta| > 3.5$, where the identical pixel ring system dominates, the hit distribution is again the same.

The same behaviour is shown in Figure 9.3, where the average number of hits as a function of the pseudo-rapidity is shown for the two layouts.

As shown in Figure 9.1a and Figure 9.1b, both layouts don't present holes in the entire η spectrum except for $\eta = 0$.

9.2.2 Coverage Studies with Flat Smearing of the Vertex Position

In order to verify the hermeticity requirement for tracks from primary vertices within ± 150 mm in z, the extreme case where z_{vertex} and R_{vertex} are uniformly distributed respectively in $[-300, 300]$ mm and $[-3, 3]$ mm is taken into account. Tracks are selected if $|z_{\text{vertex}}| < 150$ mm, $|R_{\text{vertex}}| < 2.0$ mm and the wider range is considered to understand the robustness of the two layouts against longer luminous regions and where we start loosing geometrical tracking efficiency.

Figure 9.4 shows the total number of pixel plus strip measurements on track. Compared to Figure 9.1, the primary vertex z spread provides a broader hit distribution. The number of hits is above the required value at all η for both layouts: fewer hits are available in the *Inclined* Layout when $|\eta|$ is very close to 4 and for both layouts at $\eta = 0$.

The geometrical tracking efficiency can be plotted as a function of η, z_{vertex} or R_{vertex} of the simulated tracks, as shown in Figure 9.5. The layouts proposed are optimised in order to provide hermeticity
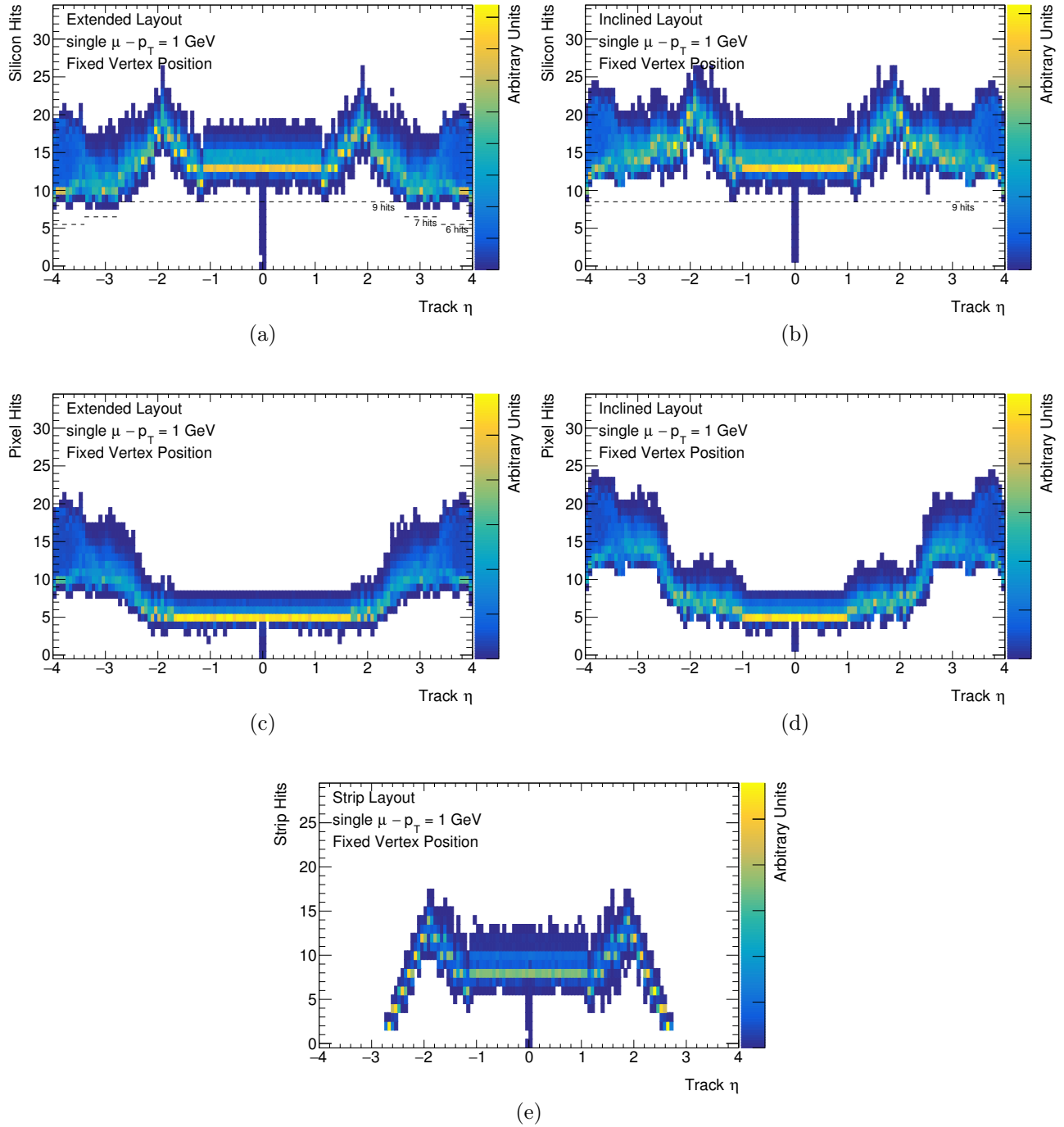
(a)

(b)

(c)

(d)

(e)

Figure 9.1: Total number of (a, b) silicon hits and (c, d) pixel hits as a function of η of the simulated tracks with fixed vertex position for the *Extended* and (b, c) *Inclined* Layout. The distribution of the number of strip hits as a function of η of the simulated tracks with fixed vertex position is shown in (e). The low number of pixel and strip hits at $\eta = 0$ is due to the gap in between sensitive sensors for both sub-systems.
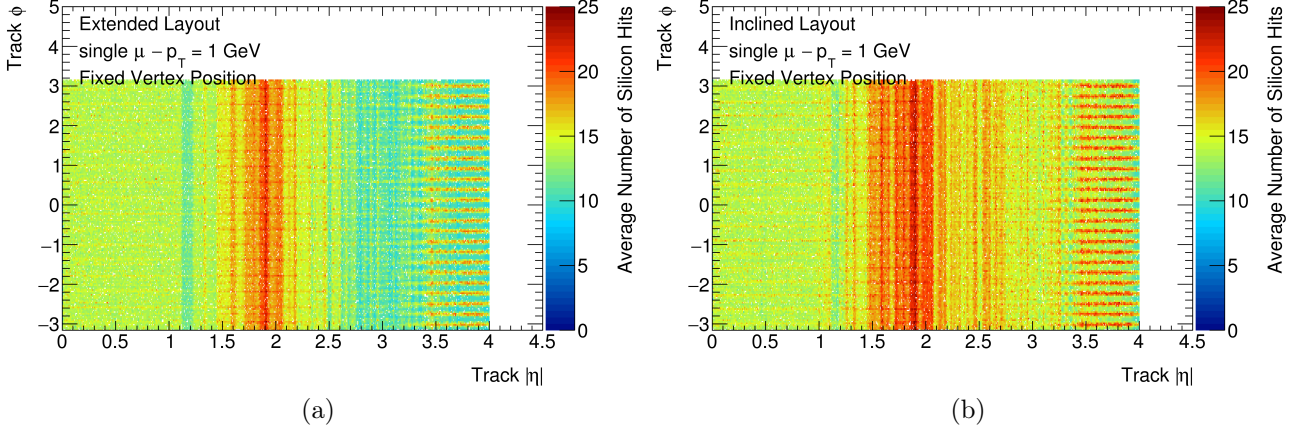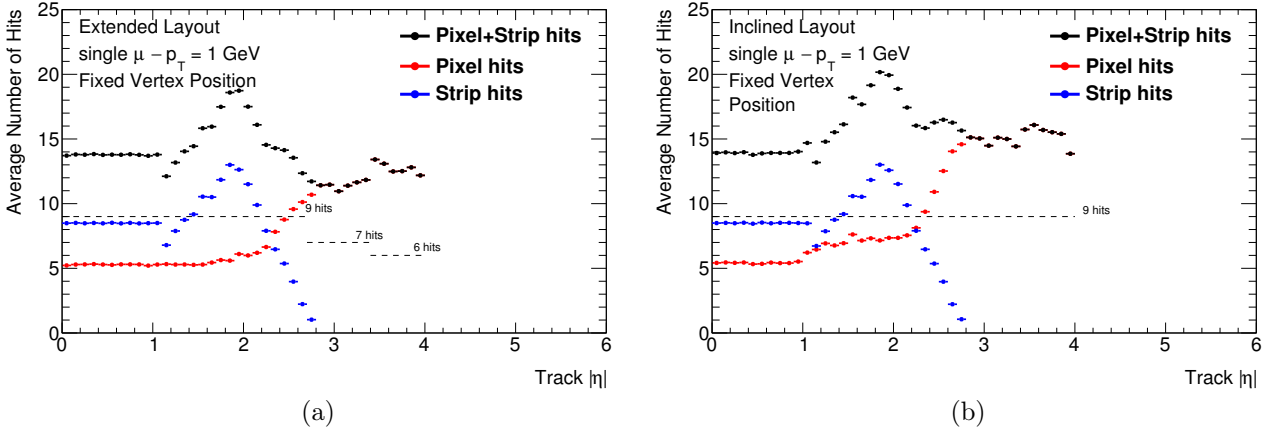
Figure 9.2: Average number of silicon hits as a function of $(|\eta|, \phi)$ of the simulated tracks with fixed vertex position for the (a) *Extended* and (b) *Inclined* Layout.

Figure 9.3: Average number of silicon hits as a function of $|\eta|$ of the simulated tracks with fixed vertex position for the (a) *Extended* and (b) *Inclined* Layout. The dashed lines correspond to the minimum number of hits in the different $|\eta|$ regions. The average number of hits exceeds the minimum requirement due to sensor overlaps. The features of the two distributions are described in detail in the text.

when the vertex position lies within ± 150 mm in z and a radial displacement of 2 mm. Indeed, the geometrical tracking efficiency slightly decreases when $|z_{\text{vertex}}| > 150$ mm. This behaviour is even more evident for the *Inclined* Layout where the hermeticity requirement is not fulfilled by tracks originated in the tilted region ($|z_{\text{vertex}}| > 180$ mm) since they can escape the detector passing in between inclined modules at small $|\eta|$.

In $|z_{\text{vertex}}| < 150$ mm and $|R_{\text{vertex}}| < 2.0$ mm, the geometrical tracking efficiency is then shown to be constant and very close to 100% proving that the two layouts don't have pathological anomalies in the modules' position.

For this vertex smearing configuration, the geometrical tracking efficiency has been studied when 2 additional hits are required in the different η regions to evaluate the robustness of the two candidate layouts. This is useful to identify some regions of the two layouts that can be more problematic for pattern recognition and tracking in case of module and channel's failures. In particular, comparing Figure 9.6 and Figure 9.5 some effects are shown:

- The geometrical tracking efficiency is reduced at the strip barrel/end-cap transition region, i.e $|\eta| \approx 1.2$, for both candidate layouts. The *Inclined* Layout partially recovers the lack of hits thanks to the module overlaps in η and ϕ in the outer inclined region. This doesn't happen for the *Extended* Layout and therefore the inefficiency results to be $\sim 5\%$ compared to $\sim 2\%$ of the *Inclined* Layout. Moreover, for the *Extended* Layout the geometrical tracking efficiency is reduced at $|\eta| \approx 2.6$ and $|\eta| \approx 3.2$ since more tracks present a lower number of hits with respect to the minimum required. For both layout, a decrease in the efficiency is shown at $|\eta| \approx 4.0$.

- Figure 9.5 indicated already that the length of the barrel-like section of the *Inclined* Layout is optimised to contain tracks from vertices within ± 150 mm in z. The effect of the z vertex position being outside this region and the request of 2 additional hits show a smooth reduction of the efficiency up to a maximum of about 10% for a maximal z displacement of the vertex of 30 cm. A small reduction of the order of 2-3% is present also for the *Extended* Layout.

- The geometrical tracking efficiency is shown to be independent on the radial displacement of the vertex for both candidate layouts.

9.2.3 Coverage Studies with Gaussian Smearing of the Vertex Position

The flat smearing of the vertex position allows to study the hermeticity of the candidate layouts with high statistics in the different configurations, e.g. looking at highly displaced vertices from the interaction point. However, considering the LHC operating parameters, the particle density in proton bunches in the longitudinal and transverse planes is more correctly described using Gaussian distributions. In order to understand the limits of the *Extended* and *Inclined* Layouts and provide a first measurement of their robustness against changing LHC conditions, single muons with $p_{\text{T}} = 1$ GeV are simulated considering a Gaussian smearing of the vertex z position with $\sigma_{z_{\text{vertex}}} = 50$ mm, 60 mm, 70 mm, 80 mm and $3 \cdot \sigma_{R_{\text{vertex}}} = 2.00$ mm, in order to contain 99.7% of the simulated tracks in a radius of 2.0 mm. Tracks are accepted if $|z_{\text{vertex}}| < 300$ mm, in order to take into account the entire spread of the vertices on the beam line, and $|d_0| < 2$ mm.

Figure 9.7 is showing the geometrical tracking efficiency as a function of η, z_{vertex} and R_{vertex} of the simulated tracks. The same is shown in Figure 9.8 adding the 2 additional hits to the required number of silicon measurements.

These plots are compatible with what has been discussed in the previous section adding further information on the actual importance on the tail of the spreading distributions. In particular, the
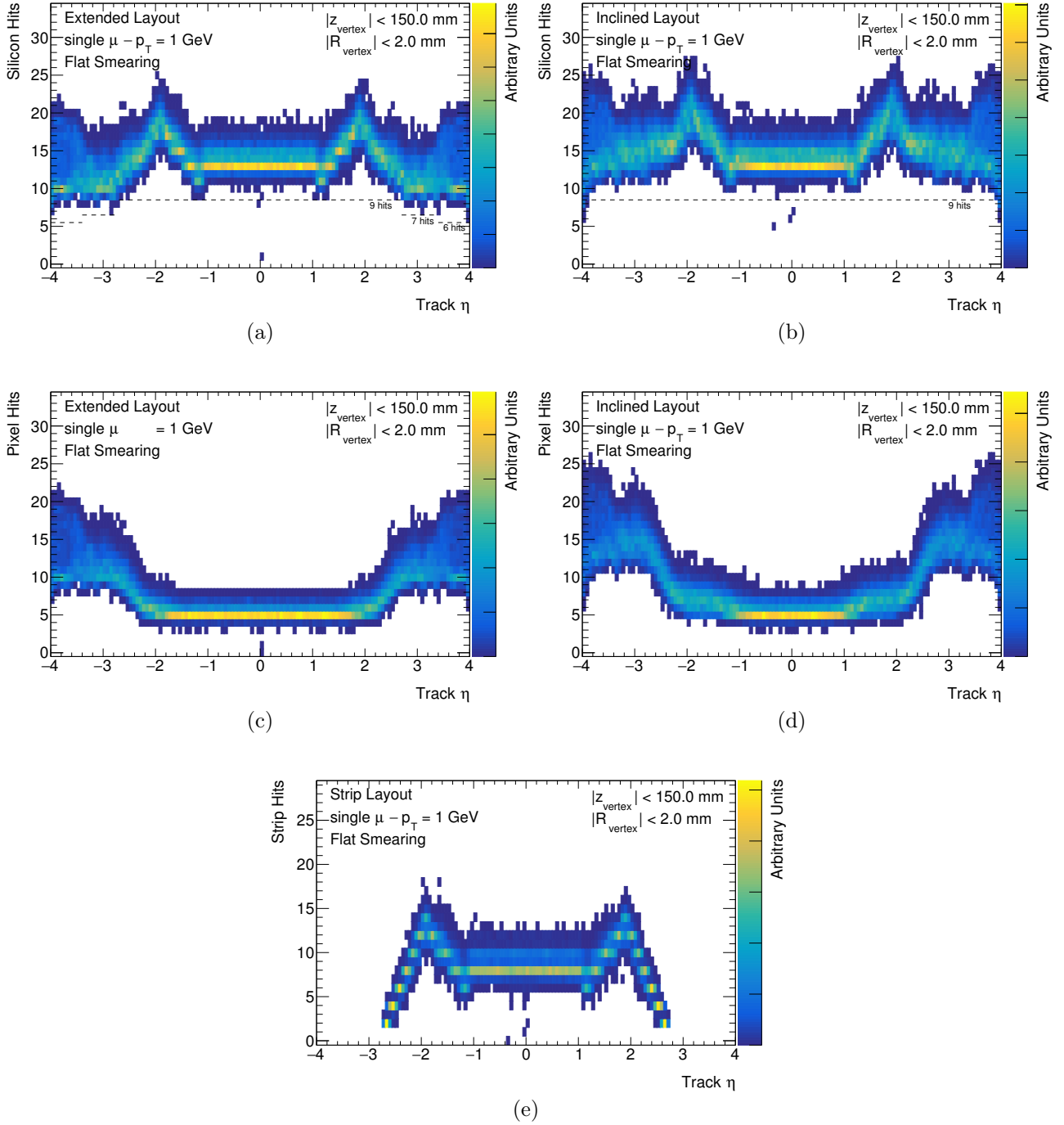
Figure 9.4: Total number of (a, b) silicon hits and (c, d) pixel hits as a function of η of the simulated tracks with flat smearing of the vertex position for the *Extended* and (b, c) *Inclined* Layout. The distribution of the number of strip hits as a function of η of the simulated tracks with fixed vertex position is shown in (e).
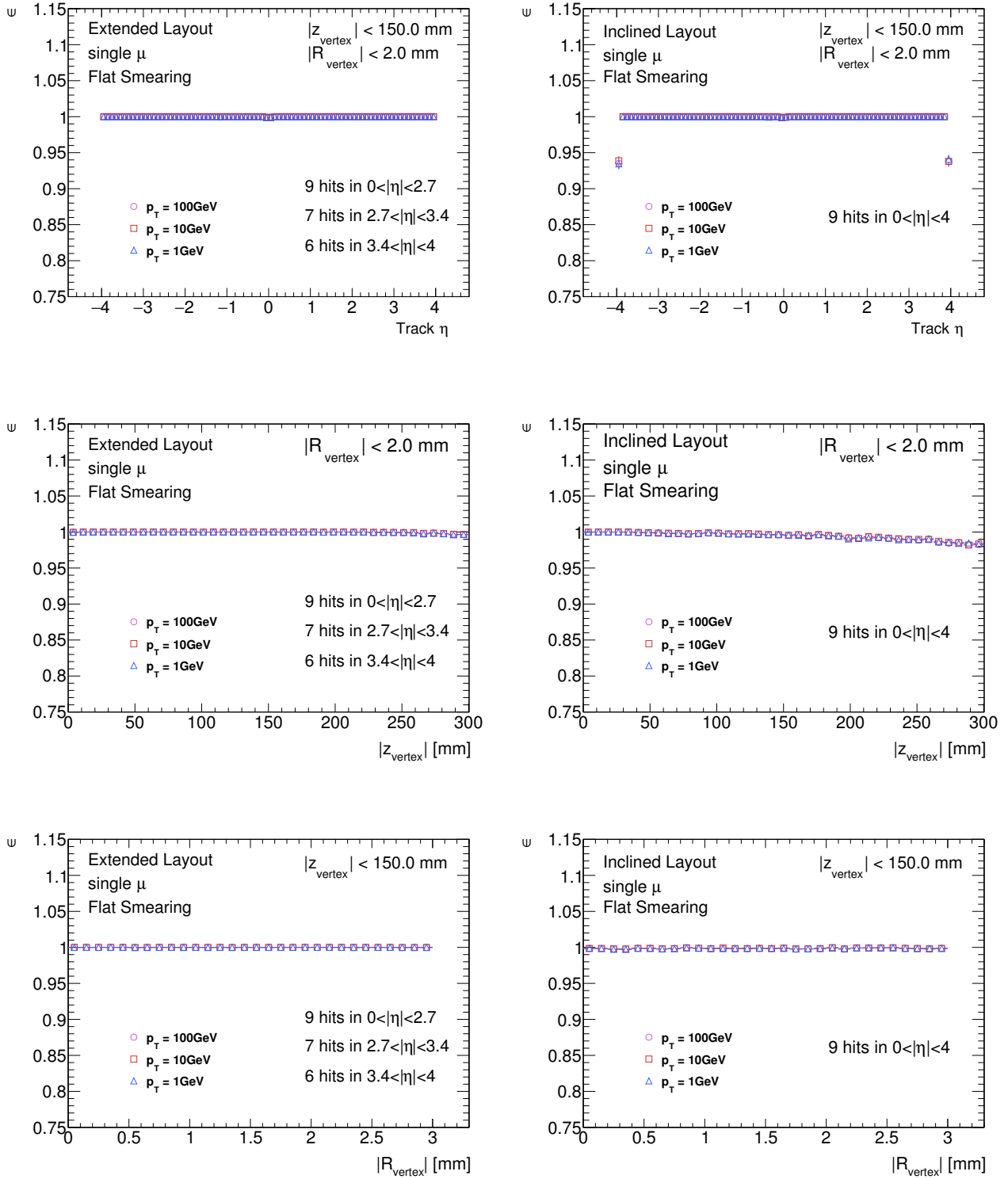
Figure 9.5: Geometrical efficiency as a function of η (top), z_{vertex} (middle) and $|R_{\text{vertex}}|$ (bottom) of the simulated tracks with flat smearing of the vertex position for the *Extended* (letf) and *Inclined* (right) Layout. Two two layouts are hermetic for vertices lying within ± 150 mm in z and with radial displacement of 2 mm. The geometrical tracking efficiency for the *Inclined* Layout slightly decreases when $|z_{\text{vertex}}| > 150$ mm: the hermeticity requirement is not fulfilled by tracks originated in the tilted region ($|z_{\text{vertex}}| > 180$ mm) that escape the detector passing in between inclined modules at small $|\eta|$. The geometrical tracking efficiency shows no strong dependence on the R displacement of the vertex.
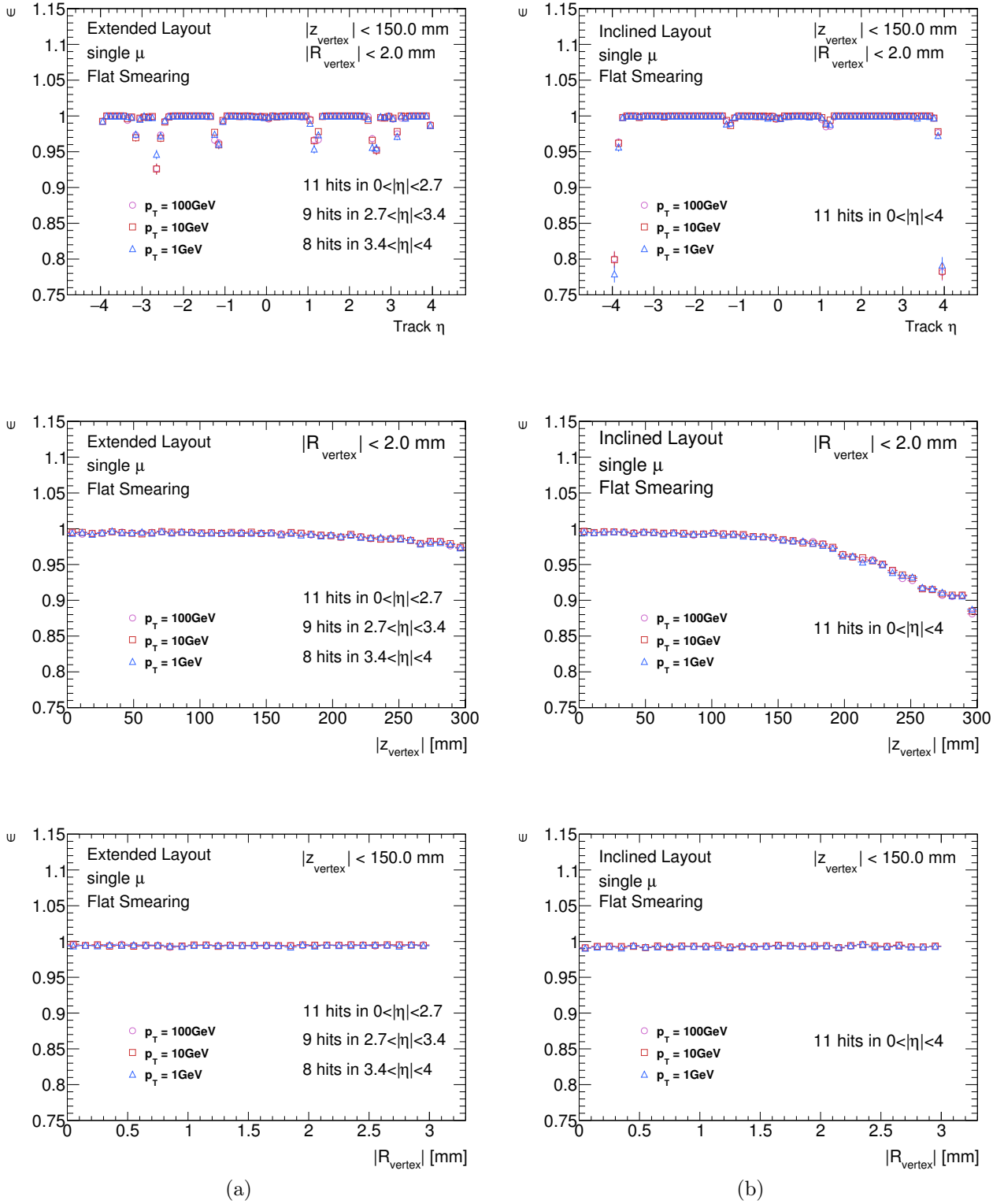
Figure 9.6: Geometrical efficiency as a function of η (top), z_{vertex} (middle) and $|R_{\text{vertex}}|$ (bottom) of the simulated tracks with flat smearing of the vertex position for the *Extended* (letf) and *Inclined* (right) Layout requiring two additional hits. The geometrical tracking efficiency is reduced of approximately $\sim 5\%$ ($\sim 2\%$) in at the strip barrel/end-cap transition region, i.e $|\eta| \approx 1.2$, for the *Extended* (*Inclined*) Layout. A reduction is also seen at $|\eta| \approx 2.6$ and $|\eta| \approx 3.2$ for the *Extended* Layout. For vertices outside ± 150 mm in z, the *Inclined* Layout shows a reduction of the efficiency up to a maximum of about 10% for a maximal z displacement of the vertex of 30 cm. The geometrical tracking efficiency shows no strong dependence on the R displacement of the vertex.

geometrical tracking efficiency decreases when $|z_{\text{vertex}}|$ is beyond 150 mm.

Keeping in mind that additional studies based on more sophisticated tools are needed to understand the impact of the luminous regions on the tracking performance, the coverage studies are showing that both layout need a proper optimisation in order to cope with a wider spread of the primary vertex position along the beam axis.

9.3   Conclusions

Both candidate layouts show full geometrical coverage in terms of required offline measurements throughout the pseudo-rapidity range as shown in Figure 9.1 and Figure 9.4. Moreover, the geometrical coverage results to be stable for the studied transverse and longitudinal vertex-smearing scenarios and different transverse momenta.

A very good geometrical coverage can be maintained by requiring an additional redundancy of 2 measurements more than the offline requirement. In this case the geometrical coverage shows a reduction in the barrel region with a stronger dip in the barrel to end-cap transition region of the strip detector: the dip is more pronounced in the *Extended* Layout, since the *Inclined* Layout can recuperate the apparent measurement loss in this region thanks to the additional hits provided by the overlaps between modules in the inclined section.

On the other hand, the geometrical coverage is more stable for the *Extended* Layout when moving outside the required 150 mm vertex region in z, as the gaps between the barrel-like and the inclined section and the tilted modules start to become harmful. Overall, both layouts satisfy the geometrical coverage requirement.
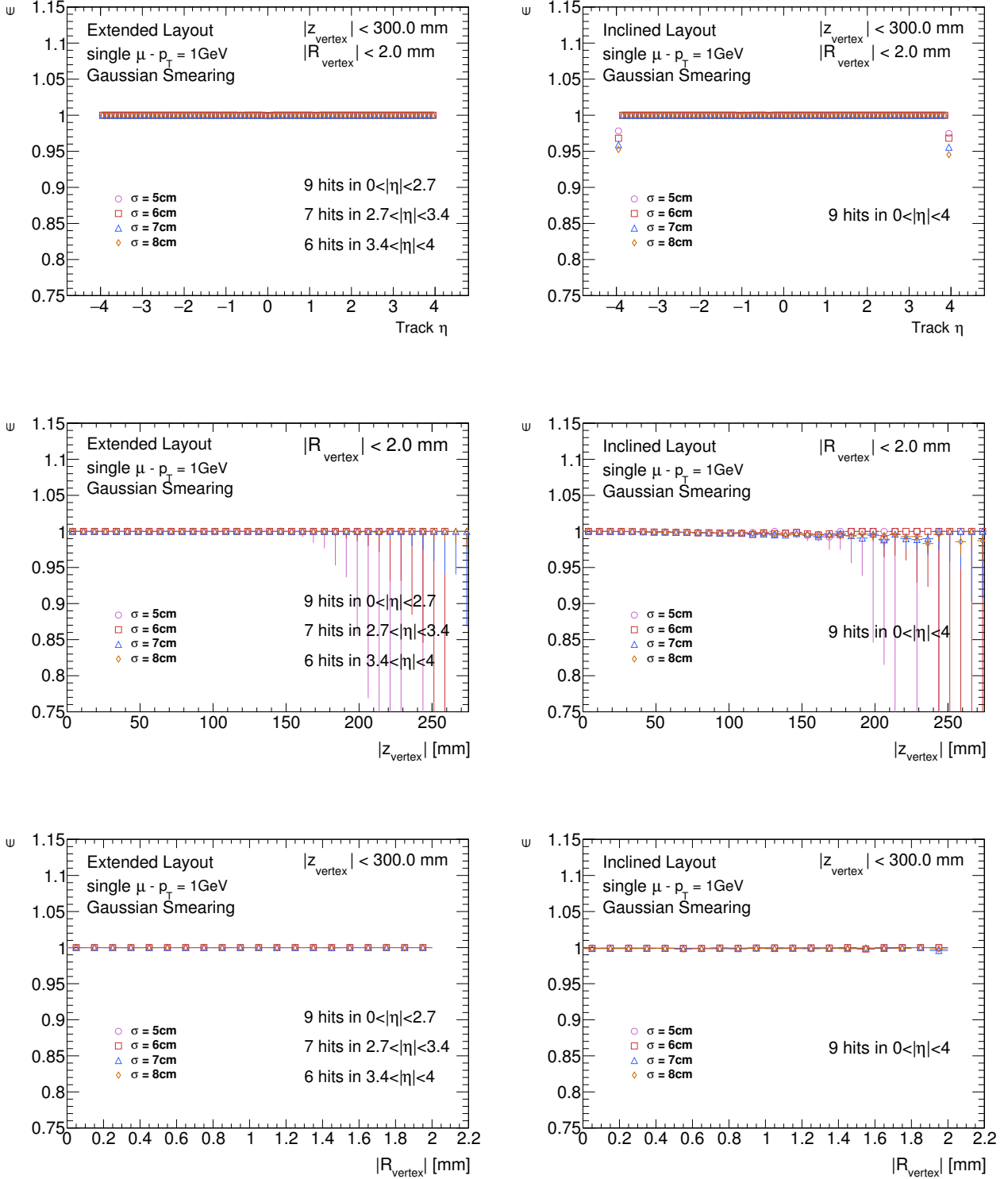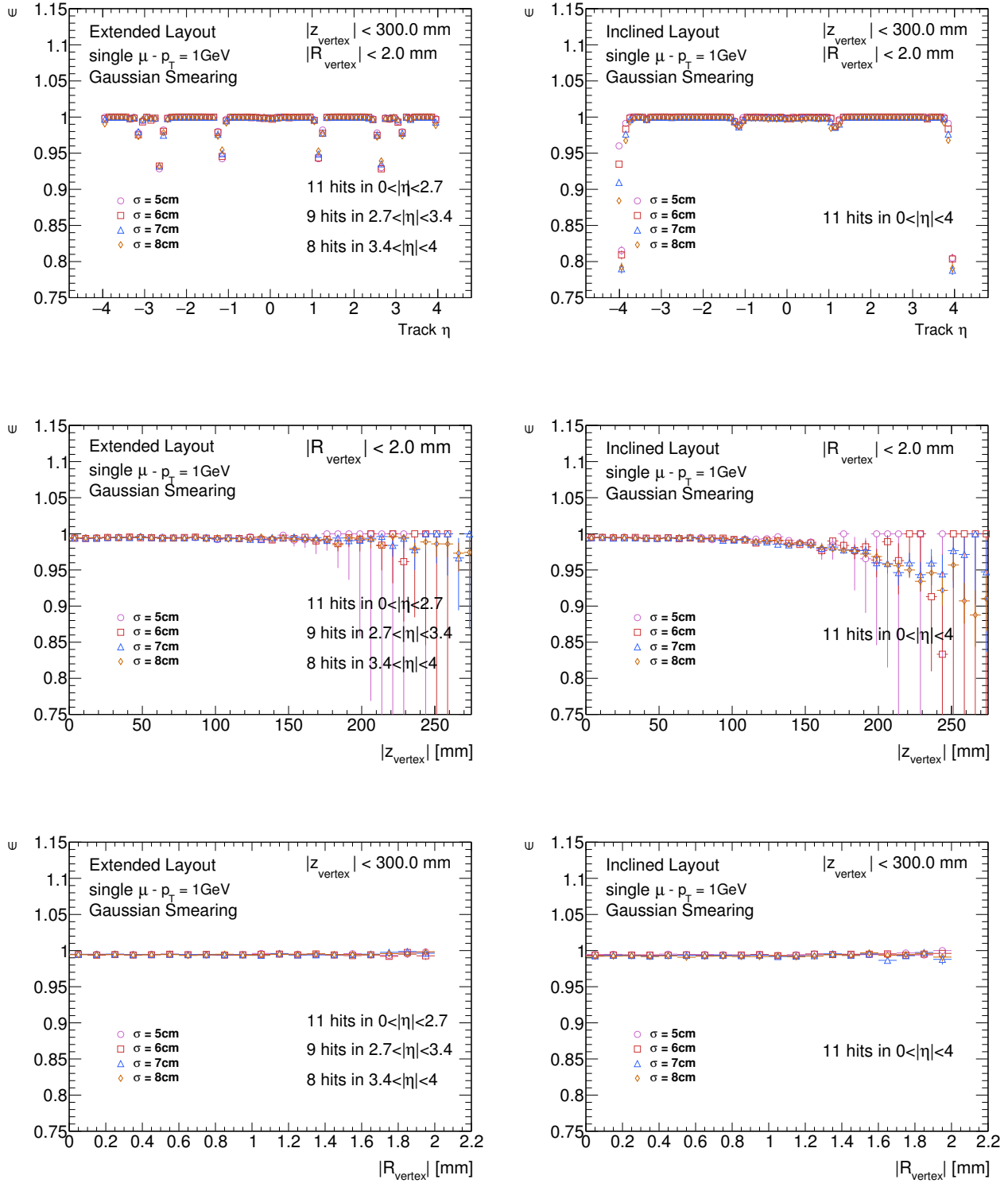
Figure 9.7: Geometrical efficiency as a function of η (top), z_{vertex} (middle) and $|R_{\text{vertex}}|$ (bottom) of the simulated tracks with Gaussian smearing of the vertex position for the *Extended* (letf) and *Inclined* (right) Layout. A reduction of the geometrical tracking efficiency is shown for the *Inclined* Layout for vertices outside ± 150 mm in z. The geometrical tracking efficiency shows no strong dependence on the R displacement of the vertex.

Figure 9.8: Geometrical efficiency as a function of η (top), z_{vertex} (middle) and $|R_{\text{vertex}}|$ (bottom) of the simulated tracks with Gaussian smearing of the vertex position for the *Extended* (letf) and *Inclined* (right) Layout requiring two additional hits. The geometrical tracking efficiency is reduced of approximately $\sim 5\%$ ($\sim 2\%$) in at the strip barrel/end-cap transition region, i.e $|\eta| \approx 1.2$, for the *Extended* (*Inclined*) Layout. A reduction is also seen at $|\eta| \approx 2.6$ and $|\eta| \approx 3.2$ for the *Extended* Layout. For vertices lying outside ± 150 mm in z, the *Inclined* Layout shows a reduced geometrical tracking efficiency. No strong dependence on the R displacement of the vertex is seen.

10

Tracking Performance Studies

Contents

10.1 Introduction

This chapter focuses on the basic track reconstruction performance of the ITk candidate layouts. Single particle samples of muons, pions, electrons and top quark pair production are used to evaluate the reconstruction performance for the specific physics objects. Track parameter resolutions, efficiencies and fake rates are studied for different layout configurations. This includes changing the radius of the innermost pixel layer or the readout segmentation, and is tested in presence of pile-up events, module misalignment and detector ageing effects. This allowed to determine strengths and weaknesses of the layout candidate's designs and to define the inputs that were used to develop the final ITk layout described into the ATLAS ITk Strip and Pixel TDRs [58, 104]. When possible, comparisons with results obtained with the ATLAS Run-2 detector are included.

10.1.1   Tracking Efficiency and Fake Rate

Two of the most important performance criteria for a tracking detector are the reconstruction efficiency and the rate of reconstructed tracks from accidental grouping of hits. It is possible, indeed, that fake tracks are reconstructed from random association of clusters or noise hits.

The reconstruction efficiency is defined as the fraction of particles which are associated with tracks passing the track quality selection cuts listed in Table 8.1. Particles considered must satisfy $p_T > 1\,\mathrm{GeV}$ and $|\eta| < 4.0$, and be produced by the primary interactions. Secondary particles produced by GEANT4 during simulation are not considered for this study.

The matching between the reconstructed and the generated charged particle is done using a measurement based matching procedure. A matching probability is defined as follows:

$$P_{\mathrm{match}} = \frac{2N_{\mathrm{common}}^{\mathrm{pixel}} + N_{\mathrm{common}}^{\mathrm{strip}}}{2N_{\mathrm{track}}^{\mathrm{pixel}} + N_{\mathrm{track}}^{\mathrm{strip}}} \tag{10.1}$$

where $N_{\mathrm{common}}^{\mathrm{pixel/strip}}$ is the number of common pixel/strip clusters between the reconstructed track and the truth particle. $N_{\mathrm{track}}^{\mathrm{pixel/strip}}$ is the number of pixel/strip measurements assigned to the track. The factor 2 in the pixel terms is a relative weight and takes into account the fact that each pixel layer provides one 2D measurement while a double sided strip layer provide two 1D measurements. The truth particle corresponding to the highest P_{match} to the reconstructed track is considered as matched. Given this definition of the matching probability, a track with clusters associated to the same truth particle has $P_{\mathrm{match}} = 1.0$. In general, the bigger the number of clusters of a reconstructed track deriving from other truth particles, the lower is the value of the matching probability. For a successful match, a $P_{\mathrm{match}} = 0.5$ is required. Hence, the tracking efficiency is defined as:

$$\varepsilon = \frac{N_{\mathrm{reco}}^{\mathrm{selected,\ matched}}}{N_{\mathrm{truth}}^{\mathrm{selected}}} \tag{10.2}$$

where the numerator contains the number of selected reconstructed tracks matched to a selected truth particle with $P_{\mathrm{match}} > 0.5$ and the denominator the number of selected truth particles.

Tracks with a matching probability smaller than 0.5 are defined as fake tracks. A unique matching to a generated particle is not possible any more due to too many measurement assignment errors. The fake rate can be then defined as:

$$r = \frac{N_{\mathrm{reco}}^{\mathrm{selected,\ unmatched}}}{N_{\mathrm{reco}}^{\mathrm{selected}}}. \tag{10.3}$$

Previous studies [62, 102] have shown that the fake rate can be well controlled requiring a sufficiently high number of measurements to define a successfully reconstructed track. In addition, a strict requirement on the number of holes, i.e. missing measurements on a track where one would expect to have hit an active sensor, has proven to be a strong suppressor of fake tracks.

Two different definitions of track reconstruction efficiency have been introduced in order to distinguish among pattern recognition and detector effects.

- The *technical track reconstruction efficiency* represents the efficiency to find "reconstructable" tracks. This is evaluated from particles that have produced sufficient measurements in the detector to pass the reconstruction cuts. By definition, this efficiency doesn't depend on the detector material and neither on layout hermeticity issues and thus tests mainly the pattern recognition quality.

- For the *physics track reconstruction efficiency*, the requirement of sufficient hits to be produced by the particles is dropped. Hence it is sensitive to the amount of material experienced by the

particle before reaching the required number of measurements and layout hermeticity. It depends on the particle type, its momentum, initial direction and production vertex.

10.1.2 Track Parameter Resolutions

The trajectory of a charged particle in presence of a solenoidal magnetic field can be parametrised with a minimum set of five parameters, the so-called track parameters. In ATLAS, the choice of the five parameters is:

$$\tau = \left(l_0, l_1, \phi, \theta, \frac{q}{p} \right) \tag{10.4}$$

where the first two parameters describe the local measurement at a given reference surface, and the latter three parameters are a global representation of the signed particle momentum. The perigee parameters define the track at its point of closest approach to the beam line. This is characterised by the transverse, d_0, and longitudinal, z_0, impact parameters as local representation. The definition of the parameters was already shown in Figure 2.10.

The measurement error is described as a 5 dimensional covariance matrix that also hosts the correlation terms between the track parameter errors. Track resolutions are noted as the difference between the measured track parameters and the true track parameters taken from the simulation input. Same selection criterion, as for the efficiency calculation, are applied to tracks used to calculate the resolution: tracks must be matched to a truth particle with $P_{match} > 0.5$. The resolution on the track parameters is obtained from the RMS of the core of the distribution of the difference between the reconstructed and true values of the parameters[1].

Since the angular resolutions are very precise and in addition not often explicitly used, focus is usually on the impact parameter and the momentum resolution as classifications of the track resolution measurement.

10.1.2.1 Impact Parameter Resolutions

The accuracy in the reconstruction of primary and secondary vertices depends on the resolutions on the impact parameters. A good impact parameter resolution is crucial to associate tracks to the correct vertex and to tag b-hadrons and τ leptons from the reconstruction of secondary vertices.

As shown in § 2.2.3.3, the impact parameter resolutions are dependent on the achievable intrinsic detector resolution, the amount of material and its location in the tracking volume and the geometrical configuration of the layout. The choice of the sensor technology, the alignment conditions and the precision in the positioning and orientation of the modules, as well as the material along the track and between the measurements can therefore affect the track parameters. In particular, while the impact parameter resolutions are mostly influenced by the intrinsic resolution, material and radial configuration close to the interaction point, the momentum resolution is sensitive to the evolution of the track through the entire tracking volume.

At the time these studies were performed, many details on the ITk pixel sensor technology were not yet decided, which left an uncertainty on the resolution prediction. In order to mitigate potential errors on the measurement estimation, different algorithms have been developed to reflect an ultimate and a pessimistic scenario. A bracketing method has then been defined, whose extremes are evaluated using the truth-based clustering algorithm to derive the ultimate performance, and the digital clustering for the pessimistic one.

The truth-based clustering algorithm is used setting the intrinsic measurement resolution to 5 μm.

---

[1]The RMS is used to catch non-Gaussian shapes in the measured distributions.

The choice of 5 μm is hereby arbitrary though motivated by the fact that it is more than a factor 2 better than a naive resolution to be achieved by assuming the pitch size. Figure 10.1 shows the residual distribution between the cluster and the true positions in the transverse plane (local x direction on the sensor) and longitudinal direction (local y direction on the sensor) on the innermost layer as a function of the local incident angle.

For the description of the pessimistic performance the digital clustering algorithm is used, as described in § 8.2.3, including the modifications for long clusters which is applied in all layouts. Compared to the truth-based clustering approach, the digital clustering takes readout thresholds into account and thus results in the most realistic cluster shapes. In addition, the ultimate approach doesn't include simulation effects within the silicon sensor, most prominently knock-off electrons are only respected accurately in the digital clustering method.

The other component contributing to the impact parameter resolution is the influence of multiple scattering on the track measurement. Multiple coulomb scattering is a stochastic process with zero mean value and a variance that depends on the amount of traversed material. It is inverse proportional to the particle's momentum [7] and dominates the resolution for low momentum particles while the intrinsic resolution dominates at high particle momentum.

10.2 Tracking Performance Studies and Results

10.2.1 Efficiency Studies in Absence of Pile-up

As described in § 8.2.3, the last steps of track reconstruction consists of building track candidates. Ambiguities in the assignment of clusters to competing tracks are resolved and the final track fits are performed.

The technical track reconstruction efficiency for track candidates from $t\bar{t}$ events without pile-up is shown in Figure 10.2, comparing the *Extended* and the *Inclined* candidate layouts. The *Extended* Layout shows a lower technical track reconstruction efficiency in a range from $2.0 < |\eta| < 3.5$, which is shown to disappear at higher momentum (see Figure 10.3). The technical track reconstruction efficiency doesn't depend on hemeticity problems neither on nuclear interaction effects. For this reason, the source of the inefficiency must thus be in the track finding or fitting stage. Further studies were then performed to recuperate the technical efficiency, as shown in Figure 10.4a. Better performance cannot be achieved by increasing by 50% the road window for the combinatorial track finding. However, relaxing in addition the initial transverse impact parameter cut for track seeds and track candidates to 10 mm allows an almost complete recovery of the technical track reconstruction efficiency. When performing the final tack fit, see Figure 10.4b, most of the additionally found tracks are anyway dropped or lost again, indicating that they suffer from a rather poor quality. Further investigations showed that the strongly non-homogeneous magnetic field in $|\eta| > 2.0$ can provide wrongly estimated seed parameters, i.e. impact parameters and transverse momentum, which are derived assuming a helical track model. This is also proved by the fact that the *Inclined* Layout results to be less affected since it allows for shorter seeds where field inhomogeneity is more harmful.

Figure 10.5a shows the technical track reconstruction efficiency for the *Extended* and *Inclined* Layouts after the ambiguity solving stage for top pair production sample without pile-up while Figure 10.5b shows the final physics track reconstruction efficiency for the same sample. The drop in efficiency for the *Extended* Layout at track candidate level (see Figure 10.2) is slightly enhanced after ambiguity solving (see Figure 10.5a), which indicates that the track scoring and track fitting reject additional candidates that are matched to generated particles. Moreover, from Figure 10.5b, the *Extended* Layout shows a lower physics efficiency in the forward region with respect to the *Inclined* Layout, even when
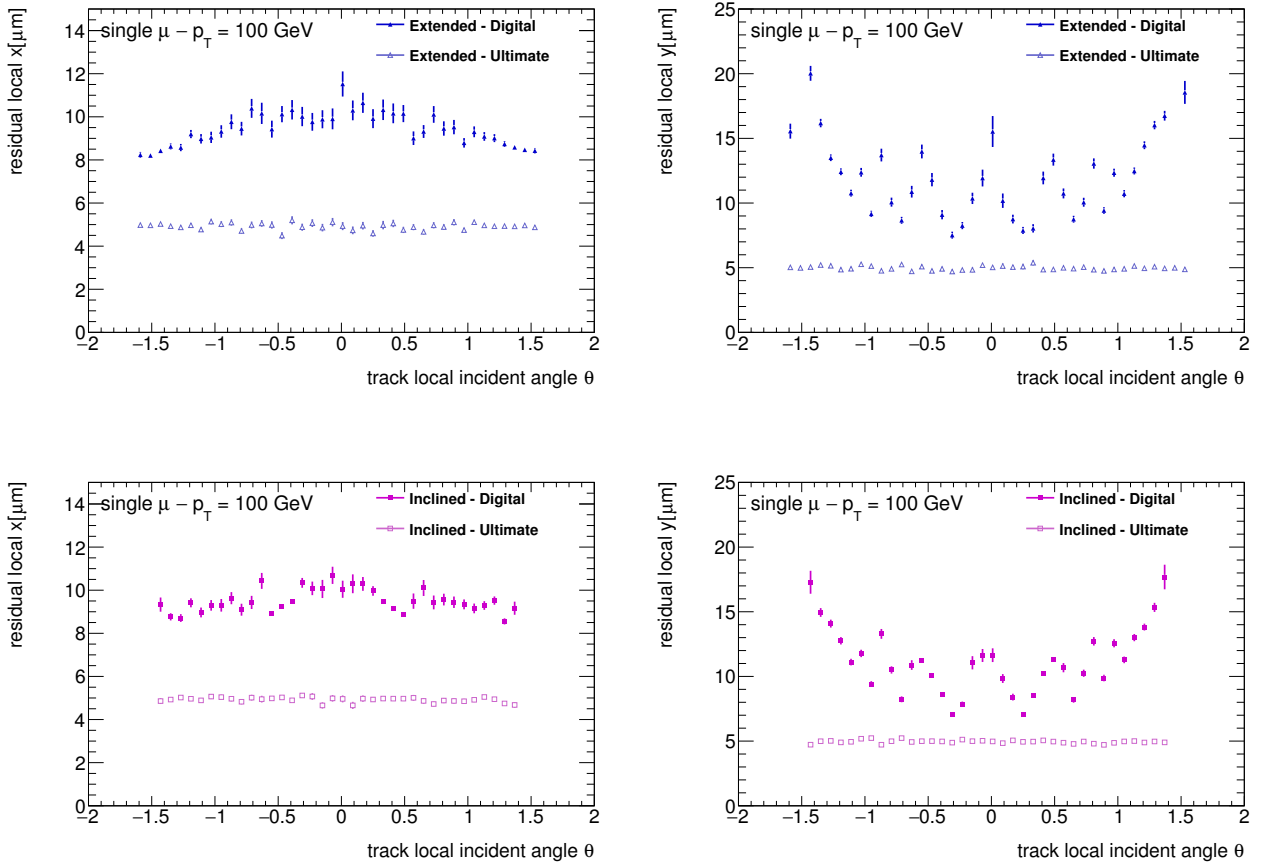
Figure 10.1: Residual distribution between the cluster and the true positions in (left) the transverse plane and (right) longitudinal direction on the innermost layer as a function of the local incident angle for (up) the *Extended* and (bottom) *Inclined* candidate layouts. The transverse plane and longitudinal directions correspond to the local-x and local-y directions on the sensor plane, respectively. The ultimate performance shows the expected 5 μm intrinsic measurement resolution.
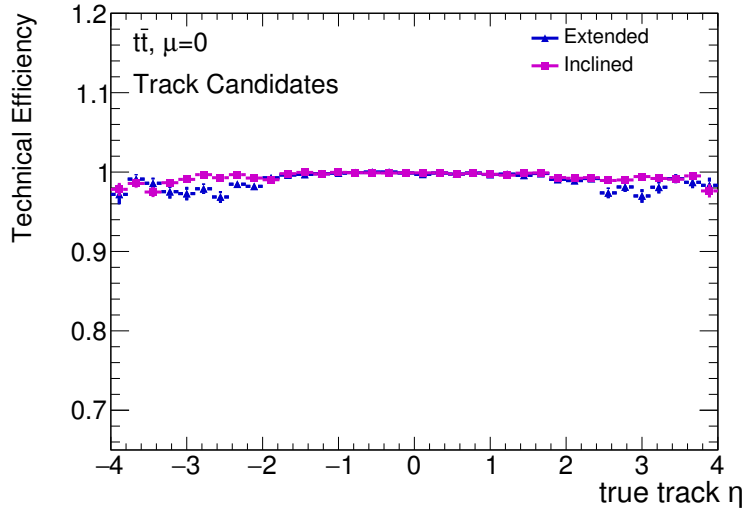
Figure 10.2: Technical track candidate efficiency for *Extended* and *Inclined* Layouts for top pair production events without pile-up [120]. The *Extended* Layout shows a lower technical track reconstruction efficiency in $2.0 < |\eta| < 3.5$ which disappears at higher transverse momentum (see Figure 10.3).

the required numbers of measurements on track is reduced.

As mentioned already, the physics track reconstruction efficiency depends on the amount of material seen by the track before reaching the required number of measurements. Previous studies [119] have shown that the number of measurements on a track is usually required to be higher than the minimum number of measurements needed to constrain the degrees of freedom in the track fit in order to suppress fake combinatorics, which rapidly decrease when raising the measurement requirement.

Figure 10.6 depicts the amount of material in terms of nuclear interaction length that is passed on average by a particle before reaching the reconstruction hit requirement for the two layout candidates. Here the layout features are visible: the excess of material in the barrel-inclined transition region (described in § 8.2.1.1) leads to a slightly alternating structure in the comparison between the two layout candidates in the region around $1.25 < |\eta| < 1.75$. This results into a higher amount of material seen by a particle in the *Inclined* Layout compared to the *Extended* Layout before reaching the required 9 hits in the region around $|\eta| \approx 1.5$. Above $|\eta| \sim 2.0$, the *Extended* Layout has a higher probability for particles to undergo nuclear interactions before reaching sufficient hits to be reconstructed which results in a lower physics reconstruction efficiency. Figure 10.5b also shows that although requiring substantially more hits for a successfully found track candidate the efficiency in the comparable region is almost identical to the ATLAS Run-2 layout. This reflect the fact that the ITk candidate layouts have relatively less material per measurement compared to the ATLAS Run-2 tracker (see Figure 10.6). The difference in the rate of nuclear interactions is also shown when considering the efficiency for single electrons and single pions (see Figure 10.7). As explained in § 8.2.3.5, the ability to reconstruct electrons is limited by the amount of material that can lead to significant energy loss through radiation. Both candidate layouts show a high reconstruction efficiency for high momentum electrons, with a slightly higher efficiency for the *Inclined* Layout. Differences between the candidate layouts are more pronounced at lower momenta and in the forward region given by the different amount of material traversed by the particles. The *Inclined* Layout shows a very much improved electron efficiency in the region $3 < |\eta| < 4$ compared to the *Extended* Layout. Again, in the barrel-inclined transition region around $|\eta| \sim 1.5$ the Extended layout performs slightly better.
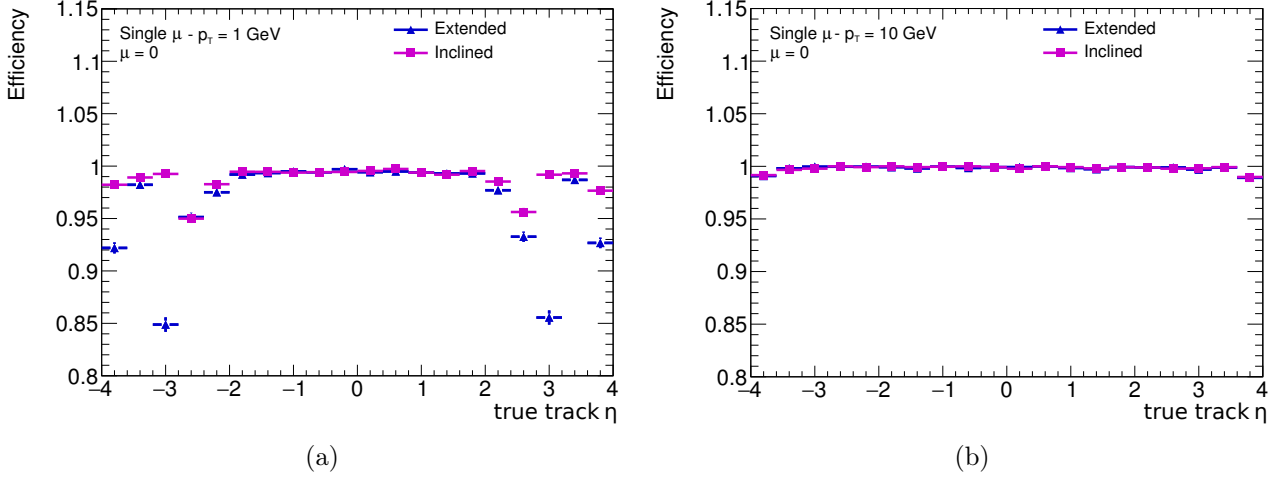
(a)　　　　　　　　　　　　　　　　(b)

Figure 10.3: Physics track candidate track reconstruction efficiency for the *Extended* and *Inclined* layout candidates for single muons with constant transverse momentum of (a) $p_T = 1$ GeV and (b) $p_T = 10$ GeV without pile-up [120]. The *Extended* Layout shows a lower physics track reconstruction efficiency in $2.0 < |\eta| < 3.5$ which disappears at higher transverse momentum.
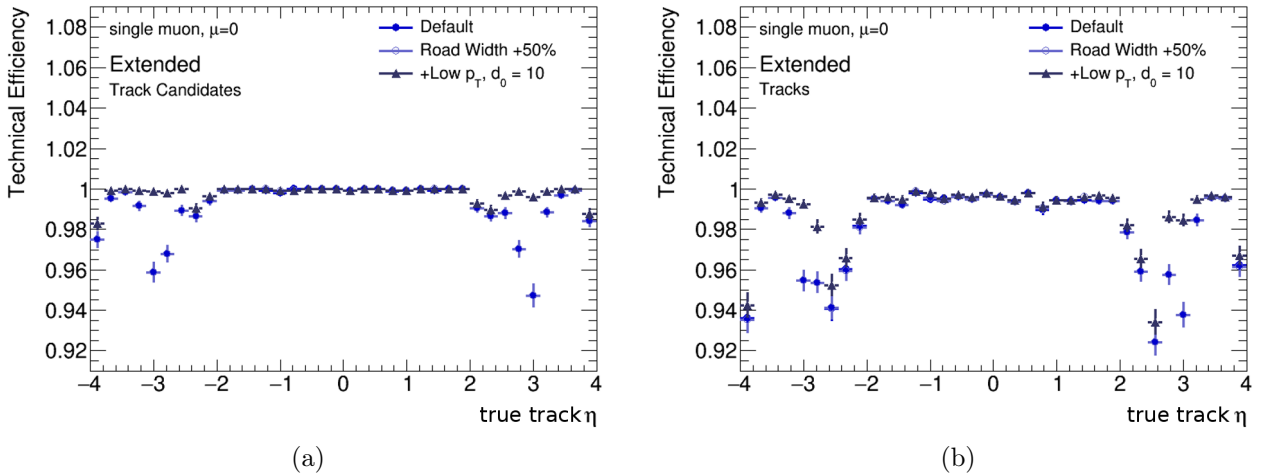

(a)　　　　　　　　　　　　　　　　(b)

Figure 10.4: Technical track reconstruction efficiency for (a) track candidates and (b) final tracks after ambiguity solving for the *Extended* Layout for single muons with constant transverse momentum of $p_T = 1$ GeV without pile-up [120]. The reconstruction cuts are relaxed in an attempt to recuperate the efficiency loss around $2 < |\eta| < 3$, as explained in the text.

(a)   (b)
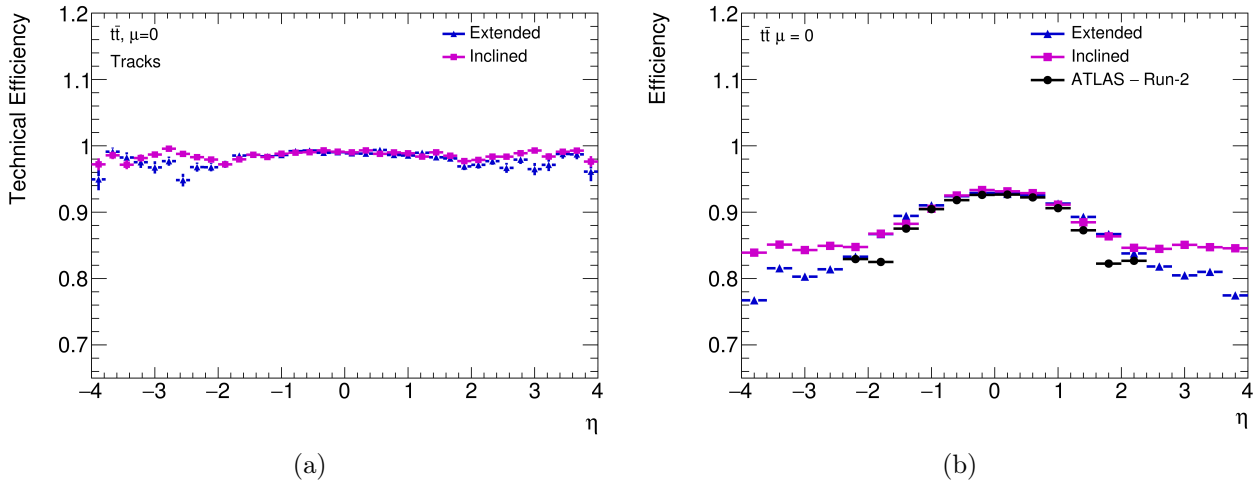
Figure 10.5: Distribution of the (a) technical track reconstruction efficiency and (b) physics track reconstruction efficiency for the *Extended* and *Inclined* Layouts for a top pair production sample without pile-up [120]. The corresponding result obtained with the ATLAS Run-2 layout is overlaid in (b). Although requiring substantially more hits for a successfully found track candidate, both layout candidates have a physics track reconstruction efficiency almost identical to the ATLAS Run-2 layout in the comparable region.
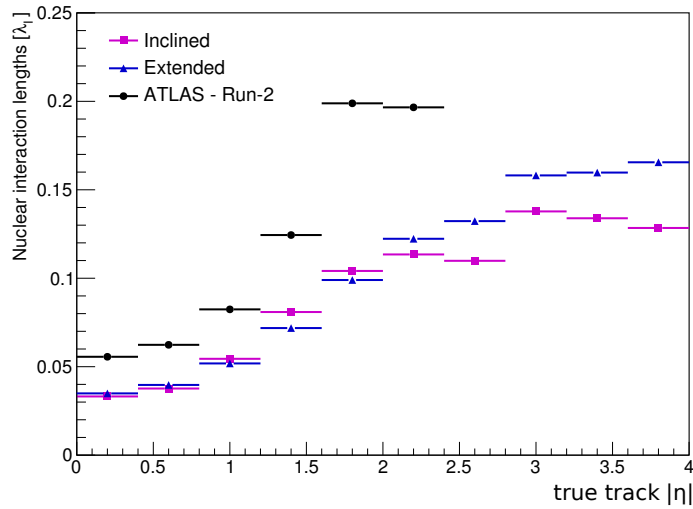
Figure 10.6: Fraction of nuclear interaction length traversed by a particle as a function of pseudo-rapidity until the reconstruction hit requirements is met for the *Extended* and *Inclined* Layouts. The corresponding result obtained with the ATLAS Run-2 layout is overlaid [111].
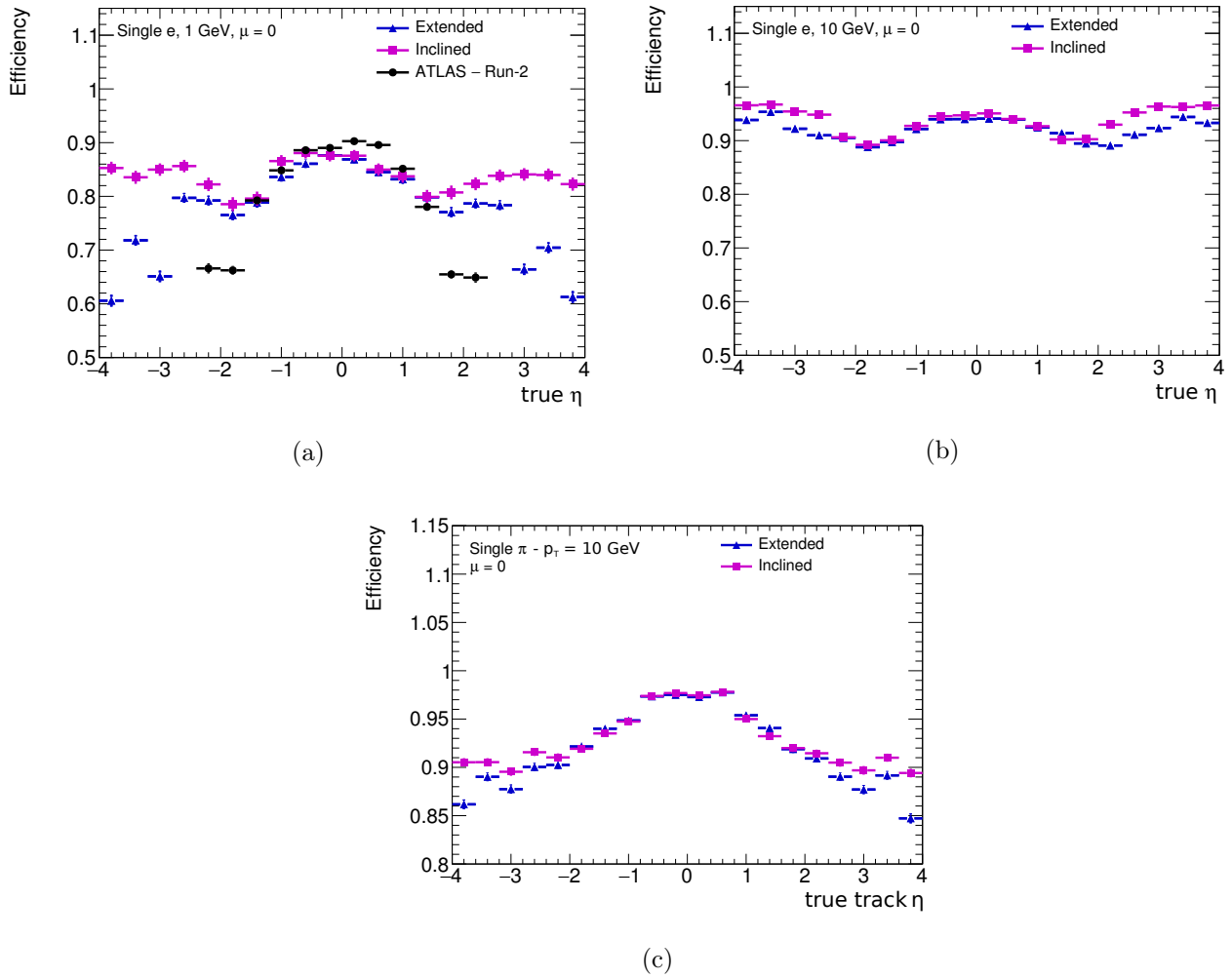
(a)

(b)

(c)

Figure 10.7: Physics track candidate track reconstruction efficiency for the *Extended* and *Inclined* layout candidates for single particle samples without pileup: single electrons with transverse momentum of (a) $p_\mathrm{T} = 1$ GeV and (b) $p_\mathrm{T} = 10$ GeV and for (c) single pions with $p_\mathrm{T} = 10$ GeV [120].

10.2.2 Track Resolution Studies

10.2.2.1 Impact Parameter and Momentum Resolution

The transverse and longitudinal impact parameter resolutions are shown in Figure 10.8 for the *Extended* and *Inclined* Layout candidates using the digital clustering. The nominal ATLAS Run-2 results are also added for comparison.

In the central region $|\eta| < 1.5$, where the two layouts are very similar both in terms of material and module positioning, almost no difference in impact parameter resolutions is visible. At higher absolute pseudo-rapidity the two layouts start to differ: for low and mid momentum, the inclination of the sensors and the additional measurements available before crossing the service material at higher pseudo-rapidity reduces the contribution of multiple scattering leading to a more precise estimation of both longitudinal and transverse impact parameters. Due to multiple scattering causing this difference, this effect is more pronounced at low momenta. At $p_T = 1$ GeV the discrepancy caused by detector material reaches about 60 (40)% at the outermost pseudo-rapidity for the transverse (longitudinal) impact parameter resolution in favour of the *Inclined* Layout. In this regime, the performance are not dependent on the chosen clustering algorithm, as shown in Figure 10.9, since multiple scattering effects dominate over the intrinsic measurement precision. In $2 < |\eta| < 2.5$ the ATLAS Run-2 performance sligthly exceeds the performance of the ITk layouts, which is caused by the smaller innermost radius provided by the IBL. A dedicated discussion on the effects of a smaller innermost radius for the ITk layouts is shown in § 10.2.2.2. In the barrel-inclined transition region, $|\eta| \approx 2.0$, where the material of the *Inclined* Layout is slightly higher compared to the *Extended* Layout, a small degradation of the *Inclined* Layout with respect to the *Extended* Layout can be seen; however, the maximum discrepancy stays below 10%. At higher transverse momentum the situation is reversed: the better resolution achieved with long clusters starts outweighing the penalty from the additional material caused by the shallow incident angle. At large pseudo-rapidity, thanks to the long clusters in the longitudinal direction, the *Extended* Layout shows better resolution for both impact parameters. In particular, for the longitudinal one the difference with the *Inclined* Layout results of about 100% in the pessimistic and about 25% in the optimistic scenario.

The comparison with the nominal ATLAS Run-2 results at high p_T shows that using charge sharing over digital clustering helps strongly to improve the impact parameter resolution, especially in the transverse component. Moreover, the smaller pixel size in the longitudinal direction for the ITk layouts with respect to the ATLAS pixel detector improves $\sigma(z_0)$ in the central pseudo-rapidity region significantly.

The momentum resolution for the two candidate layouts is shown in Figure 10.10 for muons with transverse momenta of $p_T = 1, 10, 100$ GeV. Similar performance are seen for the two candidate layouts since the inverse momentum resolution is sensitive to the overall traversed material and not on the regional differences among the two layouts.

Additional Considerations In summary, while in the central region both layouts perform very similarly, an evident difference is present in the forward region: the *Extended* Layout performs better at very high particle momenta and the *Inclined* Layout at lower particle momenta. Hence, a judgement of which layout would be preferable to be built must compare the tracking performance with respect to the expected particle momenta.

Figure 10.11a shows the p_T versus $|\eta|$ distribution of charge particles within anti-k_t $R = 0.4$ b-jets with $p_T > 20$ GeV from top decays. The average p_T of all the tracks is approximately 5 GeV. For muons from $H \rightarrow \mu\mu\mu\mu$, whose p_T versus $|\eta|$ distribution is shown in Figure 10.11b, the average muon p_T stays below 40 GeV. Figure 10.12 shows the areas in particle momenta where each of the two

layouts performs better than the alternative option for the longitudinal impact parameter resolution $\sigma(z_0)$. The plots highlights that in the overall range kinematically accessible of particle momentum an *Inclined* Layout is preferable.

10.2.2.2 Impact of Change of Innermost Radius

The impact parameter resolution depends on the positions of both the innermost and second measurements as well as their resolution; multiple scattering effects and extrapolation uncertainty reduce the influence of distant measurements in the evaluation of the impact parameters.

For the ITk layouts the innermost layer is set to 39 mm because of the constraints derived from the definition of the beam pipe and considerations regarding the maximum tolerable radiation dose (see § 7.2). To test the impact on these constraints, a dedicated study has been performed to understand the advantages in reducing the radius of the innermost layer. This has been done considering a variation of the *Extended* Layout with the innermost layer to 33 mm and replacing the ITk beam pipe with the ATLAS Run-2 beam pipe. The resulting layout is referred to as *Extended@33mm*, as mentioned in § 7.5.

Figure 10.13 shows the transverse and longitudinal impact parameter resolutions as a function of the track pseudo-rapidity for single muons with $p_T = 1, 10, 100$ GeV. At low transverse momentum, where the smallest extrapolation uncertainty can help in evaluating the impact parameters, an improvement of 10% for both $\sigma(d_0)$ and $\sigma(z_0)$ is seen across the entire pseudo-rapidity range. This improvement disappears moving to low and high transverse momentum where significantly more gain can be achieved improving the measurement resolution as shown by the performance bracket. At high transverse momentum, the impact parameter resolution tends to approach the resolution of the innermost measurement and very little gain can be achieved moving the first measurement to a smaller distance to the beam line. In the very forward region, $3.0 < |\eta| < 4.0$, a maximum improvement of about 15% is seen for the transverse impact parameter resolution.

10.2.2.3 Impact of Change of Readout Size

As anticipated, pixel sensors have a nominal pixel dimension of 50×50 μm^2. However, an alternative configuration could be using pixels of 25×100 μm^2: this would leave the number of readout channels unchanged, while changing the balance of the intrinsic measurement precision along the longitudinal direction and in the transverse plane. The two main layouts have been simulated using both readout configurations to evaluate the variation in the impact parameter resolution when reducing (increasing) the pixel pitch in the transverse (longitudinal) direction. Only the digital clustering has been used for these comparison.

Figure 10.14 and Figure 10.15 show the longitudinal and transverse impact parameter resolutions for the *Extended* and *Inclined* Layouts using the two readout scenarios.

At low transverse momentum the effects due to multiple scattering dominate with respect to the intrinsic measurement precision and very little change is seen for both layouts. For the transverse impact parameter resolution, a small improvement is seen for the *Inclined* Layout at $|\eta| > 2.5$ while the longitudinal impact parameter stays practically unchanged in both candidate layouts except for the central pseudo-rapidity region where particles traverse the modules almost at nominal incidence and the average longitudinal cluster size is small.

At $p_T = 10$ GeV, the reduced pixel pitch in the transverse plane allows to improve the transverse impact parameter resolution of about 30% in the entire pseudo-rapidity spectrum independently on the layout choice. At $p_T = 100$ GeV the improvement is even doubled.

The penalty of doubling the pixel size in the longitudinal direction starts to be visible at $p_T = 10$ GeV,
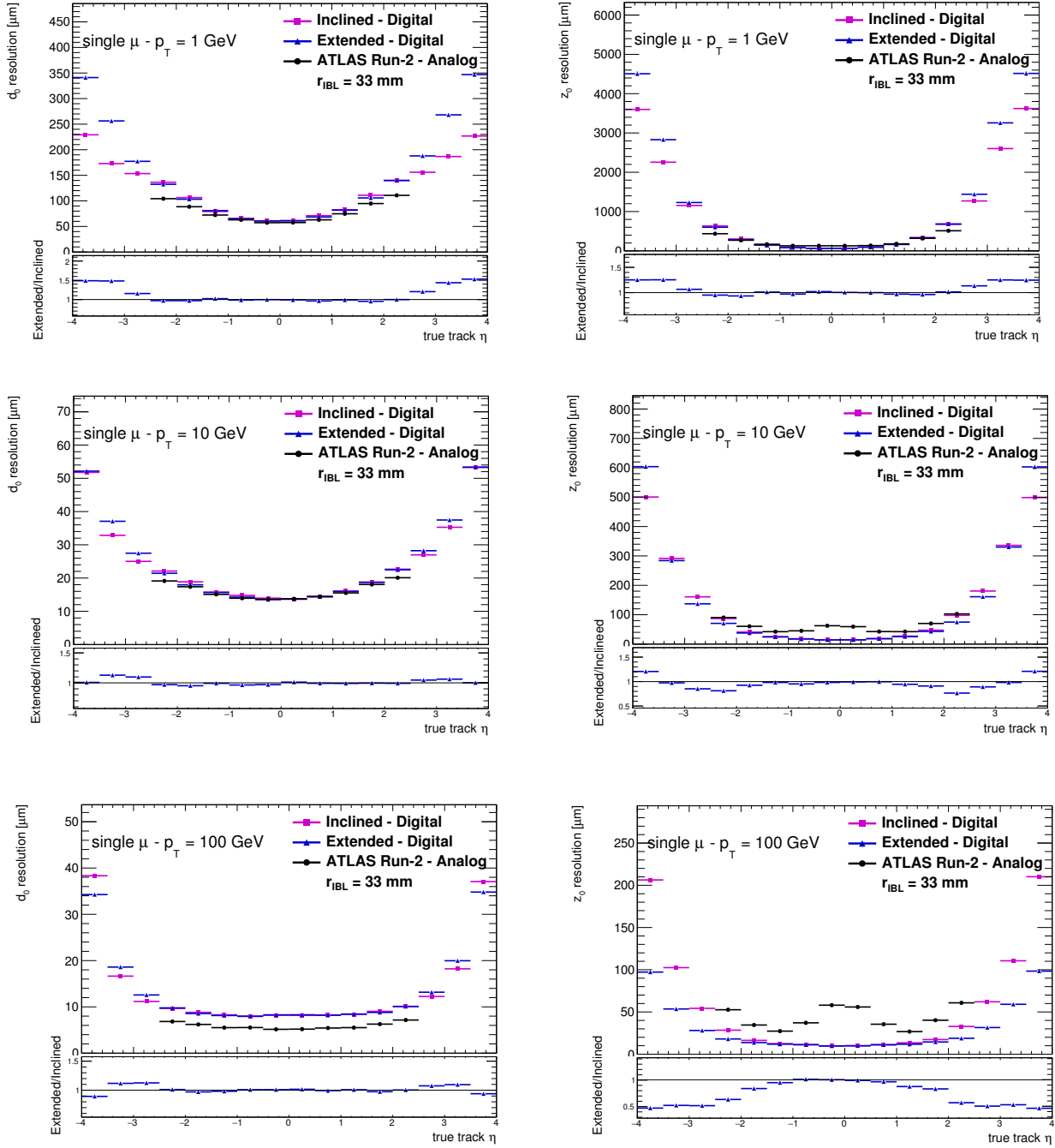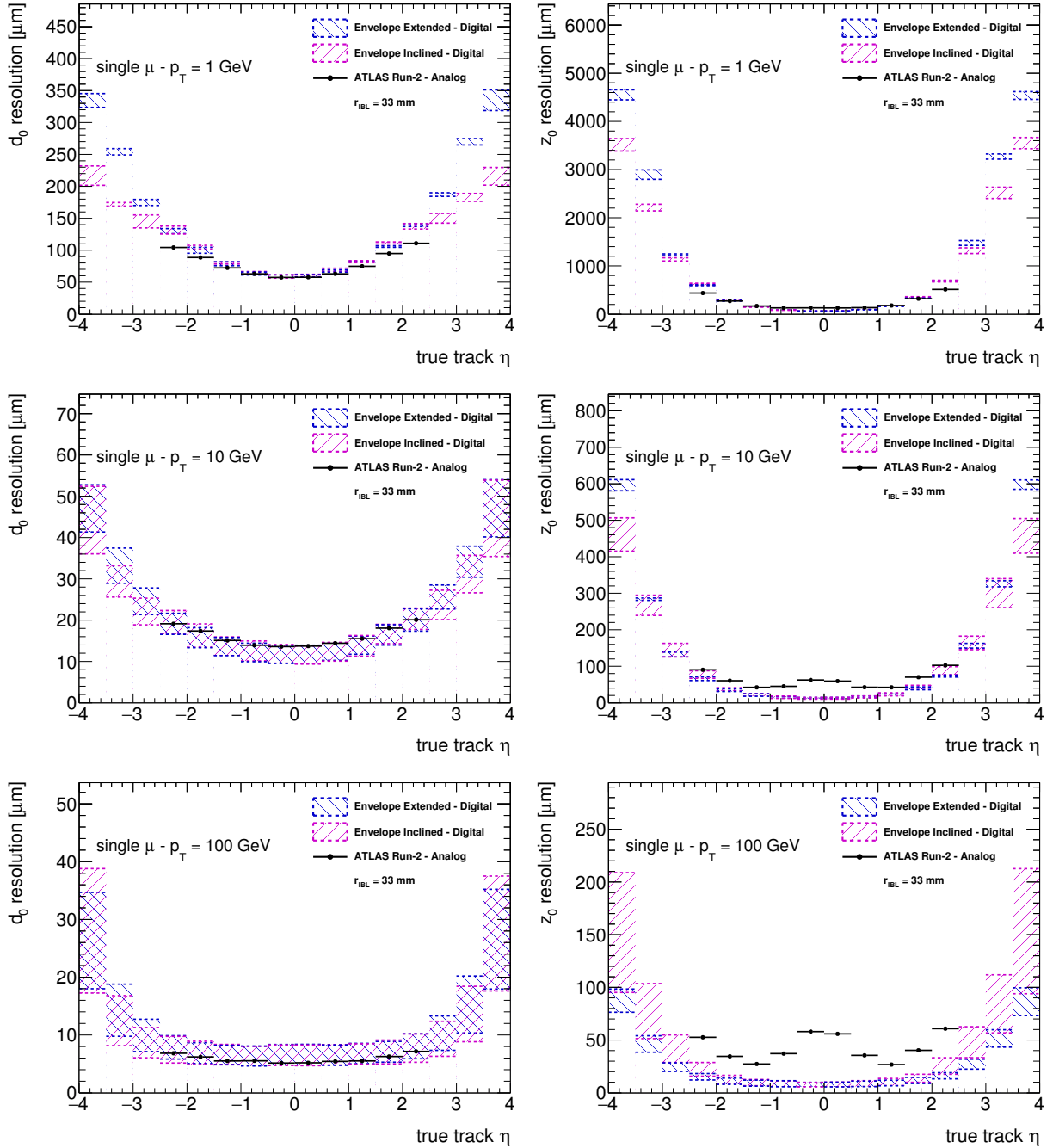
Figure 10.8: Distribution of the (left column) transverse impact parameter resolution $\sigma\left(d_0\right)$ and (right column) longitudinal impact parameter resolution $\sigma\left(z_0\right)$ as a function of the track pseudo-rapidity for single muons of constant transverse momenta of $p_\mathrm{T} = 1, 10$ and 100 GeV using for the *Extended* and *Inclined* layout candidates for the pessimistic scenario. The nominal ATLAS Run-2 results are overlaid. The bottom plot shows the ratio of the distributions for the two layouts.

The two layouts present very similar performance in $|\eta| < 1.5$. At low transverse momentum, the *Inclined* Layout returns an improvement of about $60\,(40)\%$ for the transverse (longitudinal) impact parameter resolution with respect to the *Extended* Layout. In the barrel-inclined transition region, $|\eta| \approx 2.0$, a maximum discrepancy of 10% is shown in favour of the *Extended* Layout. At higher transverse momentum, the *Extended* Layout shows better resolution for both impact parameters in the high pseudo-rapidity region.

Figure 10.9: Distribution of the (left column) transverse impact parameter resolution $\sigma(d_0)$ and (right column) longitudinal impact parameter resolution $\sigma(z_0)$ as a function of the track pseudo-rapidity for single muons of constant transverse momenta of $p_T = 1, 10$ and 100 GeV using the bracketing methods for the *Extended* and *Inclined* layout candidates. The nominal ATLAS Run-2 results are overlaid. Improving the intrinsic measurement resolution provides performance comparable to the Run-2 ATLAS ID in terms of transverse impact parameter resolution. At high transverse momentum, the performance band for the longitudinal impact parameter resolution shows an improvement of about 100% in the pessimistic and about 25% in the optimistic scenario for the *Extended* Layout with respect to the *Inclined* Layout.

(a)

(b)

(c)
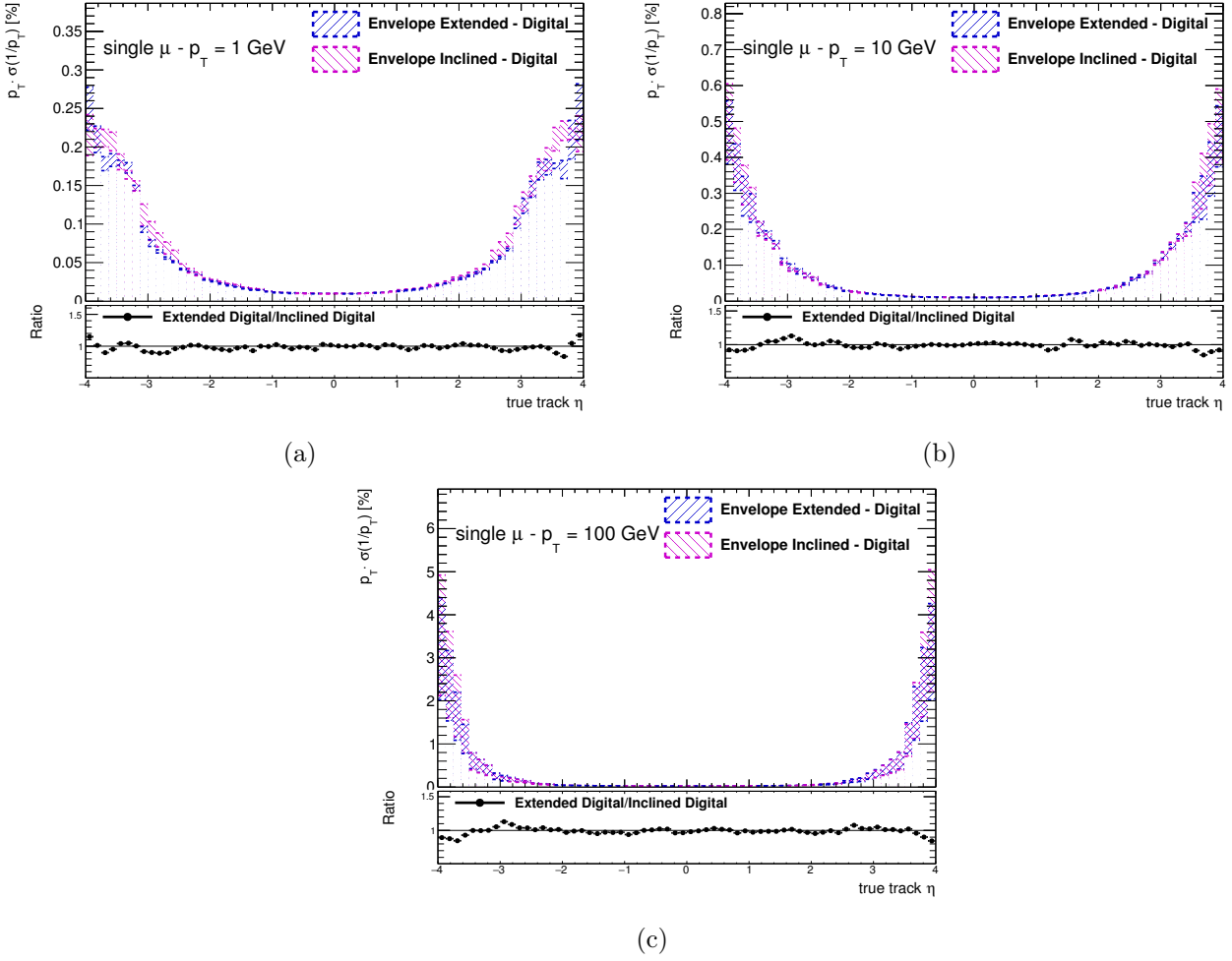
Figure 10.10: Relative inverse momentum resolution as a function of the track pseudo-rapidity for single muons of constant transverse momenta of $p_\mathrm{T} = 1, 10$ and 100 GeV using the bracketing methods for the *Extended* and *Inclined* layout candidates. The bottom plot shows the ration of the pessimistic scenarios for the two layouts. Similar performance are seen for the two candidate layouts since the inverse momentum resolution is sensitive to the overall traversed material and not on the regional differences among the two layouts.

(a)

(b)
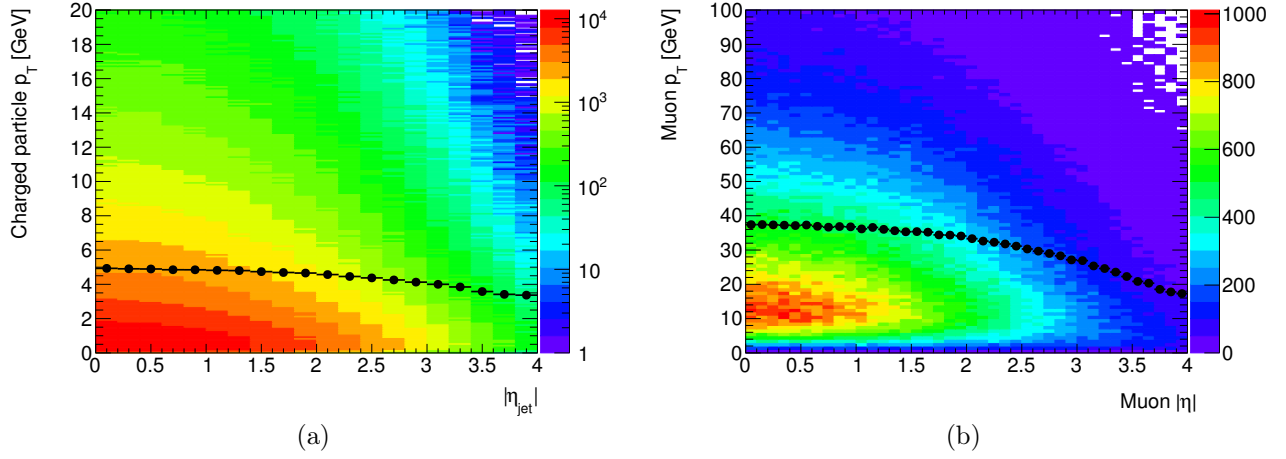
Figure 10.11: Transverse momentum p_T as a function of $|\eta|$ for (a) charged particles within anti-k_t $R = 0.4$ b-jets from top decays with jets $p_T > 20$ GeV and (b) muons from $H \to \mu\mu\mu\mu$ decays. The black dots show the average p_T of the events.
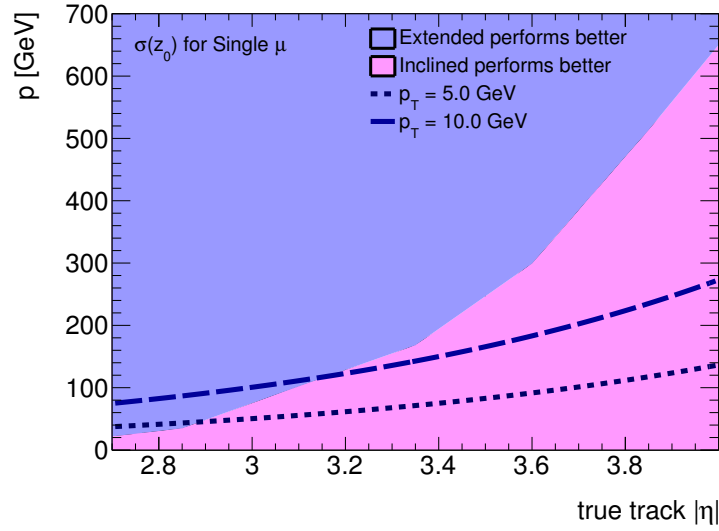
Figure 10.12: Momentum ranges in which the different layout candidates perform better in the longitudinal impact parameter resolution $\sigma(z_0)$ [120]. The lines indicate constant transverse momentum of 5 GeV and 10 GeV.
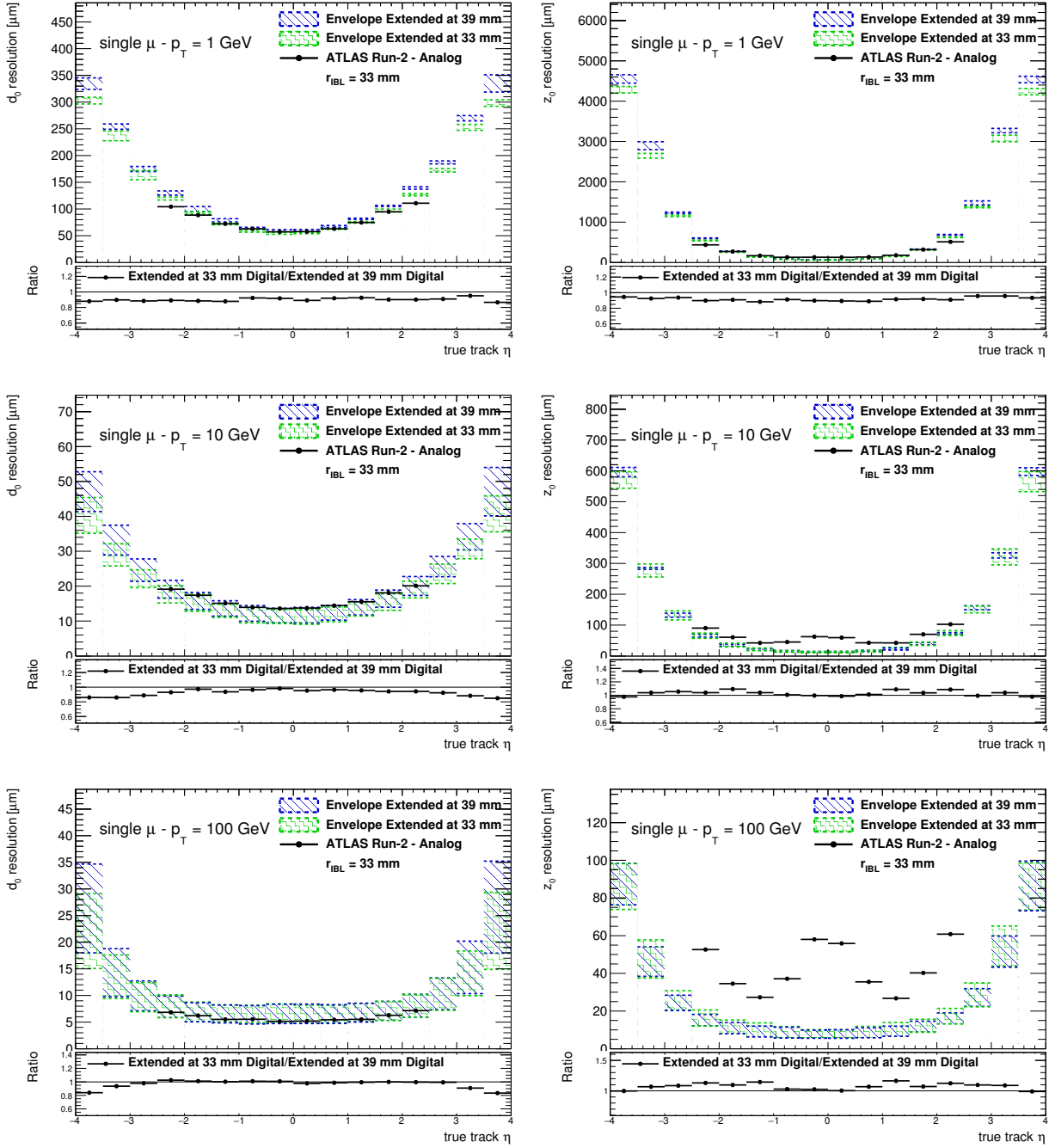
Figure 10.13: Distribution of the (left column) transverse impact parameter resolution $\sigma\left(d_0\right)$ and (right column) longitudinal impact parameter resolution $\sigma\left(z_0\right)$ as a function of the track pseudo-rapidity for single muons of constant transverse momenta of $p_\mathrm{T} = 1, 10$ and 100 GeV using the bracketing methods for the *Extended* and *Extended*@33 layout candidates. The nominal ATLAS Run-2 results are overlaid. The bottom plots show the ratios of the distributions for the pessimistic scenario for the *Extended* and *Extended*@33 layout.

At low transverse momentum, an improvement of 10% for both $\sigma\left(d_0\right)$ and $\sigma\left(z_0\right)$ is seen across the entire pseudo-rapidity range. At high transverse momentum very little gain can be achieved moving the first measurement to a smaller distance to the beam line. For $3.0 < |\eta| < 4.0$, a maximum improvement of about 15% is seen for the transverse impact parameter resolution. Significant gain can be achieved improving the measurement resolution as shown by the performance bracket.

where both layouts show a maximal degradation of about 50% in the central pseudo-rapidity region which decreases when moving in the forward region. At $p_T = 100$ GeV the longitudinal impact parameter resolutions deteriorates by 20 to 80% for both layouts in different detector region.

Figure 10.16 shown the change in the relative inverse momentum resolution for the *Extended* and *Inclined* Layouts when using 50×50 μm^2 and 25×100 μm^2 pixel dimensions. The improved transverse impact parameter resolution translates into a more precise measurement of the transverse momentum. At higher p_T, where for both layouts a sizeable effect is seen, an improvement of 20 to 50% when moving from the central to the forward pseudo-rapidity region.

Better performance for both the impact parameter and momentum resolutions can be achieved when using the analog clustering which improves the intrinsic measurement precision.

10.2.2.4 Impact of Change of Sensor Thickness

The nominal thickness of pixel sensors has been defined to be 100 μm for layers and rings inside the IST and 150 μm elsewhere. However, during the first iterations of the layout definition, a different scenario using only sensors with a thickness of 150 μm was studied. Digital clustering is being used in these comparisons.

Decreasing the sensor thickness leads to a reduction of the traversed material which translates into a reduction of material effects in the silicon, such as δ-ray production and multiple scattering. On the other side, a shorter path in the sensitive area implies a smaller cluster size in both directions. Figure 10.17 shows the cluster size in the two directions for the *Extended* and *Inclined* Layouts with sensor thickness of 100 μm and 150 μm. By definition, the *Extended* Layout is characterised by very long clusters in the longitudinal direction with respect to the *Inclined* Layout. In the transverse plane, the cluster size is driven by the Lorentz shift: in the tilted region of the *Inclined* Layout, where the electric field in the sensor and the solenoidal magnetic field are not perpendicular, the magnitude of the Lorentz shift is reduced. Thicker sensors imply a bigger cluster size in both directions as expected. Figure 10.18 and Figure 10.19 show a comparison of the transverse and longitudinal impact parameter resolutions for the two thickness scenarios for the *Extended* Layout and *Inclined* Layout respectively. At low momenta, the change in the sensor thickness has a small effect of about $\sim 5\%$. In this regime where multiple scattering is dominating, the different cluster sizes are negligible.

At $p_T = 10$ GeV, changing the thickness from 150 μm to 100 μm provides an improvement in the longitudinal impact parameter resolution of about 30% and 15% respectively for the *Extended* and *Inclined* candidate. Moreover, for the *Inclined* Layout this improvement is restricted to the inclined part of the barrel. At higher momenta, where the cluster size plays a more important role, the two layouts behave differently. The reason of the different behaviour has to be derived from the difference in the cluster sizes for the two layout concepts. The reduction of the cluster size implies better control of the pattern recognition for the *Extended* Layout that is then translated into better resolution, in particular in the longitudinal direction. On the contrary the reduced charge sharing effects for smaller clusters degrades the performance of the *Inclined* Layout. As shown in Figure 10.18 and Figure 10.19, at $p_T = 100$ GeV thinner sensors allow the *Extended* Layout to gain up to a factor 2 in resolution in the longitudinal direction and 50% in the transverse plane while a degradation of about $\sim 20\%$ in both $\sigma(d_0)$ and $\sigma(z_0)$ is shown in the forward region for the *Inclined* Layout.

10.2.2.5 Integration of Angular Measurement into the Track Fit

The *Extended* Layout is characterised by long clusters in the innermost barrel layers produced by particles traversing modules at higher pseudo-rapidity. From the measurement of such long clusters, which represent small tracklet measurements, it is possible to derive the track angular information.
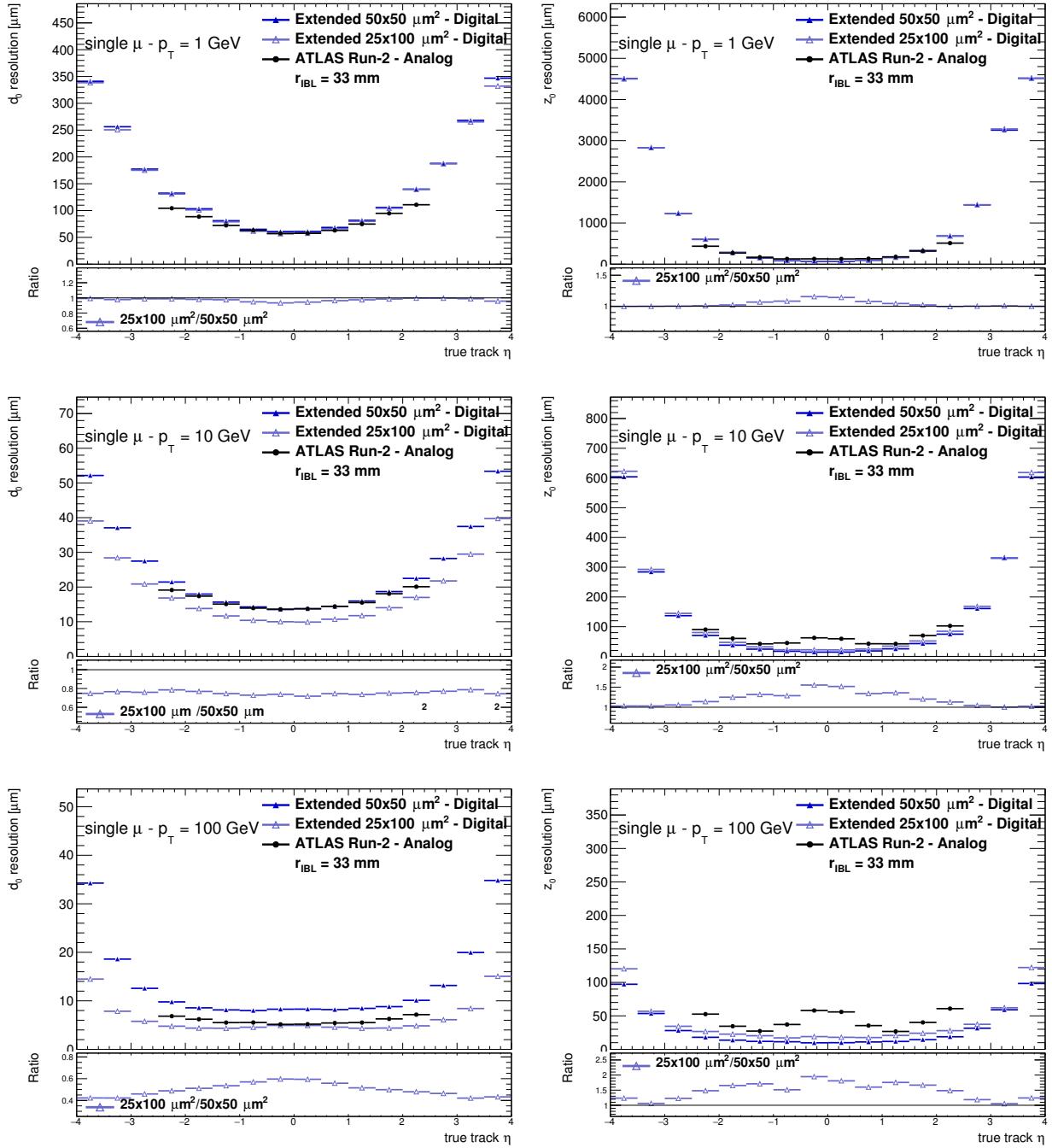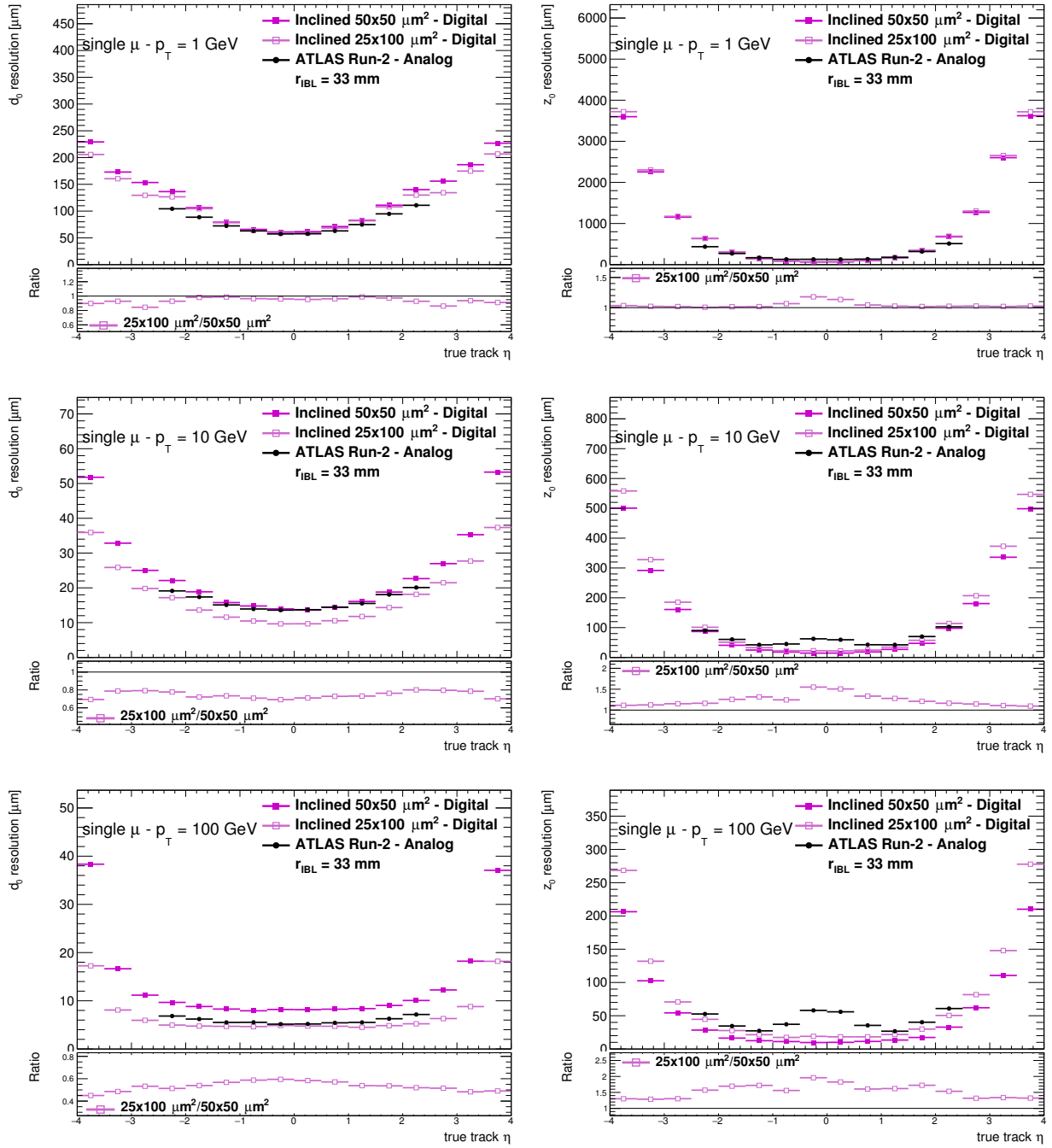
Figure 10.14: Distribution of the (left column) transverse impact parameter resolution $\sigma(d_0)$ and (right column) longitudinal impact parameter resolution $\sigma(z_0)$ as a function of the track pseudorapidity for single muons of constant transverse momenta of $p_T = 1, 10$ and 100 GeV comparing the *Extended* Layout with different readout segmentations. The nominal ATLAS Run-2 results are overlaid. The bottom plots show the ratios of the distributions for 25×100 μm^2 and 50×50 μm^2 pixel masks.

Very little changes are seen at low transverse momentum where multiple scattering effects dominate. Using 25×100 μm^2 pixels allows to improve the transverse impact parameter resolution of about 30% (60%) at $p_T = 10$ GeV ($p_T = 10$ GeV) at a cost of a deterioration of 20 to 80% for the longitudinal impact parameter resolution.
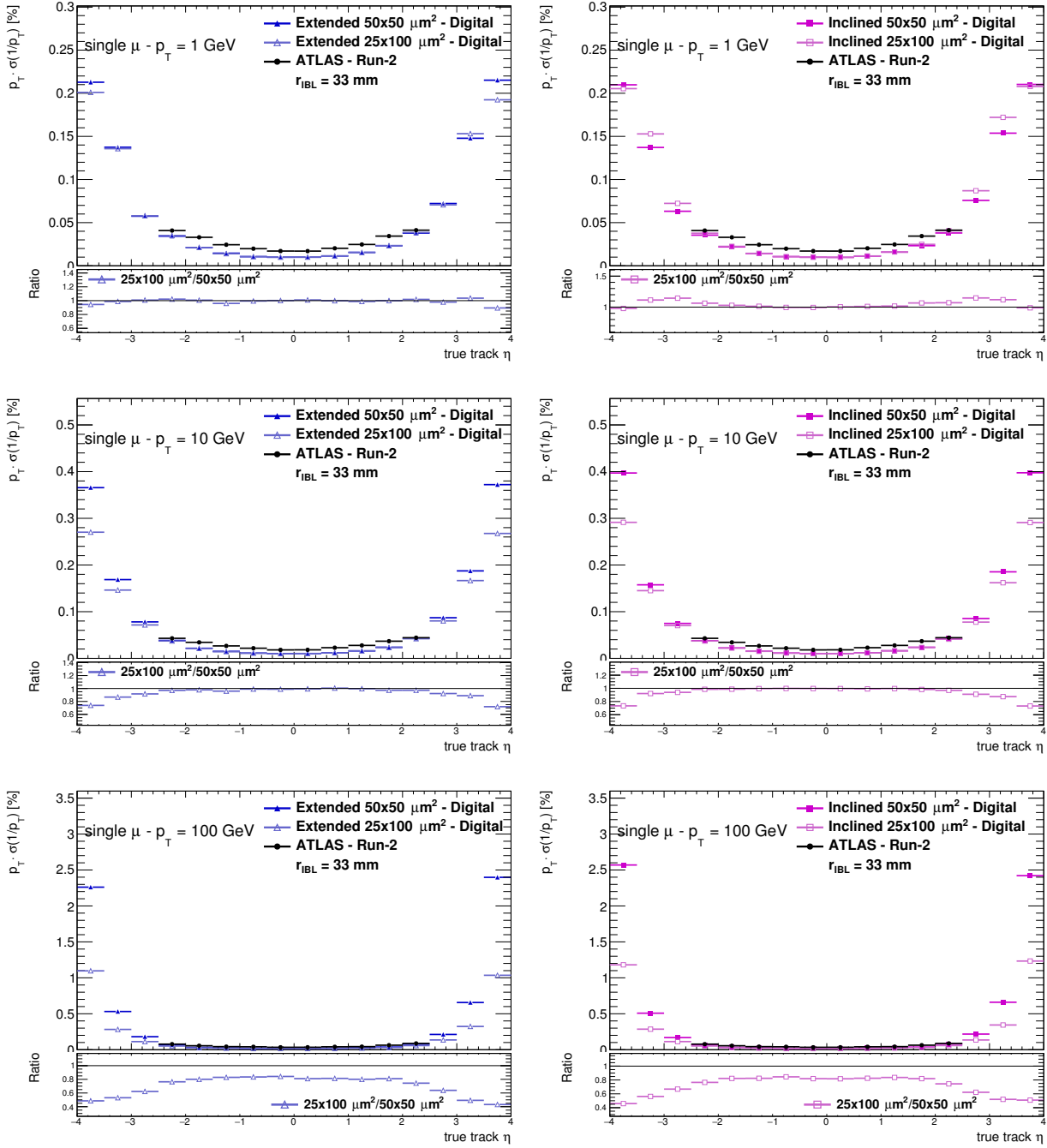
Figure 10.15: Distribution of the (left column) transverse impact parameter resolution $\sigma\left(d_0\right)$ and (right column) longitudinal impact parameter resolution $\sigma\left(z_0\right)$ as a function of the track pseudo-rapidity for single muons of constant transverse momenta of $p_{\mathrm{T}} = 1, 10$ and 100 GeV comparing the *Inclined* Layout with different readout segmentations. The nominal ATLAS Run-2 results are overlaid. The bottom plots show the ratios of the distributions for $25 \times 100\ \mu\mathrm{m}^2$ and $50 \times 50\ \mu\mathrm{m}^2$ pixel masks. Very little changes are seen at low transverse momentum where multiple scattering effects dominate. Using $25 \times 100\ \mu\mathrm{m}^2$ pixels allows to improve the transverse impact parameter resolution of about 30% (60%) at $p_{\mathrm{T}} = 10$ GeV $(p_{\mathrm{T}} = 10$ GeV$)$ at a cost of a deterioration of 20 to 80% for the longitudinal impact parameter resolution.

Figure 10.16: Relative inverse traverse momentum resolution as a function of the track pseudo-rapidity for single muons of constant transverse momenta of $p_\mathrm{T} = 1, 10$ and 100 GeV for the (left column) *Extended* and (right column) *Inclined* layout candidates with different readout segmentations. The nominal ATLAS Run-2 results are overlaid. The bottom plots show the ratios of the distributions for $25 \times 100~\mu\mathrm{m}^2$ and $50 \times 50~\mu\mathrm{m}^2$ pixel masks.

At higher p_T, using $25 \times 100~\mu\mathrm{m}^2$ pixels results in an improvement of 20 to 50% when moving from the central to the forward pseudo-rapidity region.
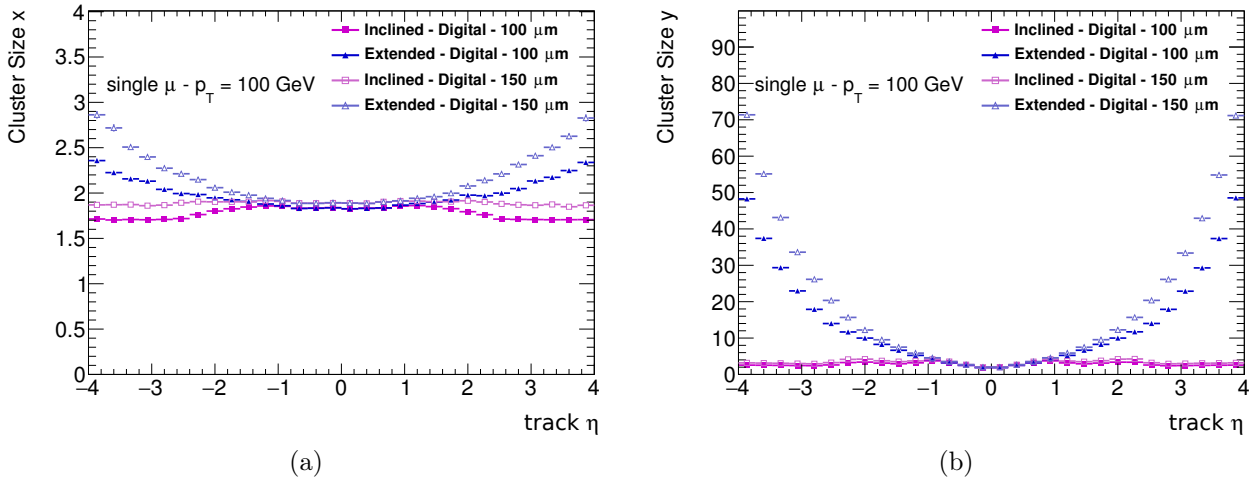
Figure 10.17: Comparison of the cluster size in the (a) local-x and (b) local-y directions on the sensor for the *Extended* and *Inclined* Layouts with changed pixel sensor thickness using single muons with $p_T = 100$ GeV. The local x and local y directions on the sensor correspond respectively to the transverse plane and longitudinal directions. The *Extended* Layout is characterised by very long clusters in the longitudinal direction with respect to the *Inclined* Layout. In the transverse plane, the cluster size is driven by the Lorentz shift: in the tilted region of the *Inclined* Layout, where the electric field in the sensor and the solenoidal magnetic field are not perpendicular, the magnitude of the Lorentz shift is reduced. Thicker sensors imply a bigger cluster size in both directions.

This can be used in the pattern recognition to guide the seed finding as described in § 8.2.3.2. Moreover, the additional information can be helpful during track fitting as it adds additional constraints on the track trajectory and therefore improves the track resolution. This has been done using the digital clustering and the ultimate clustering algorithms and applied in the final track fit of single muons with $p_T = 1, 10$ and 100 GeV. For the digital clustering, the global θ angle has been evaluated by using the cluster length and the direction between the first and last pixel of the cluster in the longitudinal direction. The error has been calculated varying the cluster length by one pixel. For the ultimate clustering, the truth particle θ angle has been taken and smeared with the same error as evaluated for the digital clustering. Only clusters with a minimal longitudinal cluster length of 10 have been used for this study. The study was done using the Kalman filter which was tested to give compatible results to the baseline global χ^2 fitting technique.

Figure 10.20 shows the comparison of the impact parameter resolutions for single muons of $p_T = 1, 10$ and 100 GeV with and without the inclusion of the additional θ measurement. Although the θ measurement is very precise in the forward region, the effect of including it into the track fit is shadowed by the uncertainty caused by multiple scatting. Only a limited improvement in the very forward for ultra-high momentum particles can be achieved. No significant effect on the transverse impact parameter measurement is expected.

10.2.3   Robustness Studies Regarding Pile-up, Alignment, Component Failures and Detector Ageing

10.2.3.1   Track Resolution and Track Reconstruction Stability with Increasing Pile-up

High hit activity in the detector can cause errors in the hit association, which can worsen the track parameter resolutions. Previous studies [119] with ATLAS have shown that these effects are negligible
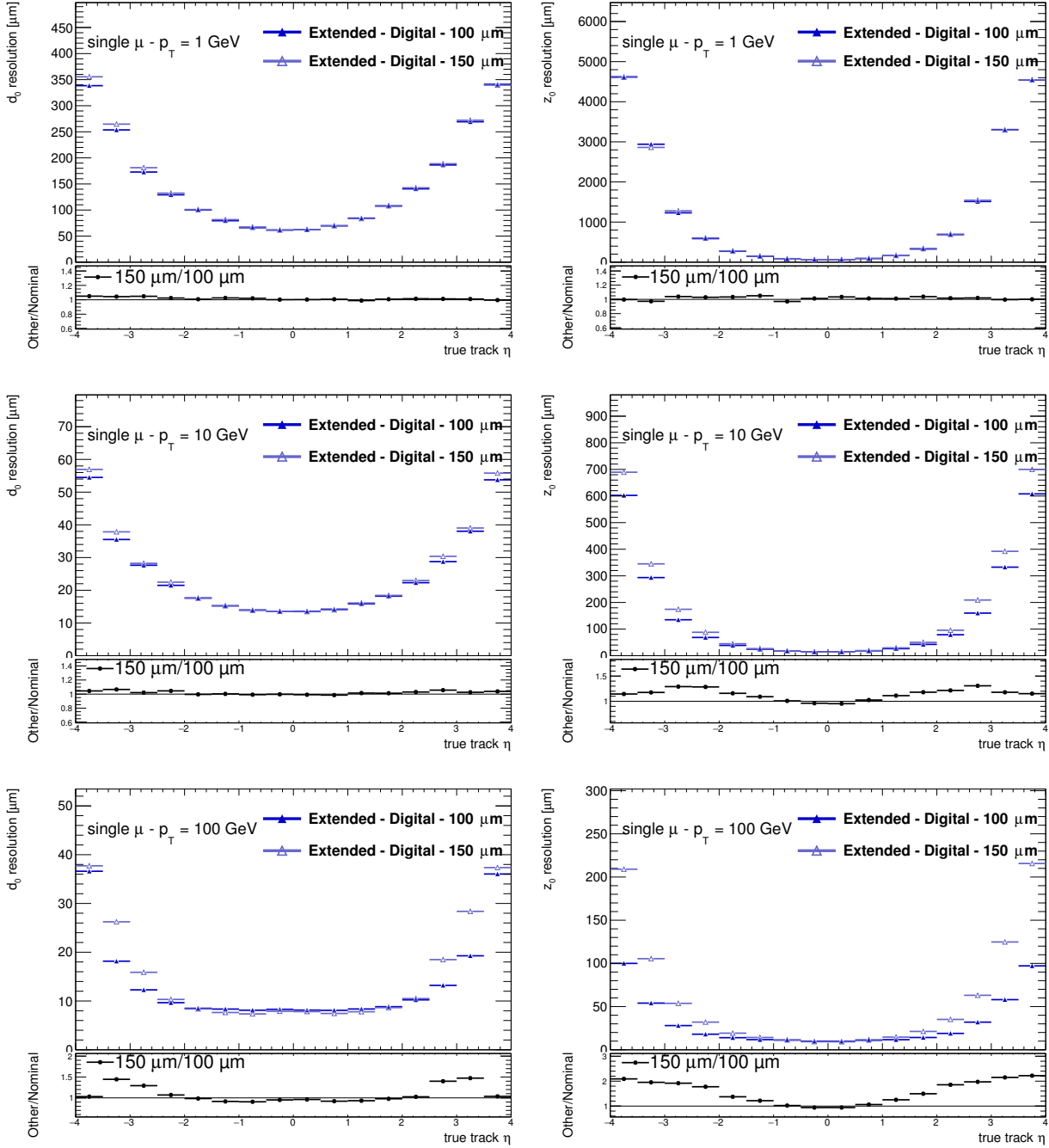
Figure 10.18: Distribution of the (left column) transverse impact parameter resolution $\sigma\left(d_0\right)$ and (right column) longitudinal impact parameter resolution $\sigma\left(z_0\right)$ as a function of the track pseudorapidity for single muons of constant transverse momenta of $p_{\mathrm{T}} = 1, 10$ and 100 GeV comparing the *Extended* Layout with different pixel sensor thickness. The bottom plots show the ratios of the distributions for pixel sensors with thickness of $150\ \mu m$ and $100\ \mu m$.

At $p_{\mathrm{T}} = 10$ GeV, changing the thickness from $150\ \mu m$ to $100\ \mu m$ provides an improvement in the longitudinal impact parameter resolution of about 30%. At higher momenta, the reduced cluster size implies better control of the pattern recognition that is then translated into better resolution, in particular in the longitudinal direction. At $p_{\mathrm{T}} = 100$ GeV, thinner sensors allow to gain up to a factor 2 in resolution in the longitudinal direction and 50% in the transverse plane.
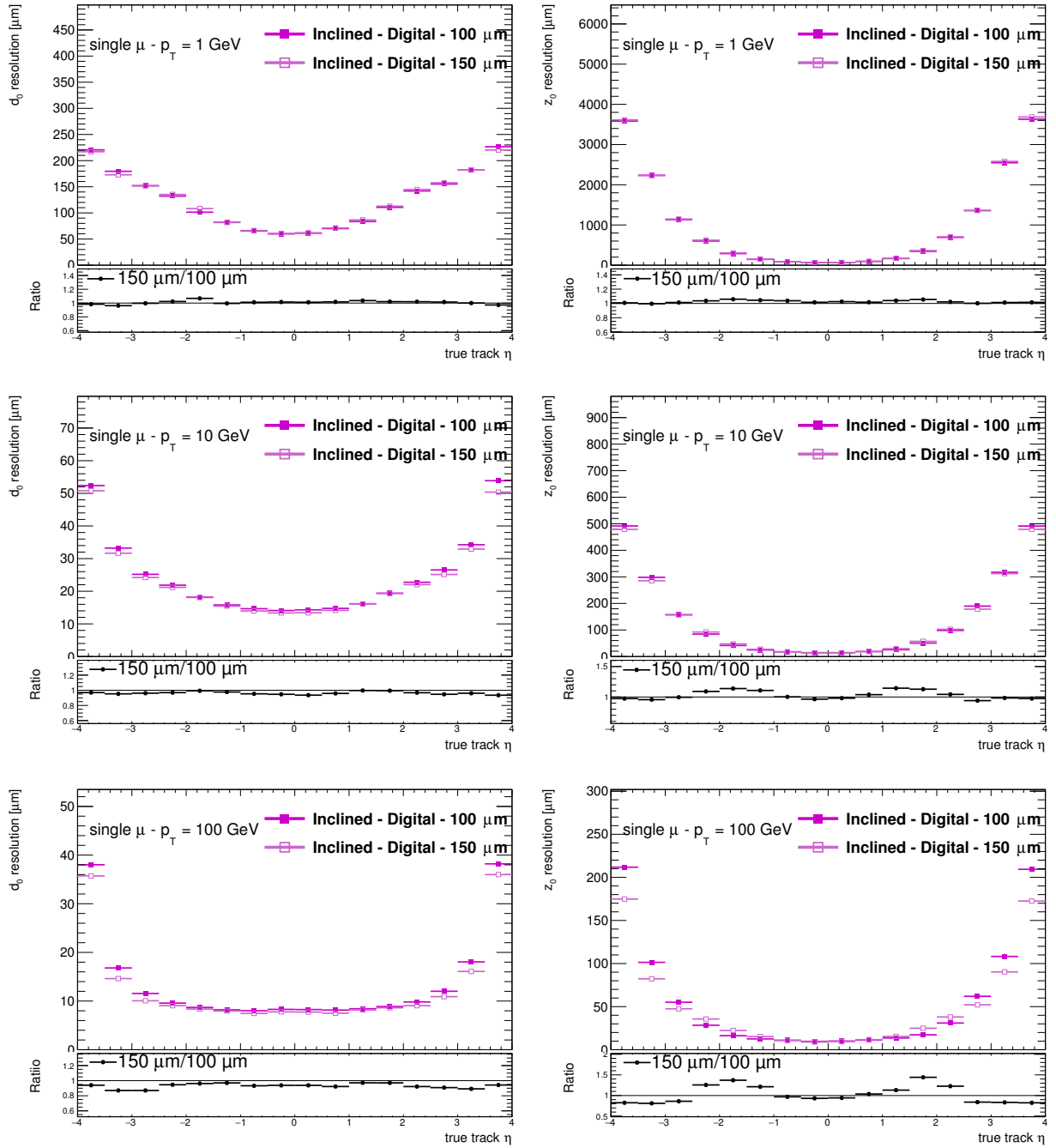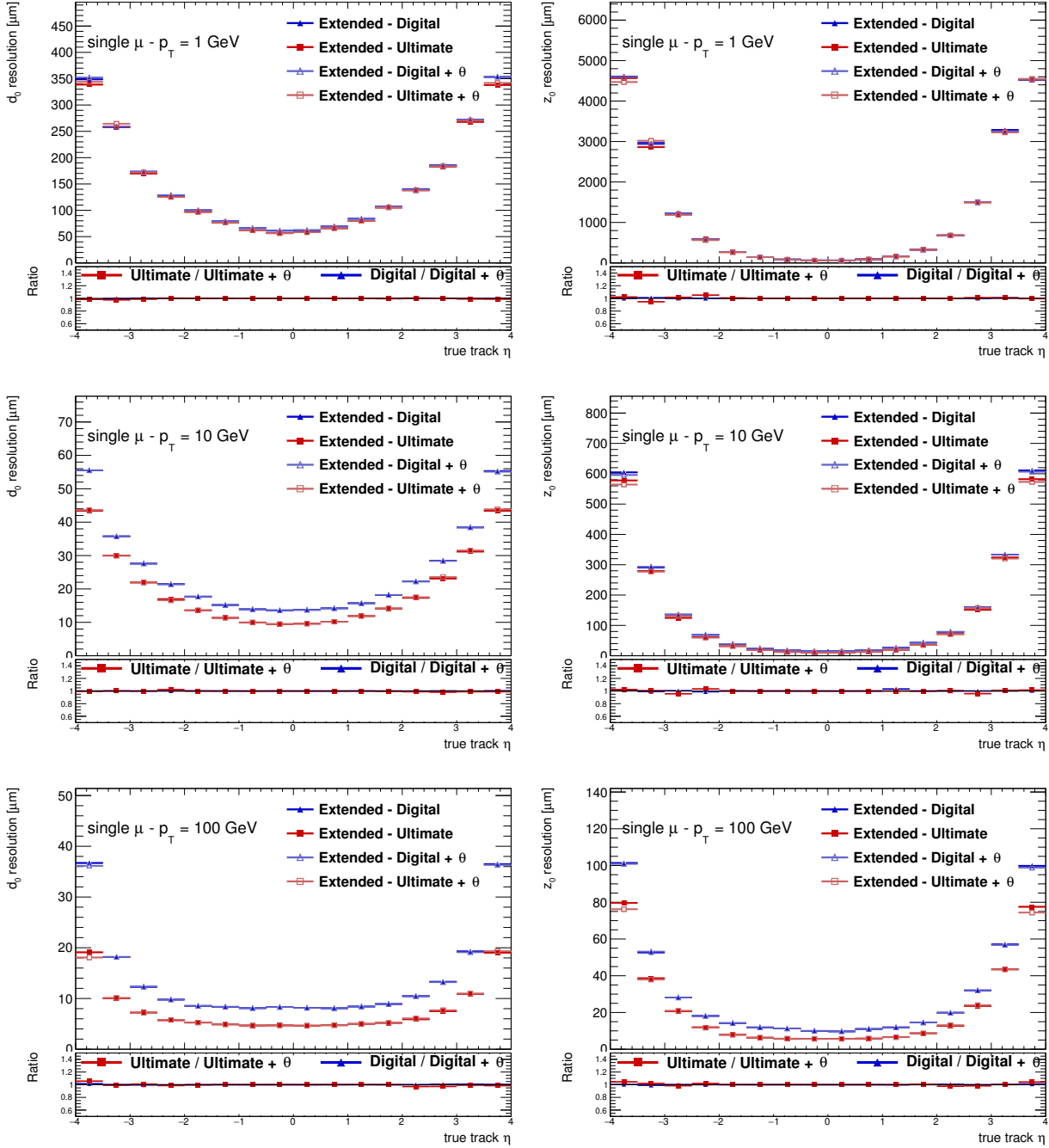
Figure 10.19: Distribution of the (left column) transverse impact parameter resolution $\sigma\left(d_0\right)$ and (right column) longitudinal impact parameter resolution $\sigma\left(z_0\right)$ as a function of the track pseudo-rapidity for single muons of constant transverse momenta of $p_{\mathrm{T}} = 1, 10$ and $100\,\mathrm{GeV}$ comparing the *Inclined* Layout with different pixel sensor thickness. The bottom plots show the ratios of the distributions for pixel sensors with thickness of $150\,\mu\mathrm{m}$ and $100\,\mu\mathrm{m}$.

At $p_{\mathrm{T}} = 10\,\mathrm{GeV}$, changing the thickness from $150\,\mu\mathrm{m}$ to $100\,\mu\mathrm{m}$ provides an improvement in the longitudinal impact parameter resolution of about 15%. At higher momenta, the reduced charge sharing effects for smaller clusters degrades the performance. At $p_{\mathrm{T}} = 100\,\mathrm{GeV}$, thinner sensors allow to gain 30-40% in resolution in the longitudinal direction for $1.0 < |\eta| < 2.4$ with a degradation of about $\sim 20\%$ in both $\sigma\left(d_0\right)$ and $\sigma\left(z_0\right)$ in the forward pseudo-rapidity region.

Figure 10.20: Distribution of the (left column) transverse impact parameter resolution $\sigma\left(d_0\right)$ and (right column) longitudinal impact parameter resolution $\sigma\left(z_0\right)$ as a function of the track pseudorapidity for single muons of constant transverse momenta of $p_{\mathrm{T}} = 1, 10$ and 100 GeV comparing the *Extended* Layout when including the measurement of θ provided by the long clusters in the track fitting stage. The bottom plot shows the ratios of both the pessimistic and optimistic scenarios with and without the additional information.

Although the θ measurement is very precise in the forward region, the effect of including it into the track fit is shadowed by the uncertainty caused by multiple scatting. Only a limited improvement in the very forward for ultra-high momentum particles can be achieved. No significant effect on the transverse impact parameter measurement is expected.

for pile-up values reached during Run-1 and Run-2 of the LHC data taking campaigns. However, when studying lead-lead collisions with the ATLAS detector a sizeable increase of tails in the impact parameter resolutions has been noted [121]. This could have negative effects for b-tagging and track-to-vertex associations and should be avoided as much as possible. Figure 10.21 shows the main track parameter resolutions for tracks from a top pair production events with 200 overlaid pile-up events. Following the trend seen in absence of overlaid pile-up events(§ 10.2.2.1), an improved resolution for impact parameters and momentum is obtained for the *Inclined* Layout compared to the *Extended* Layout.

Figure 10.22 shows the technical track reconstruction efficiency and the physics track reconstruction efficiency for top pair production events with 200 overlaid pile-up events for both candidate layouts. The technical track reconstruction efficiency shows the same features around $|\eta| \approx 2$, which have been described in detail in § 10.2.1. As for $\mu = 0$, the *Inclined* Layout is slightly more efficient in the forward region. A particular important aspect is to sustain a stable track reconstruction efficiency over the expected pile-up at the HL-LHC. Previous studies have shown that requiring a high number of hits per track, while only allowing very few holes and shared hit assignments is very helpful in controlling the fake rate in high pile-up scenarios [119]. The necessary hit requirement needed to stabilize the track reconstruction have beed derived in previous upgrade studies [62, 122] and used as a guidance for the ITk candidate layout design. The ITk layouts show excellent stability with pile-up with fake rates below 0.02% over the entire detector range, as depicted in Figures 10.23 and 10.24.

The fake rate, as described in § 10.1.1, is based on the particle-to-track matching and thus sensitive to matching characteristics suffering from some technical problems: as the truth record cannot be kept for every single interaction in the detector in order to regulate the output file size, truth information might already be dropped at simulation stage making a fully reliable matching impossible. A second way to measure the stability of the track reconstruction versus the event pile-up is the ratio of reconstructed tracks over generated charged particles (within the reconstruction phase space). At a fixed tracking efficiency, problems in the track reconstruction would result in an increase in this ratio as a function of pile-up. As can be seen in Figure 10.25, the ratio results to be flat over the full range of pile-up studied between 40 and 250 except for the two outermost $|\eta|$ bins for the *Extended* Layout, which indicates effects of pattern recognition confusion and wrong hit assignments. The ratio is in general higher than the tracking efficiency itself, indicating that additional tracks are reconstructed with a p_T above 1 GeV. Several of these tracks are due to secondaries from particles interacting in the material of the tracker. Because of the limited momentum resolution, the dominant contribution to the additional reconstructed tracks in the forward region is due to mis-measured low-p_T tracks that have a reconstructed transverse momentum above 1 GeV.

10.2.3.2   Track Resolution Stability with Misalignment

The studies presented so far, including the comparison with the ATLAS detector, have assumed perfect detector alignment. In reality, however, module and structural misalignment will contribute to the measurement accuracy and have to be considered. Misalignments can appear on different levels, from large structural misplacements to sectoral mispositioning or component deformation to individual modules misplacements. Additionally, module and sensor deformations can be regarded as misalignments as they cause degradations of the resolution.

The current ATLAS Run-2 Inner Detector alignment procedure is based on an iterative track alignment using tracks to minimize a global multidimensional χ^2 function. It has shown great performance throughout the data taking campaign [123]. Recently, caused by the time-dependent change of the
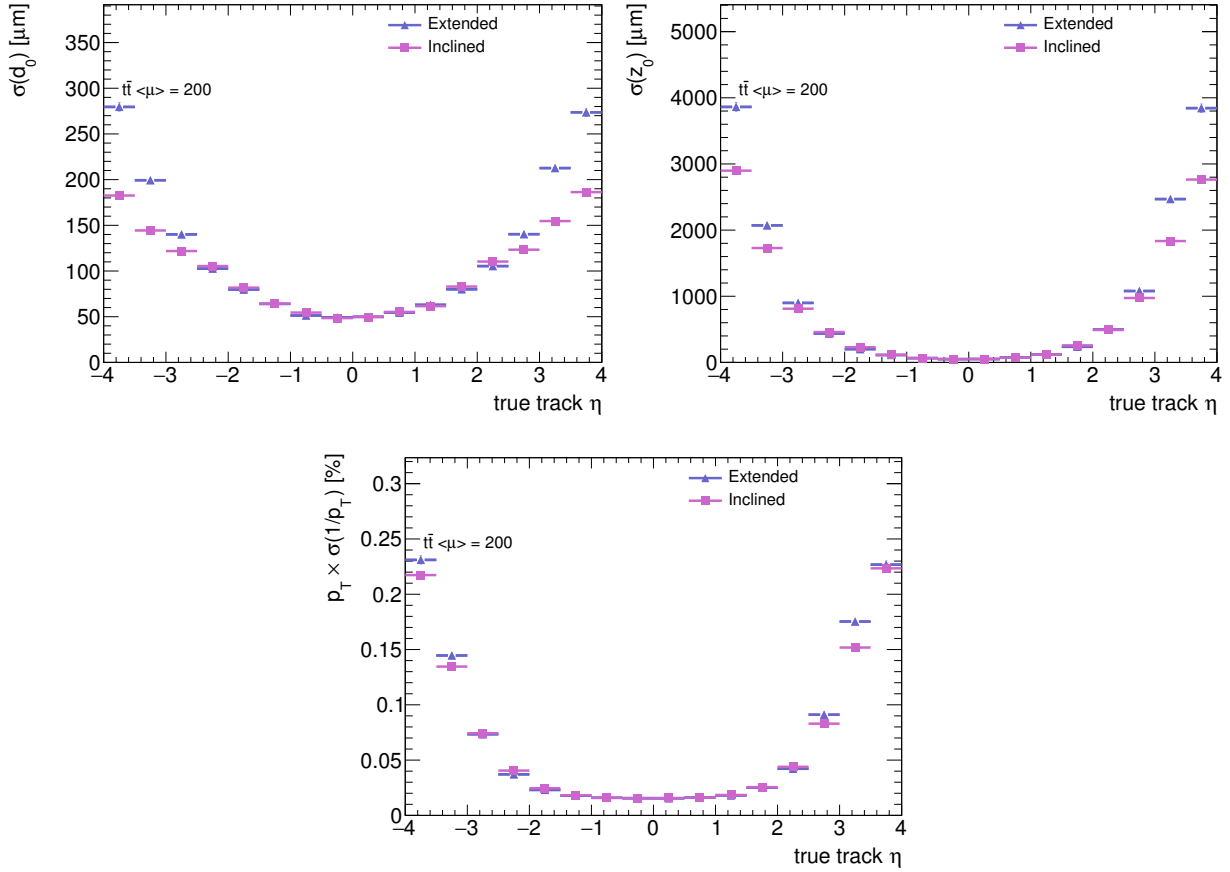
Figure 10.21: Distribution of the (top left) transverse impact parameter resolution $\sigma\left(d_0\right)$, (top right) longitudinal impact parameter resolution $\sigma\left(z_0\right)$ and (bottom) relative inverse traverse momentum resolution as a function of the track pseudo-rapidity for tracks from top pair production events with 200 overlaid pile-up events comparing the *Extended* and *Inclined* layout candidates. Improved resolution for impact parameters and momentum is obtained for the *Inclined* Layout compared to the *Extended* Layout.
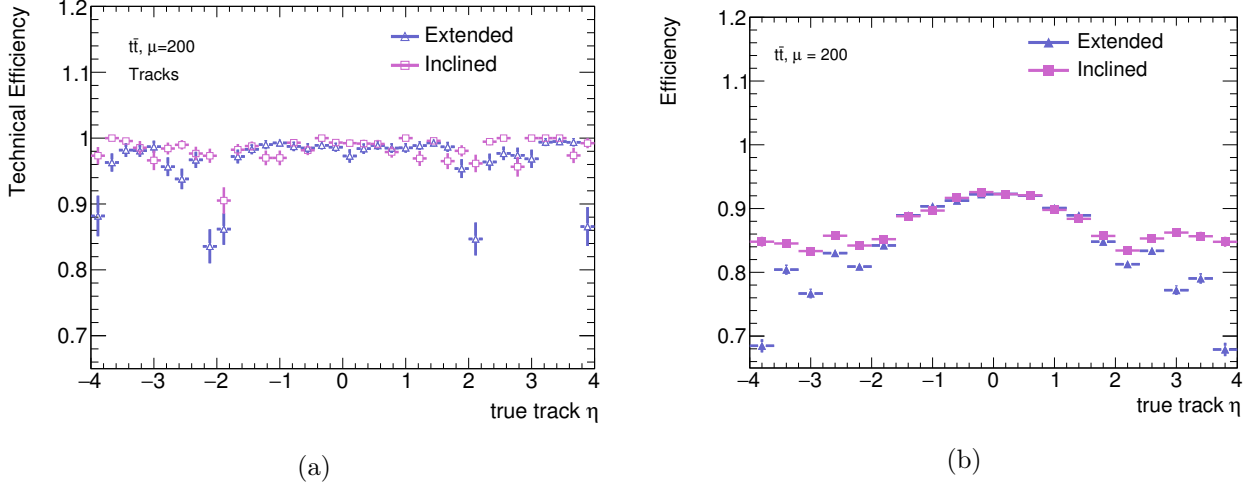
Figure 10.22: Distribution of the (a) technical track reconstruction efficiency and (b) physics track reconstruction efficiency for top pair production events with 200 overlaid pile-up events for the *Extended* and *Inclined* Layouts [120]. As for $\mu = 0$, the *Inclined* Layout is slightly more efficient in the forward region.
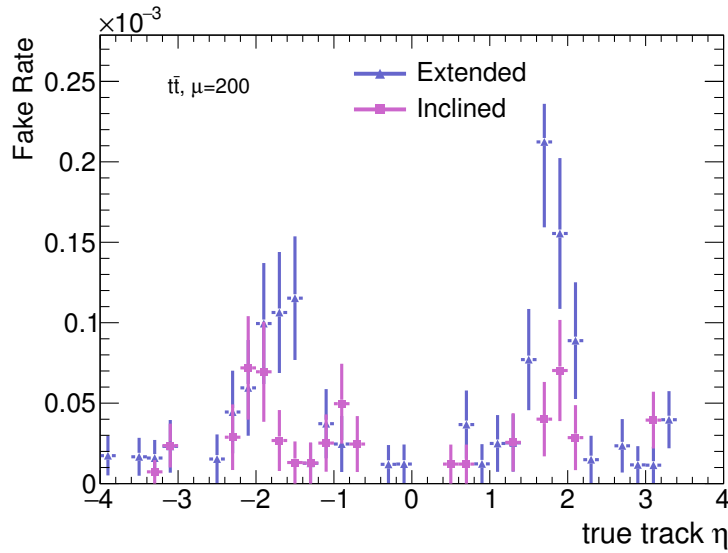
Figure 10.23: Fake rate for reconstructed tracks for top pair production events with 200 overlaid pile-up events for the *Extended* and *Inclined* Layouts [120]. The fake rate stays below 0.02% over the entire detector range for both candidate layouts.
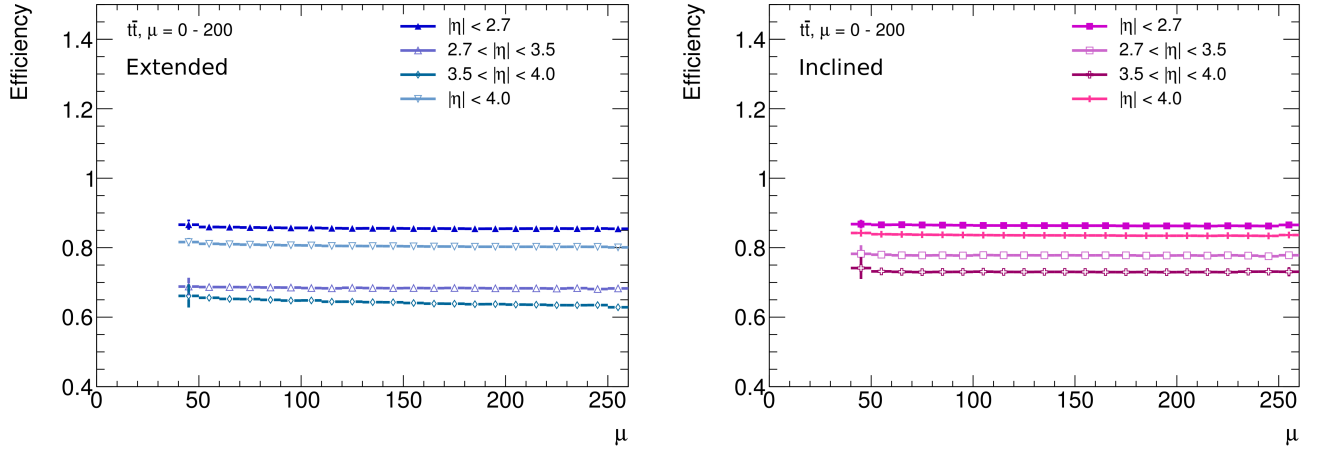
Figure 10.24: Physics track reconstruction efficiency for the *Extended* and *Inclined* layout candidates for top pair production events as a function of pile-up for top pair events with 40 to 250 overlaid pile-up events, for different pseudo-rapidity regions [120]. The efficiency results to be flat over the full range of pile-up studied. A slight decrease of the primary tracking efficiency for the two outermost $|\eta|$ bins for the *Extended* Layout, which indicates effects of pattern recognition confusion and wrong hit assignments.
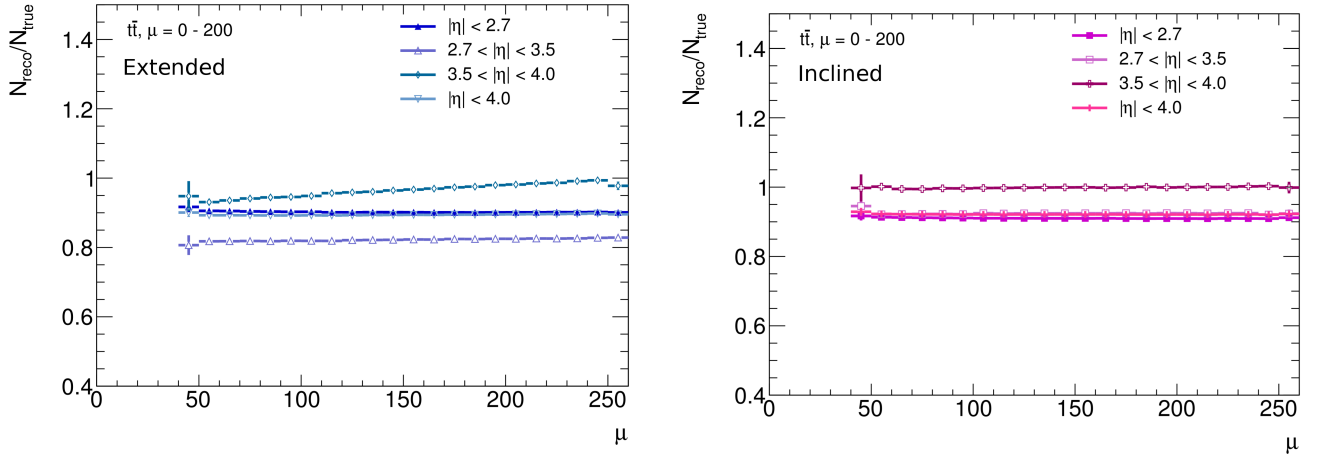
Figure 10.25: Ratio of the number of reconstructed to generated particles for the *Extended* and *Inclined* layout candidates for top pair production events as a function of pile-up for top pair events with 40 to 250 overlaid pile-up events, for different pseudo-rapidity regions [120]. The ratio results to be flat over the full range of pile-up studied except for the two outermost $|\eta|$ bins for the *Extended* Layout, which indicates effects of pattern recognition confusion and wrong hit assignments.

IBL during a single run a dedicated alignment procedure per luminosity block [2] has been introduced. At the time these studies have been performed, the absence of a final stave design and a fully engineered version of an ITk layout prohibited to predict the type of misalignments that could become apparent and to which level they could be corrected for using a dedicated alignment procedure. Nevertheless, it was important to quantify the impact of potential misalignments on the track reconstruction performance for the two candidate layouts. For this reason, a random misalignment of 1, 3, 10 μm on module level has been investigated. The values have been drawn from Gaussian distributions, with $\mu = 0$ μm and $\sigma = 1, 3, 10$ μm, and applied to the centre of the modules in the local x, y and z coordinates. Only the position of the modules has been randomly put out of place with no additional tilt or twist applied to the original orientation. Effects from gravitational sagging or mounting tension, such as stave or module bowing are not considered.

In the low momentum region, see Figure 10.26, the misalignments are rather small compared to the uncertainty from multiple scattering and a very small degradation of the impact parameter resolutions is seen for both layouts. Random module misalignment at the level of micrometers is important for high momentum particles. Figure 10.27 and Figure 10.28 show the effects of random module misalignment with different magnitude on the impact parameter resolutions individually for the *Extended* and *Inclined* layout candidates for muons with $p_\mathrm{T} = 100$ GeV, respectively. Due to the different module orientation with respect to the particle direction, the same misalignment distortion on local module level introduces a different effect on the measured track quantities. In particular the longitudinal track direction measured in the forward region is very sensitive to module misalignment, especially for the *Extended* Layout. A small global radial misalignment (which corresponds to a small local out of plane misalignment on module level) translates into a large global longitudinal misalignment. For single muons with $p_\mathrm{T} = 100$ GeV in $2.5 < |\eta| < 4$, a local misalignment of 10 μm causes the z_0 resolution of the *Extended* Layout to be a factor of 3.5 times larger than for perfect alignment. For the *Inclined* Layout, the same local misalignment causes a degradation of 40% for the z_0 resolution which rises up to a factor 2 in $1.4 < |\eta| < 2.6$.

Figure 10.29 summarize the effect of 10 μm local misalignment on the impact parameter resolution by displaying the performance bracket with respect to the perfectly aligned geometry. The effect is very strong in the forward region for the transverse and even more for the longitudinal impact parameter resolution due to the aforementioned geometrical effects. In particular, the performance band for the *Inclined* Layout is well contained in the one corresponding to the *Extended* Layout.

It is fair to believe that an applied alignment procedure will – given a stable detector over a long period of time – achieve a better module positioning than the displayed worst-case scenario. However, perfect placement or orientation cannot be assumed as never achieved in past experiments.

10.2.3.3   Track Resolution and Track Efficiency Stability with Detector Ageing and Component Failures

In the following, two different detector ageing effects have been studied:

- Component failures, such as inactive modules that are known and described in the conditions data-base of the detector, called known inefficiency;

- Detector inefficiencies due to irradiation that affect single channels appear as unknown inefficiency.

---

[2]The luminosity block (LB) is the atomic unit of the ATLAS data. One LB contains roughly 2 minutes of data taking, but this can vary due to run conditions and other operational issues.
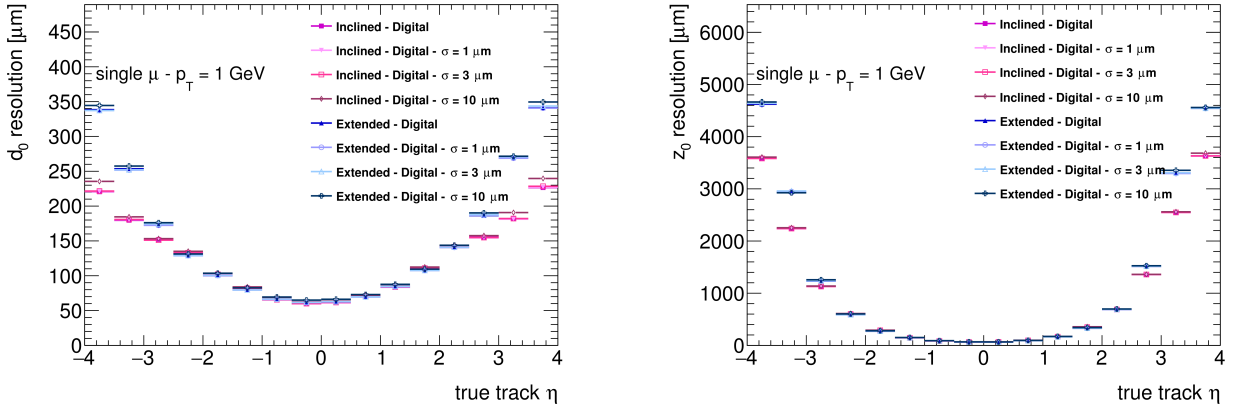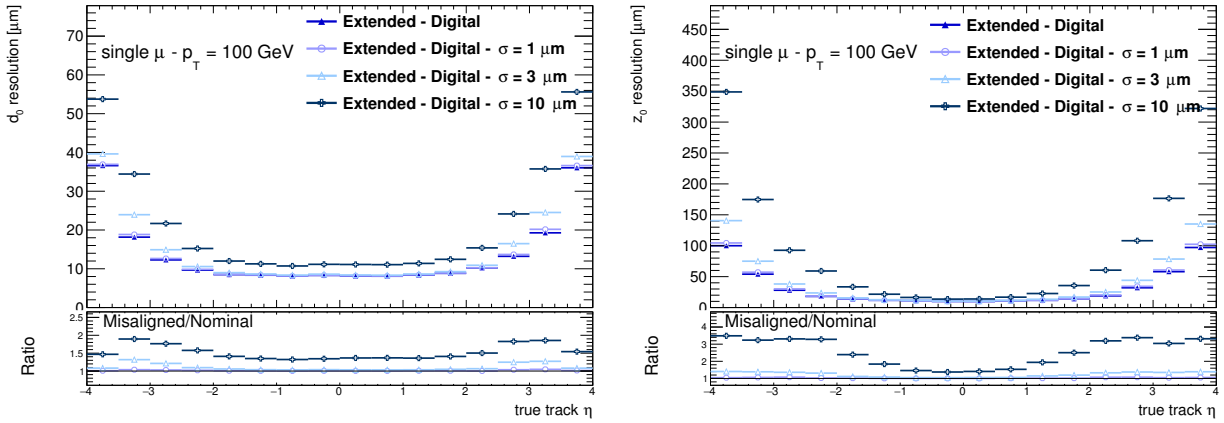
Figure 10.26: Change of (left) transverse impact parameter resolution $\sigma(d_0)$ and (right) longitudinal impact parameter resolution $\sigma(z_0)$ for single muons with $p_T = 1$ GeV when applying random local misalignment of $\sigma = 1, 3, 10$ μm for the *Extended* and *Inclined* Layouts compared to perfect alignment. A very small degradation of the impact parameter resolutions is seen for both candidate layouts as misalignment effects are rather small compared to multiple scattering uncertainties.

Figure 10.27: Change of (left) transverse impact parameter resolution $\sigma(d_0)$ and (right) longitudinal impact parameter resolution $\sigma(z_0)$ for single muons with $p_T = 100$ GeV when applying random local misalignment of $\sigma = 1, 3, 10$ μm for the *Extended* Layout compared to perfect alignment. In $2.5 < |\eta| < 4$, a local misalignment of 10 μm causes the z_0 resolution to be a factor of 3.5 times larger than for perfect alignment. Also the transverse impact parameter resolution degrades up to a factor 2 at $|\eta| \sim 3.5$.
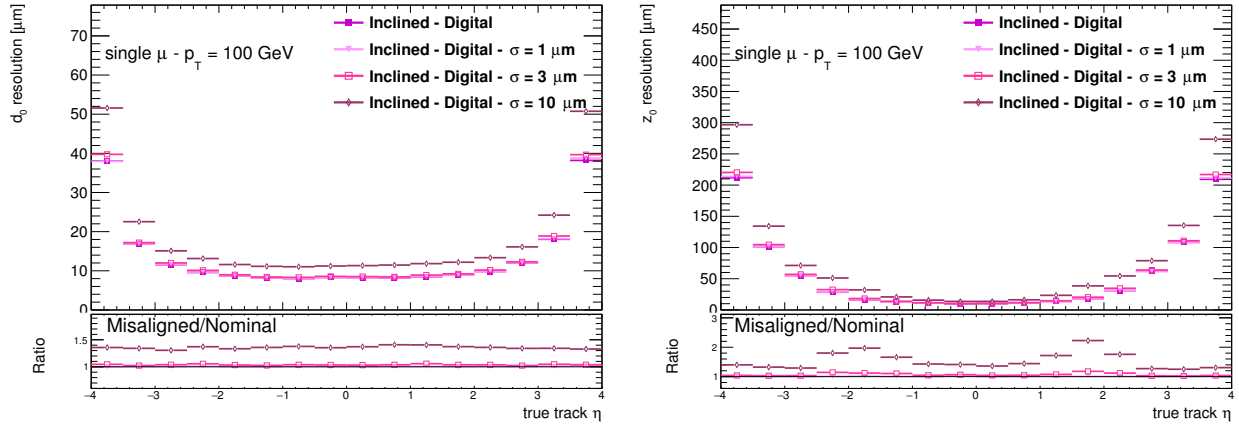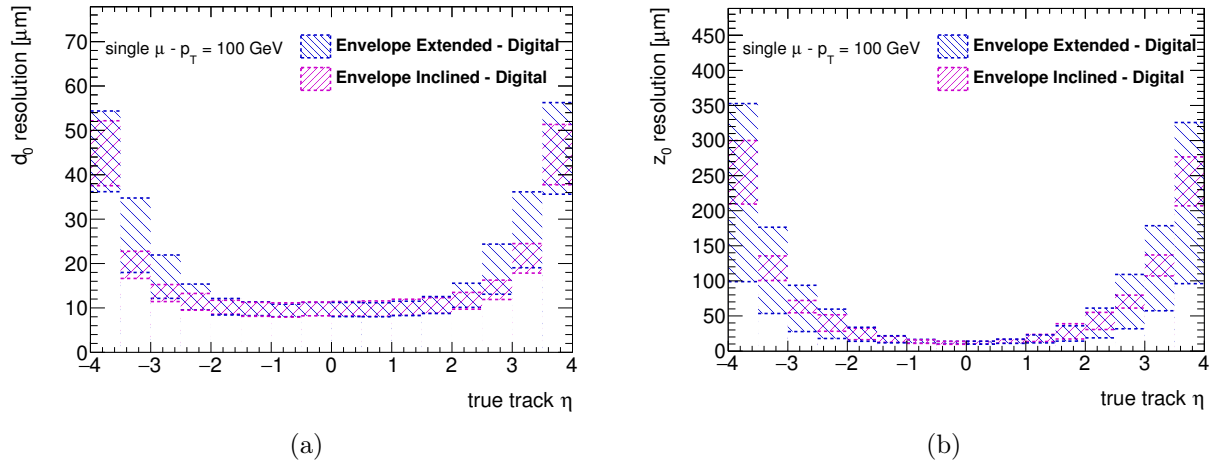
Figure 10.28: Change of (left) transverse impact parameter resolution $\sigma(d_0)$ and (right) longitudinal impact parameter resolution $\sigma(z_0)$ for single muons with $p_T = 100$ GeV when applying random local misalignment of $\sigma = 1, 3, 10$ μm for the *Inclined* Layout compared to perfect alignment. A local misalignment of 10 μm causes a degradation of 40% for the z_0 resolution. It rises up to a factor 2 in $1.4 < |\eta| < 2.6$. Approximately 40% degradation is shown for the transverse impact parameter resolution with respect to the perfectly aligned geometry.

Figure 10.29: Change of (a) transverse impact parameter resolution $\sigma(d_0)$ and (b) longitudinal impact parameter resolution $\sigma(z_0)$ for single muons with $p_T = 100$ GeV when applying random local misalignment of $\sigma = 10$ μm for the *Extended* and *Inclined* layout candidates displayed as performance bracket compared to perfectly aligned geometry. The effect of the local misalignment is very strong in the forward region for the transverse and even more for the longitudinal impact parameter resolution, especially for the *Extended* Layout. The performance band for the *Inclined* Layout is well contained in the one corresponding to the *Extended* Layout.

Inactive modules change the measurement arrangement and therefore influence the track resolution. An inactive module causes a loss of the measurement in the specific layer while still adds the additional noise from multiple scattering and energy loss, hence they are particularly harmful when they appear in the innermost measurement layers. Inactive channels can also create the loss of the measurement, or change the position of the estimated cluster. They appear increasingly during the operation time of the detector due to radiation damages.

Figure 10.30 shows the change of number of holes on track when introducing 1, 3 and 5% random pixel channel inefficiency and the corresponding change of track reconstruction efficiency for the *Extended* and *Inclined* layout candidates. For both layouts the rate of holes increases with increased channel inefficiency, as expected. This increase is slightly less pronounced in the *Extended* Layout where the long clusters are present and the cluster merging setup (§ 8.2.3.1) can potentially recuperate inactive pixels. Figure 10.30b and Figure 10.30d show no effect in the physics track reconstruction efficiency in the central region when introducing a channel inefficiency up to 5%, while a small degradation appears for $|\eta| > 2.0$. The maximum effect is present in the very forward region where the measurement multiplicity is dominated by the pixel ring system and where cluster sizes in the rings are small. An inefficiency of one channel can thus lead directly to the loss of measurement and hence increase the chance of failing the requirement of minimum number of measurements on track.

Inactive modules are easier to treat in the track reconstruction, but still can have a strong harming effect. Inactive modules are flagged as such in the conditions database, independently whether this is caused by a permanent failure or temporary source. When a track candidate is built and is predicted to cross an inactive module, the missed measurement is not counted as a hole, but rather as a valid measurement on track. For this reason, a relatively large fraction of inactive modules does not translate into a similarly large number of holes on track. Figure 10.31 shows the number of holes on track for the *Extended* and *Inclined* Layouts with 5 and 10% percent of inactive pixel modules. These numbers have been chosen in accordance to the numbers present in the ATLAS pixel detector at the end of Run-1 [124]. The strategy to count an inactive module as a fully efficient measurement has been chosen in order not to penalise tracks in detector regions where many inactive modules are present. However, it can only be applied in a robust way to modules between the first and the last actual measurements on track in order to avoid biases in the track length. Hence, even known inactive modules can lead to a decreased track reconstruction efficiency when they appear on either end of the track trajectory. In addition, inactive modules often result in a worse track resolution, in particular the impact parameter resolution degrades significantly when losing a measurement close to the interaction region.

Figure 10.34 and Figure 10.33 show the effect of randomly introducing 5 and 10% of inactive pixel modules to the candidate layouts in terms of physics track reconstruction efficiency and track parameter resolution and compare the results to the nominal setup. There are larger differences between the candidate layouts when introducing known module inefficiencies. The lower number of pixel measurements available in the *Extended* Layout starting from $|\eta| > 1.0$ makes the layout more sensitive to losing single modules along the track. As a result, the track reconstruction efficiency decreases significantly with an increased number of inactive modules. This loss of efficiency is far less pronounced in the *Inclined* Layout, as the inclined regions add multiple measurements to the track and the total measurement count is far above the minimum number of measurements required (bottom plots in Figure 10.33). In a similar manner, the track parameter resolutions, as shown in Figure 10.34, degrade more strongly for the *Extended* Layout in presence of module failure, because the multiple hits per layer provided by the inclined regions soften the effect of loosing a single and/or multiple measurements. This is particularly striking in the forward direction.

All the studies described in detail in this chapter allowed to establish the list of recommendations that guided the choice of the layout of the ATLAS Phase-II tracker and its optimisation. The next chapter is dedicated to the discussion of the recommended characteristics of the final ITk layout.
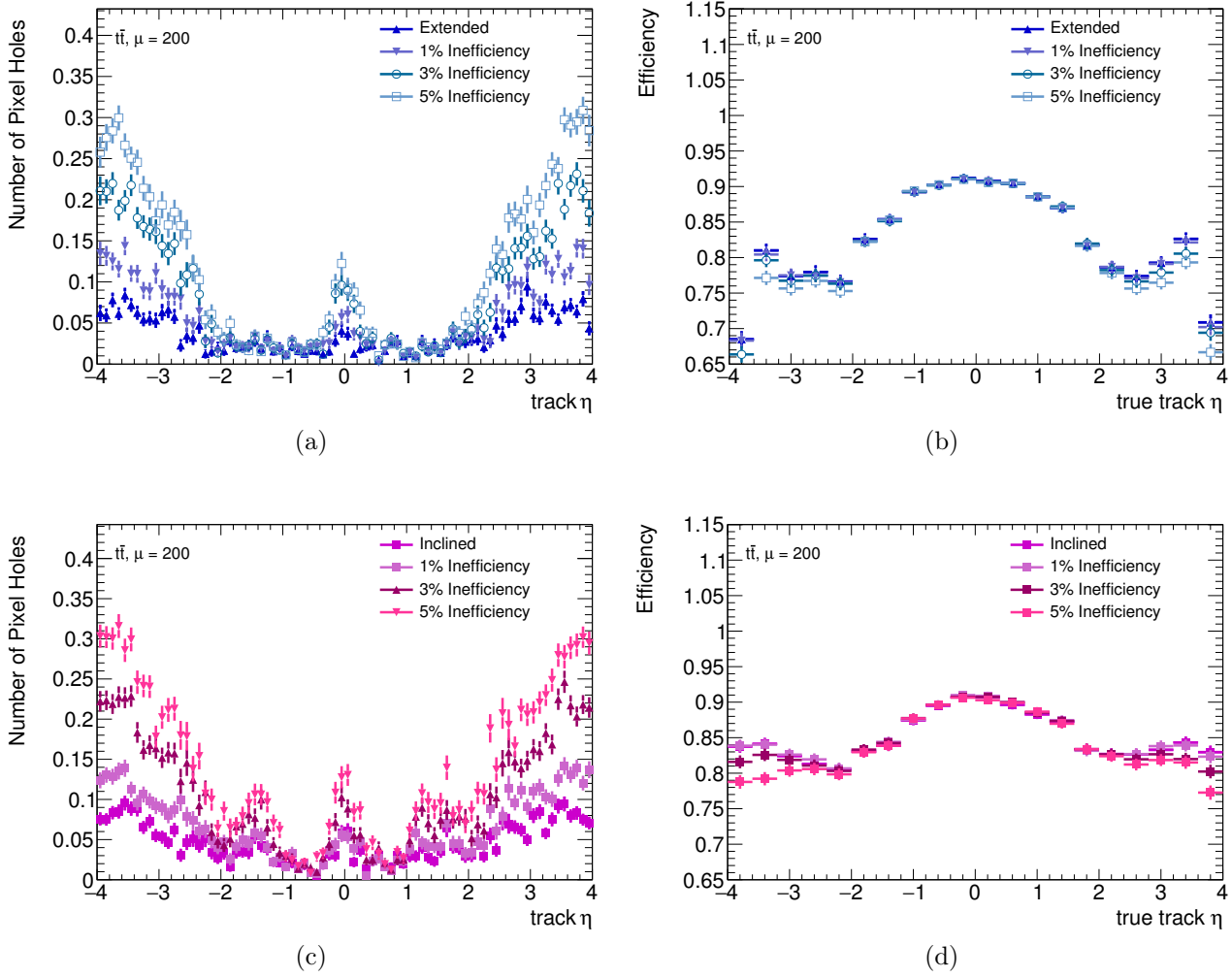
(a)

(b)

(c)

(d)

Figure 10.30: Change of (left) number of pixel holes on track and (right) corresponding physics track reconstruction efficiency for tracks from top pair production events with 200 overlaid pile-up events for the (top) *Extended* and (bottom) *Inclined* layout candidates with 1, 3 and 5% random pixel channel inefficiency [120]. For both layouts the rate of holes increases with increased channel inefficiency. A small degradation in the physics track reconstruction efficiency appears for $|\eta| > 2.0$ introducing up to 5% channel inefficiency.
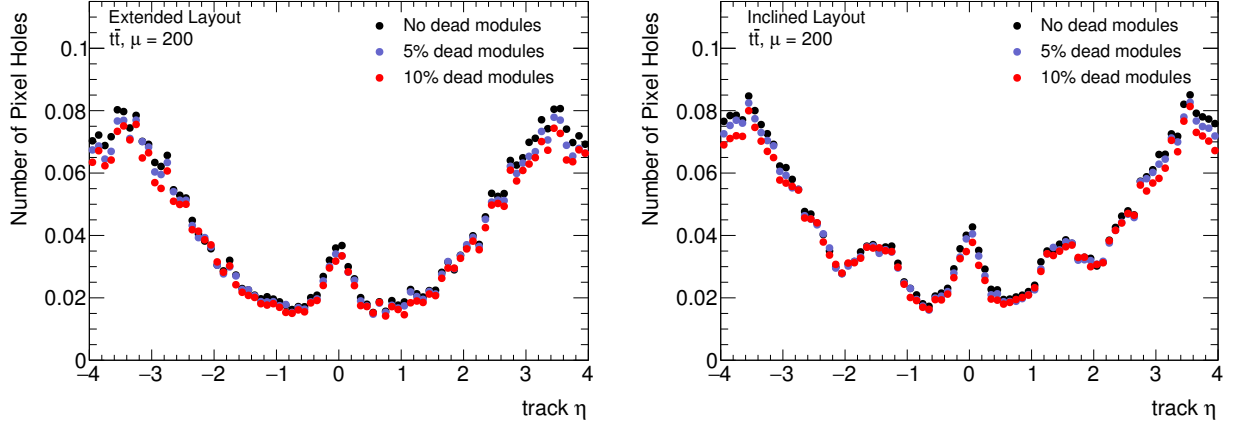
Figure 10.31: Change of number of pixel holes on track for tracks from top pair production events with 200 overlaid pile-up events comparing the *Extended* and *Inclined* layout candidates when introducing 5 and 10% of inactive pixel modules [125].
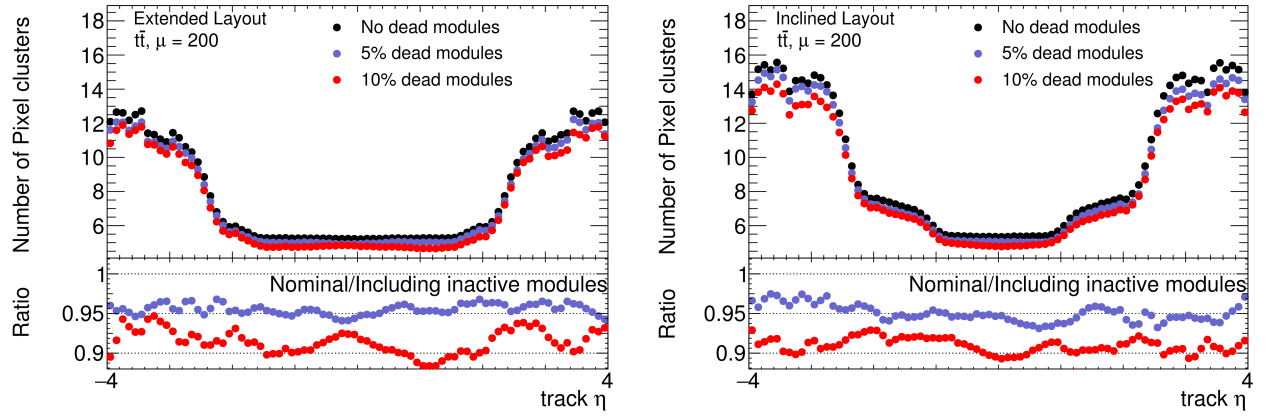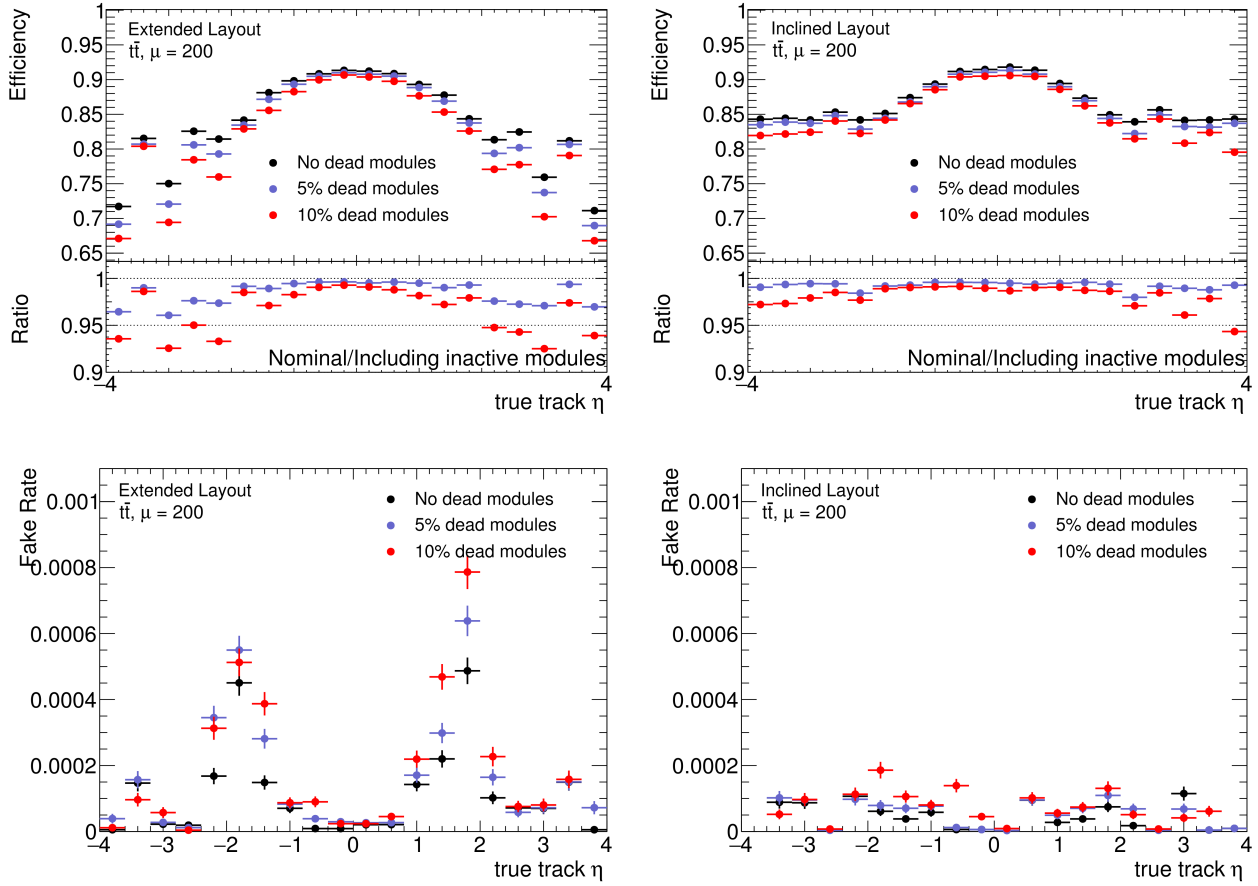

Figure 10.32: Change of number of pixel clusters on track for tracks from top pair production events with 200 overlaid pile-up events comparing the *Extended* and *Inclined* layout candidates when introducing 5 and 10% of inactive pixel modules [125].

Figure 10.33: Distribution of the (top) physics track reconstruction efficiency and (bottom) fake rates (bottom) for tracks from top pair production events with 200 overlaid pile-up events comparing the *Extended* and *Inclined* layout candidates when introducing 5 and 10% of inactive pixel modules [125]. The lower number of pixel measurements available in the *Extended* Layout starting from $|\eta| > 1.0$ makes the layout more sensitive to losing single modules along the track. As a result, the track reconstruction efficiency decreases significantly with an increased number of inactive modules for the *Extended* Layout while it stays less pronounced in the *Inclined* Layout given the larger number of measurements on tracks, well above the minimum number of measurements required.
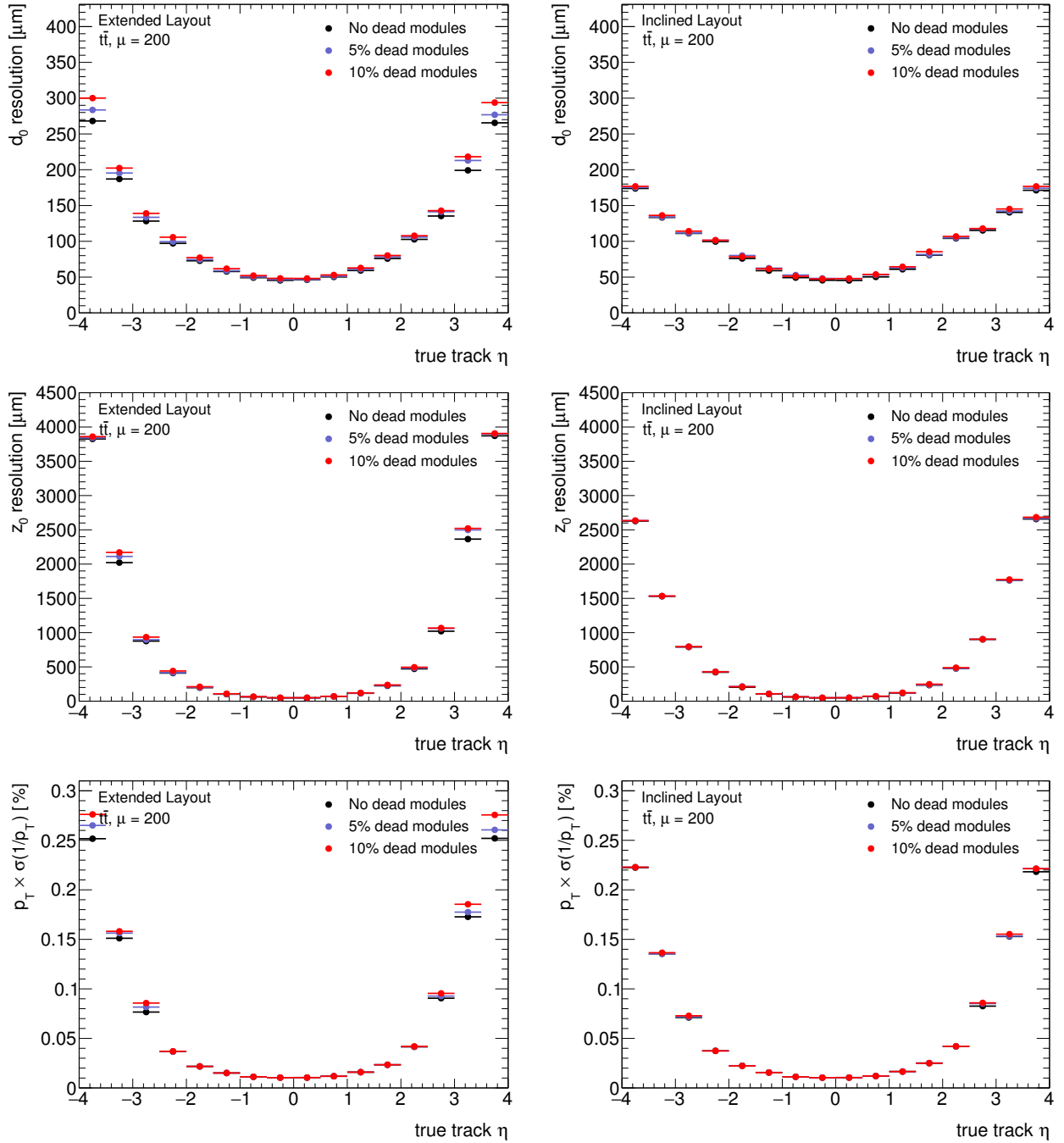
Figure 10.34: Change of (top) transverse impact parameter resolution $\sigma(d_0)$, (middle) longitudinal impact parameter resolution $\sigma(z_0)$ and (bottom) relative inverse traverse momentum resolution for tracks from top pair production events with 200 overlaid pile-up events comparing the *Extended* and *Inclined* layout candidates when introducing 5 and 10% of inactive pixel modules [125]. The track resolutions degrade stronger for the *Extended* Layout in presence of module failure, because the multiple hits per layer provided by the inclined regions soften the effect of loosing single and/or multiple measurements. This is particularly striking in the forward direction.

11

ITk Layout Recommendations

Contents

The studies presented in the previous chapter allowed to establish a list of recommendations. The provided list has guided the choice of the layout of the ATLAS Phase-II tracker and its optimisation, as described in the ITk Strip and Pixel Detector TDRs [58, 104].

This chapter will be dedicated to the discussion of the list of recommended characteristics of the final ITk layout. The last section will describe the most recent ITk layout and its tracking performance.

11.1 ITk Layout Recommendation

11.1.1 Pseudo-rapidity Coverage

Up to $|\eta| = 2.5$, which coincide with the pseudo-rapidity coverage of the Run-2 ATLAS Inner Detector, the expected performance of the ITk candidate layouts operated at pile-up 200 results to be similar or

better than the Run-2 detector operated at a mean pile-up of about 30. Such a direct comparison is not available for $|\eta| > 2.5$. After the initial studies reported in [102], the results presented in the previous chapters represent the first detailed estimation of the potential track reconstruction performance of an inner tracking system with pseudo-rapidity coverage extended up to $|\eta| = 4.0$.

The excellent tracking performance with the consequent enrichment of the physics performance of the ATLAS Phase-II program established the benefits of an extended pseudo-rapidity coverage for the ITk layout [58, 104]. Particular care should be taken in further optimising the distribution of the detector material, especially for the forward region where it can be very harmful for both tracking and calorimetry performance.

11.1.2 Inner Pixel Barrel System

The set of results reported in the previous chapter has shown that both candidate layouts perform extremely well also in presence of high pile-up values both in terms of track reconstruction efficiency and resolution of the track parameters. While the similar configuration of the central region provides similar performance for both layouts, significant differences are seen in the forward region where the main features of the two layouts are located. For this reason, the recommendation for the two innermost layers of the pixel detector is based on the performance in the pseudorapidity region of $|\eta| > 2$. Several inputs are taken into account:

- **Impact parameter and momentum resolution studies:** Considering the typical momentum spectrum of charged particles at the HL-LHC, the *Inclined* Layout presents better impact parameter resolution compared to the *Extended* Layout except for a small region around $|\eta| \approx 2.0$ (see Figure 10.8). The advantages of using long cluster in the forward region to create precise measurements are compromised by effects associated with the additional traversed material as shown in Figure 10.12. They are apparent at very high momenta which are at the limits of the momentum of the physics program at the HL-LHC. Moreover, the precise measurement of the longitudinal track component given by the long clusters at very high particle momenta is also particularly sensitive to out-of-plane misalignments (see Figure 10.29).

- **Track reconstruction efficiency studies:** The *Inclined* Layout presents higher efficiency for muons, pions and electrons with respect to the *Extended* Layout, as shown in Figures 10.3 and 10.7. The reconstruction efficiencies for pions and electrons are very sensitive to the amount of material in the tracking volume, and are therefore penalised in the forward region by the increased traversed material in the *Extended* Layout. This effects leads as well to a lower physics track reconstruction efficiency as summarised in Figure 10.5b. While the *Inclined* Layout profits from multiple measurements per layer which aid the pattern recognition leading to shorter extrapolation distances between the space points, the *Extended* Layout relies on the reconstruction of small track segments that include information on the track direction. For low momentum tracks, where uncertainties due to material effects dominate, this leads to poor seed and track quality for the *Extended* Layout at $|\eta| > 2.0$ which is translated into a very low muon track reconstruction efficiency as shown in Figures 10.3 and 10.4.

- **Robustness studies:** The *Inclined* Layout is shown to be more robust than the *Extended* Layout against the loss of entire pixel modules, as shown in Figure 10.33. The additional measurements per layer provided in the forward region, allows the *Inclined* Layout to sustain stable track reconstruction efficiency and small distances between consecutive measurements mitigate the impact on the track resolutions caused by losing complete measurements (see Figure 10.34). The

longer clusters of the *Extended* Layout results to be more robust in the forward region against pixel channel inefficiency, see Figure 10.30, since single pixel failures can be compensated by re-clustering algorithms. The effect due to the missing individual pixel channel is anyway smaller compared to missing individual modules.

- **Combined performance and physics studies:** Preliminary studies comparing physics results for the two layout candidates have shown that the *Inclined* Layout is characterised by improved track-to-vertex association, better pile-up rejection, improved E_T^{miss} resolution and b-tagging performance in the forward region when compared to the *Extended* Layout [126].

- **Silicon surface estimates:** Thanks to inclined modules at high pseudo-rapidity, the *Inclined* Layout is characterised by a reduced silicon surface when compared to the *Extended* Layout (see § 7.5). As stated in Table 7.7, a reduced number of pixel modules is also foreseen.

The considerations described above clarify the strengths of the *Inclined* Layout with respect to the *Extended* Layout. An inner pixel system based on the *Inclined* Layout concept is recommended for the future ITk. In particular, it is strongly recommended the ability to provide multiple measurements in the innermost layer before traversing the big amount of material placed in the barrel to end-cap transition region. Further optimisation is needed to establish the final features of the layout: radii of the layers, radial offset of the inclined modules with respect to the straight ones, inclination angle, position of the straight to inclined transition region, etc..

11.1.2.1 Radius of the Innermost Layer

The radius of the innermost layer of the pixel detector was set to 39 mm in the LoI layout. Many inputs are taken into account to describe the actual benefit of reducing the innermost radius, such as fluences, detector and bandwidth occupancy, silicon surface and tracking performance. An improvement of about 10% in the impact parameter resolution for low momentum tracks is achieved by reducing the innermost radius from 39 mm to 33 mm (see § 10.2.2.2 and Figure 10.13). Moreover, a reduction of the barrel length and hence silicon surface of about 10-15% is foreseen, while maintaining the same hermeticity. On the other hand, lowering the innermost radius imply higher integrated radiation dose for the innermost pixel detector which would need more than one replacement to ensure high sensor efficiency. Nevertheless, data transmission on 5 Gb/s copper long links is already extremely challenging for the baseline layout with the current innermost radius at 39 mm. At 33 mm, an increase in channel and cluster occupancy of about 10-30% is expected which will result even more challenging.
The combination of all these factors suggested to keep the innermost layer at a radius of 39 mm with minor variation ($O(\pm 1$ mm)) driven by engineering considerations and constraints. Moreover, if needed and feasible the *Inclined* Layout concept provides the additional flexibility to define two different radii for the straight and inclined sections.

11.1.3 Outer Pixel Barrel System

For the outer pixel barrel system, the major input to be taken into account is the difference in terms of silicon surface when comparing the two candidate layout. As shown in Table 7.7, the *Inclined* Layout presents a reduction of about 25% in the silicon surface of the outer pixel barrel system with respect to the *Extended* Layout. On the other hand, this is not correlated to a reduction of the number of modules because of different types pixel modules used in the two candidate layouts. The *Inclined* Layout presents, indeed, $\sim$ 10% more modules than the *Extended* Layout (see Table 7.8).

Because of the similar number of measurements provided by the outer system in both candidate layouts, no significant changes are expected in terms of track parameter resolution and track reconstruction efficiency by inclining modules in the outer pixel layers.

Given these considerations, no recommendation is provided for the pixel outer barrel system.

11.1.4 Pixel End-cap System

For the pixel end-cap region, the single concept developed is the pixel ring end-cap system which can complement both the *Extended* and *Inclined* Layout. The ring system described in § 7.4.2, is a very powerful alternative to a more traditional disk system by offering the flexibility of moving the single rings to ensure the required hermeticity and number of measurements in the forward region. By routing the services on the mechanical supports between the rings, it is possible to move the inactive material outside the tracking region.

11.1.5 Additional Considerations

11.1.5.1 Pixel Size

§ 10.2.2.3 describes the results comparing two pixel sensor cell sizes, $50 \times 50 \ \mu\text{m}^2$ and $25 \times 100 \ \mu\text{m}^2$. The choice of the readout size doesn't impact the layout configuration while mainly affects the intrinsic measurement precision and hence the resolution of the track parameters (see Figures 10.14 and 10.15). In this aspects, the *Extended* and *Inclined* Layouts behave very similar.

Further studies are needed to fully assess the performance implications of the different options for the pixel pitch especially in the context of *b*-tagging and track-to-vertex efficiency.

11.1.5.2 Digital and Analog Pixel Readout

Improved performance can be achieved with a better intrinsic measurement precision than the one provided by the digital clustering algorithm. This was also shown in Figure 10.8: the performance of the ATLAS Run-2 ID at high momentum is significantly better than the digital clustering approach used for the ITk candidate layouts. Moreover, the charge information used to better refine the cluster resolution can be used as an even more powerful tool for track reconstruction in dense environments, as explained in § 8.2.3.5. When the local track density gets so high that clusters from close-by particles merge or overlap, e.g. in the core of boosted jets or as a product of a decay of a boosted object, the charge pattern in such shared clusters can be used in order to flag or potentially even split them. Figure 11.1 shows a comparison of the τ reconstruction efficiency in the 3-prong decay channel as a function of the momentum of the τ and its change when allowing cluster splitting on different subsets of layers.

All five layers should be therefore equipped with analog readout providing a comparable or better charge or time-over-threshold information as the current ATLAS IBL (4-bit ToT information) in order to maximise the performance in dense environment.

11.2 Layout Development Based on the List of Recommendation

Following the guidelines described in the previous section, the results presented in the previous chapter and detailed physics studies collected in the final Report of the Layout Task Force [126], the *Inclined* Layout concept has been defined as baseline for the Phase-II ATLAS Tracker.

The first description of the ITk *Inclined* Layout and its performance are documented in the TDR for
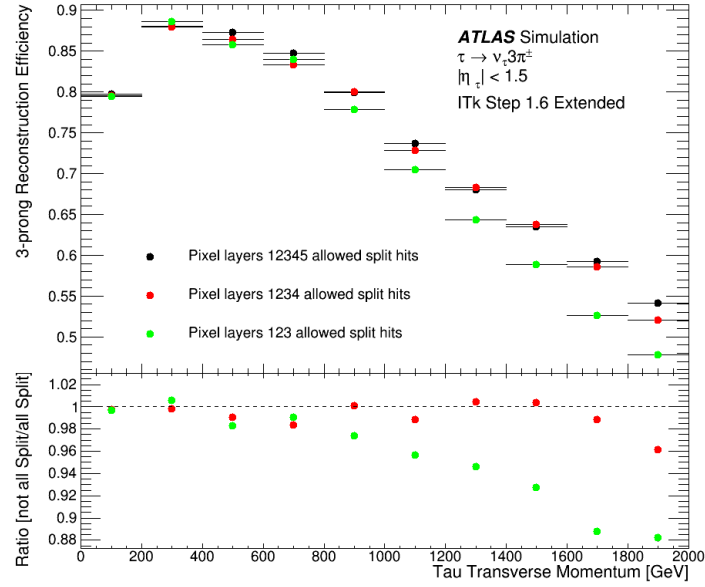
Figure 11.1: τ reconstruction performance versus τ momentum in the 3-prong decay channel. Different cluster splitting scenarios are shown. L12 denotes cluster splitting in the two innermost layers, L123 in the inner three and so on [58].

the ATLAS Inner Tracker Strip Detector [58]. Since the time of the Strip TDR, the pixel layout has been subject to a process of optimisation which converged in the ITk *Inclined Duals* Layout, whose performance are described in the TDR for the ATLAS Inner Tracker Pixel Detector [104].

While the ITk *Inclined Duals* Layout maintains almost unchanged the configuration of the strip detector, the design of the pixel detector underwent many changes mainly driven by the list of recommendation presented above and more engineering details and constraints. The *Inclined* Layout and the *Inclined Duals* Layout are shown respectively in Figure 11.2 and Figure 11.3 and the main differences among them are summarised below:

- The optimisation of the end-cap system to remove the excess of hits in the forward region allowed to lower the number of measurements to 9 hits for $|\eta| > 2.7$. The 9 hits requirement is fulfilled in the entire η range, as shown in Figure 11.4.

- The staves of the five layers were staggered in z (with an offset of 6 mm) to avoid losing tracks at $\eta = 0.0$, as shown in Figure 9.1.

- The active size of the pixel read-out chip was increased to 19.2 mm $\times$ 20.0 mm, which led to slightly larger double and quad modules compared to Figure 7.10.

- The optimised definition of the envelopes triggered changes in the barrel layer radii, as well as in the radii of the end-cap system.

- For the inner pixel barrel system the longeron solution (see § 7.4.1.2 and Figure 7.8) was dropped in favour of a dual shell structure in order to increase the layout stability. In this configuration the two layers inside the IST are decoupled allowing for a different number of staves per layer. This number was optimised to provide the required hermeticity while reducing module overlaps. The radius of the flat section of the second layer was also increased to better space out the first two measurements in radius.

- The inner radius of the inclined section of the innermost layer was decreased to 36 mm which allowed for the shortening of the barrel section in z still covering up to $|\eta| = 4$.

- Accordingly to the bigger module size, the number of hits was kept as stable as possible with the introduction of quad modules in the inclined region of the second layer significantly simplifying the layout of the outer end-cap system and reducing the total pixel surface needed.

- The inclination angle was also increased to 75° in the inclined section of the two innermost layers keeping an inclination angle of 56° degrees in the other layers.

- The length of the outer pixel barrel system was synchronised with the length of the inner barrel region with the main motivation of not lining up the barrel to end-cap transition region in the pixel and strip detectors.

- The flat part of the outer system was extended to avoid lining up the straight to inclined transition regions for the inner and outer pixel barrel systems. This allowed to extend the coverage of the flat region before the inclined modules take over minimising the number of modules per stave.

- The radius of the flat section of the outer barrel layers was increase by 5 mm with respect to the inclined region to maximally increase the lever arm in the central region of the pixel detector and to reduce the complexity of engineering in the flat to inclined transition on the stave, mainly related to the bending of the cooling pipes.

- The end-cap system was supplemented of an inner ring layer to improve the coverage close to $|\eta| = 4$ and to reduce the extrapolation distance between the end of the barrel and the first hit in the end-caps.

After these changes, the exact layer radii and sensor positions have been re-optimised to ensure full hermeticity for particles originating from a luminous region extending up to $\pm$ 15 cm in z. The resulting layout is shown in Figure 11.3 with both the overall layout of the ITk and the zoom into the pixel system.

Tables 11.1 to 11.3 detail the main design parameters of the *Inclined Duals* Layout. Figure 11.4a shows the total number of pixel-plus-strip measurements on track, demonstrating that the number of hits is above 9 at all η except very close to $|\eta|$ of 4, while Figure 11.4b shows the number of pixel measurements as a function of η. The number of hits exceeds the minimum requirement of 9 hits due to primary vertex z spread and sensor overlaps.

Table 11.4 summarises the difference in total silicon surface needed for the different parts of the detector for the *Inclined* and *Inclined Duals* Layout. In total the pixel surface is reduced from 13.48 m^2 in the *Inclined* Layout to 12.53 m^2 in the *Inclined Duals* Layout, mainly because of the reduced hit requirement for $|\eta| > 2.7$.

The track reconstruction requirements have been re-evaluated for the different pseudo-rapidity ranges and are shown in Table 11.5.

Figure 11.5 shows the summary of the material distribution of X_0 versus η for the for the *Inclined Duals* Layout and the current ATLAS ID. The material of the new detector will be significantly less for nearly all η.
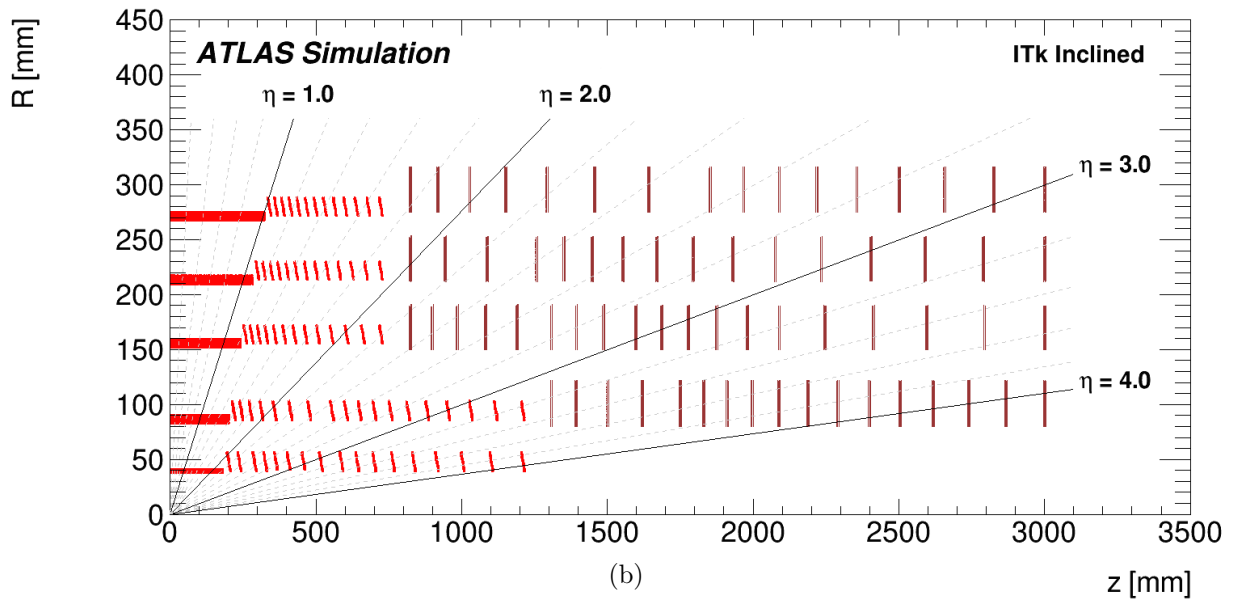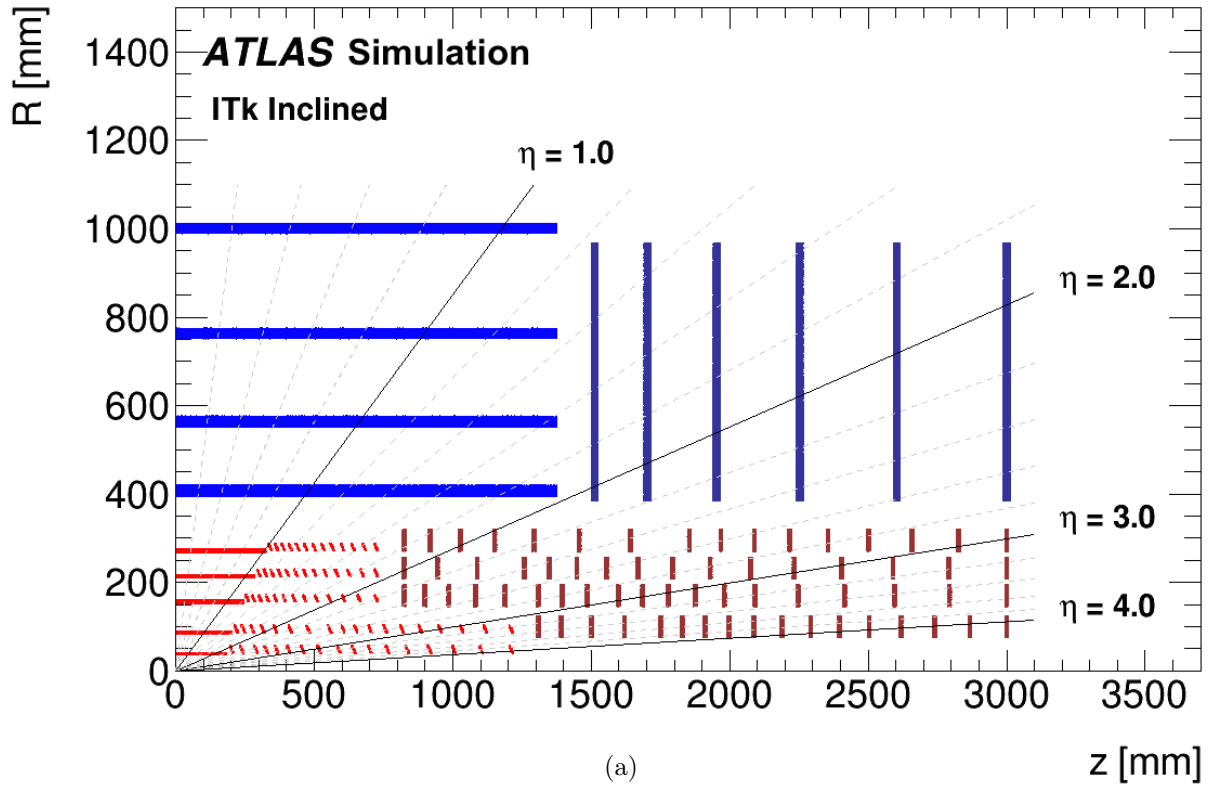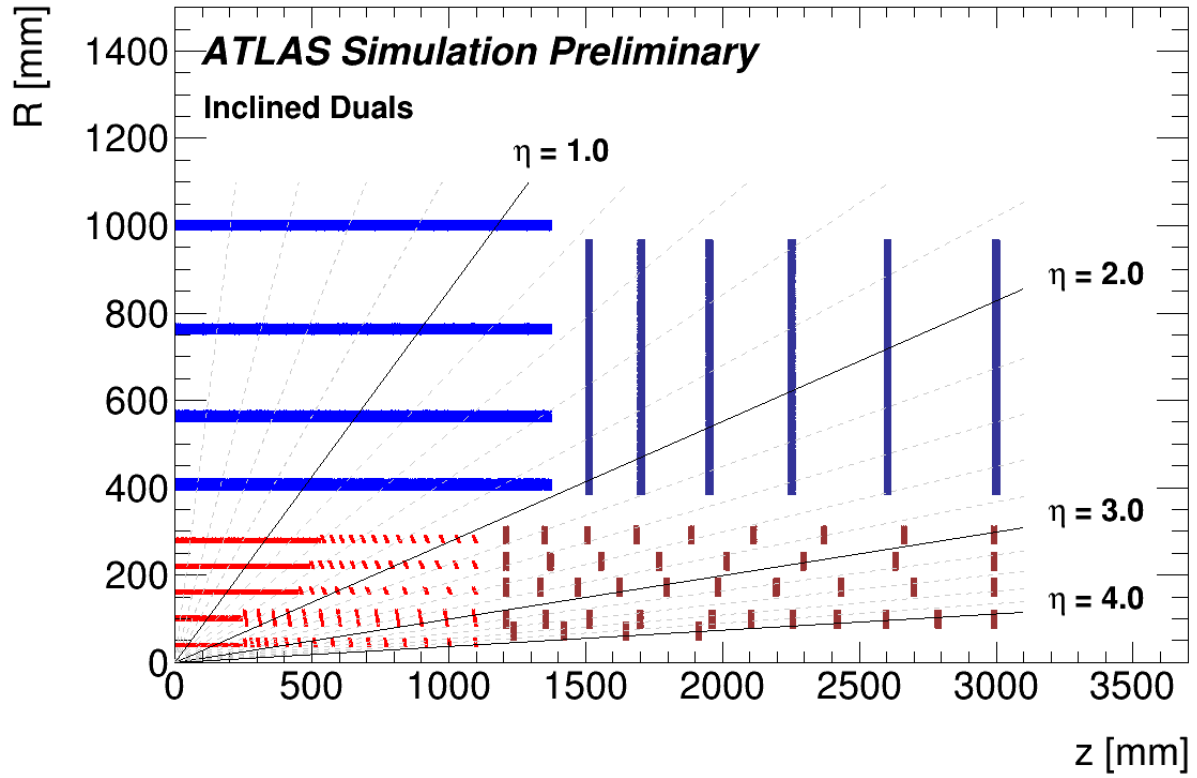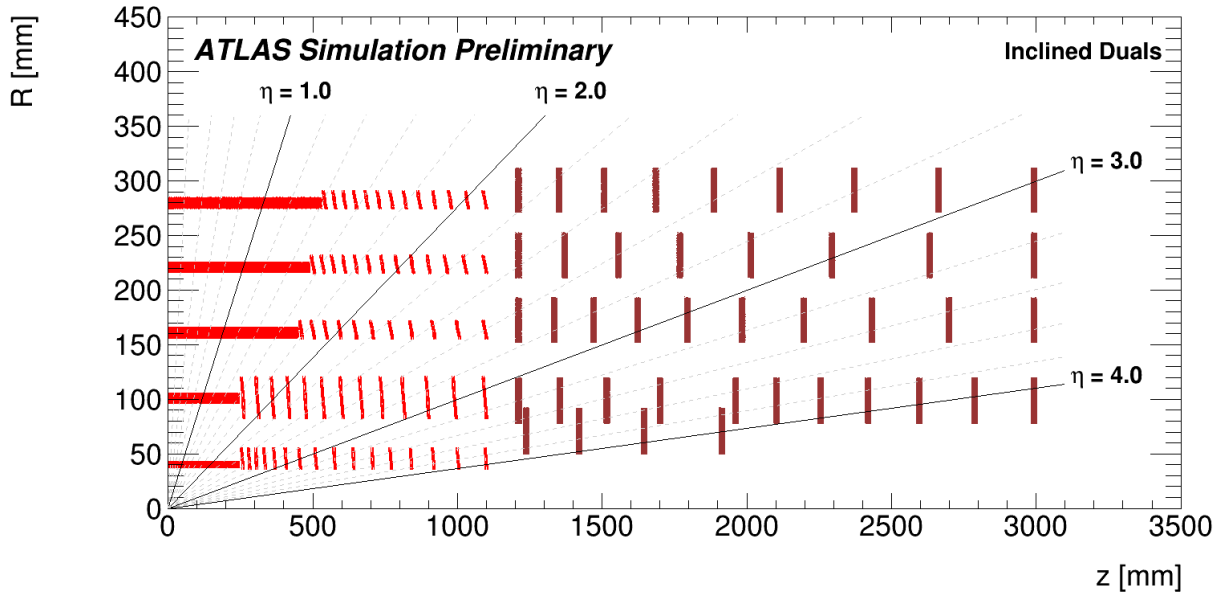
Figure 11.2: (a) Schematic layout of the ITk *Inclined* Layout for the HL-LHC phase with the pixel layout as presented in the Technical Design Report for the ATLAS Inner Tracker Strip Detector. (b) Zoom into the Pixel Detector. Only one quadrant and only active detector elements are shown for both diagrams [58].

(a)

(b)

Figure 11.3: (a) Schematic layout of the ITk *Inclined Duals* Layout for the HL-LHC phase with the pixel layout as presented in the Technical Design Report for the ATLAS Inner Tracker Pixel Detector. (b) Zoom into the Pixel Detector. Only one quadrant and only active detector elements are shown for both diagrams [104].
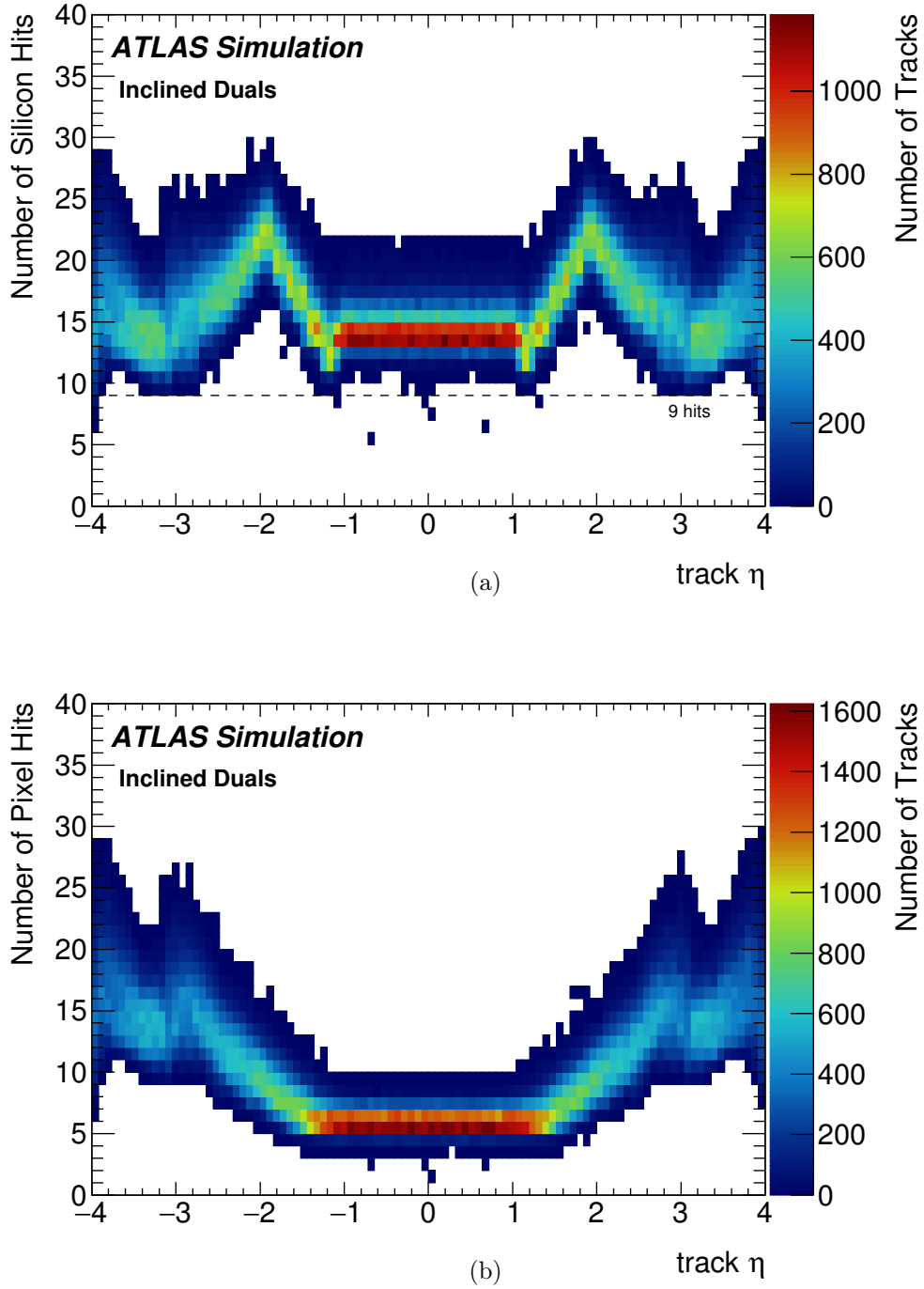
Figure 11.4: (a) Total number of strip plus pixel measurements (hits) on track as a function of η. (b) Number of pixel measurements (hits) on track as a function of η. For this figure a sample of single muon events with $p_\mathrm{T} = 1$ GeV is used. The muons are produced with a flat distribution between -15 to 15 cm in z_{vertex} and between 0.0 to 2.0 cm in R_{vertex}, respectively [104]. The same plots for the *Inclined* Layout are shown in Figure 9.4.

Layer	Radius [mm]		Staves	1/2 Stave Length [mm]	Sensors on 1/2 Stave		Sensor Size [mm²]	
	Straight Region	Inclined Region			Straight Region	Inclined Region	Straight Region	Inclined Region
0	39	36	16	1100	6	16	40.0 × 19.2	19.2 × 20.0
1	99	80	20	1100	6	13	40.0 × 38.4	38.4 × 40.0
2	160	155	30	1100	11	11	40.0 × 38.4	19.2 × 40.0
3	220	215	40	1100	12	13	40.0 × 38.4	19.2 × 40.0
4	279	274	50	1100	13	13	40.0 × 38.4	19.2 × 40.0

Table 11.1: Layout parameters for the barrel-like region of the *Inclined Duals* Pixel Barrel Layout.

Layer	Positions of the Inclined Modules on the Stave [mm]
0	253.6 276.8 301.6 330.7 364.9 405.1 452.3 507.8 573.0 638.5 703.9 766.9 836.5 913.9 999.7 1095.1
1	253.6 303.6 356.3 411.4 468.8 529.8 594.3 662.3 733.6 808.2 891.6 985.0 1089.6
2	454.2 494.7 539.1 587.8 641.3 699.8 764.1 834.5 911.7 996.4 1089.3
3	494.8 528.5 564.6 603.0 644.0 687.8 734.6 784.5 837.8 894.6 955.3 1020.1 1089.3
4	535.4 568.7 604.0 641.3 680.7 722.4 766.4 813.0 862.3 914.4 969.5 1027.7 1089.3

Table 11.2: Layout parameters for the inclined region of the *Inclined Duals* Pixel Barrel Layout.

Ring Layer	Inner Radius [mm]	Sensors per Ring	Sensor Size [mm^2]	Position [mm]
0	50.0	16	40.0 × 38.4	1238.0 1420.0 1646.0 1913.0
1	80.0	22	40.0 × 38.4	1211.0 1353.8 1515.9 1699.7 1962.0 2103.2 2255.4 2419.4 2596.2 2786.8 2992
2	150.0	32	40.0 × 38.4	1211.0 1333.8 1470.7 1623.5 1794.0 1984.3 2196.5 2433.3 2697.5 2992
3	212.5	44	40.0 × 38.4	1211.0 1371.4 1556.0 1768.5 2013.2 2294.8 2632.0 2992
4	275.0	52	40.0 × 38.4	1211.0 1350.1 1507.4 1685.3 1886.5 2114.1 2371.5 2662.7 2992

Table 11.3: Layout parameters for the *Inclined Duals* Ring End-cap Layout.

11.3 Tracking Performance of the ITk Inclined Duals Layout

This section is dedicated to the discussion of the expected performance of the *Inclined Duals* Layout. Results are presented on tracking efficiency, fake rates at different levels of pile-up, track parameter resolution and robustness of tracking with respect to detector defects. The performance of the primary vertex reconstruction is also shown as well as results for *b*-tagging and pile-up mitigation for jets. When possible, the performance of the ITk layout is compared to the performance of the current ATLAS ID. Performance of the current ID are obtained using the analog clustering and, in case of pile-up, an average of 20 overlaid pile-up events.

11.3.1 Tracking and Vertexing Performance

11.3.1.1 Tracking Efficiency and Fake Rates

Following the same prescriptions shown in § 10.1.1 and § 10.2.3.1, the physics track reconstruction efficiency and the rate of fake tracks have been studied for different type of particles and at different levels of pile-up. Figure 11.6a shows the efficiency to reconstruct single muons, pions and electrons at p_T as a function of the pseudo-rapidity. For single muons, the efficiency is close to 100% in the entire pseudo-rapidity region. Given the reduction of the detector material in the *Inclined Duals* Layout with respect to the current ATLAS ID (see Figure 11.5), better efficiency to reconstruct pions and electrons is achieved.

The physics track reconstruction efficiency for $t\bar{t}$ events with an average of 200 overlaid pile-up events, compared to the current detector performance, is shown in Figure 11.6b. Moreover, as shown in Figure 11.7a, the track reconstruction efficiency is found to be stable to better than 1% for $t\bar{t}$ events for pileup values between 40 and 250.

As described in § 10.2.3.1, an inclusive measurement of the rate of fake or mis-reconstructed tracks is the ratio of reconstructed to the number of generated track particles. For the *Inclined Duals* Layout, the ratio results to be very stable over the full range of pile-up studied for all η regions, as depicted in Figure 11.7b. The fake rate is reported in Figure 11.8. It is compared to the current detector with requiring two different track selections. Despite a factor 10 more in the average number of overlaid pile-up events, the ITk layout is outperforming the Run-2 detector in terms of fake rate; this is due to the enlarged lever arm and the higher granularity.

| | Surface [m²] | |
	Inclined Layout	*Inclined Duals* Layout
Inner Barrel Straight	0.35	0.44
Inner Barrel Inclined	0.64	1.00
Inner Barrel Total	1.00	1.44
Inner Rings	1.11	0.83
Outer Barrel Straight	2.53	4.49
Outer Barrel Inclined	2.28	2.30
Outer Barrel Total	4.82	6.79
Endcap Outer Rings	6.55	3.47
Barrel Total	5.82	8.23
Endcap Rings Total	7.66	4.30
Total	13.48	12.53

Table 11.4: Summary of Pixel surface in the *Inclined* Layout and *Inclined Duals* Layout [104].

Requirement	Pseudo-rapidity Interval		
	$\lvert\eta\rvert < 2.0$	$2.0 < \lvert\eta\rvert < 2.6$	$2.6 < \lvert\eta\rvert < 4.0$
pixel+strip measurements	≥ 9	≥ 8	≥ 7
pixel measurements	≥ 1	≥ 1	≥ 1
holes	< 2	< 2	< 2
strip double holes	≤ 1	≤ 1	≤ 1
pixel holes	< 2	< 2	< 2
strip holes	< 2	< 2	< 2
p_T [MeV]	> 900	> 400	> 400
$\lvert d_0 \rvert$ [mm]	≤ 2	≤ 2	≤ 10
$\lvert z_0 \rvert$ [cm]	≤ 20	≤ 20	≤ 20

Table 11.5: Set of requirements applied during the track reconstruction depending on the pseudo-rapidity interval for the *Inclined Duals* Layout [104].
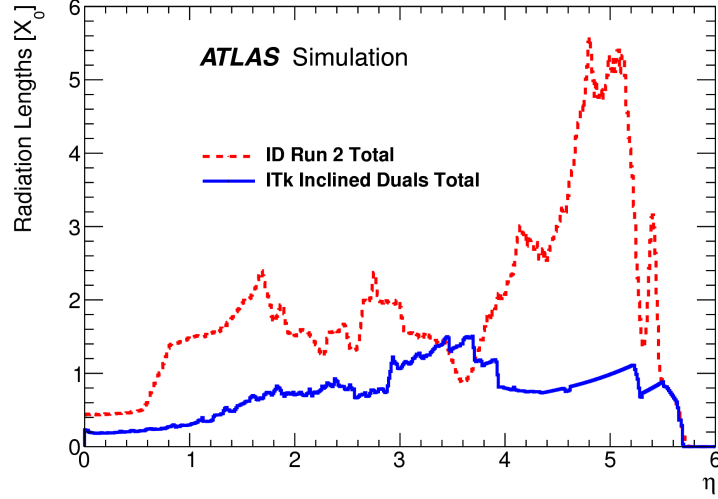
Figure 11.5: Total radiation length X_0 versus the pseudo-rapidity η for the current ATLAS Inner Detector and the ITk *Inclined Duals* Layouts. The material of the new detector will be significantly less for nearly all η [104].
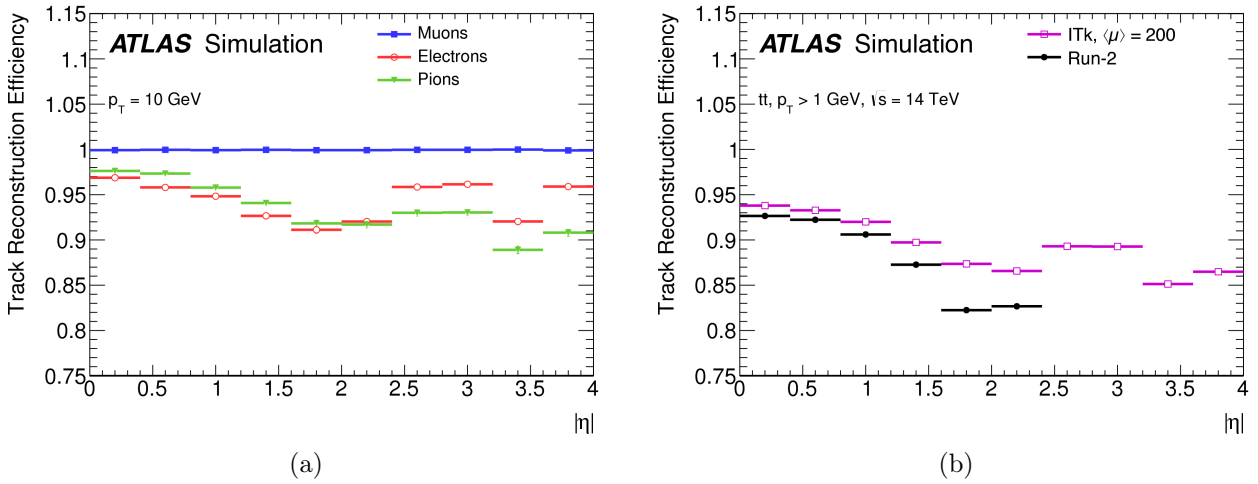

Figure 11.6: (a) Physics track reconstruction efficiency as a function of the pseudo-rapidity for single muons, pions and electrons with $p_T = 10$ GeV. (b) Physics track reconstruction efficiency as a function of the pseudo-rapidity for $t\bar{t}$ events with an average of 200 overlaid pile-up events. The performance of the current ATLAS ID are evaluated considering an average of 20 overlaid pile-up events [104].

(a)   (b)
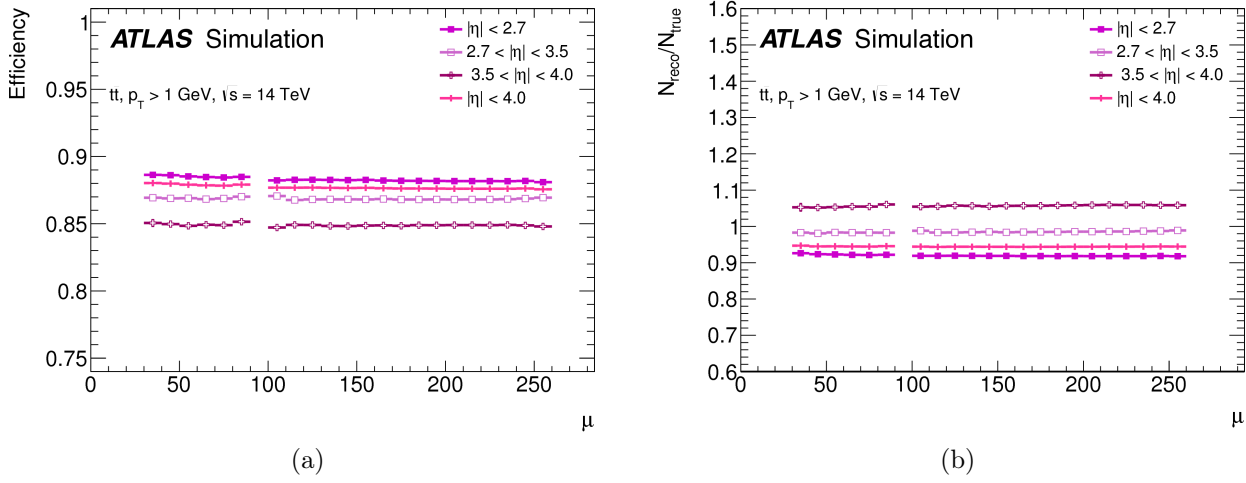
Figure 11.7: (a) Physics track reconstruction efficiency as a function of pile-up for top pair events with 40 to 250 overlaid pile-up events, for different pseudo-rapidity regions. (b) Ratio of the number of reconstructed to generated particles as a function of pile-up for top pair events with 40 to 250 overlaid pile-up events, for different pseudo-rapidity regions. Both variables result to be very flat over the full range of pile-up studied [104].
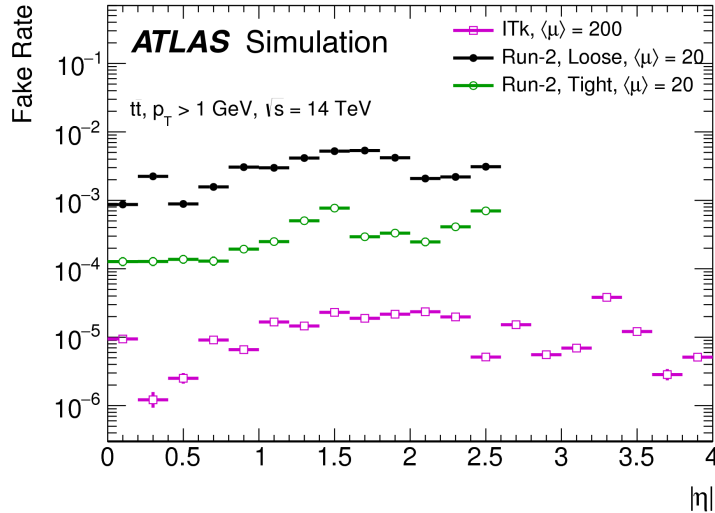
Figure 11.8: Fake rate for reconstructed tracks for top pair production events. The ITk *Inclined Duals* Layout is compared to the current ATLAS ID with two different track selections. $t\bar{t}$ events are overlaid with an average of 200 (20) pile-up events for the ITk *Inclined Duals* (ATLAS ID). The ITk layout is outperforming the Run-2 detector in terms of fake rate; this is due to the enlarged lever arm and the higher granularity [104].

11.3.1.2   Track Parameter Resolutions

Track parameter resolutions are evaluated for the *Inclined Duals* Layout using single muons with $p_T = 1, 10, 100$ GeV. They are shown in Figure 11.9. The ITk layout is simulated with 50×50 μm^2 pixels and digital clustering.

At low p_T values, the d_0 resolution is mostly dominated by multiple scattering contributions and the values for the ITk layout are very comparable to the Run-2 detector for $|\eta| < 2.5$. At large η, the resolution remains good, indicating that useful information will be provided by these tracks, e.g. for pile-up jet rejection and b-tagging purposes. At higher p_T values, the ITk layout presents a worse resolution than the current ATLAS ID. In this regime the intrinsic measurement resolution dominates and the ATLAS ID detector takes advantage of the use of the analog clustering and the smaller radius of the first pixel measurement. $\sigma(z_0)$ is significantly better for the *Inclined Duals* Lyout than for the current ID at all values of p_T, primarily due to the decreased pixel pitch in the z direction. Thanks to the higher precision of the ITk strip tracker compared to the TRT and the reduced material, the ITk layout achieves a factor of two better momentum resolution.

Figure 11.10 shows the track parameter resolutions using the analog clustering for single muons with $p_T = 100$ GeV and 50×50 μm^2 and 25×100 μm^2 pixel dimensions. Thanks to the improved intrinsic measurement resolution, the ITk layout outperforms the current detector in both pixel dimension scenarios. With 25×100 μm^2 pixels, $\sigma(d_0)$ is improved by nearly a factor of two over the full pseudo-rapidity range, at the cost of about 35% loss in $\sigma(z_0)$. Also the momentum resolution is improved using 25×100 μm^2 pixels: it is improved by 20% in the barrel while more than a factor two improvement is achieved in the forward region.

11.3.1.3   Alignment Studies

For the *Inclined Duals* layout, the effect on the track parameter resolutions due to local misalignment at the module level and global deformation of the inner barrel structure are studied. Figure 11.11 shows that in case of a global misplacement of 10 μm of the pixel barrel system in x and y, the nominal track parameter resolution can be completely recovered by the ATLAS alignment procedure, as described in § 10.2.3.2.

11.3.1.4   Detector Performance Stability with Ageing and Component Failures

The effect of component failures and detector inefficiencies (see § 10.2.3.3) on the ITk *Inclined Duals* Layout is shown in Figure 11.12. The layout is simulated with 15% inactive modules and a rate of 3% and 1% random channel inefficiencies for pixel and strip sensors, respectively, and compared to the nominal configuration without defects. The physics track reconstruction efficiency and the fake rate as a function of η are evaluated using $t\bar{t}$ events with an average of 200 overlaid pile-up events. The inclusion of defects in the simulation implies a deterioration of the physics track reconstruction efficiency and an increase in the fake rate with respect to the nominal configuration, especially in the barrel region.

11.3.1.5   Primary Vertex Reconstruction

The goals of the primary vertex reconstruction are to find and determine the position of the hard-scatter and pile-up interaction vertices in collision event using information on the reconstructed tracks and on the beam spot position and shape for each period in an LHC run. Two different approaches are used for the reconstruction of the primary vertex in Run-2 and Phase-II simulation which have been optimised considering the corresponding levels of pile-up.
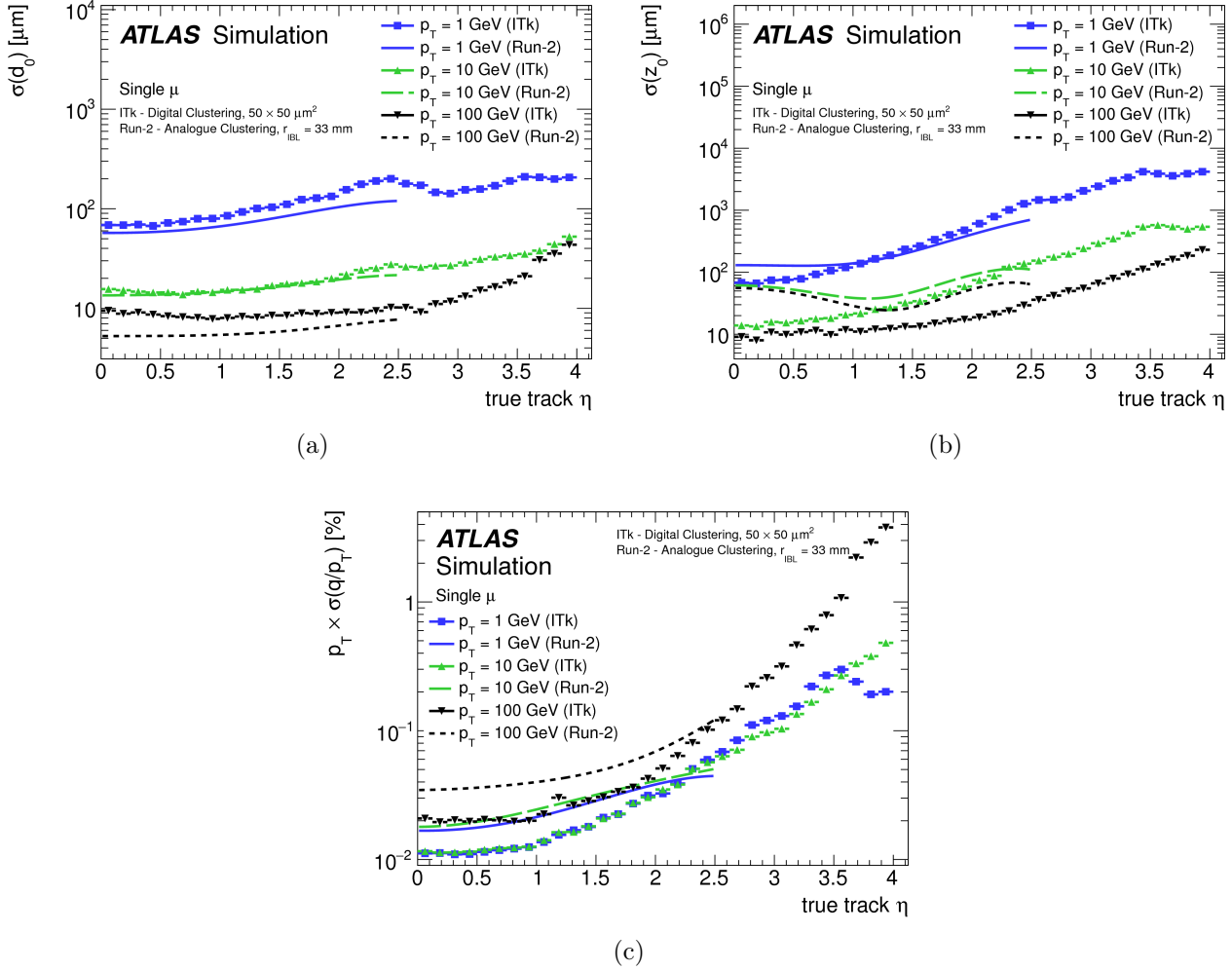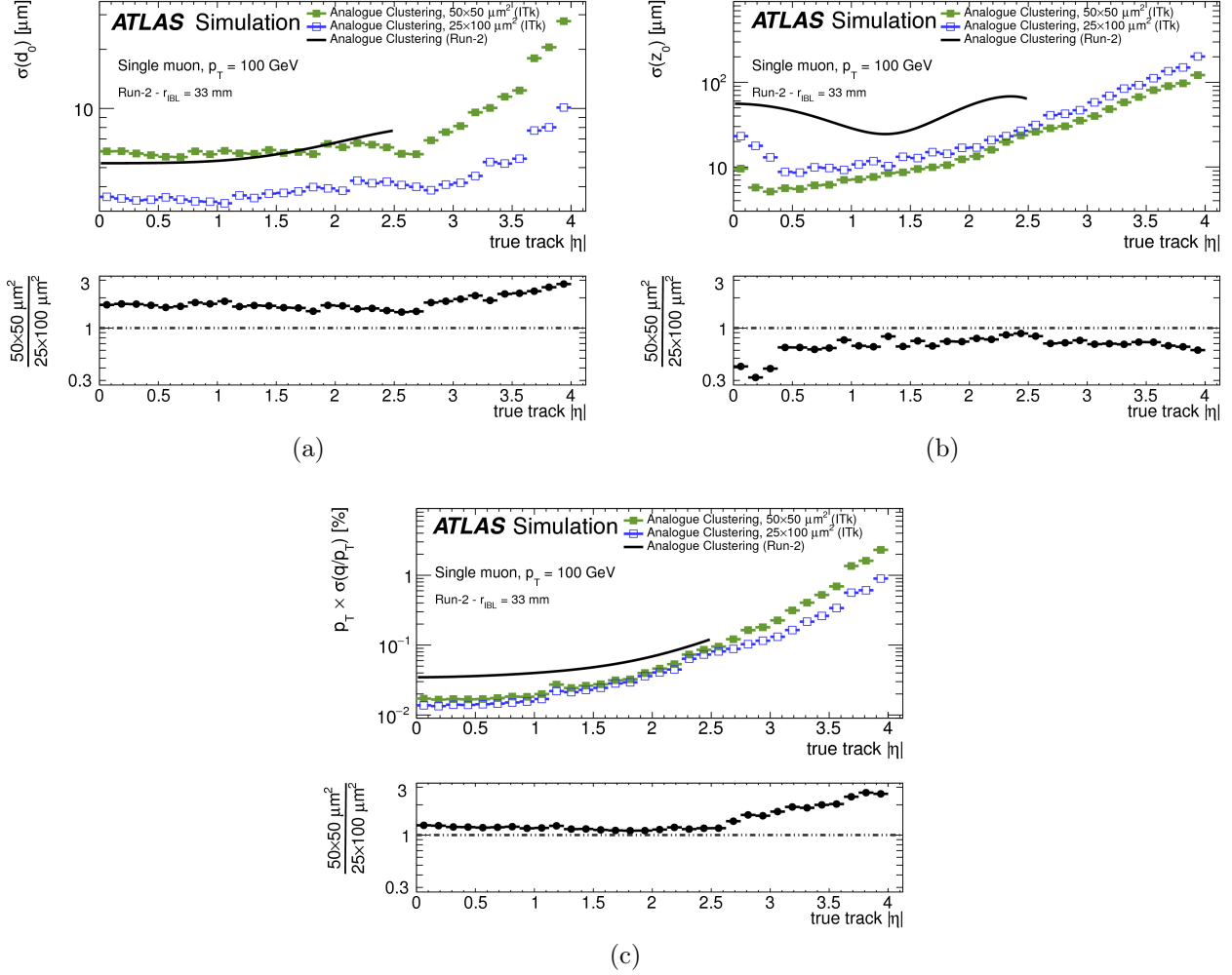
(a)

(b)

(c)

Figure 11.9: Track parameter resolution in (a) d_0, (b) z_0 and (c) $p_{\rm T}$ as a function of the pseudo-rapidity for single muons with $p_{\rm T} = 1, 10, 100$ GeV. The ITk layout is simulated using 50×50 $\mu{\rm m}^2$ pixels and digital clustering. Comparisons with the current ID are shown. At low $p_{\rm T}$ values, the ITk layout shows results comparable to the Run-2 detector for the d_0 resolution for $|\eta| < 2.5$. At higher $p_{\rm T}$ values, the ITk layout presents a worse resolution than the current ATLAS ID, since the latter takes advantage of the use of the analog clustering and of the smaller radius of the first pixel layer. $\sigma(z_0)$ is significantly better for the *Inclined Duals* than for the ID at all values of $p_{\rm T}$. Thanks to the higher precision of the ITk strip tracker compared to the TRT and the reduced material, the ITk layout achieves a factor of two better momentum resolution [104].

Figure 11.10: Track parameter resolution in (a) d_0, (b) z_0 and (c) p_T as a function of the pseudo-rapidity for single muons with $p_T = 100$ GeV. The ITk layout is simulated using analog clustering and both 50×50 μm^2 and 25×100 μm^2 pixel dimensions. Comparisons with the current ID are shown. Thanks to the improved intrinsic measurement resolution, the ITk layout outperforms the current detector with both pixel dimensions. With a pixel dimension of 25×100 μm^2, $\sigma(d_0)$ is improved by nearly a factor of two over the full pseudo-rapidity range, at the cost of about 35% loss in $\sigma(z_0)$. The momentum resolution is improved by 20% in the barrel while more than a factor two improvement is achieved in the forward region [104].

(a)   (b)
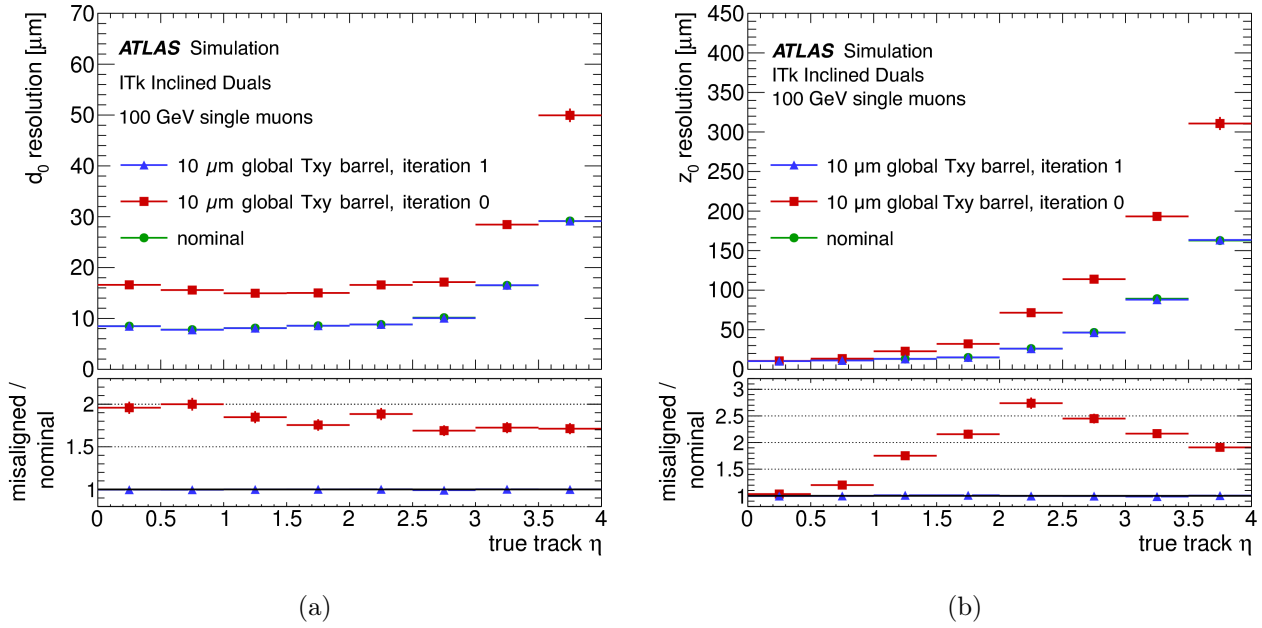
Figure 11.11: Alignment study showing the effect of a global 10 μm displacement of the pixel system in x and y on (a) the transverse and (b) the longitudinal impact parameter resolutions for single muons with $p_\mathrm{T} = 100$ GeV, before (iteration 0) and after (iteration 1) realignment [104].

(a)   (b)
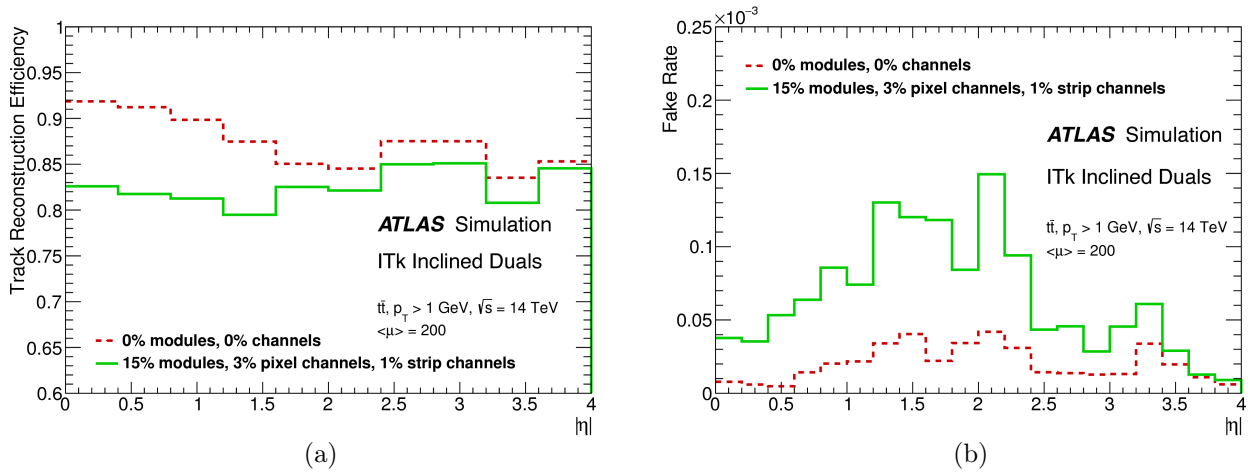
Figure 11.12: (a) Physics track reconstruction efficiency and (b) fake rate for the *Inclined Duals* Layout with and without 15% inactive modules and a rate of 3% and 1% random channel inefficiencies for pixel and strip sensors, respectively. The results are shown as a function of η for $t\bar{t}$ events with an average of 200 overlaid pile-up events. The inclusion of defects in the simulation implies a deterioration of the physics track reconstruction efficiency and an increase in the fake rate with respect to the nominal configuration, especially in the barrel region [104].
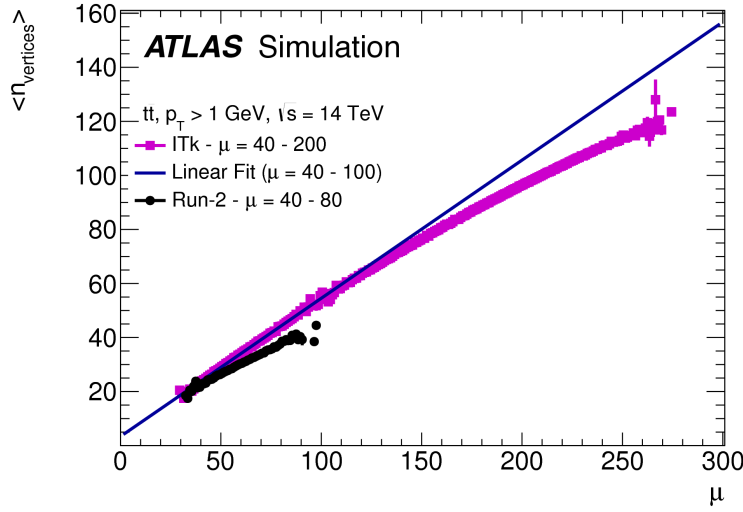
Figure 11.13: The number of reconstructed primary vertices as a function of pile-up for $t\bar{t}$ events with a pile-up between 30 and 270. A linear fit to the number of vertices for pile-up values between 40 and 100 extrapolated up to 270 pile-up is superimposed. Results are also shown for the Run-2 simulation sample. The Run-2 sample has a lower pile-up vertex efficiency, as can be seen from the different slope vs μ [104].

Figure 11.13 shows the number of reconstructed vertices as a function of pile-up for $t\bar{t}$ events with overlaid pile-up events between 30 and 270. At a constant efficiency, the number of reconstructed vertices is expected to depend linearly on pile-up, while vertex merging and splitting effects need to be taken into account. At typical Phase-II pile-up levels, the number of reconstructed vertices deviates from the linear form, indicating that vertex merging effects are present in the result. The Run-2 sample has a lower pile-up vertex efficiency, as can be seen from the different slope vs μ.
Figure 11.14 shows the transverse ($r = \sqrt{x^2 + y^2}$) and longitudinal (z) primary vertex resolutions as a function of the true local pile-up density in a $\pm$ 2 mm window around the primary interaction. It is evaluated for top pair events with an average of 200 pile-up events. No dependency on the local pile-up density is seen in the resolution of the primary vertex for the ITk *Inclined Duals* Layout, despite an increased probability for merging nearby pile-up vertices into the primary vertex. For the Run-2 detector the resolution degrades at high local pile-up densities.

11.3.2   Flavour Tagging Performance

One of the primary roles of a pixel detector is to provide precise track measurements required for the impact parameter measurement. The precision on the impact parameter translates into the b-tagging performance. The main requirement of the ATLAS Phase-II ITk is to preserve, and if possible improve, the current Run-2 b-tagging performance despite the very challenging pile-up scenario. Moreover, the extension of the η coverage allows physics analysis to use the b-tagging information also in the forward region. The b-tagging performance is characterised by the probability to identify a jet containing a b-hadron (b-jet efficiency) and by the inverse of the probability to identify a jet not containing a b- or c-hadron as a b-jet (light-jet rejection). In ATLAS b-tagging algorithms are based on multivariate techniques, which combine several information on the impact parameters of the tracks, on secondary vertices and on the kinematics of the event. One of this is the MV2 multi-variant tagger [127].

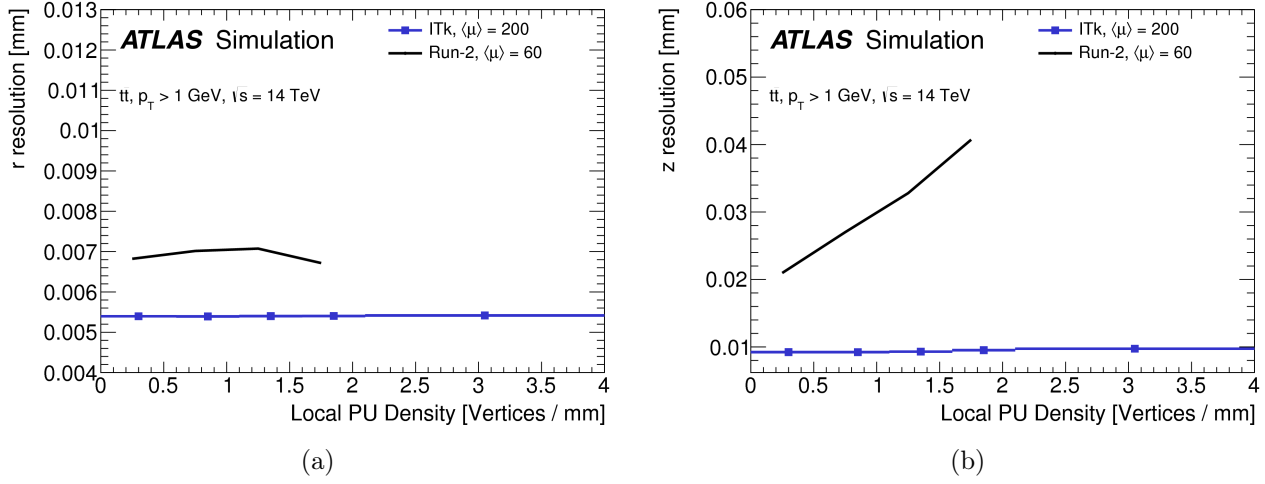(a)   (b)

Figure 11.14: The resolution for (a) the transverse and (b) the longitudinal coordinates of the primary vertex as a function of the pile-up density. Results are also shown for the Run-2 simulation sample. No dependency on the local pile-up density is seen in the resolution of the primary vertex for the ITk *Inclined Duals* Layout, despite an increased probability for merging nearby pile-up vertices into the primary vertex. For the Run-2 detector the resolution degrades at high local pile-up densities [104].

Figure 11.15a and Figure 11.15b show the light-jet rejection and the c-jet rejection as a function of the b-jet efficiency using the MV2 b-tagging algorithm. Despite the high level of pile-up, the ITk layout performs better than the current ID. The *Inclined Duals* Layout allows to discriminate between b- and light-/c-jets also in the very forward region.

11.3.3   Pile-up Jet Rejection

Another important design goal of the optimisation process is the maximisation of the ability of the pixel detector to help rejecting pile-up contributions to jet. This can be achieved using the separation along z of primary and pile-up vertices. Here again, extending the pseudo-rapidity range over which this information can be used is vital to maximise the physics performance of the experiment for Phase-II.

The simplest discriminant to tag and suppress pile-up jets is $R_{p\mathrm{T}}$, defined as the scalar p_T sum of the tracks that are associated with the jet and originate from the hard-scatter vertex PV_0 divided by the fully calibrated jet p_T, i.e.:

$$R_{p\mathrm{T}} = \frac{\sum_k p_\mathrm{T}^{\mathrm{trk}_k}(\mathrm{PV0})}{p_\mathrm{T}^{\mathrm{jet}}}. \tag{11.1}$$

The value of $R_{p\mathrm{T}}$ defines if a jet is more likely to be a pile-up jet or not. The performance in pile-up jet suppression of the detector is highly correlated to the z_0 impact parameter resolution, which determines the track-to-vertex association efficiency, and the p_T resolution of the tracks.

Figure 11.16 shows the rejection of pile-up jets using $R_{p\mathrm{T}}$ as a function of the efficiency of hard-scatter jets. It is evaluated using $t\bar{t}$ events with an average of 200 overlaid pile-up events. At a typical working point of 50 in pile-up jet rejection, good efficiency is obtained for all pseudo-rapidity values.
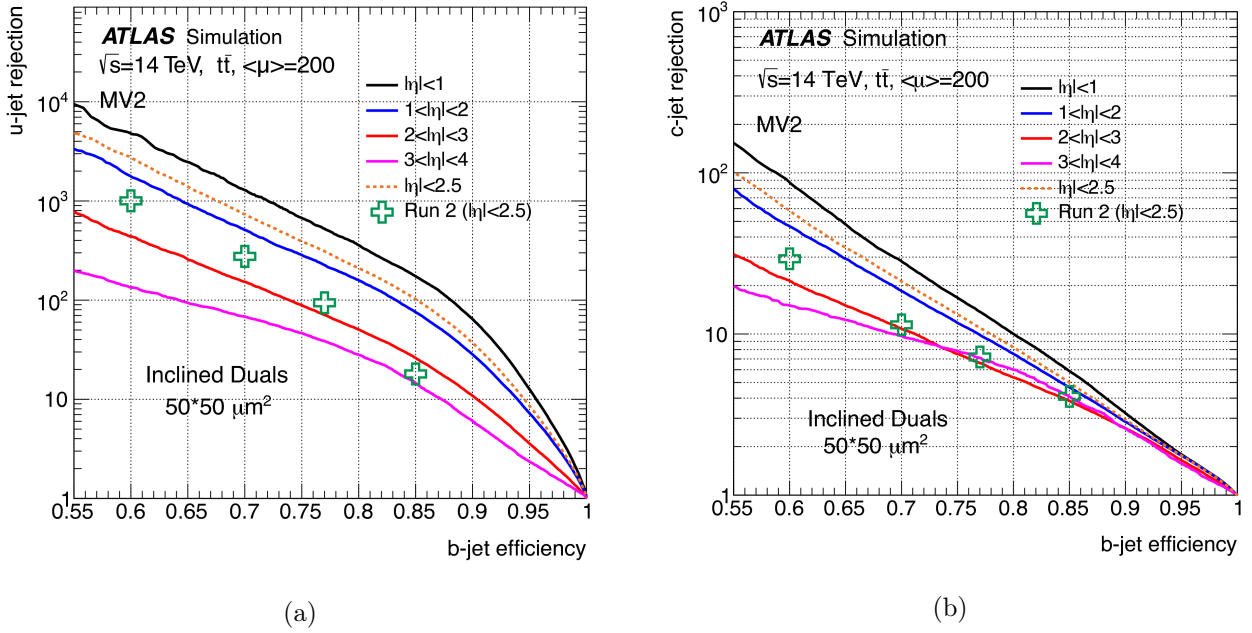
(a)

(b)

Figure 11.15: Performance of the MV2 b-tagging algorithms in $t\bar{t}$ events with 200 pile-up for the ITk *Inclined Duals* Layout. The rejection of (a) light-jets and (b) c-jets for different pseudo-rapidity regions is shown as a function of b-jet efficiency. Despite the high level of pile-up, the *Inclined Duals* layout performs better than the current ID. The new tracking detector allows to discriminate between b- and light-/c-jets also in the very forward region [104].

(a)

(b)
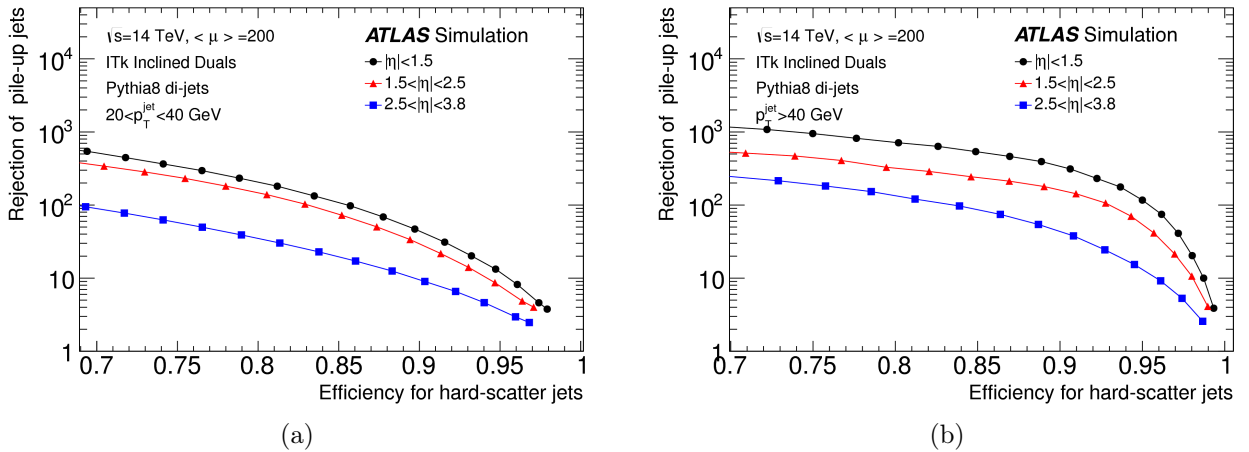
Figure 11.16: The rejection of pile-up jets as a function of the efficiency for hard-scatter jets with (a) $20 < p_T < 40$ GeV and (b) $p_T > 40$ GeV using the R_{p_T} discriminant in di-jet events with an average of 200 pile-up events. At a typical working point of 50 in pile-up jet rejection, good efficiency is obtained for all pseudo-rapidity values [104].

11.4 Conclusions

This chapter has discussed the list of recommended characteristics of the final ITk layout and the evolution of the ITk *Inclined* Layout into the ITk *Inclined Duals* Layout. The performance of the *Inclined Duals* Layout has been discussed and compared to the current ATLAS Inner Detector. Excellent tracking performance has been achieved using the ITk layout. Despite a factor 10 more in the number of overlaid pile-up events, the ITk *Inclined Duals* layout is outperforming the Run-2 detector in terms of physics tracking reconstruction efficiency for several objects, fake rate at different levels of pile-up, track parameter resolutions, primary vertex reconstruction, b-tagging and pile-up jet rejection. These results demonstrate the importance of the optimisation of the ATLAS Phase-II ITk layout to further expand the experiment physics reach.

Conclusion

This thesis describes major contributions to jet and track reconstruction. In a first part, it describes the improvement in jet reconstruction performance and its application in the search for diboson resonances in fully hadronic final states, and, in a second part, it presents the design and preparation of the ATLAS tracking system for the future High Luminosity LHC physics program.

Because of proton-proton collisions at high centre-of-mass energy, vector bosons are often produced with a transverse momentum higher than their mass. For this reason, the two-quark system produced in their hadronic decay, is collimated along the boson momentum direction. At high transverse momentum, the parton showers generated by the two quarks significantly overlap and can no longer be resolved. Boosted vector bosons can be therefore reconstructed as large radius jets to fully contain all of the energy deposits from their hadronic decay. Exploiting the internal substructure of these jets in new reconstruction and tagging techniques is therefore essential to distinguish jets containing the decay products of W and Z bosons from QCD-jets. These techniques are extremely important in the search for diboson resonances decaying hadronically.

A new reconstruction method has been developed in order to unify track and topo-cluster information into one single object, the Track-CaloCluster. This object exploits the excellent tracker spatial resolution and calorimeter energy resolution to improve jet substructure techniques at high p_T. Different types of Track-CaloCluster jets are studied and compared to topo-cluster jets. Track-CaloCluster jets provide superior mass resolution for $p_T > 2$ TeV with respect to topo-cluster jets, significantly outperforming for the resolution of the energy correlation variable D_2 in the entire p_T spectrum considered. A factor of two improvement in D_2 resolution is obtained for highest p_T jets. Profiting from the improved jet-substructure performance, a novel boosted boson tagging algorithm has been developed and optimised. Unlike previous techniques, optimised for maximising the background rejection for fixed signal efficiencies, this novel approach is designed to provide the maximum significance for boosted W/Z-jets with respect to QCD-jets. p_T dependent cuts on jet mass and D_2 are evaluated to provide the largest discrimination between boson-jets and QCD-jets. The algorithm has been optimised to identify W and Z bosons for both Track-CaloCluster and topo-cluster jets in order to provide a quantitative comparison of the physics reach when profiting from the improved jet substructure performance of Track-CaloCluster jets. It has been been shown that, compared to LC topo-cluster jets, Track-CaloCluster jets can provide approximatively 45% higher significance for 4 TeV W' resonances predicted by the heavy vector triplet model.

The vector boson identification algorithm is adopted in the search for WW, WZ and ZZ resonances with 79 fb^{-1} of proton-proton collisions collected at the LHC with the ATLAS detector in 2015-2017. Thanks to the use of the novel techniques described in this thesis, the analysis has been able to largely improve on past results.

The second part of this thesis focuses on the design optimisation of the ATLAS Phase-II Inner Tracker (ITk) and the evaluation of the performance of the candidate layouts. Two main layout choices were considered for the barrel region of the pixel system, an *Extended* and an *Inclined* Layout, both of them coupled with the same pixel ring system in the end-cap and a common strip system. Track parameter resolutions, efficiencies and fake rates have been studied for different layout configurations. This includes changing the radius of the innermost pixel layer or the readout segmentation, and is tested in presence of pile-up events, module misalignment and detector ageing effects. This allowed to identify strengths and weaknesses of the layout candidates and to define a list of recommended characteristics for the final design. Following these guidelines, the *Inclined* Layout concept has been defined as baseline for the ITk. The first description of the ITk *Inclined* Layout and its performance are documented in the Technical Design Report (TDR) for the ATLAS Inner Tracker Strip Detector.

Since the time of the Strip TDR, the pixel layout has been subject to a process of optimisation which converged in the ITk *Inclined Duals* Layout, whose performance are described in the TDR for the ATLAS Inner Tracker Pixel Detector. Despite the very challenging pile-up scenario, the ITk *Inclined Duals* layout is outperforming the Run-2 detector in terms of physics tracking reconstruction efficiency for several objects, fake rate at different levels of pile-up, track parameter resolutions, primary vertex reconstruction, b-tagging and pile-up jet rejection.

These results demonstrate the importance of the optimisation of the ATLAS Phase-II ITk layout to further expand the experiment physics reach.

Bibliography

[1] S. Glashow, *Partial Symmetries of Weak Interactions*, Nucl. Phys. **22** (1961) 579.

[2] S. Weinberg, *A Model of Leptons*, Phys. Rev. Lett. **19** (1967) 1264.

[3] A. Salam, *Weak and Electromagnetic Interactions*, Conf. Proc. **C680519** (1968) 367–377.

[4] P. W. Higgs, *Broken Symmetries and the Masses of Gauge Bosons*, Phys. Rev. Lett. **13** (1964) 508–509.

[5] F. Englert and R. Brout, *Broken Symmetry and the Mass of Gauge Vector Mesons*, Phys. Rev. Lett. **13** (1964) 321–323.

[6] S. Weinberg, *The Quantum Theory of Fields*, vol. 1. Cambridge University Press, 1995.

[7] Particle Data Group Collaboration, *Review of Particle Physics*, Chin. Phys. **C40** (2016) 100001.

[8] N. Cabibbo, *Unitary Symmetry and Leptonic Decays*, Phys. Rev. Lett. **10** (1963) 531–533, `https://link.aps.org/doi/10.1103/PhysRevLett.10.531`.

[9] M. Kobayashi and T. Maskawa, *CP Violation in the Renormalizable Theory of Weak Interaction*, Prog. Theor. Phys. **49** (1973) 652–657.

[10] ATLAS Collaboration, *Observation of a new particle in the search for the Standard Model Higgs boson with the ATLAS detector at the LHC*, Phys. Lett. **B716** (2012) 1–29, `arXiv:1207.7214 [hep-ex]`.

[11] CMS Collaboration, *Observation of a new boson at a mass of 125 GeV with the CMS experiment at the LHC*, Phys. Lett. **B716** (2012) 30–61, `arXiv:1207.7235 [hep-ex]`.

[12] ATLAS Collaboration, CMS Collaboration, *Combined Measurement of the Higgs Boson Mass in pp Collisions at $\sqrt{s} = 7$ and 8 TeV with the ATLAS and CMS Experiments*, Phys. Rev. Lett. **114** (2015) 191803, `arXiv:1503.07589 [hep-ex]`.

[13] ATLAS Collaboration, *Study of the spin and parity of the Higgs boson in diboson decays with the ATLAS detector*, Eur. Phys. J. **C75** (2015) 476, `arXiv:1506.05669 [hep-ex]`, [Erratum: Eur. Phys. J.C76,no.3,152(2016)].

[14] CMS Collaboration, *Inclusive search for the standard model Higgs boson produced in pp collisions at $\sqrt{s} = 13$ TeV using $H \to b\bar{b}$ decays*, Tech. Rep. CMS-PAS-HIG-17-010, CERN, Geneva, 2017. `https://cds.cern.ch/record/2266164`.

[15] ATLAS Collaboration, *Summary plots from the ATLAS Standard Model physics group*, `https://atlas.web.cern.ch/Atlas/GROUPS/PHYSICS/CombinedSummaryPlots/SM/index.html`.

[16] G. Altarelli, B. Mele, and M. Ruiz-Altaba, *Searching for new heavy vector bosons in $p\bar{p}$ colliders*, Zeitschrift für Physik C Particles and Fields **45** (1989) 109–121, `https://doi.org/10.1007/BF01556677`.

[17] E. Eichten, I. Hinchliffe, K. Lane, and C. Quigg, *Supercollider physics*, Rev. Mod. Phys. **56** (1984) 579–707, `https://link.aps.org/doi/10.1103/RevModPhys.56.579`.

[18] D. Barducci, A. Belyaev, S. Moretti, S. De Curtis, and G. M. Pruna, *LHC physics of extra gauge bosons in the 4D Composite Higgs Model*, EPJ Web Conf. **60** (2013) 20049, arXiv:1307.1782 [hep-ph].

[19] M. Perelstein, *Little Higgs models and their phenomenology*, Prog. Part. Nucl. Phys. **58** (2007) 247–291, arXiv:hep-ph/0512128 [hep-ph].

[20] G. C. Branco, P. M. Ferreira, L. Lavoura, M. N. Rebelo, M. Sher, and J. P. Silva, *Theory and phenomenology of two-Higgs-doublet models*, Phys. Rept. **516** (2012) 1–102, arXiv:1106.0034 [hep-ph].

[21] H. Georgi and S. L. Glashow, *Unity of All Elementary Particle Forces*, Phys. Rev. Lett. **32** (1974) 438–441.

[22] H. Fritzsch and P. Minkowski, *Unified Interactions of Leptons and Hadrons*, Annals Phys. **93** (1975) 193–266.

[23] F. Sannino, *Technicolor and Beyond: Unification in Theory Space*, J. Phys. Conf. Ser. **259** (2010) 012003, arXiv:1010.3461 [hep-ph].

[24] S. Catterall, L. Del Debbio, J. Giedt, and L. Keegan, *MCRG Minimal Walking Technicolor*, Phys. Rev. **D85** (2012) 094501, arXiv:1108.3794 [hep-ph].

[25] L. Randall and R. Sundrum, *A Large mass hierarchy from a small extra dimension*, Phys. Rev. Lett. **83** (1999) 3370–3373, arXiv:hep-ph/9905221 [hep-ph].

[26] T. Han, J. D. Lykken, and R.-J. Zhang, *On Kaluza-Klein states from large extra dimensions*, Phys. Rev. **D59** (1999) 105006, arXiv:hep-ph/9811350 [hep-ph].

[27] D. Pappadopulo, A. Thamm, R. Torre, and A. Wulzer, *Heavy Vector Triplets: Bridging Theory and Data*, JHEP **09** (2014) 060, arXiv:1402.4431 [hep-ph].

[28] ATLAS Collaboration, *Search for diboson resonances with boson-tagged jets in pp collisions at $\sqrt{s} = 13$ TeV with the ATLAS detector*, Phys. Lett. **B777** (2018) 91–113, arXiv:1708.04445 [hep-ex].

[29] ATLAS Collaboration, *Search for WZ resonances in the fully leptonic channel using pp collisions at $\sqrt{s} = 8$ TeV with the ATLAS detector*, Phys. Lett. **B737** (2014) 223–243, arXiv:1406.4456 [hep-ex].

[30] CMS Collaboration, *Search for new resonances decaying via WZ to leptons in proton-proton collisions at $\sqrt{s} = 8$ TeV*, Phys. Lett. **B740** (2015) 83–104, arXiv:1407.3476 [hep-ex].

[31] ATLAS Collaboration, *Search for resonant diboson production in the $\ell\ell q\bar{q}$ final state in pp collisions at $\sqrt{s} = 8$ TeV with the ATLAS detector*, Eur. Phys. J. **C75** (2015) 69, arXiv:1409.6190 [hep-ex].

[32] ATLAS Collaboration, *Search for production of WW/WZ resonances decaying to a lepton, neutrino and jets in pp collisions at $\sqrt{s} = 8$ TeV with the ATLAS detector*, Eur. Phys. J. **C75** (2015) 209, arXiv:1503.04677 [hep-ex], [Erratum: Eur. Phys. J.C75,370(2015)].

[33] ATLAS Collaboration, *Search for high-mass diboson resonances with boson-tagged jets in proton-proton collisions at $\sqrt{s} = 8$ TeV with the ATLAS detector*, JHEP **12** (2015) 055, arXiv:1506.00962 [hep-ex].

[34] CMS Collaboration, *Search for massive resonances in dijet systems containing jets tagged as W or Z boson decays in pp collisions at $\sqrt{s} = 8$ TeV*, JHEP **08** (2014) 173, `arXiv:1405.1994` `[hep-ex]`.

[35] ATLAS Collaboration, *Combination of searches for WW, WZ, and ZZ resonances in pp collisions at $\sqrt{s} = 8$ TeV with the ATLAS detector*, Phys. Lett. **B755** (2016) 285–305, `arXiv:1512.05099` `[hep-ex]`.

[36] ATLAS Collaboration, *Search for WW/WZ resonance production in $\ell\nu qq$ final states in pp collisions at $\sqrt{s} = 13$ TeV with the ATLAS detector*, `arXiv:1710.07235` `[hep-ex]`.

[37] ATLAS Collaboration, *Searches for heavy ZZ and ZW resonances in the $\ell\ell qq$ and $\nu\nu qq$ final states in pp collisions at $\sqrt{s} = 13$ TeV with the ATLAS detector*, `arXiv:1708.09638` `[hep-ex]`.

[38] L. Evans and P. Bryant, *LHC Machine*, JINST **3** (2008) S08001.

[39] ATLAS Collaboration, *Luminosity Results for Run1 (2010-2012)*, `https://twiki.cern.ch/twiki/bin/view/AtlasPublic/LuminosityPublicResultsRun2`.

[40] ATLAS Collaboration, *Luminosity Results for Run2 (2015-2017)*, `https://twiki.cern.ch/twiki/bin/view/AtlasPublic/LuminosityPublicResults`.

[41] ATLAS Collaboration, *The ATLAS Experiment at the CERN Large Hadron Collider*, JINST **3** (2008) S08003.

[42] CMS Collaboration, *The CMS Experiment at the CERN LHC*, JINST **3** (2008) S08004.

[43] ALICE Collaboration, *The ALICE experiment at the CERN LHC*, JINST **3** (2008) S08002.

[44] LHCb Collaboration, *The LHCb Detector at the LHC*, JINST **3** (2008) S08005.

[45] TOTEM Collaboration, *The TOTEM experiment at the CERN Large Hadron Collider*, JINST **3** (2008) S08007.

[46] LHCf Collaboration, *Technical design report of the LHCf experiment: Measurement of photons and neutral pions in the very forward region of LHC*, CERN-LHCC-2006-004.

[47] P. Jenni and M. Nessi, *ATLAS Forward Detectors for Luminosity Measurement and Monitoring*, Tech. Rep. CERN-LHCC-2004-010. LHCC-I-014, CERN, Geneva, Mar, 2004. `https://cds.cern.ch/record/721908`.

[48] MoEDAL Collaboration, *Technical Design Report of the MoEDAL Experiment*, CERN-LHCC-2009-006, MoEDAL-TDR-001.

[49] ATLAS Collaboration, *ATLAS detector and physics performance: Technical Design Report, 1*. Technical Design Report ATLAS. CERN, Geneva, 1999. `https://cds.cern.ch/record/391176`.

[50] S. Parker, C. Kenney, and J. Segal, *3D – A proposed new architecture for solid-state radiation detectors*, Nuclear Instruments and Methods in Physics Research Section A: Accelerators, Spectrometers, Detectors and Associated Equipment **395** (1997) 328 – 343, `http://www.sciencedirect.com/science/article/pii/S0168900297006943`, Proceedings of the Third International Workshop on Semiconductor Pixel Detectors for Particles and X-rays.

[51] F. Hartmann, *Silicon tracking detectors in high-energy physics*, Nuclear Instruments and Methods in Physics Research Section A: Accelerators, Spectrometers, Detectors and Associated Equipment **666** (2012) 25 – 46, http://www.sciencedirect.com/science/article/pii/S0168900211020389, Advanced Instrumentation.

[52] C. D. Via, M. Boscardin, G.-F. D. Betta, G. Darbo, C. Fleta, C. Gemme, P. Grenier, S. Grinstein, T.-E. Hansen, J. Hasi, C. Kenney, A. Kok, S. Parker, G. Pellegrini, E. Vianello, and N. Zorzi, *3D silicon sensors: Design, large area production and quality assurance for the ATLAS IBL pixel detector upgrade*, Nuclear Instruments and Methods in Physics Research Section A: Accelerators, Spectrometers, Detectors and Associated Equipment **694** (2012) 321 – 330, http://www.sciencedirect.com/science/article/pii/S0168900212008509.

[53] R. Gluckstern, *Uncertainties in track momentum and direction, due to multiple scattering and measurement errors*, Nuclear Instruments and Methods **24** (1963) 381 – 389, http://www.sciencedirect.com/science/article/pii/0029554X63903471.

[54] S. Haywood, *Impact Parameter Resolution in the Presence of Multiple-Scattering*, ATL-INDET-94-091, ATL-I-PN-91, CERN-ATL-INDET-94-091.

[55] ATLAS Collaboration, *Track Reconstruction Performance of the ATLAS Inner Detector at $\sqrt{s} = 13$ TeV*, Tech. Rep. ATL-PHYS-PUB-2015-018, CERN, Geneva, Jul, 2015. https://cds.cern.ch/record/2037683.

[56] ATLAS Collaboration, A. Antonov, N. Korotkova, A. Romaniouk, E. Shulga, S. Timoshenko, E. Hines, and A. Alonso, *Performance of the TRT in Heavy Ion Collisions*, Tech. Rep. ATL-COM-PHYS-2012-1544, CERN, Geneva, Oct, 2012. https://cds.cern.ch/record/1489962.

[57] ATLAS Collaboration, *Study of the material of the ATLAS inner detector for Run2 of the LHC*, Tech. Rep. CERN-EP-2017-081, CERN, Jul, 2017. https://cds.cern.ch/record/2273894.

[58] ATLAS Collaboration, *Technical Design Report for the ATLAS Inner Tracker Strip Detector*, Tech. Rep. CERN-LHCC-2017-005. ATLAS-TDR-025, CERN, Geneva, Apr, 2017. https://cds.cern.ch/record/2257755.

[59] ATLAS Collaboration, *Letter of Intent for the Phase-I Upgrade of the ATLAS Experiment*, Tech. Rep. CERN-LHCC-2011-012. LHCC-I-020, CERN, Geneva, Nov, 2011. https://cds.cern.ch/record/1402470.

[60] ATLAS Collaboration, T. Kawamoto, S. Vlachos, L. Pontecorvo, J. Dubbert, G. Mikenberg, P. Iengo, C. Dallapiccola, C. Amelung, L. Levinson, R. Richter, and D. Lellouch, *New Small Wheel Technical Design Report*, Tech. Rep. CERN-LHCC-2013-006. ATLAS-TDR-020, CERN, Jun, 2013. https://cds.cern.ch/record/1552862.

[61] L. Rossi and O. Brüning, *High Luminosity Large Hadron Collider A description for the European Strategy Preparatory Group*, Tech. Rep. CERN-ATS-2012-236, CERN, Geneva, Aug, 2012. https://cds.cern.ch/record/1471000. The project is partially supported by the EC as FP7 HiLumi LHC Design Study under grant no. 284404 Collaboration.

[62] ATLAS Collaboration, *Letter of Intent for the Phase-II Upgrade of the ATLAS Experiment*, LHCC-I-023, CERN-LHCC-2012-022.

[63] *High Luminosity upgrade for the LHC*,
`http://hilumilhcds.web.cern.ch/about/hl-lhc-project`.

[64] ATLAS Collaboration, *Performance of jet substructure techniques for large-R jets in proton-proton collisions at $\sqrt{s} = 7$ TeV using the ATLAS detector*, JHEP **09** (2013) 076, `arXiv:1306.4945 [hep-ex]`.

[65] J. E. Huth et al., *Toward a standardization of jet definitions*, 1990 DPF Summer Study on High-energy Physics: Research Directions for the Decade, Snowmass, Colorado, June 25-July 13, 1990, 134–136, `http://lss.fnal.gov/cgi-bin/find_paper.pl?conf-90-249`.

[66] G. P. Salam, *Towards Jetography*, Eur. Phys. J. **C67** (2010) 637–686, `arXiv:0906.1833 [hep-ph]`.

[67] S. D. Ellis and D. E. Soper, *Successive combination jet algorithm for hadron collisions*, Phys. Rev. **D48** (1993) 3160–3166, `arXiv:hep-ph/9305266 [hep-ph]`.

[68] S. Catani, Y. Dokshitzer, M. Seymour, and B. Webber, *Longitudinally-invariant k_t-clustering algorithms for hadron-hadron collisions*, Nuclear Physics B **406** (1993) 187 – 224, `http://www.sciencedirect.com/science/article/pii/055032139390166M`.

[69] Y. L. Dokshitzer, G. D. Leder, S. Moretti, and B. R. Webber, *Better jet clustering algorithms*, JHEP **08** (1997) 001, `arXiv:hep-ph/9707323 [hep-ph]`.

[70] M. Cacciari, G. P. Salam, and G. Soyez, *The Anti-k_t jet clustering algorithm*, JHEP **04** (2008) 063, `arXiv:0802.1189 [hep-ph]`.

[71] D. Krohn, J. Thaler, and L.-T. Wang, *Jet Trimming*, JHEP **02** (2010) 084, `arXiv:0912.1342 [hep-ph]`.

[72] J. M. Butterworth, A. R. Davison, M. Rubin, and G. P. Salam, *Jet substructure as a new Higgs search channel at the LHC*, Phys. Rev. Lett. **100** (2008) 242001, `arXiv:0802.2470 [hep-ph]`.

[73] S. D. Ellis, C. K. Vermilion, and J. R. Walsh, *Recombination Algorithms and Jet Substructure: Pruning as a Tool for Heavy Particle Searches*, Phys. Rev. **D81** (2010) 094023, `arXiv:0912.0033 [hep-ph]`.

[74] ATLAS Collaboration, *Monte Carlo Calibration and Combination of In-situ Measurements of Jet Energy Scale, Jet Energy Resolution and Jet Mass in ATLAS*, ATLAS-CONF-2015-037.

[75] ATLAS Collaboration, *Jet mass reconstruction with the ATLAS Detector in early Run2 data*, ATLAS-CONF-2016-035.

[76] ATLAS Collaboration, *Jet energy measurement with the ATLAS detector in proton-proton collisions at $\sqrt{s} = 7$ TeV*, The European Physical Journal C **73** (2013) 2304, `https://doi.org/10.1140/epjc/s10052-013-2304-2`.

[77] ATLAS Collaboration, *Identification of boosted, hadronically decaying W bosons and comparisons with ATLAS data taken at $\sqrt{s} = 8$ TeV*, Eur. Phys. J. **C76** (2016) 154, `arXiv:1510.05821 [hep-ex]`.

[78] A. J. Larkoski, G. P. Salam, and J. Thaler, *Energy Correlation Functions for Jet Substructure*, JHEP **06** (2013) 108, `arXiv:1305.0007 [hep-ph]`.

[79] A. J. Larkoski, I. Moult, and D. Neill, *Power Counting to Better Jet Observables*, JHEP **12** (2014) 009, arXiv:1409.6298 [hep-ph].

[80] A. J. Larkoski, I. Moult, and D. Neill, *Analytic Boosted Boson Discrimination*, JHEP **05** (2016) 117, arXiv:1507.03018 [hep-ph].

[81] ATLAS Collaboration, *Identification of boosted, hadronically-decaying W and Z bosons in $\sqrt{s} = 13$ TeV Monte Carlo Simulations for ATLAS*, Tech. Rep. ATL-PHYS-PUB-2015-033, CERN, Geneva, Aug, 2015. http://cds.cern.ch/record/2041461.

[82] ATLAS Collaboration, *Expected Performance of Boosted Higgs ($\to b\bar{b}$) Boson Identification with the ATLAS Detector at $\sqrt{s} = 13$ TeV*, Tech. Rep. ATL-PHYS-PUB-2015-035, CERN, Geneva, Aug, 2015. https://cds.cern.ch/record/2042155.

[83] ATLAS Collaboration, *Boosted hadronic top identification at ATLAS for early 13 TeV data*, Tech. Rep. ATL-PHYS-PUB-2015-053, CERN, Geneva, Dec, 2015. https://cds.cern.ch/record/2116351.

[84] ATLAS Collaboration, *Quark versus Gluon Jet Tagging Using Charged Particle Multiplicity with the ATLAS Detector*, Tech. Rep. ATL-PHYS-PUB-2017-009, CERN, Geneva, May, 2017. https://cds.cern.ch/record/2263679.

[85] ATLAS Collaboration, *Measurements of $t\bar{t}$ differential cross-sections of highly boosted top quarks decaying to all-hadronic final states in pp collisions at $\sqrt{s} = 13$ TeV using the ATLAS detector*, Tech. Rep. CERN-EP-2017-226, CERN, Geneva, Jan, 2018. https://cds.cern.ch/record/2299430.

[86] ATLAS Collaboration, *Performance of the ATLAS Track Reconstruction Algorithms in Dense Environments in LHC Run2*, Eur. Phys. J. **C77** (2017) 673, arXiv:1704.07983 [hep-ex].

[87] ATLAS Collaboration, *Topological cell clustering in the ATLAS calorimeters and its performance in LHC Run1*, Eur. Phys. J. **C77** (2017) 490, arXiv:1603.02934 [hep-ex].

[88] ATLAS Collaboration, *Improving jet substructure performance in ATLAS using Track-CaloClusters*, Tech. Rep. ATL-PHYS-PUB-2017-015, CERN, Geneva, Jul, 2017. https://cds.cern.ch/record/2275636.

[89] T. Sjostrand, S. Mrenna, and P. Z. Skands, *A Brief Introduction to PYTHIA 8.1*, Comput. Phys. Commun. **178** (2008) 852–867, arXiv:0710.3820 [hep-ph].

[90] ATLAS Collaboration, *ATLAS Run1 Pythia8 tunes*, Tech. Rep. ATL-PHYS-PUB-2014-021, CERN, Geneva, Nov, 2014. https://cds.cern.ch/record/1966419.

[91] R. D. Ball et al., *Parton distributions with LHC data*, Nucl. Phys. **B867** (2013) 244–289, arXiv:1207.1303 [hep-ph].

[92] ATLAS Collaboration, *Jet reconstruction and performance using particle flow with the ATLAS Detector*, Eur. Phys. J. **C77** (2017) 466, arXiv:1703.10485 [hep-ex].

[93] ATLAS Collaboration, *Search for diboson resonances with jets in 79 fb^{-1} of pp collisions at $\sqrt{s} = 13$ TeV with the ATLAS detector*, Tech. Rep. CONF-EXOT-2018-07, CERN, Geneva, May, 2018.

[94] G. Punzi, *Sensitivity of searches for new signals and its optimization*, eConf **C030908** (2003) MODT002, `arXiv:physics/0308063 [physics]`, [,79(2003)].

[95] Courtesy of Roland Jansky.

[96] T. Gleisberg, S. Hoeche, F. Krauss, M. Schonherr, S. Schumann, F. Siegert, and J. Winter, *Event generation with SHERPA 1.1*, JHEP **02** (2009) 007, `arXiv:0811.4622 [hep-ph]`.

[97] H.-L. Lai, M. Guzzi, J. Huston, Z. Li, P. M. Nadolsky, J. Pumplin, and C. P. Yuan, *New parton distributions for collider physics*, Phys. Rev. **D82** (2010) 074024, `arXiv:1007.2241 [hep-ph]`.

[98] ATLAS Collaboration, *Measurement of the W-boson mass in pp collisions at $\sqrt{s} = 7$ TeV with the ATLAS detector*, `arXiv:1701.07240 [hep-ex]`.

[99] CMS Collaboration, LHCb Collaboration, *Observation of the rare $B_s^0 \to \mu^+\mu^-$ decay from the combined analysis of CMS and LHCb data*, Nature **522** (2015) 68–72, `arXiv:1411.4413 [hep-ex]`.

[100] LHCb Collaboration, *Measurement of the $B_s^0 \to \mu^+\mu^-$ Branching Fraction and Effective Lifetime and Search for $B^0 \to \mu^+\mu^-$ Decays*, Phys. Rev. Lett. **118** (2017) 191801, `https://link.aps.org/doi/10.1103/PhysRevLett.118.191801`.

[101] D. Bertolini, P. Harris, M. Low, and N. Tran, *Pileup per particle identification*, Journal of High Energy Physics **2014** (2014) 59, `https://doi.org/10.1007/JHEP10(2014)059`.

[102] ATLAS Collaboration, *ATLAS Phase-II Upgrade Scoping Document*, Tech. Rep. CERN-LHCC-2015-020. LHCC-G-166, CERN, Geneva, Sep, 2015. `https://cds.cern.ch/record/2055248`.

[103] ATLAS Collaboration, *Measurement prospects for VBF $H \to WW^{(*)} \to e\nu\mu\nu$ production with $3\ ab^{-1}$ of HL-LHC pp-collisions*, Tech. Rep. ATL-PHYS-PUB-2016-018, CERN, Geneva, Aug, 2016. `https://cds.cern.ch/record/2209092`.

[104] ATLAS Collaboration, *Technical Design Report for the ATLAS Inner Tracker Pixel Detector*, Tech. Rep. CERN-LHCC-2017-021. ATLAS-TDR-030, CERN, Geneva, Sep, 2017. `https://cds.cern.ch/record/2285585`.

[105] N. Hessey, *IDRES program*, `http://hessey.web.cern.ch/hessey/ITk/idres.html`.

[106] A. Salzburger, S. Todorova, and M. Wolter, *The ATLAS Tracking Geometry Description*, Tech. Rep. ATL-SOFT-PUB-2007-004. ATL-COM-SOFT-2007-009, CERN, Geneva, Jun, 2007. `https://cds.cern.ch/record/1038098`.

[107] GEANT4 Collaboration, *GEANT4: A Simulation toolkit*, Nucl. Instrum. Meth. **A506** (2003) 250–303.

[108] J. Boudreau and V. Tsulaia, *The GeoModel Toolkit for Detector Description*, `https://cds.cern.ch/record/865601`.

[109] N. Calace and A. Salzburger, *ATLAS Tracking Detector Upgrade studies using the Fast Simulation Engine*, Journal of Physics: Conference Series **664** (2015) 072005, `http://stacks.iop.org/1742-6596/664/i=7/a=072005`.

[110] *The Virtual Point 1 website*, `https://atlas-vp1.web.cern.ch/atlas-vp1/home/`.

[111] Courtesy of Ben Harry Smart.

[112] T. Cornelissen, M. Elsing, S. Fleischmann, W. Liebig, E. Moyse, and A. Salzburger, *Concepts, Design and Implementation of the ATLAS New Tracking (NEWT)*, Tech. Rep. ATL-SOFT-PUB-2007-007. ATL-COM-SOFT-2007-002, CERN, Geneva, Mar, 2007. `https://cds.cern.ch/record/1020106`.

[113] A. Rosenfeld and J. L. Pfaltz, *Sequential Operations in Digital Picture Processing*, J. ACM **13** (1966) 471–494, `http://doi.acm.org/10.1145/321356.321357`.

[114] ATLAS Collaboration, *A neural network clustering algorithm for the ATLAS silicon pixel detector*, JINST **9** (2014) P09009, `arXiv:1406.7690 [hep-ex]`.

[115] K. Edmonds, S. Fleischmann, T. Lenz, C. Magass, J. Mechnich, and A. Salzburger, *The Fast ATLAS Track Simulation (FATRAS)*, Tech. Rep. ATL-SOFT-PUB-2008-001. ATL-COM-SOFT-2008-002, CERN, Geneva, Mar, 2008. `https://cds.cern.ch/record/1091969`.

[116] ATLAS Collaboration, *Properties of clusters and seeds for the ITk*, `https://atlas.web.cern.ch/Atlas/GROUPS/PHYSICS/PLOTS/IDTR-2016-011`, IDTR-2016-011.

[117] R. Fruhwirth, *Application of Kalman filtering to track and vertex fitting*, Nucl. Instrum. Meth. **A262** (1987) 444–450.

[118] ATLAS Collaboration, *The Optimization of ATLAS Track Reconstruction in Dense Environments*, Tech. Rep. ATL-PHYS-PUB-2015-006, CERN, Geneva, Mar, 2015. `https://cds.cern.ch/record/2002609`.

[119] ATLAS Collaboration, *Performance of the ATLAS Inner Detector Track and Vertex Reconstruction in the High Pile-Up LHC Environment*, Tech. Rep. ATLAS-CONF-2012-042, CERN, Geneva, Mar, 2012. `https://cds.cern.ch/record/1435196`.

[120] Courtesy of Nora Emilia Pettersson.

[121] A. Salzburger, *Track Reconstruction in Pb-Pb collisions at $\sqrt{s_{NN}} = 2.76$ TeV*, Tech. Rep. ATL-COM-PHYS-2011-015, CERN, Geneva, Jan, 2011. `https://cds.cern.ch/record/1321154`.

[122] ATLAS Collaboration, *Final Report: ATLAS Phase-2 Tracker Upgrade Layout Task Force*, Tech. Rep. ATL-UPGRADE-PUB-2012-004, CERN, Geneva, Oct, 2012. `https://cds.cern.ch/record/1482960`.

[123] ATLAS Collaboration, *Alignment of the ATLAS Inner Detector with the initial LHC data at $\sqrt{s} = 13$ TeV*, Tech. Rep. ATL-PHYS-PUB-2015-031, CERN, Geneva, Jul, 2015. `https://cds.cern.ch/record/2038139`.

[124] K. Motohashi, *Fractions of Inactive Modules at the end of Run1, during the LS1 and at the beginning of Run2*, Tech. Rep. ATL-INDET-INT-2016-001, CERN, Geneva, Jan, 2016. `https://cds.cern.ch/record/2120796`.

[125] Courtesy of Maximilian Emanuel Goblirsch-Kolb.

[126] ATLAS Collaboration, *Final Report of the ITk Layout Task Force*, Tech. Rep. ATL-COM-UPGRADE-2016-042, CERN, Geneva, Dec, 2016. https://cds.cern.ch/record/2239573.

[127] ATLAS Collaboration, *Performance of b-Jet Identification in the ATLAS Experiment*, JINST **11** (2016) P04008, arXiv:1512.01094 [hep-ex].

Acknowledgements

so much together that I can't imagine my last years without your great conviction and dedication. Nora, you deserve all my appreciation, gratitude and penguins 🐧 .

Sono stata particolarmente fortunata ad incontrare Nora Pettersson, compagna meravigliosa e straordinaria. Ho goduto di ogni momento trascorso insieme a ridere, lamentarci, spettegolare, impazzire e, sì, lavorare. Abbiamo condiviso così tanto insieme che non riuscirei ad immaginare gli ultimi anni senza il tuo impegno e la tua determinazione. Nora, ti meriti tutta la mia stima, la mia gratitudine e i miei pinguini 🐧 .

I also would like to thank all the current and past members of the UniGe group. It has been extremely fruitful being part of such an amazing group, plenty of expert and bright scientist. Thank you all for the productive discussions, for being supportive and enthusiastic, and sharing your interesting ideas. I felt really accepted!

Vorrei inoltre ringraziare tutti i membri, presenti e passati, dell'Università di Ginevra. È stato estremamente proficuo far parte di questo gruppo straordinario pieno di menti brillanti ed esperte. Grazie per i dialoghi costruttivi, per essere sempre stati entusiasti e incoraggianti, per aver condiviso le vostre idee interessanti. Mi sono sempre sentita accettata!

Thank you to the ITk Simulation & Performance and Upgrade Tracking groups. Thank you all for the confidence you expressed in me and your full support. It was a pleasure to work with all of you during these exciting years!

Grazie a coloro che hanno fatto parte dei gruppi ITk Simulation & Performance e Upgrade Tracking per la fiducia che mi avete dimostrato e il vostro sostegno. È stato un piacere lavorare con tutti voi in questi anni emozionanti.

I would also like to say a special thank you to all the people that have share with me the D-side of the 3rd floor of B40. Among them, I must especially thank Julia, who turned out to be a very good friend. Thank you for the dinners together, the funny chats and the cups of tee!

Un ringraziamento speciale va fatto alle persone con cui condivido il corridoio D al terzo piano del B40. Tra loro, vorrei ringraziare in maniera particolare Julia, che si è rivelata un'ottima amica. Grazie per le cene insieme, le chiacchierate divertenti e le tazze di tè.

Thanks to Ludovica, my first office mate at CERN, for her unquestionable expertise on clothes and fashion, and to Louis, without whom my French summary would have been a mess!

Grazie a Ludovica, con la quale ho condiviso il mio primo ufficio al CERN, per la sua indubbia competenza sulla moda, e a Louis, senza il quale l'abstract in francese sarebbe stato un vero disastro!

Thanks (again) to the little-Italy corner. Thanks to Nicola, Felice, Mirko, Maddalena, Silvio who became the best friend ever to share lunches, dinners, tears and laughs. Thanks to Ylenia, the best friend I have ever met: I still believe our friendship is among the most wonderful things the last years returned me.

Grazie (di nuovo) all'angolo di Italia. Grazie a Nicola, Felice, Mirko, Maddalena, Silvio che sono diventati i migliori amici di sempre per condividere pranzi, cene, lacrime e risate. Grazie ad Ylenia, la migliore amica che abbia mai incontrato: penso ancora che la nostra amicizia sia tra le cose più belle che ho ricevuto negli ultimi anni.

To my always-present friends for keeping close in distance and always being there: Thank you Elena

and Anna!
Grazie alle amiche di sempre per essermi vicine nonostante la distanza ed essere sempre presenti.
Grazie Elena e Anna!

I believe nobody can thank his own family enough.
Penso che nessuno possa ringraziare abbastanza la propria famiglia.

I must deeply thank my parents-in-law Fiorenza and Ciro, and my sister-in-law Rosalinda for the
affection I always receive.
Devo ringraziare profondamente i miei suoceri Fiorenza e Ciro, e mia cognata Rosalinda per l'affetto
che ricevo.

To my grandparents. To Grandma Flavia and Grandpa Lello for your immense love and continuous
support. To Grandma Lina and Grandpa Antonio for holding my hands and, silently, indicating me
the way.
Grazie ai miei nonni. A nonna Flavia e nonno Lello per il loro immenso amore e supporto continuo. A
nonna Lina e nonno Antonio, perché mi tengono sempre per mano e silenziosamente mi indicano la via.

A huge thank you to my parents, Rosaria and Alberto, because they have always stood by my side
through all the ups and downs of life, unconditionally. Thank you for being the best parents in the
world!
Un enorme Grazie ai miei genitori, Rosaria e Alberto, perché mi sono sempre stati al mio fianco tra
gli alti e bassi della vita, in maniera incondizionata. Grazie per essere i migliori genitori al mondo!

Thank you to my brother Antonio and my sister Debora, because you are always there when I need.
To my little sister Beatrice, since she wanted a few lines devoted to her. Thank you for the long talks
we have at all hours of the day and night, for trusting each other and for being, always, so similar. I
see myself in you, but bolder, stronger and braver!
Grazie a mio fratello Antonio e a mia sorella Debora, perché sono sempre presenti nel momento del
bisogno. Alla mia sorellina Beatrice, perché voleva un paio di linee di ringraziamento tutte per lei.
Grazie per le lunghe chiacchierate a qualunque ora del giorno e della notte, per la fiducia recip-
roca e per essere sempre così simili. In te rivedo me stessa, ma più ambiziosa, più forte e più coraggiosa!

I would like to offer my sincerest gratitude to my loving husband and soul-mate Francesco. The
journey was not always simple, but your everlasting faith has made a difference at crucial times.
Thank you.
Desidero esprimere la mia più sincera gratitudine al mio marito amorevole e anima gemella Francesco.
Il viaggio non è stato sempre semplice, ma la tua continua fiducia ha fatto la differenza nei momenti
più difficili. Grazie.

Lastly, Thanks to me.
Infine, Grazie a me stessa.